



Politechnika Wrocławska

FIELD OF SCIENCE:

DISCIPLINE OF SCIENCE: Mechanical Engineering

DOCTORAL DISSERTATION

Title of the doctoral dissertation

Investigation of properties of cobalt-based alloys with high glass-forming ability developed by selective laser melting and plasma spraying

Badania właściwości stopów na bazie kobaltu o wysokiej zdolności do zeszklenia wytworzonych za pomocą selektywnego stapiania laserowego oraz natryskiwania plazmowego

MSc Eng. Anna Maria Kuś

Supervisor:

DSc Eng. Wirginia Pilarczyk, Assoc. Prof.

Assistant supervisor:

DSc Eng. Aleksandra Małachowska

Keywords: metallic glass, amorphous metal, BMG, selective laser melting, plasma spraying, pressure casting

CONTENTS

List of abbreviations.....	4
I. Abstract	5
1. English version abstract	5
2. Polish version abstract	7
II. Thesis IntrOduction	11
III. State-of-the-art	13
1. Definition of amorphous metals	13
2. Fabrication conditions of amorphous metal.....	14
3. Classification of metallic glasses	16
4. Manufacturing technologies of metallic glasses.....	21
4.1. Casting	23
4.2. Atomization	24
4.3. Selective laser melting	25
4.4. Plasma spraying.....	27
5. Selected properties of metallic glasses	31
5.1. Mechanical	32
5.2. Thermal	41
5.3. Chemical	42
5.4. Processability.....	42
6. Applications	43
7. Co-based metallic glasses.....	47
7.1. Classification and properties.....	47
7.2. Manufacturing and applications	51
IV. Research Methods.....	54
1. Research plan	54
2. Alloys selection.....	56
3. Manufacturing processes	58
3.1. Casting	58
3.2. Atomization process.....	59
3.3. Selective laser melting	61
3.4. Atmospheric plasma spraying	63
4. Samples analysis.....	64
4.1. Atomized powders	64
4.2. Cast plates	65

4.3.	Selective laser melting bulk samples	66
4.4.	Plasma sprayed coatings	67
V.	Results	69
1.	CoBFeSiNb results	69
1.1.	CoBFeSiNb atomized powder	69
1.2.	CoBFeSiNb cast plate.....	72
1.3.	CoBFeSiNb selective laser melting printed BMG	74
1.4.	CoBFeSiNb atmospheric plasma sprayed coatings	81
2.	CoBFeTaSiCu results	87
2.1.	CoBFeTaSiCu atomized powder	87
2.2.	CoBFeTaSiCu cast plate	90
2.3.	CoBFeTaSiCu cast ribbon.....	93
2.4.	CoBFeTaSiCu selective laser melting printed BMG.....	94
2.5.	CoBFeTaSiCu atmospheric plasma sprayed coating	102
VI.	Discussion	107
1.	CoBFeSiNb discussion.....	107
1.1.	CoBFeSiNb atomized powder.....	107
1.2.	CoBFeSiNb cast plate.....	108
1.3.	CoBFeSiNb selective laser melting printed BMG	109
1.4.	CoBFeSiNb atmospheric plasma sprayed coating.....	113
2.	Comparison of CoBFeSiNb samples	116
3.	CoBFeTaSiCu discussion	118
3.1.	CoBFeTaSiCu atomized powder	118
3.2.	CoBFeTaSiCu cast plate	119
3.3.	CoBFeTaSiCu cast ribbon.....	121
3.4.	CoBFeTaSiCu selective laser melting printed BMG.....	122
3.5.	CoBFeTaSiCu atmospheric plasma sprayed coating	125
4.	Comparison of CoBFeTaSiCu samples	127
5.	Comparison of CoBFeSiNb to CoBFeTaSiCu	130
VII.	Conclusions.....	131
VIII.	Bibliography.....	133
IX.	List of tables	150
X.	List of figures	152

List of abbreviations

Abbreviation	Unit	Description	Abbreviation	Description
D _c	mm	critical diameter	APS	atmospheric plasma spaying
ED	J/mm ³	energy density	BMG	bulk metallic glasses
E _{IT}	GPa	indentation modulus	BSE	backscattered-electron imaging (material contrast)
F	N	normal load	DSC	differential scanning calorimetry
h	mm	hatch distance	DTA	differential thermal analyses
H	mm	layer thickness	ED	energy density
H _{IT}	GPa	indentation hardness	EDS	energy-dispersive spectroscopy
K _c	MPa ^{1/2}	fracture toughness	GFA	glass forming ability
L	mm	sliding distance	HAZ	heat affected zone
P	W	laser power	HRTEM	high-resolution transmission electron microscopy
R _c	°C/s	critical cooling rate	LRO	long range order
T _g	°C	glass transition temperature	MG	metallic glasses
T _l	°C	liquidus temperature	MGC	metallic glass composite
T _m	°C	melting temperature	MRO	medium range order
T _p	°C	crystallization peak temperature	SE	secondary electron imaging (topography contrast)
T _x	°C	crystallization onset temperature	SEM	scanning electron microscopy
v	mm/s	scanning speed	SLM	selective laser melting
V _w	mm ³	volume loss	SRO	short range order
W _s	(mm ³)/Nm	specific wear resistance	STEM	scanning transmission electron microscopy
ΔT	°C	supercooled liquid region	TEM	transmission electron microscopy
σ _y	MPa	yield strength	TTT	time-temperature-transformation
			XRD	X-ray diffraction

I. ABSTRACT

1. English version abstract

The doctoral dissertation entitled "*Investigation of properties of cobalt-based alloys with high glass-forming ability developed by selective laser melting and plasma spraying*" concerns research on the development of amorphous structures in cobalt-based alloys using advanced manufacturing technologies such as selective laser melting and atmospheric plasma spraying. The aim of the research is to obtain an amorphous structure from cobalt-based alloys using these technologies, while achieving mechanical properties comparable to those of samples obtained by well-established casting methods. This aim has enabled a deeper understanding of the manufacturing of these modern alloys, which has so far been limited to casting methods such as die casting or vacuum casting and continuous casting on a wheel (melt spinning). Selective laser melting and plasma spraying offer the possibility of manufacturing more complex shapes with larger surface area or volume than those developed by casting, making them an area of research interest.

The research contained in the doctoral dissertation is organized around two main hypotheses. The first hypothesis states the possibility of obtaining an amorphous structure from a cobalt-based alloy using selective laser melting or atmospheric plasma spraying. The second hypothesis concerns the mechanical properties of the manufactured samples, which should be comparable to those manufactured using conventional manufacturing methods, namely casting. To confirm these hypotheses, the doctoral dissertation includes the following chapters: *Literature Review*, *Research Methods*, *Results*, *Discussion*, and *Conclusions*. The *Literature Review* chapter provides a comprehensive overview of the definition and types of amorphous metals, along with an overview of the technologies used to manufacture them and their applications. The *Literature Review* also provides insight into the unique properties of cobalt-based alloys and knowledge of their manufacturing, enabling the execution of the plan of experimental studies. The next chapter, *Research Methods*, describes in detail the research plan carried out as part of the doctoral dissertation. The results of these studies are collected and presented in the *Results* chapter. The analysis of the research results is included in the *Discussion* chapter, and finally, the conclusions, summary, and confirmation of the hypotheses are presented in the *Conclusions* chapter.

In the *Research Methods* chapter, based on the literature review, two cobalt-based alloys were selected and described: $\text{Co}_{47.6}\text{Fe}_{20.4}\text{B}_{21.9}\text{Si}_{5.1}\text{Nb}_5$ and $\text{Co}_{42}\text{B}_{26.5}\text{Fe}_{20}\text{Ta}_{5.5}\text{Si}_5\text{Cu}_1$. The experimental part of the work includes a description of the development of reference samples by casting, and then atomization to prepare powder for selective laser melting and plasma spraying. As a result, samples such as cast plates and ribbons, gas-atomized powders, printed bulk samples, and plasma-sprayed coatings were obtained. Subsequently, analytical techniques such as digital microscopy, scanning electron microscopy, X-ray diffraction, calorimetric studies, and nanoindentation were used to assess the structure and mechanical properties of the manufactured samples.

The *Results* chapter is divided according to the alloys studied and then according to the manufacturing technologies used. The analysis of manufacturing parameters allowed for obtaining fully amorphous bulk samples and amorphous cobalt-based coatings using selective laser melting and plasma spraying techniques, respectively. The results of the experiments and the conclusions drawn from them confirmed both scientific hypotheses regarding the $\text{Co}_{47.6}\text{Fe}_{20.4}\text{B}_{21.9}\text{Si}_{5.1}\text{Nb}_5$ alloy. Samples made of $\text{Co}_{47.6}\text{Fe}_{20.4}\text{B}_{21.9}\text{Si}_{5.1}\text{Nb}_5$ using die casting, selective laser melting, and plasma spraying showed a range of values for the supercooled liquid region

from 41 to 50°C. Each of the applied manufacturing technologies with appropriately selected parameters enabled the development of fully amorphous structures, which was confirmed by the presence of a glass transition temperature on the graphs of differential scanning calorimetry tests. These results were confirmed by X-ray diffraction analysis, which did not detect evidence of crystallization; instead, an amorphous halo was recorded with a maximum for the angle at $46^\circ 2\theta$ (Cu K α irradiation). Additionally, digital and electron microscopy confirmed the presence of only one phase without the presence of precipitations. Optical microscopy revealed the porosity of samples prepared using both alternative manufacturing technologies. Although porosity can affect the strength of the material and reduce the elastic modulus. Another research challenge, observed in all printed samples, was the cracking of the structure, which requires a solution in future studies. Suggestions for solving this challenge arising from this research dissertation are included in the *Conclusions* chapter. The hardness and elastic modulus of bulk samples and coatings were lower than those of cast samples; however, this difference was a maximum of 10%. The hardness of the printed samples was 14.5 GPa, the coatings 14.2 GPa; cast samples showed a hardness of 15.6 GPa. The elastic modulus for the printed samples was 200.6 GPa, and for the coatings 213.7 GPa; the cast samples had an elastic modulus of 222.8 GPa. The observed decrease in hardness and elastic modulus is attributed to differences in cooling rates between technologies and potential structural relaxation related to the heat-affected zone present in both alternative manufacturing processes but absent in casting. The literature review and experimental studies of the $\text{Co}_{47.6}\text{Fe}_{20.4}\text{B}_{21.9}\text{Si}_{5.1}\text{Nb}_5$ alloy have shown that the optimal energy density using selective laser melting is in the range of 39 to 68 J/mm³. The lower limit of energy density provides sufficient heat to melt the powder particles in order to join them. The upper limit limits the value of residual stress in the samples, which could lead to their destruction during processing. In plasma spraying experiments, the energy supplied to melt the powder in the plasma stream was also regulated to avoid overheating the substrates on which the powder particles were deposited. For this purpose, argon was used as a plasma-forming gas, which proved effective in limiting heat transfer at spraying distances between 90 and 110 mm, enabling the development of amorphous coatings. The coatings thus developed showed a favorably low abrasive wear coefficient of $2.0 \cdot 10^{-5} \pm 0.2 \cdot 10^{-5} \text{ mm}^3/\text{Nm}$.

The analysis of the second alloy revealed significant problems with crystallization in most samples. The cast plate showed significant crystallization, leading to an additional casting process to obtain a fully amorphous reference sample. For this purpose, melt spinning was used, which allowed to manufacture a fully amorphous ribbon with a thickness of about 50 μm . X-ray diffraction and differential scanning calorimetry confirmed the amorphous state of the ribbon, while scanning electron microscopy imaging did not show any crystalline phases or the presence of impurities. The hardness of the ribbon was 15.1 GPa, and the elastic modulus was 190.1 GPa. To obtain bulk samples from $\text{Co}_{42}\text{B}_{26.5}\text{Fe}_{20}\text{Ta}_{5.5}\text{Si}_5\text{Cu}_1$ powder using the selective laser melting process, the energy density had to be precisely controlled. Experiments have shown that the best results were obtained in a narrow range from 41 to 50 J/mm³. Despite these limitations, the samples exhibited severe cracking problems caused by high stresses during the rapid solidification of the weld pool. Scanning electron microscope (SEM) observations, confirmed by Rietveld analysis, showed the presence of crystallization in the printed samples at the level of approximately 50% volume. The crystals formed nano- and micro-precipitates inside the amorphous matrix, which was observed using scanning electron microscopy (SEM) and transmission electron microscopy (TEM). Diffraction patterns obtained using the mentioned analysis confirmed the presence of both an amorphous phase and crystalline phases, including $\text{Co}_5\text{Si}_2\text{B}$ and TaB_2 . The presence of crystallization at this level led to a significant increase in the hardness of the material, amounting to 18 GPa. This increase in hardness was attributed to the hardening of the amorphous material through mechanisms including solid solution hardening by

nanocrystallization or interactions between phases boundaries (amorphous and crystalline) boundaries. The elastic modulus of the coatings was 10% higher than in the case of the ribbon reference and was 225.4 GPa.

The coating developed using plasma spraying from $\text{Co}_{42}\text{B}_{26.5}\text{Fe}_{20}\text{Ta}_{5.5}\text{Si}_5\text{Cu}_1$ showed almost complete crystallization with a residual content of the amorphous phase and a problem with high porosity. However, a positive effect on the reduction of porosity by approximately 3 percentage points (from 11.2% to 8.5%) was observed by reducing the spraying distance from 110 to 90 mm. The obtained coating showed good wear resistance, with a wear rate of approximately $1.9 \cdot 10^{-5} \pm 0.20 \cdot 10^{-5} \text{ mm}^3/\text{Nm}$. The hardness of the coating was approximately 14.0 GPa – 7% lower than in the case of the rolled ribbon reference. The decrease in hardness is typical for crystallized alloys compared to their amorphous state. The elastic modulus was similar to that in the case of the ribbon and was 198.2 GPa. The high crystallization of the coatings was attributed to the low glass-forming ability of the $\text{Co}_{42}\text{B}_{26.5}\text{Fe}_{20}\text{Ta}_{5.5}\text{Si}_5\text{Cu}_1$ alloy, which was the result of insufficient homogenization of the alloy during its development from pure elements and then atomization of the powder. As in the case of other forms of the $\text{Co}_{42}\text{B}_{26.5}\text{Fe}_{20}\text{Ta}_{5.5}\text{Si}_5\text{Cu}_1$ alloy, the presence of the TaB_2 phase was observed in the powder; this phase was characterized by irregular shapes of precipitates of various sizes. The presence of this phase was attributed to the lack of sufficient remelting of the pure chemical element, namely tantalum, the melting point of which reaches 3000°C. The insufficiently homogenized liquid phase of the alloy during casting led to a reduction in the glass-forming ability of the $\text{Co}_{42}\text{B}_{26.5}\text{Fe}_{20}\text{Ta}_{5.5}\text{Si}_5\text{Cu}_1$ alloy and, in the case of most manufacturing technologies (except for those with very high cooling rates), resulted in significant crystallization of the samples.

The doctoral dissertation successfully confirmed the hypotheses regarding $\text{Co}_{47.6}\text{Fe}_{20.4}\text{B}_{21.9}\text{Si}_{5.1}\text{Nb}_5$ alloy. This alloy showed a high ability to produce an amorphous structure, enabling pioneering research on the use of cobalt-based alloys with an amorphous structure using selective laser melting and plasma spraying. In addition, studies of the second alloy $\text{Co}_{42}\text{B}_{26.5}\text{Fe}_{20}\text{Ta}_{5.5}\text{Si}_5\text{Cu}_1$, which in the doctoral dissertation was partially amorphous and partially crystalline, contributed to a deeper understanding of the group of alloys with a composite structure and their behavior during manufacturing. The achievements documented in this doctoral dissertation represent a significant advance in the field of mechanical sciences, which have also been published to make the findings available to a wider scientific community. This dissertation makes a significant contribution to expanding knowledge in the field of amorphous metals and their composites and the use of selective laser melting and plasma spraying technologies, confirming research hypotheses and providing insight into the behavior of cobalt-based alloys under various manufacturing conditions. The work sets a promising path for future research on the development of cobalt-based amorphous metals using innovative technologies such as selective laser melting and plasma spraying.

2. Polish version abstract

Rozprawa doktorska zatytułowana *"Badania właściwości stopów na bazie kobaltu o wysokiej zdolności do zeszklenia wytworzonych za pomocą selektywnego stapiania laserowego oraz natryskiwania plazmowego"* dotyczy badań nad rozwojem struktur amorficznych stopów na bazie kobaltu przy użyciu zaawansowanych technologii wytwarzania, takich jak selektywne topienie laserowe i natryskiwanie plazmowe. Celem badań jest otrzymanie struktury amorficznej ze stopów na bazie kobaltu przy użyciu wspomnianych technologii, przy jednoczesnym uzyskaniu właściwości mechanicznych na poziomie podobnym do próbek uzyskanych przez odlewanie. Cel ten umożliwił pogłębienie wiedzy na temat wytwarzania tych nowoczesnych stopów, które dotychczas były

wytwarzane za pomocą metod odlewania, takich jak odlewanie ciśnieniowe lub próżniowe oraz odlewanie ciągłe na bębnie. Selektywne topienie laserowe i natryskiwanie plazmowe oferują możliwość wytworzenia elementów o bardziej złożonych kształtach, o większej powierzchni lub objętości od elementów wytwarzanych za pomocą odlewania, co czyni je interesujące w kontekście badawczym.

Plan badawczy, zawarty w rozprawie doktorskiej, miał na celu walidację prawdziwości postawionych dwóch hipotez badawczych. Pierwsza z hipotez dotyczy możliwości uzyskania struktury amorficznej ze stopu na bazie kobaltu przy użyciu selektywnego topienia laserowego i natryskiwania plazmowego. Druga z hipotez dotyczy właściwości mechanicznych wytworzonych próbek, które powinny być porównywalne z właściwościami próbek wytwarzanych przy użyciu konwencjonalnych metod wytwarzania, tj. odlewania. W celu potwierdzenia hipotez, rozprawa doktorska została podzielona na następujące rozdziały: *Przegląd literatury*, *Metody badań*, *Wyniki*, *Dyskusja* i *Wnioski*. Rozdział *Przegląd literatury* przedstawia definicję i rodzaje metali amorficznych, wraz z przeglądem technologii stosowanych do ich wytwarzania oraz zastosowania. Przegląd literatury dostarcza również wglądu w unikalne właściwości stopów na bazie kobaltu oraz wiedzę na temat ich wytwarzania, która została wykorzystana w celu wykonania planu badań eksperymentalnych. Kolejny rozdział, *Metody badań*, opisuje szczegółowo metodykę badań wykonanych w ramach rozprawy doktorskiej. Wyniki badań zostały zebrane i przedstawione w rozdziale *Wyniki*. Analiza wyników badań została zawarta w rozdziale *Dyskusja*, a ostateczne wnioski, podsumowanie oraz potwierdzenie hipotez przedstawiono w rozdziale *Wnioski*.

W rozdziale *Metody badań*, na podstawie przeglądu literatury, wybrano i opisano dwa stopy na bazie kobaltu: $\text{Co}_{47,6}\text{Fe}_{20,4}\text{B}_{21,9}\text{Si}_{5,1}\text{Nb}_5$ i $\text{Co}_{42}\text{B}_{26,5}\text{Fe}_{20}\text{Ta}_{5,5}\text{Si}_5\text{Cu}_1$. Część eksperymentalna pracy obejmuje opis wytworzenia próbek referencyjnych poprzez odlewanie, a następnie atomizację w celu przygotowania proszku do selektywnego topienia laserowego i natryskiwania plazmowego. W efekcie uzyskano próbki takie jak odlane płytki i taśmy, atomizowane gazem proszki, wydrukowane masywne próbki oraz naniesione plazmowo powłoki. W celu oceny struktury i właściwości mechanicznych wytworzonych próbek zastosowano techniki analityczne takie jak mikroskopię cyfrową, mikroskopię elektronową skaningową, dyfrakcję rentgenowską, badania kalorymetryczne a także nanoindentację.

Rozdział *Wyniki* został podzielony według badanych stopów, a następnie według zastosowanych technologii wytwarzania. Przeprowadzona analiza parametrów wytwarzania pozwoliła na uzyskanie w pełni amorficznych próbek masowych i powłok na bazie kobaltu przy użyciu odpowiednio techniki selektywnego topienia laserowego oraz natryskiwania plazmowego. Wyniki przeprowadzonych eksperymentów i wnioski z nich płynące potwierdziły postawione hipotezy naukowe dla stopu $\text{Co}_{47,6}\text{Fe}_{20,4}\text{B}_{21,9}\text{Si}_{5,1}\text{Nb}_5$. Każda z zastosowanych technologii wytwarzania, z odpowiednio dobranymi parametrami, umożliwiła wytworzenie w pełni zeszlonych struktur, co zostało potwierdzone przez obecność temperatury zeszklenia w badaniach skaningowej kalorymetrii różnicowej. Wyniki te zostały dodatkowo potwierdzone przez analizę dyfrakcji rentgenowskiej, które nie wykryły linii dyfrakcyjnych pochodzących od faz krystalicznych. Zaobserwowane natomiast amorficzne halo z maksimum dla wartości kąta 2θ równym 46° (promieniowanie $\text{Cu K}\alpha$). Dodatkowo, mikroskopia cyfrowa i elektronowa potwierdziły obecność tylko jednej fazy bez obecności wydzieli. Mikroskopia optyczna ujawniła obecność porowatości w próbkach przygotowanych przy użyciu obu alternatywnych technologii wytwarzania. Porowatość może wpływać na wytrzymałość materiału oraz zmniejszać moduł sprężystości. Innym wyzwaniem badawczym, które wymaga rozwiązania w przyszłych badaniach są pęknięcia obecne w wytworzonych próbkach zarówno drukowanych jak i natrykiwanych. Sugestie rozwiązania tego problemu zamieszczono w rozdziale *Wnioski*. Własności mechaniczne, twardość i moduł sprężystości, masywnych próbek i powłok były niższe, niż w przypadku próbek

odlewanym; różnica ta jednak wynosiła maksymalnie 10%. Twardość wydrukowanych próbek wynosiła 14,5 GPa, powłok 14,2 GPa; próbki odlewane wykazywały twardość 15,6 GPa. Moduł sprężystości dla wydrukowanych próbek wynosił 200,6 GPa, a dla powłok 213,7 GPa. Próbkę odlewane miały moduł sprężystości równy 222,8 GPa. Zaobserwowany spadek twardości i modułu sprężystości przypisuje się różnicom w szybkości chłodzenia między technologiami oraz potencjalnej relaksacji struktury związanej ze strefą wpływu ciepła obecną w zastosowanych procesach wytwarzania.

Przegląd literatury oraz studia eksperymentalne stopu $\text{Co}_{47,6}\text{Fe}_{20,4}\text{B}_{21,9}\text{Si}_{5,1}\text{Nb}_5$ wykazały, iż optymalną gęstość energii przy użyciu selektywnego topienia laserowego mieści się w zakresie od 39 do 68 J/mm³. Dolne ograniczenie gęstości energii zapewnia wystarczającą ilość ciepła do stopienia cząstek proszku w celu ich połączenia. Górna granica ogranicza wartość naprężeń resztkowych w próbkach, które mogłyby prowadzić do ich zniszczenia podczas obróbki. W eksperymentach dotyczących natryskiwania plazmowego, energia dostarczana do stopienia proszku w strumieniu plazmowym była również regulowana w celu uniknięcia przegrzania podłoża, na którym osadzały się cząstki proszku. W tym celu zastosowano argon jako gaz plazmotwórczy, który wykazał skuteczne ograniczenie transferu ciepła do podłoża. Zastosowane odległości natryskiwania mieściła się między 90 a 110 mm przy mocy palnika plazmowego 22 kW. Tak wytworzone powłoki wykazały się posiadaniem korzystnie niskiego współczynnika zużycia ściernego wynoszącego $2,0 \cdot 10^{-5} \pm 0,2 \cdot 10^{-5} \text{ mm}^3/\text{Nm}$.

Analiza drugiego stopu, $\text{Co}_{42}\text{B}_{26,5}\text{Fe}_{20}\text{Ta}_{5,5}\text{Si}_5\text{Cu}_1$, ujawniła znaczne problemy z krystalizacją stopu. Odlewana płytką uległa krystalizacji, co skutkowało koniecznością przeprowadzenia dodatkowego procesu odlewania w celu uzyskania w pełni amorficznej, referencyjnej próbki. W tym celu zastosowano odlewanie ciągłe na wirującym bębnie, które pozwoliło na wytworzenie w pełni amorficznej taśmy o grubości 50 µm. Dyfrakcja rentgenowska i skaningowa kalorymetria różnicowa potwierdziły amorficzny stan odlanych taśm, podczas gdy obserwacje skaningowym mikroskopem elektronowym nie wykazały obecności wydzieli ani zanieczyszczeń. Twardość taśm wynosiła 15,1 GPa, moduł sprężystości 190,1 GPa. Aby uzyskać masywne próbki z proszku $\text{Co}_{42}\text{B}_{26,5}\text{Fe}_{20}\text{Ta}_{5,5}\text{Si}_5\text{Cu}_1$ przy użyciu procesu selektywnego topienia laserowego, energia gęstości musiała być precyzyjnie kontrolowana. Eksperymenty wykazały, że najlepsze wyniki uzyskano w wąskim zakresie gęstości energii od 41 do 50 J/mm³. Pomimo tych ograniczeń, próbki wykazywały poważne problemy z pękaniem spowodowanym wysokimi naprężeniami podczas szybkiego zestalania się jeziora ciekłego metalu w procesie selektywnego stapiania laserowego. Obserwacje wykonane przy użyciu skaningowego mikroskopu elektronowego, potwierdzone przez analizy Rietvelde, wykazały obecność krystalizacji w wydrukowanych próbkach na poziomie około 50% objętości. Krystalizacja przyjęła formę nano- i mikro-wydzieli wewnątrz amorficznej osnowy, co zaobserwowano za pomocą skaningowej mikroskopii elektronowej oraz transmisyjnej mikroskopii elektronowej. Analiza dyfrakcji przy użyciu mikroskopii transmisyjnej elektronowej potwierdziła obecność zarówno fazy amorficznej, jak i faz krystalicznych, w tym $\text{Co}_5\text{Si}_2\text{B}$ i TaB_2 . Obecność krystalizacji na poziomie około 50% wpłynęła na podwyższenie twardości materiału do 18 GPa. Taki wzrost twardości przypisano utwardzaniu materiału amorficznego poprzez mechanizmy obejmujące utwardzanie roztworu stałego przez nanokrystalizację lub interakcje między granicami faz (amorficznymi i krystalicznymi). Moduł sprężystości wydruków był 10% wyższy od próbki referencyjnej (taśmy) i wynosił 225,4 GPa.

Powłoki wytworzone przy użyciu natryskiwania plazmowego z $\text{Co}_{42}\text{B}_{26,5}\text{Fe}_{20}\text{Ta}_{5,5}\text{Si}_5\text{Cu}_1$ wykazywały krystalizację w większości objętości powłok z resztkową zawartością fazy amorficznej oraz problem z porowatością. Zaobserwowano jednak pozytywny wpływ na redukcję porowatości (z 11,2% do 8,5%) poprzez zmniejszenie odległości natryskiwania z 110 do 90 mm. Uzyskane powłoki posiadały dobrą odporność na zużycie ściernie, z współczynnikiem zużycia ściernego

wynoszącego około $1,9 \cdot 10^{-5} \pm 0,20 \cdot 10^{-5} \text{ mm}^3/\text{Nm}$. Twardość powłoki wynosiła około 14,0 GPa – o 7% mniej niż w przypadku taśmy. Spadek twardości jest typowy dla stopów w stanie krystalicznym w porównaniu z ich twardością w stanie amorficznym. Moduł sprężystości wynosił 198,2 GPa. Wysoka krystalizacja powłok została przypisana niskiej zdolności do zeszklenia stopu $\text{Co}_{42}\text{B}_{26,5}\text{Fe}_{20}\text{Ta}_{5,5}\text{Si}_5\text{Cu}_1$, która była skutkiem niewystarczającej homogenizacji stopu podczas jego wytwarzania z czystych pierwiastków. Podobnie jak w przypadku innych form stopu $\text{Co}_{42}\text{B}_{26,5}\text{Fe}_{20}\text{Ta}_{5,5}\text{Si}_5\text{Cu}_1$, w proszku zaobserwowano obecność fazy TaB_2 . Faza ta odznaczała się nieregularnymi kształtami wydzielen o różnych rozmiarach. Obecność tej fazy była spowodowana brakiem wystarczającego przetopu czystego pierwiastka chemicznego, mianowicie tantalu, którego temperatura topnienia sięga 3000°C. Niewystarczająco ujednoliconą fazą ciekłą stopu podczas odlewania doprowadziła do obniżenia zdolności do zeszklenia stopu $\text{Co}_{42}\text{B}_{26,5}\text{Fe}_{20}\text{Ta}_{5,5}\text{Si}_5\text{Cu}_1$ i w przypadku większości technologii wytwórczych (z wyjątkiem tych o bardzo wysokich szybkościach chłodzenia) spowodowała znaczną krystalizację próbek.

Badania zawarte w rozprawie doktorskiej pt. *"Badania właściwości stopów na bazie kobaltu o wysokiej zdolności do zeszklenia wytworzonych za pomocą selektywnego stapiania laserowego oraz natryskiwania plazmowego"* potwierdziły postawione hipotezy dotyczące stopu $\text{Co}_{47,6}\text{Fe}_{20,4}\text{B}_{21,9}\text{Si}_{5,1}\text{Nb}_5$. Stop ten wykazał wysoką zdolnością do zeszklenia, umożliwiając pionierskie badania nad wykorzystaniem stopów na bazie kobaltu o strukturze amorficznej do zastosowania selektywnego topienia laserowego oraz natryskiwania plazmowego. Badania dotyczące drugiego stopu $\text{Co}_{42}\text{B}_{26,5}\text{Fe}_{20}\text{Ta}_{5,5}\text{Si}_5\text{Cu}_1$, który w rozprawie doktorskiej wykazał strukturę kompozytową o osnowie amorficznej z krystalicznymi wydzieleniami, przyczyniły się do poszerzenia wiedzy o grupie stopów o kompozytowej budowie, w tym ich właściwości oraz zachowanie podczas ich wytwarzania. Osiągnięcia udokumentowane w tej rozprawie doktorskiej reprezentują znaczący postęp w dziedzinie nauk mechanicznych, które zostały również opublikowane w formie artykułów. Rozprawa ta w znaczący sposób przyczynia się do poszerzenia wiedzy z zakresu metali amorficznych, ich kompozytów oraz wykorzystania technologii selektywnego stapiania laserowego oraz natryskiwania plazmowego, oraz dostarcza wiedzy o zachowaniu się stopów na bazie kobaltu w różnych warunkach wytwarzania.

II. THESIS INTRODUCTION

This PhD thesis focuses on investigating the properties of amorphous structures developed from cobalt-based alloys utilizing additive manufacturing and thermal spraying methods. Amorphous metal alloys based on cobalt exhibit remarkable mechanical properties, particularly extraordinary hardness. However, utilization of amorphous metals is still limited due to the restricted value of the cooling rate, which in turn imposes constraints on the achievable dimensions of the fabricated components, thereby affecting their scalability and practical applications in industrial manufacturing. This research establishes novel results about tested manufacturing methodologies capable of overcoming existing dimensional constraints in Co-based amorphous metals development, thereby expanding the potential applications of these sophisticated metallic systems. Through comprehensive literature research and experimental approach involving additive manufacturing and thermal spraying technologies, the research aims to generate bulk samples and coatings from Co-based alloys while preserving the amorphous structures with exceptional mechanical characteristics.

The primary scientific goal of the work is to obtain an amorphous structure from cobalt-based alloys using additive manufacturing and plasma spraying while maintaining the mechanical properties of the obtained materials at a level similar to those obtained through casting. To achieve this goal, the thesis began with a comprehensive analysis of existing manufacturing technologies currently used for developing amorphous alloys based on various chemical elements. This step provides insights into the capabilities and limitations of those technologies, leading to a focus on selective laser melting technology and atmospheric plasma spraying. A subsequent in-depth literature review of cobalt-based alloys with high glass-forming ability enabled systematization of characteristic properties of this group of alloys, guiding the selection of two specific alloy compositions that became the focus of this research. Selected alloys demonstrate superior mechanical performance and exceptional potential for amorphous structure formation.

The research plan incorporates manufacturing parameters based on extensive literature review to establish the best set of parameters for the researched group of materials. The obtained samples were then analyzed to evaluate structure and mechanical properties with the ultimate goal of validating selected manufacturing technologies- atmospheric plasma spraying and selective laser melting. The validation includes comparison of the results to reference samples obtained through casting. This PhD thesis explores the complex relationship between advanced manufacturing techniques and resultant material properties, directly addressing current development limitations. As a result, this research contributes substantively to the advancement of mechanical science and potential engineering applications of advanced materials such as cobalt-based amorphous alloys.

As a measure of obtaining the scientific goal of the thesis the two hypotheses were established. The first hypothesis considers the possibility of obtaining amorphous structure from researched alloys with selected technologies and the second hypothesis evaluates the mechanical properties of obtained forms of alloys.

- **Hypothesis on amorphous structure development:** amorphous structure can be successfully developed using additive manufacturing techniques and spraying methods with cobalt-based alloys that have a high glass-forming ability (e.g., $\text{Co}_{47.6}\text{Fe}_{20.4}\text{B}_{21.9}\text{Si}_{5.1}\text{Nb}_5$ and $\text{Co}_{42}\text{B}_{26.5}\text{Fe}_{20}\text{Ta}_{5.5}\text{Si}_5\text{Cu}_1$).
- **Hypothesis on mechanical properties of amorphous structure:** cobalt-based alloys with high glass-forming ability, when processed through additive manufacturing techniques and spraying methods, will achieve mechanical properties comparable to those of the same alloys developed via traditional casting methods.

III. STATE-OF-THE-ART

1. Definition of amorphous metals

The basic division of solid states of metal alloys by the inner structure criterion is their atoms arrangement. Objects in solid state can have atoms arranged in repeating long-range order (LRO) or do not have that order [1–3]. This description divides materials into those with crystalline structure (Fig. 1 a) and with amorphous structure (Fig. 1 b), respectively. The crystalline structure without defects, built from a continuous crystal lattice with strict atom arrangement, is called a monocrystal [4]. Monocrystal elements can be found in turbine engines, due to their intrinsic ability to resist creep at elevated temperatures [5]. However, utility goods and most construction elements made from metal alloys have a polycrystalline structure, which means that their structure is built from more than one crystal (polycrystal). If a material structure is built from nanometer-sized crystals (often suspended in an amorphous matrix) it is called a nanocrystalline structure (Fig. 1 c)[6]. Crystalline structures are marked by having an LRO of atoms, which indicates that the order of atoms is preserved over a range greater than 20 Å (angstroms). When the order of the atoms is below 20 Å the term medium-range order (MRO) (5–20 Å) and the short-range order (SRO) (2–5 Å) is used. These terms are usually used to describe amorphous structures [7,8]. Amorphous structure, in addition to metal alloys, is also present in quartz glass or polymers. LRO is described as a translation repeating structure, while in 1984 Shechtman discovered structures that have a rotational symmetric structure [3,9]. This kind of structure is called quasicrystals, because of the different types of atoms order compared to the crystal structure (Fig. 1 d). The application of quasicrystal can be found in a low friction coating or as a hardening particles in steel [10].

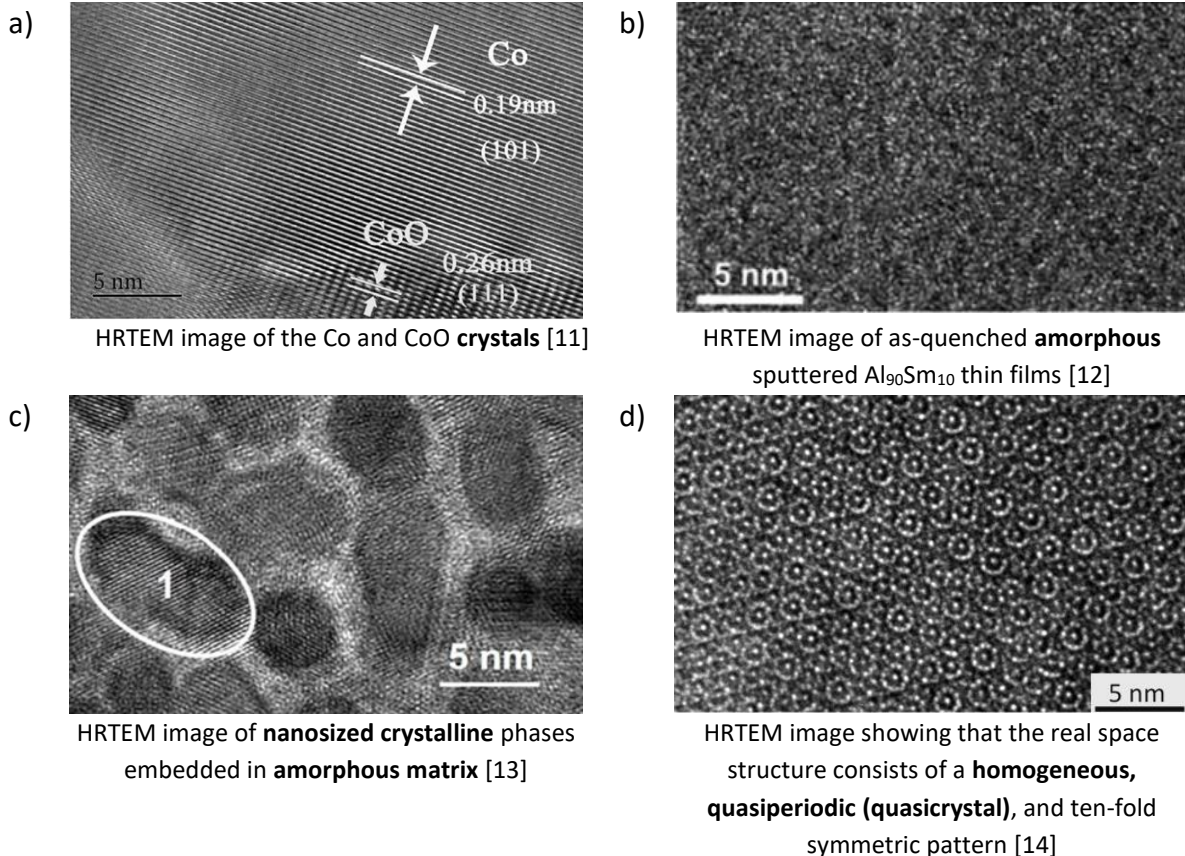


Fig. 1. Samples of different structures in the solid state

2. Fabrication conditions of amorphous metal

Amorphous metals, as previously described, are alloys with an inner structure that do not have a long-range order. To obtain that amorphous structure, the alloy in liquid form (temperature above liquidus temperature T_l) must be cooled rapidly with a continuous cooling rate greater than a critical cooling rate (R_c). The R_c can be determined experimentally or read from a time-temperature transformation graph (TTT). In Fig. 2 a) an example of a TTT graph of an amorphous metal is presented. The black line with arrow represents the R_c . If the cooling rate is lower than R_c , the line representing it will cross the crystalline area, indicating that crystallization occurs. If the cooling rate is only slightly lower than R_c or lower in some period during cooling of the material, the nanocrystal will nucleate in the amorphous matrix. This partial crystallization is often observed in developed metallic glasses and can be found in the literature under the name of metallic glasses composite (MGC). If cooling speed is significantly lower than R_c , then the sample will be fully crystallized. Cross sections of the sample from alloy with good glass forming ability cooled faster than R_c is shown in the top of Fig. 2 b) and with much slower in the bottom of Fig. 2 b). In the second case (cooling rate $< R_c$) the phase transition into crystallized structure is clearly visible, while in the first case (cooling rate $> R_c$) the image of the sample did not change.

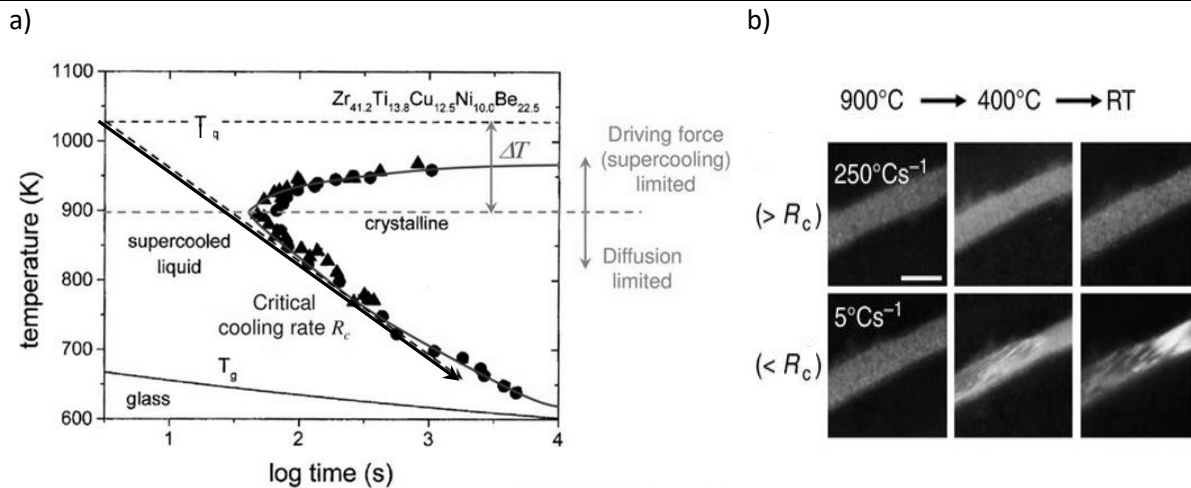


Fig. 2. a) Time-temperature-transformation diagram with marked R_c [15], b) phase transition of amorphous metal upon cooling using in situ TEM [16], RT- room temperature

According to [17] the other definition of an amorphous metal is an undercooled metal alloy, in which the undercooling is significant enough to prevent the dynamic fluctuation of atoms, thereby rendering the material resistant to shear stress. Amorphous metals in the literature are also named metallic glass. The suffix "glass" represents the group of amorphous materials that exhibit glass transition temperature T_g . This temperature can be read from a thermal analysis curve of a heated material in glassy state (Fig. 3) as the characteristic inflection point before any exothermal peak is registered. The exothermal peaks represent the crystallization of the material, and the onset of it is the crystallization temperature T_x . Beside metallic glasses, the glassy state was previously observed and widely described for silicate materials or polymers. In summary, amorphous materials are a larger group that include glassy materials [7].

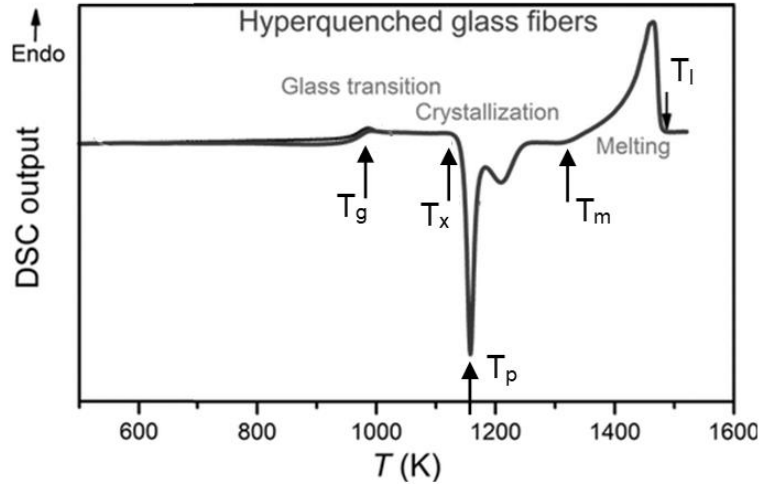


Fig. 3. Graphic representation of the glass transition with differential thermal analysis (DTA) [18]

To describe the ability of a material to form a glassy state, the term glass formation ability (GFA) was proposed. In book [11], it was noted that GFA, in addition to the ability to form a glassy state, describes the ability of material to suppress the crystal nucleation during a cooling process. To quantitatively measure GFA, the researchers established different parameters. Those depended on the characteristic temperatures of material were collected and described in [7]. The results of researcher's work are shown in Tab. 1. Except for parameters based on temperature, the GFA can be determined by the critical diameter D_c . The critical diameter of the material is determined by the highest diameter of the cast rod, which is still fully amorphous.

Tab. 1. Summary of the quantitative criteria proposed to evaluate the GFA [7]

Criterion/parameter	Equation	Reference
Reduced glass transition temperature	$T_{rg} = \frac{T_g}{T_l}$	[19]
ΔT_x supercooled liquid region	$\Delta T_x = T_x - T_g$	[20]
α parameter	$\alpha = \frac{T_x}{T_l}$	[21]
β parameter	$\beta = 1 + \frac{T_x}{T_l} = 1 + \alpha$	[21]
New β parameter	$\beta = \frac{T_x \times T_g}{(T_l - T_x)^2}$	[22]
γ parameter	$\gamma = \frac{T_x}{T_g + T_l}$	[23] [24]
γ_m parameter	$\gamma_m = \frac{2T_x - T_g}{T_l}$	[25]
δ parameter	$\delta = \frac{T_x}{T_l - T_g}$	[26]
K_{gl} parameter	$K_{gl} = \frac{T_x - T_g}{T_m - T_x}$	[27]
φ parameter	$\phi = T_{rg} \left(\frac{\Delta T_x}{T_g} \right)^{0.143}$	[28]

T_{rx} parameter	$T_{rx} = \frac{T_x}{T_m}$	[29]
ω parameter	$\omega = \frac{T_g}{T_x} - \frac{2T_g}{T_g + T_l}$	[30,31]

T_g, T_x, T_m, T_l - temperature of glass transition, crystallization, melting, and liquidus, respectively

3. Classification of metallic glasses

The first amorphous alloy was reported in the work [32] in 1960. In the paper researchers used the term "non-crystalline" to describe newly observed structure of metal alloy. The chemical composition of that research was $Au_{75}Si_{25}$ and was obtained by liquid quenching. It was the first amorphous alloy to be obtained by quenching. In literature and industry, metal alloys with amorphous structure can be found under few equal terms that are shown in Fig. 4. In scientific research the terms metallic glass (MG) or amorphous metal are the most common terms and will be used in this thesis. The term "bulk" can be added as a prefix, implicating that the material discussed does not have a dimension much smaller than the rest of the two (it is 3-dimensional material).

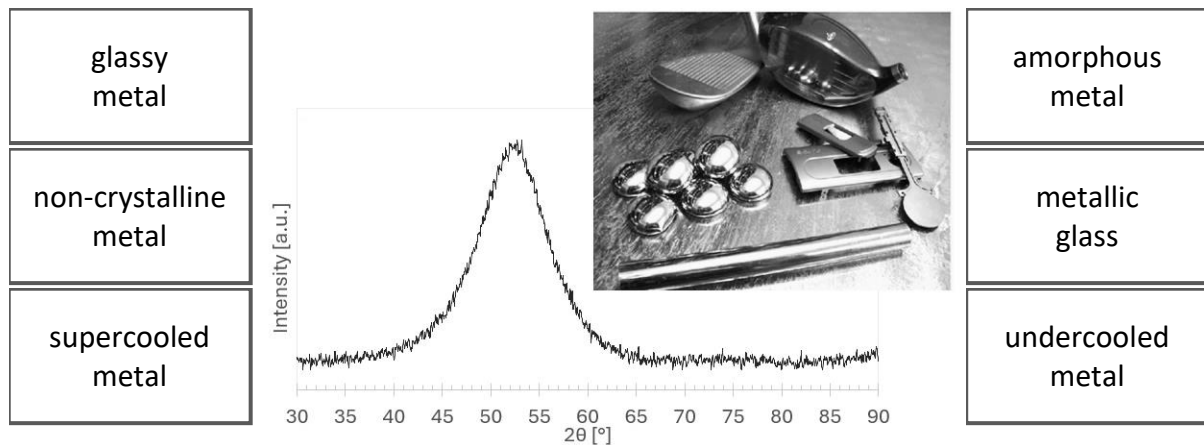


Fig. 4. Term used for alloys with amorphous structure. In the center the X-ray diffraction representation of amorphous metal and examples of applications from work [33]

In the 1960s, scientists developed numerous amorphous metals. The various works on developing metallic glasses led to the collection of a large group of new materials which needed to be grouped. Below are shown the typical categories that metallic glasses can be divided by:

a) Presence of metalloids

The first metallic glass reported was a binary alloy composed of a metal-metal-type (transition metal) element and a metal-metalloid-type element Au-Si. Today, this type of metal-metalloid alloys is more complex, usually built from metalloids like B, Si, Ge, Sb, Te (and often non-metals C and P) with transition (d-block elements) and basic metals (part of p-block elements) like Fe, Co, Ni, Pd, Zr, Mo, Pt, etc. The second type is metal-metal type MG such as Fe-Zr, Ni-Nb, Mg-Zn, Cu-Zr, Hf-V, and Zr-V.

b) Base metal

Another way to classify MG is by the dominant chemical element. A good summary from the end of 2021 showed work [34] which is presented in Fig. 5.

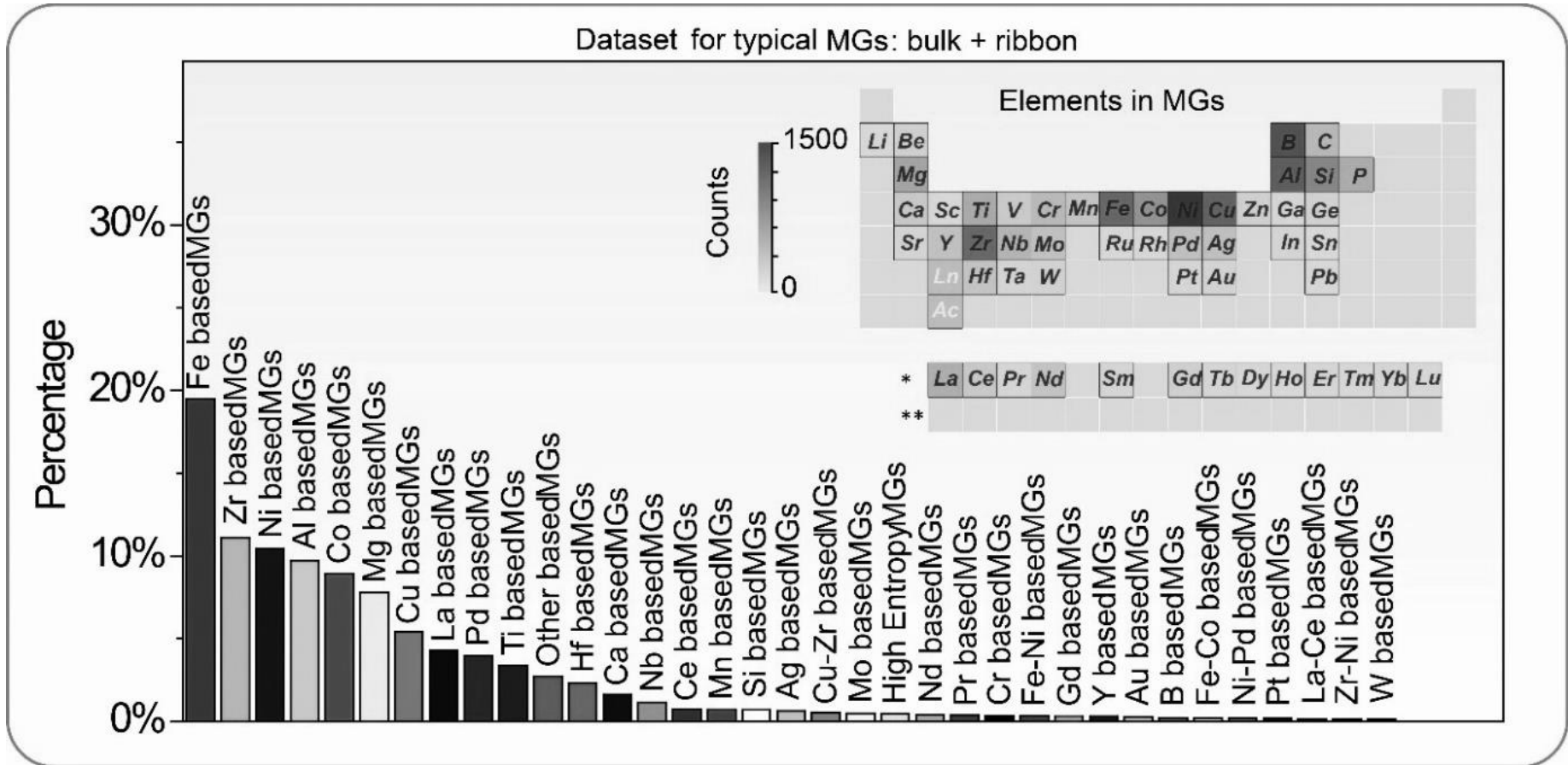


Fig. 5. Percentage of MG classified by base material. The inset table in the upper right corner highlights the number of times an chemical element is counted in all MG compositions reported as of December 2021 [34]

From this analysis, it can be assumed that the most researched MGs are based on Fe, next on Zr-, Ni-, Al-, and Co-based MG. Zr-based alloys are characterized by very good GFA and the elements developed from them have an even centimeter diameter. Additionally, Zr-based MG shows that good plasticity, which is an exception among a MG [35–37], however, the cons of Zr are its high price compared to the twice as popular Fe-based MG. The popularity of Fe-based alloys is motivated by the very low price of chemical components combined with the high GFA ability and high mechanical strength of these alloys. In addition, Fe-based metallic glasses can show good magnetic properties [7,38–40]. Similar attributes are true for alloys based on Co. The difference is the even better mechanical strength of Co-based alloys (and the higher hardness) but the higher price than Fe. Ni-based alloys have a competitive corrosion resistance property and are commonly used in corrosive environments similar to Al-based alloys, with additional showing a low density of developed elements, also both Al-based and Ni which have a high ductility among MG [41–44].

In addition to the most common based material used for MG in the right corner of Fig. 5. is also presented the analysis of the most common chemical elements that can be found in the composition of MG. Analysis shows the similarity in the high occurrence of chemical elements in MG with the popularity of base metals for MG such as Zr, B, Al, Fe, Ni, Cu, and Si. However, one of the differences is the high occurrence of B and Si elements in MG, which are associated with the enhancement of GFA and, consequently, the material ability to form an amorphous structure. At the same time, B and Si are not the base elements in any MG. Additionally, analysis of chemical elements occurrence in MG shows that almost all rare-earth elements were used as a component of metallic glasses. This group of chemical elements can significantly increase GFA due to the large atomic radii that hinder nucleation; Additionally, these elements tend to purify the MG of the oxygen content [45–47], and their addition leads to a more dispersed distribution of element radius sizes in the alloy composition, but the cons of using rare earth elements is the very high cost of them [34]. Elements used to increase the plasticity of MG are Zr, Ni, or Cu, while others are used to increase the corrosion resistance, such as Cr or Ti. Proper addition of elements can enhance some of the properties, starting from mechanical properties such as tensile strength, durability or plasticity; chemical properties such as corrosion resistance; magnetic properties such as soft magnetic properties; and with thermal stability of MG such as increasing the glass-forming ability. However, each addition of chemical element can have different influences on a particular alloy, so the general rules of influence of chemical elements should be tested experimentally and used with caution. Examples of the reported influence of single chemical elements on metallic glasses are shown in the Tab. 2.

Tab. 2. Examples of reported influence of the addition of chemical elements to metallic glasses

Chemical element	Possible effect of addition the element on metallic glass	Reference
Boron (B)	- improve GFA, stabilize the amorphous structure, - reduces magnetic anisotropy, which is beneficial for soft magnetic properties,	[48–50]
Silicon (Si)	- improve the GFA and thermal stability, - improve corrosion resistance,	[51,52]

Carbon (C)	- improve the GFA, - improve the hardness and wear resistance,	[50,53]
Iron (Fe)	- improve magnetic properties, - improve mechanical properties, e.g. strength and durability,	[54–56]
Nickel (Ni)	- reduce coercivity and improve soft magnetic behavior, - improve corrosion resistance and plasticity,	[57,58]
Zirconium (Zr)	- improve the glass-forming ability, - improve mechanical strength and corrosion resistance,	[59–61]
Niobium (Nb)	- improve the thermal stability and GFA, - magnetic properties,	[54,62,63]
Molybdenum (Mo)	- improve the hardness, wear resistance, - improve magnetic properties, - improve corrosion resistance,	[64,65]
Copper (Cu)	- improve corrosion resistance, - promote the formation of nanocrystalline phases which increase the plasticity of MG,	[66,67]
Tungsten (W)	- increase the hardness and wear resistance, mechanical strength, - improve magnetic properties,	[64,65,68]
Titanium (Ti)	- improves the glass-forming ability, - improve the mechanical strength and corrosion resistance,	[69,70]
Chromium (Cr)	- improve corrosion resistance, - improve hardness and wear resistance,	[52,71,72]
Tantalum (Ta)	- improve mechanical properties - improve corrosion resistance,	[52,73]
Yttrium (Y)	- improve glass forming ability and thermal stability - reduced the oxygen level	[63,74]

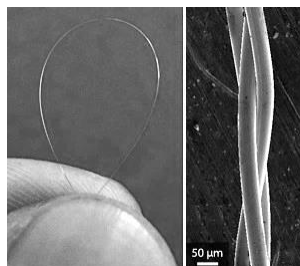
c) Shape

The shapes of the MG are limited by the technology used for development. The very high cooling rate needed to produce MG limits the shapes of products that can be obtained from these materials. Despite the mentioned limitations, the scientists and engineers were able to develop various shapes of MG from 1 dimension (1D) to 3 dimensions (3D). In Fig. 6 representation of mostly common shapes of MG are shown, both hollow and bulk. To obtain fully amorphous alloys with repeatable properties, the safest choice are thin foils and ribbons (2-dimensional shapes). Foils and ribbons have a high area to volume ratio, which allows for high heat transfer to the environment, and consequently, very high R_c . These shapes are commonly used for the development core of an electric

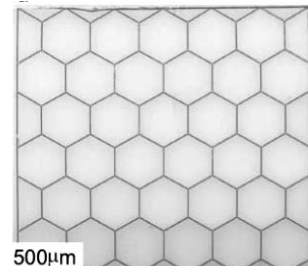
transformer by stacking the thin ribbons/foils into needed shapes. Another thin form of the MG is coating. The thickness of the MG coatings starts at several dozen nanometers (often called metallic glass thin film- MGTF [75]) to several hundreds of micrometers [76]. MG coatings ensure a very high hardness and wear resistance of the surface, and some of the coatings show a very good corrosion resistance. The next form of MG with low thickness but more complex shapes are thermoformed sheets. Some of metallic glasses can be formed when heated to their supercooled liquid region and then shaped into desired 3D elements, such as watch cases, small sieves, etc. [77,78]. The next 3D structures from MG (still with small values of one of the dimensions) are rods, plates, disks, etc. usually obtained by casting. Those shapes are used to develop golf clubs or phone covers. The one of the last groups of shapes, shown in the last rows of the table in Fig. 6 are fully 3-dimensional objects, theoretically without limited shapes and sizes. These shapes can have a hollow, lattice, or solid structure. This group of shapes are named bulk metallic glasses (BMGs) and are typically obtained by additive manufacturing. Finally, the shapes commonly used as an intermediate product (do not used in daily life) are powders. Powders are small, usually spherical particles smaller than 100 μm in diameter. They are used as feedstock to produce BMG with the use of the AM technologies mentioned above or hot isostatic pressing (HIP).



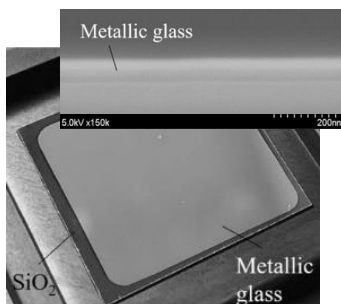
1D powder [79]



2D wire [80]



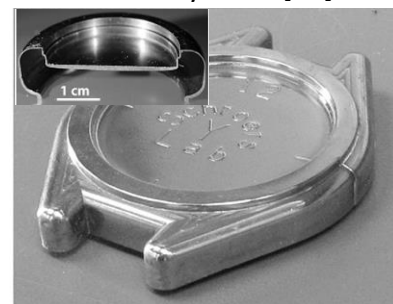
2D honeycomb [81]



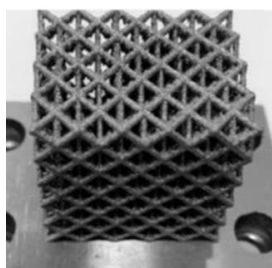
2D coating [82]



2D ribbon [79]



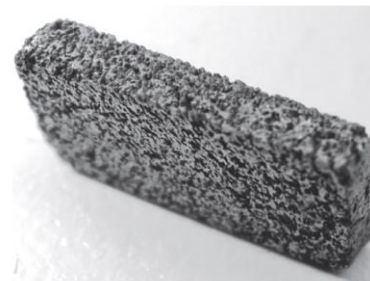
3D shell element [83]



3D mesh structure [84]



3D hollow [84]



3D foams [85]

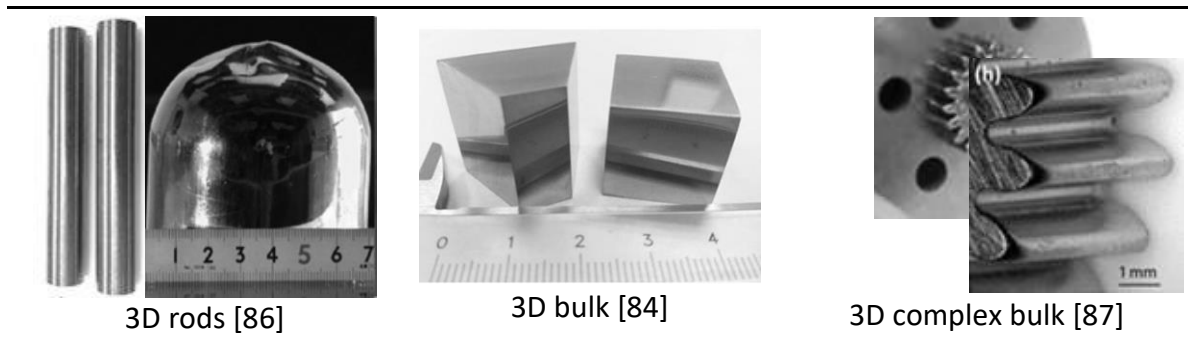


Fig. 6. Possible shapes of metallic glasses successfully developed

d) Manufacturing technology

The last proposed classification of metallic glasses is classification by the technology of manufacturing. Due to the importance of this topic to this work, the extended review of the literature on manufacturing technologies is shown in a separate chapter. However, MG manufacturing technologies can be divided into three main categories:

- rapid solidification process- the MG are obtained directly from liquid state into solid undercooled metal,
- solid stated processing- amorphous structure is obtained from solid amorphous or solid crystal structure with skipping liquidus phase,
- other- amorphous structures are obtained through vaporization, electrochemical process etc.

4. Manufacturing technologies of metallic glasses

Manufacturing technologies can be divided into three groups Fig. 7. One of them is rapid solidification processes which are a large group of common-use manufacturing technologies. RSP includes casting, atomization, thermal spraying, and AM. Casting is a group of RSP processes where the liquid alloy is poured into mold, roller, etc., which ensure high cooling rates by conducting heat out from cast alloy. Usually, the casting limitation is the thickness of the cast elements. Next technologies of the RSP group are atomization. It is a process of obtaining powder form of metallic glasses by melting the alloy and breaking the liquid into droplets, which then solidify. Different types of atomization methods oscillate between the cost of the process and the shape of the particles obtained, which is important especially for thermal spraying methods. Those methods are the next group of RSP. In thermal spraying, different processes like electric arc, plasma induction, or combustion are used to supply thermal energy and accelerate the feedstock, which then hits the substrate on which solidify, forms the coating. In thermal spraying the most popular form of feedstock is powder, however the spraying can be done from suspension or from the wire like, e.g. wire arc spraying. AM is one of the newest groups due to the development of computer-aided manufacturing at the turn of the 20th and 21st centuries. Additive manufacturing is the process of manufacturing 3 dimensional elements by developing a ready-to-use object layer by layer. Development of elements is possible due to computer-aided manufacturing programs and computerized numerical control machines. In manufacturing metallic glasses, the feedstock used for developing elements by AM can have different forms depending on the process but could include powders (direct metal deposition, powder bed fusion methods including SLM), foils (laser foil printings) or wires (fused filament fabrication, laser cladding).

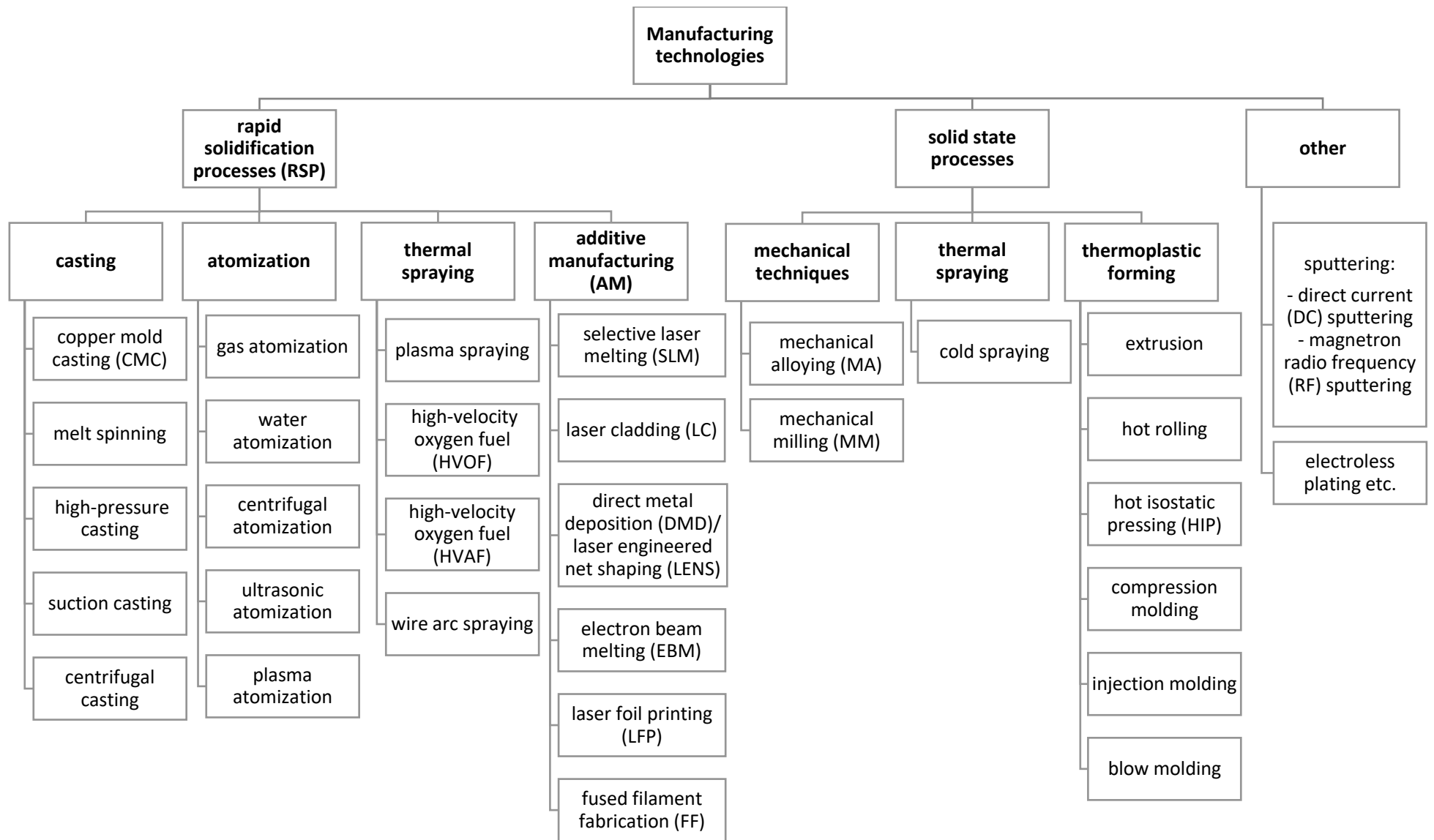


Fig. 7. Classification of metallic glasses manufacturing technologies [88]

4.1. Casting

The most popular group of technologies to develop MG are casting methods. The process usually consists of the high thermally conductive element on or in which the liquid MG is poured using gravity, high pressure, vacuum or centrifugal force. The most popular process from this group is casting into a copper mold and melt spinning. In the copper mold casting, the alloy is heated by an induction coil until it reaches the liquid state. Next, by the high-pressure, vacuum or gravity force the metal is poured into a copper die. Copper has a very good thermal conductive property, which ensures high cooling rates for solidifying alloy. For larger cast elements or alloys with lower GFA the die can be cooled with water, liquid nitrogen or other medium to increase the cooling rate [89]. Schematic illustration of casting with vacuum (suction casting) is shown in Fig. 8 a) and with high pressure in Fig. 8 b). High pressure casting can reach hundreds of megapascals, and the time of filling the die is counted in milliseconds [35,90–93]. High-pressure die casting of bulk metallic glasses is already used to successfully produce components such as cell phone parts for medical devices [92,94–96]. Furthermore, the casting parameters, in addition to the pressures and GFA of the alloy, are the geometry and heat capacity of the mold system, melting temperature, and solidification temperature of the alloy. Another important parameter is the low value of the overheating casting alloy. In works [97,98] casting the Zr-based alloy from 1550 K temperature resulted in a reduction of the free volume in the cast due to the extra time for the atoms to form a cluster and consequently a reduction in the toughness of the alloy and a higher hardness compared to rods cast from 1250 K.

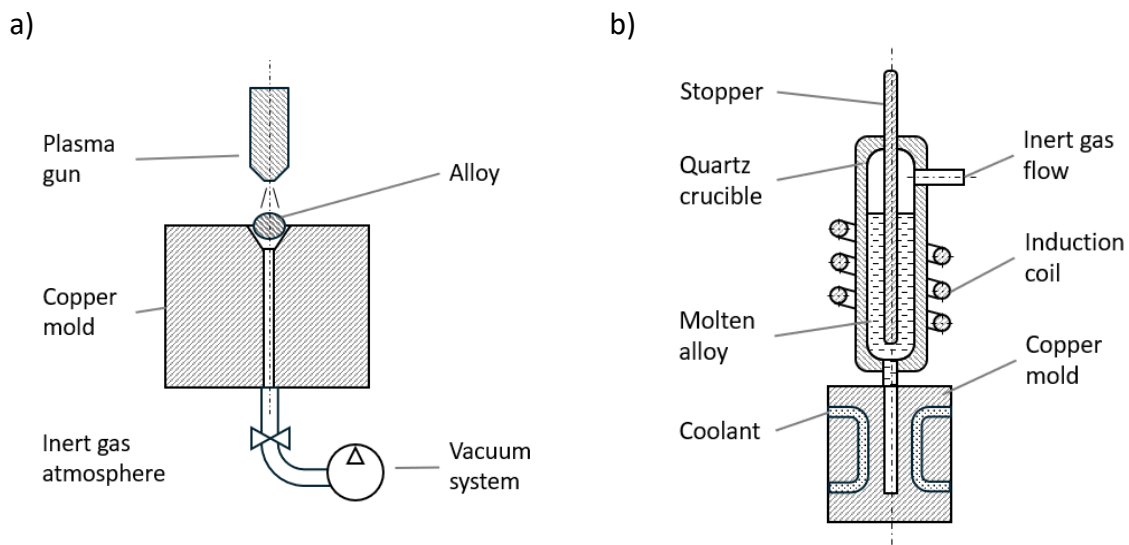


Fig. 8. Schematic illustration of BMG development by a) suction die casting system [99] b) high pressure die casting with cooling system [35]

The next casting technique that will be discussed is melt spinning (Fig. 9 a). It is the technique of a continuous casting on the copper turning cylinder (wheel, drum) where the solidification takes place instantly. On a rotating cylinder, the poured metal is momentarily cooled because of the high mass of the cylinder and the high thermal conductivity. In results, the poured metal solidifies and, due to constant rotation velocity of cylinder, the process is continuous. The obtained product is a metallic glass ribbon that is then wound onto reels. Additionally, the cylinder can be cooled by a cooled medium circulation and inside canals or by immersing the cylinder in the coolant. The developed casts are very thin, usually several

dozen micrometers thick. The width of the ribbons depends on several factors, such as the volume of poured melted alloy, the overheating of the alloy, the rotation speed of the cylinder, the shape of the nozzles of the crucible, and the pressure to push the molten alloy from the crucible. This process is widely used in electrotechnical, electronic and electrocatalysis industries [100–104]. Sometimes, this method can also be found under the name of rapid quenching because of very high cooling rates. An example of ribbons developed by melt spinning is shown in Fig. 9 b).

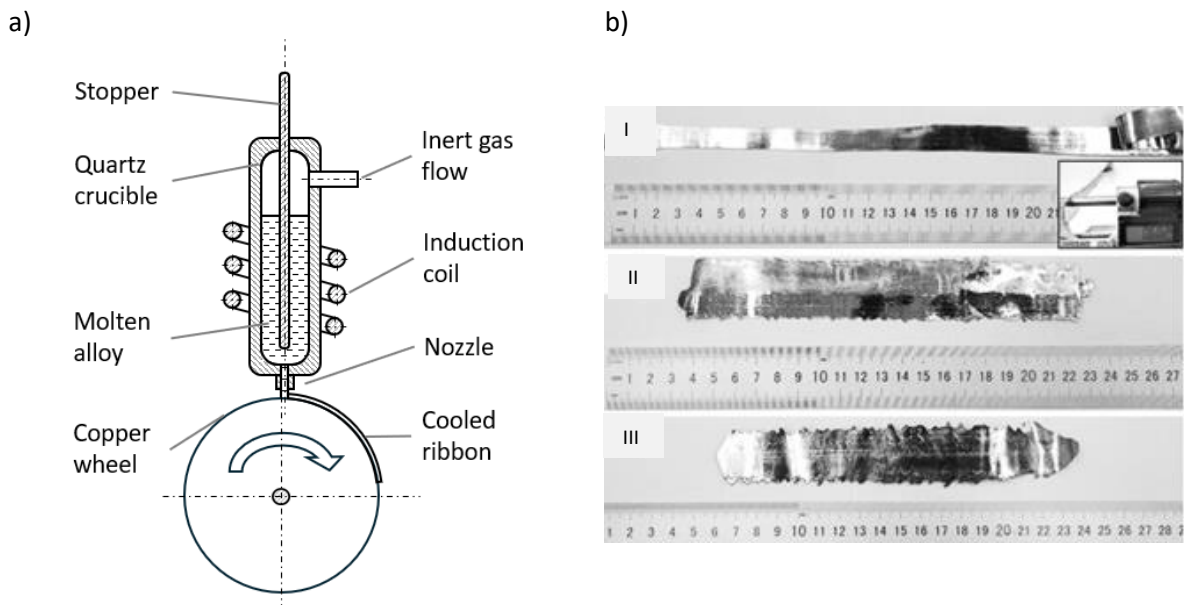


Fig. 9. a) schematic illustration of the single-roll melt-spinning method [105] b) example of MG ribbon alloys: I- metallic glass Vit.1, II- metallic glass ZrCuAlNi , III- metallic glass composite ZrCuNiBe + β -Ti crystals [106]

4.2. Atomization

Atomization is the process of obtaining powder from the master alloy. The master alloy is heated to the liquid state and, by using external force, is accelerated breaking it into small droplets, which then solidify and slow down before hitting the walls of the atomization chamber. Gas atomization is a process in which the high-pressure gas jet breaks the liquid metal, and the liquid is usually delivered in the form of a thin stream flowing by gravity force from the heated crucible. As a gas, usually inert gas is used, such as nitrogen, helium, or argon. The whole process is carried out in a chamber with lowered pressure or under vacuum. This method can be used to produce powders from Ni, Fe, Co, Sn, or Pb alloys and to receive primarily spherical powder sizes from 10 to 200 μm . In this method, the porosity of the powders is possible due to the tendency to trap the gas in liquid metal; also, this method has a tendency to develop some elongated shapes and satellite particles in addition to spherical powders [107,108]. Those particles are the result of collisions of the not solidified jet inside the chamber [109,110] and are undesirable to the quality of the developed MG. Water atomization differs from gas atomization by medium used to break the molten alloy. For water atomization the water is the medium while for gas atomization usually the inert gas is used such as argon. The application of water (exactly high-pressure water spray) instead of a gas reduces the cost of the process and is suitable for manufacturing powders from Au, Zn, Ag, or Cu alloys. However, after the process, an additional operation must be performed, such as dehydration [111]. Plasma atomization is the next method of obtaining powder. In this

method, the generated plasma can both accelerate the liquid metal to break it into droplets and deliver heat to the master alloy to melt it. The master alloy can be delivered in the form of a wire. This method has many advantages, such as satellite-free sphericity shapes, low porosity, and high purity of the powder. However, this method has a limitation on the material to atomize and the plasmatic gas makes it an expensive process [112]. Schematic presentation of mentioned methods is shown in Fig. 10.

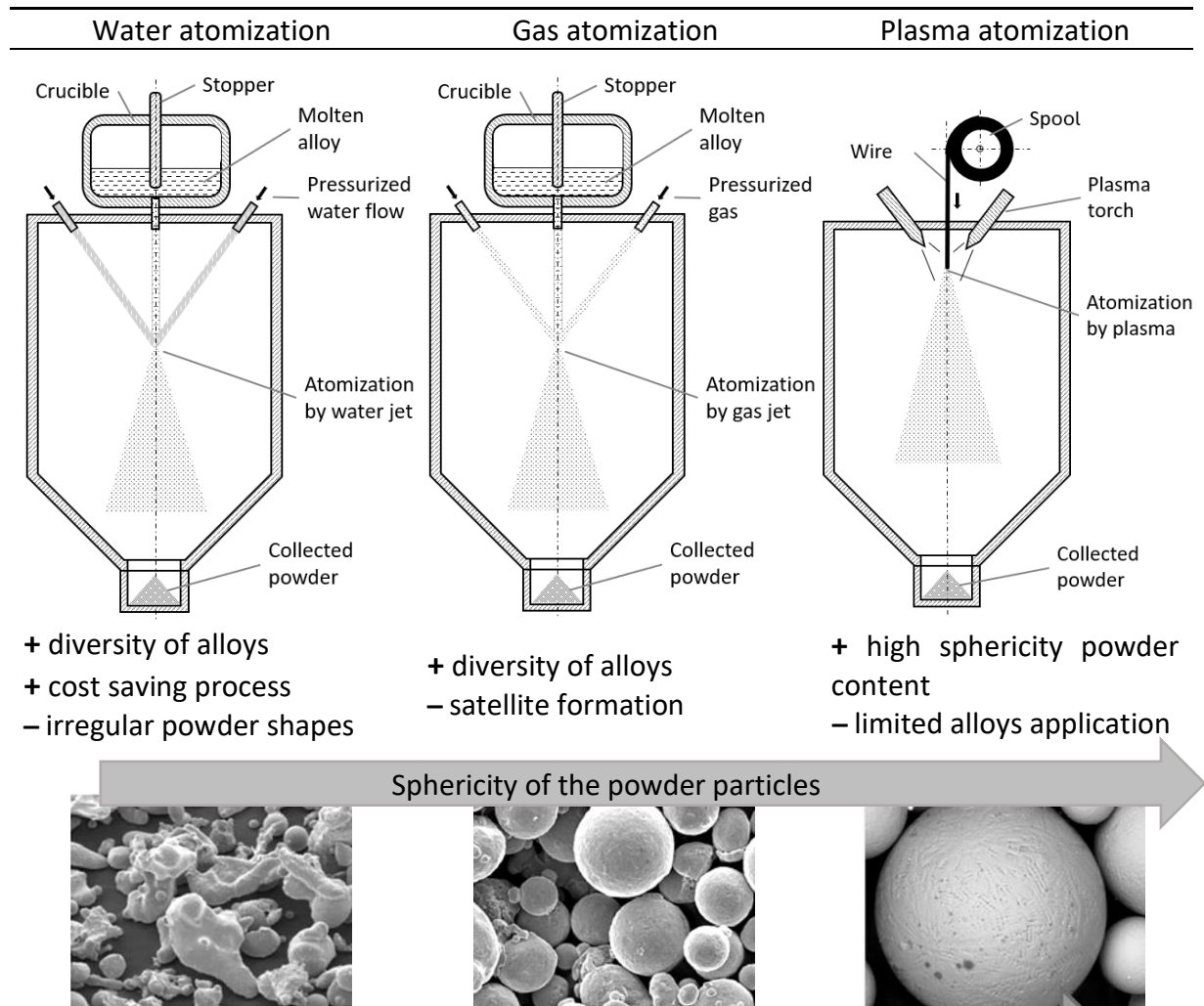


Fig. 10. Atomization methods scheme [113–115]

The parameters of processes concern the material feed like wire diameters and rate of feeding the wire in plasma method or the liquid metal flow rate, quality of water spray/ pressure of inert gas/ power of plasma that is responsible for breaking the liquid metal and forming droplets, the overheat and homogeneity of master alloy.

4.3. Selective laser melting

Selective laser melting is an additive manufacturing technology that belongs to laser powder-bed fusion methods. Laser powder-bed fusion technologies consist of first a laser which is the source of energy to melt the powder, and second the powder bed which is used as a source material to build a final printed element. The development of the element by selective laser melting in sequence involves spreading the thin powder layer by a feeder (roller) and then selectively melting it by a laser. The whole process is repeated until the shape

of the designed element is obtained. Then, the element is removed from the building platform on which it was printed and cleaned from excess of unmelted feedstock and supports. The schematic illustration of this process and the equipment is shown in Fig. 11.

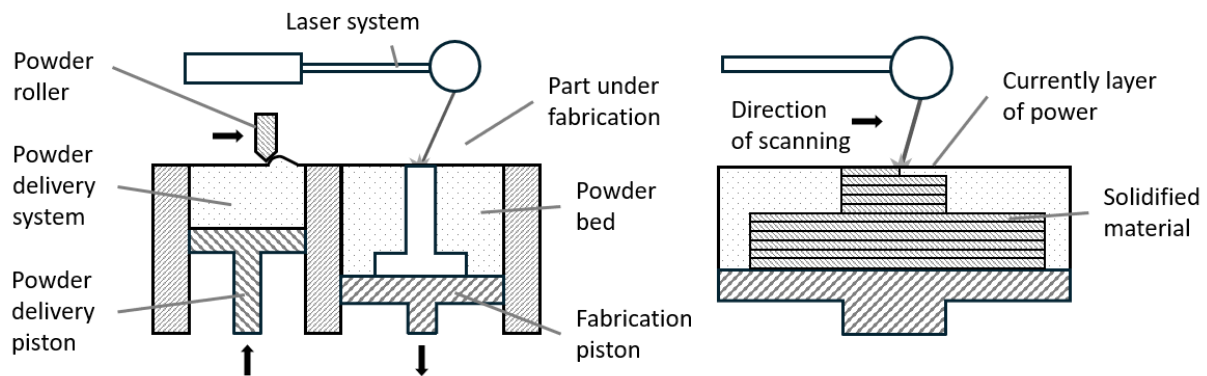


Fig. 11. Schematic illustration of the selective laser melting process [116]

Laser powder bed fusion technologies provide a very high cooling rate of 10^4 to 10^7 °C/s, making this technology desirable for the development of metallic glasses that are marked as a material that has critical cooling rates at the level of 10^2 to 10^4 °C/s [37,117–119]. Another important advantage is that there is theoretically no limitation in shape and infill degree allowing one to produce a hollow or lattice structure. The development of a dense thick structure by other methods is also limited by the cooling rates that can be achieved. In the selective laser melting method by additive character of the material, each melted point solidifies instantly, ensuring high cooling rates. The low energy input that is delivered to each melted point on the layer is possible due to a very high-density energy source - laser. Examples of fully dense, hollow, or lattice elements are shown in Fig. 12. Works [40,120–122] describe the successes in manufacturing BMG by additive manufacturing with different geometric and density structures, these applications are biomedical implants, drug delivery, micro and nanoelectromechanical systems, aerospace and sports equipment.

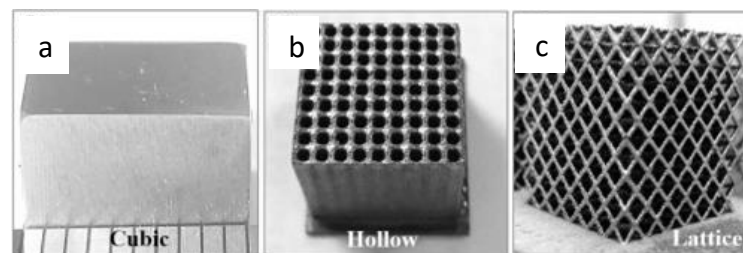


Fig. 12. Selective laser melting $\text{Zr}_{55}\text{Cu}_{30}\text{Ni}_5\text{Al}_{10}$ metallic glasses samples with different type of geometry a) cubic, b) hollow, c) lattice [119]

The SLM process has many parameters that influence the result of developing MG. Most of them regard the amount of energy that will be delivered to the feedstock. Those parameters are laser power, the speed of laser scanning the feedstock, hatch spacing, type of laser, the continuous or pulsating scanning type, and the scanning pattern and thickness of layer. The parameter that helps to calculate the amount of supplied energy is the volumetric energy density, often the acronym is ED. The formula of ED is shown in Eq. 1 [123,124].

Eq. 1. Energy density formula: P- laser power [W], v- scanning speed [mm/s], h- hatch spacing [mm], H- layer thickness [mm]

$$ED = \frac{P}{v \cdot h \cdot H} , \left[\frac{J}{mm^3} \right]$$

Other important factors concern the purity of the working gas - the atmosphere that is in the working chamber. Gas used for those purposes is typically argon or nitrogen. The impurity that should be checked is the H₂O content. This is also considered for feedstock that should be dried before printing [125–128]. Theoretically, the high GFA of the alloy should not be a concern because of the very high cooling speed rate of the SLM process. However, due to the heat affected zone (HAZ) and the phenomena that occur in the melt pool (like Marangoni effect) the segregation and clusters forming (reducing free volume) or even crystallization can sometimes take place in the BMG developed [129,130] [131–133] [134]. The addition of a too high cooling rate can also cause a problem due to the too high thermal residual stress accumulated in the printed elements [135].

4.4. Plasma spraying

The plasma spraying process is part of a larger group of thermal spraying methods. In plasma spraying plasma is generated to accelerate and melt feedstock that is then deposited on the substrate, forming lamellar splats and, consequently, coating [136,137]. The plasma jet is generated by plasmatic gas flow between the cathode and an anode nozzle where high voltage electric discharge takes place [138]. Into generated plasma, the feedstock can be supplied axial or radial. The spraying gun is additionally cooled to preserve the nozzle from melting. The gun can be mounted in robotic arms to spray coating onto more complicated surfaces. In the other case, if the plasma gun is fixed, then the substrate can be mounted on a moving holder, which can provide additional cooling of samples, which is desirable for developing amorphous metal coating [139,140]. Different variations of spraying guns and stands are shown in Fig. 13.

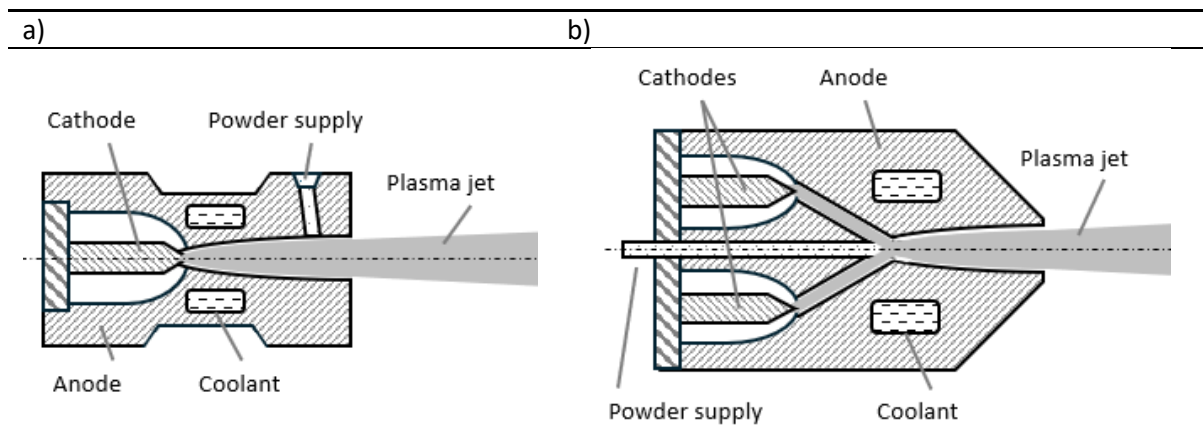






Fig. 13. Schematic illustration of plasma spraying gun a) with radial powder supply and [141] b) with axial powder supply [142]

Plasma spraying can be divided into low pressure plasma spraying, vacuum plasma spraying, atmospheric plasma spraying, or plasma spraying under inert gas [143]. Atmospheric plasma spraying (APS) generates a high flame temperature up to 10.000°C while particles can be heated up to 3.800°C, however cooling rates for depositing coating range from 10⁵-10⁷ °C/s, which is enough to establish the amorphous structure of the deposited alloy with high glass-

forming ability [144]. Atmospheric plasma spraying is the most common type among plasma spraying methods due to cost-saving processes, which do not require a special surrounding condition such as a vacuum chamber. However, low pressure plasma spraying has the advantage of better control of the spraying condition by controlling the environment. Control of environment provide the high bonding strength of coating due too low oxidation of the depositing feedstock [145]. The method that uses an inverse condition is high pressure plasma spraying where in the depositing chamber the pressure is increased. In work [146] an increase in pressure up to 300 kPa provides very high dense and hard coating due to an increase in the temperature of the deposited particles that can be established due to this increased pressure, which is necessary to melt material with a high melting point, such as zirconia. Factors that influence the plasma spraying deposition process include plasmatic gas flow rate, plasma power input, stand-off distance, size distribution, feedstock flowability, shape, characteristic temperatures, hardness, and powder feed rate [147–151]. For example, typical plasmatic gases that are used for spraying are nitrogen, hydrogen, argon, or helium (or the mixture of them). The difference between gases is the characteristic temperatures, energy they supply, and cost, and parameters and advantages typical gases are shown in the Tab. 3.

Tab. 3. Typical gases used for plasma generation for plasma spraying coating depositions [140]

Gas/ symbol	
<p>Nitrogen/ N_2</p>  <ul style="list-style-type: none"> + inert except for nitridization sensitive materials (like Ti alloys) + the cheapest gas + yellow plasma color + first ionization energy 14.53 eV 	<p>Argon/ Ar</p>  <ul style="list-style-type: none"> + inert for all materials + relatively low temperature plasma + low heat conductivity + less aggressive on the spray equipment, than nitrogen or hydrogen + blue plasma color + first ionization energy 15.75 eV
<p>Hydrogen/ H_2</p>  <ul style="list-style-type: none"> + inert for all materials + secondary gas, up to 20 vol. %. + increases heat conduction + red plasma jet + first ionization energy 13.60 eV 	<p>Helium/ He</p>  <ul style="list-style-type: none"> + inert to all materials + mainly secondary gas + very expensive, used only when other gases have a negative effect on deposited material + good heat conduction + typically used for carbide coating deposition + first ionization energy 24.58 eV

The efficiency of feedstock deposition depends on the state of feedstock in the moment of the deposition on the substrate/ earlier deposited feedstock. If feedstock is melted partially or fully it will form splats and increase the thickness of the coating, but if it solidifies again or will not be melted then it will rebound [139]. According to [152,153] smaller feedstock sizes had a positive effect on the degree of particle melting and the results are that they tend to form a more dense coating with higher adhesion, hardness and wear resistance compared to particles coating developed with larger feedstock. Work [152] compared feedstock sizes 15 μm to 33 μm and [153] 33 μm to 84 μm . However, reducing the size of the feedstock particles can result in a higher oxygen content in the obtained coating [154,155]. The flip side of providing too much energy by the plasms jet is local reheating of the coating, which can lead to local chemical element segregation, reducing free volume and even crystallization of

coating developed from alloys with high glass forming ability. In addition to the parameters described, other factors can also influence the coating formation. These factors are shown in Fig. 15.

Thermal spraying technologies, including plasma spraying of MG coatings, are now used to protect the surface of gas and hydraulic turbine blades [125,156]. Those applications are submitted because of the high wear resistance or corrosion resistance of MG. Plasma spraying MG coatings are also being investigated as a potential thermal barrier coating to obtain very low thermal diffusivity values of barriers [76,81]. Plasma spraying ensures high enough cooling rates to establish fully or almost fully amorphous structures of alloys with good GFA from alloys based on Ni, Fe, Zr, Cu, Ti, etc. [143,157–162]. An example of a coating developed by atmospheric plasma spraying of Fe-based MG is shown in Fig. 14.

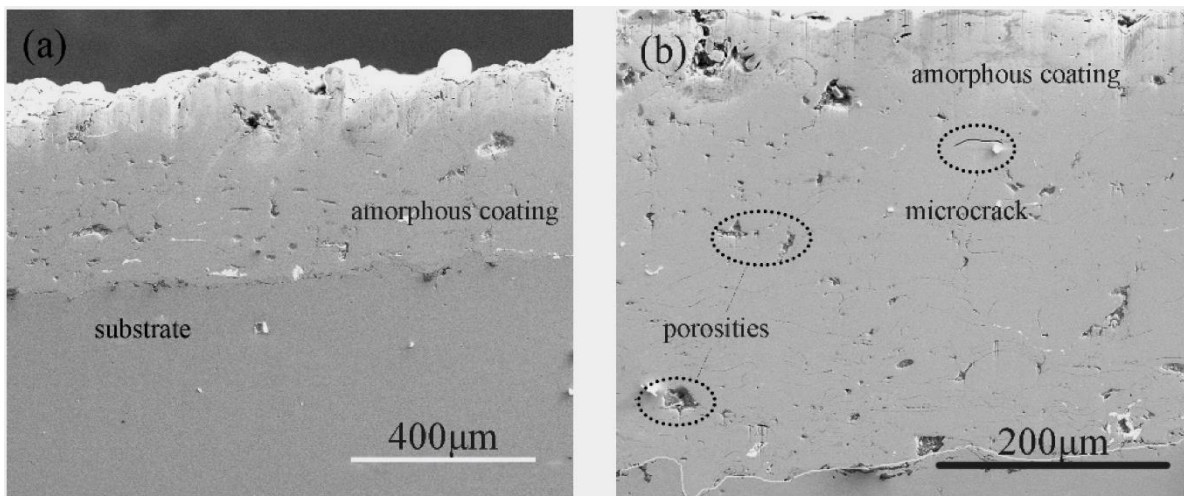


Fig. 14. Example of Fe-based MG coating obtained by atmospheric plasma spraying [163]

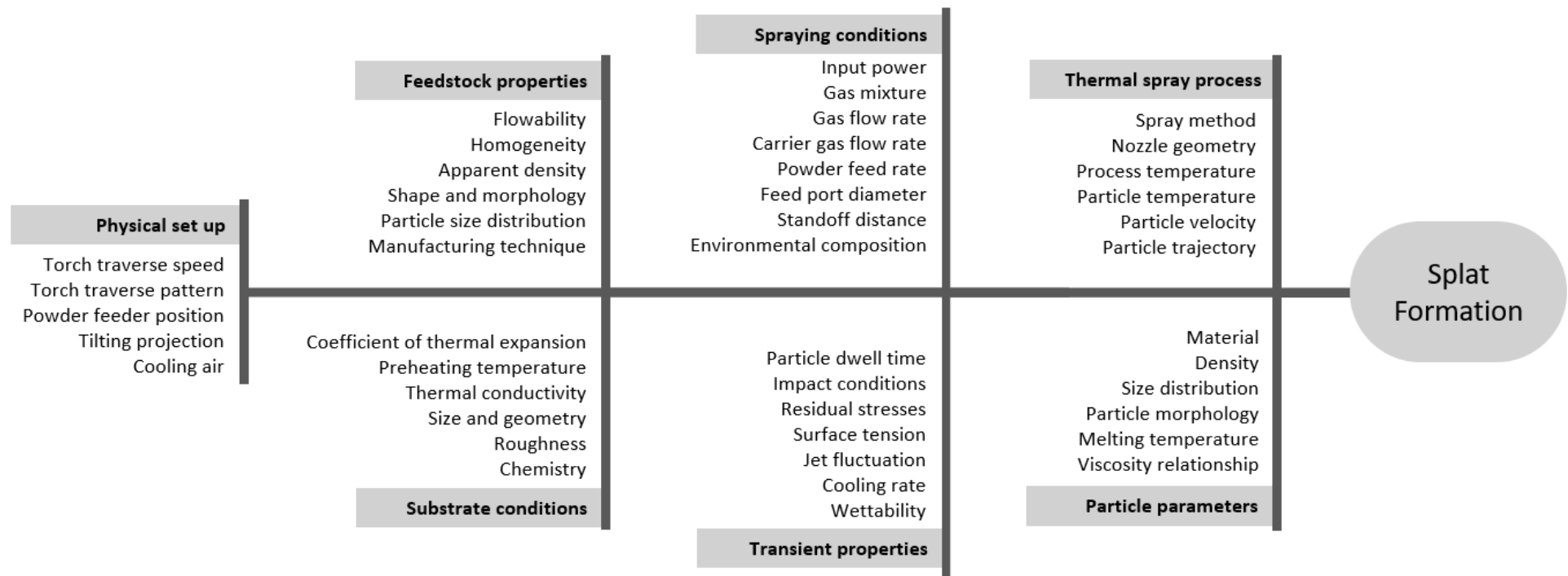


Fig. 15. Detailed factors of plasma spraying process that influence on the splats formation [164]

5. Selected properties of metallic glasses

Metallic glasses have different properties than traditional metal alloys. The biggest difference comes from the different atoms arrangement, MGs are characterized by a short and medium range order of the atoms, while traditional crystal metals have a long range order of atoms [165–167]. Additionally, the chemical composition of MG is very different from the composition of crystal metals, due to the often addition of large amounts of metalloids (but not larger than 20%). These differences result in the unique properties of the MG engineering material group. From the perspective and knowledge about properties of typical crystal alloys, the review of MG properties from work [168] are shown in the Tab. 4.

Tab. 4. Properties of metallic glasses related to potential applications [168]

Attributes	Attractive attributes	Unattractive
General	<ul style="list-style-type: none"> - Absence of microstructural features: such as phase or grain boundaries 	<ul style="list-style-type: none"> - High cost of components and processing - Optimization of composition for glass-forming ability prevents easy optimization for other properties, including low density
Mechanical	<ul style="list-style-type: none"> - High hardness - Good wear and abrasion resistance - High yield strength - Low mechanical damping (indication of the energy absorbing potential [169]) 	<ul style="list-style-type: none"> - Very low ductility in tension due to only several localizations of plastic flow (shear-banding) in whole material - Fracture toughness can be very low - Embrittled by annealing or using in elevated temperature can occur
Thermal	<ul style="list-style-type: none"> - supercooled liquid temperatures ($T_g < T_x$) for some metallic glasses allow thermoplastic processing them 	<ul style="list-style-type: none"> - Change of properties above T_x temperature can limit the use of MG
Electrical and magnetic	<ul style="list-style-type: none"> - High magnetic permeability - Resistivity is nearly independent of temperature 	<ul style="list-style-type: none"> - Relatively high magnetostriction gives energy loss in oscillating field
Chemical	<ul style="list-style-type: none"> - Lack of structure defects, such as grain boundaries, gives very high corrosion resistance of some MG 	
Environmental	<ul style="list-style-type: none"> - Some compositions biocompatible 	<ul style="list-style-type: none"> - Not easily recycled once in a product (non-conventional compositions)
Processing	<ul style="list-style-type: none"> - Low solidification shrinkage and lack of grain structure give high precision and finish in castings - The high viscosity and low strain-rate sensitivity of the supercooled liquid permit thermoplastic forming 	<ul style="list-style-type: none"> - The current need for vacuum die-casting gives relatively slow development rate

Aesthetic	<ul style="list-style-type: none"> - Lack of grain structure allows a very high polish - High hardness and corrosion resistance gives durability 	
Potential markets	<ul style="list-style-type: none"> - Aesthetics, present novelty and rarity make metallic glasses attractive for high-end “life-style” products - Properties and processing favor μm-to-mm scale structures 	<ul style="list-style-type: none"> - Current high cost of material and processing limits applications to those with high value-added

5.1. Mechanical

5.1.1. Hardness

Mechanical properties are of interest in this thesis. Properties such as hardness, young modules, and poison ratio will be reviewed in different MG. The hardness of metallic glasses is usually measured by the Vickers method (with microscale indents) or by the nanoindentation (nano scale indents). According to work [170] the highest hardness values obtained for iron-based MGs, especially those with a cobalt component, reach the value of 12.3 GPa. However, the hardness values of MG can establish much higher values, such as 16.1 GPa for Co-based MG [171], 19.2 GPa for Zr-based MG [172] or up to 25 GPa for Fe-based MG [173]. [173] research (Fig. 16) confirms the maximum hardness of alloys based on Fe and Zr at a level of up to 19 GPa and mentions that Co-based and Cr-based alloys can also establish high value of hardness [174–186].

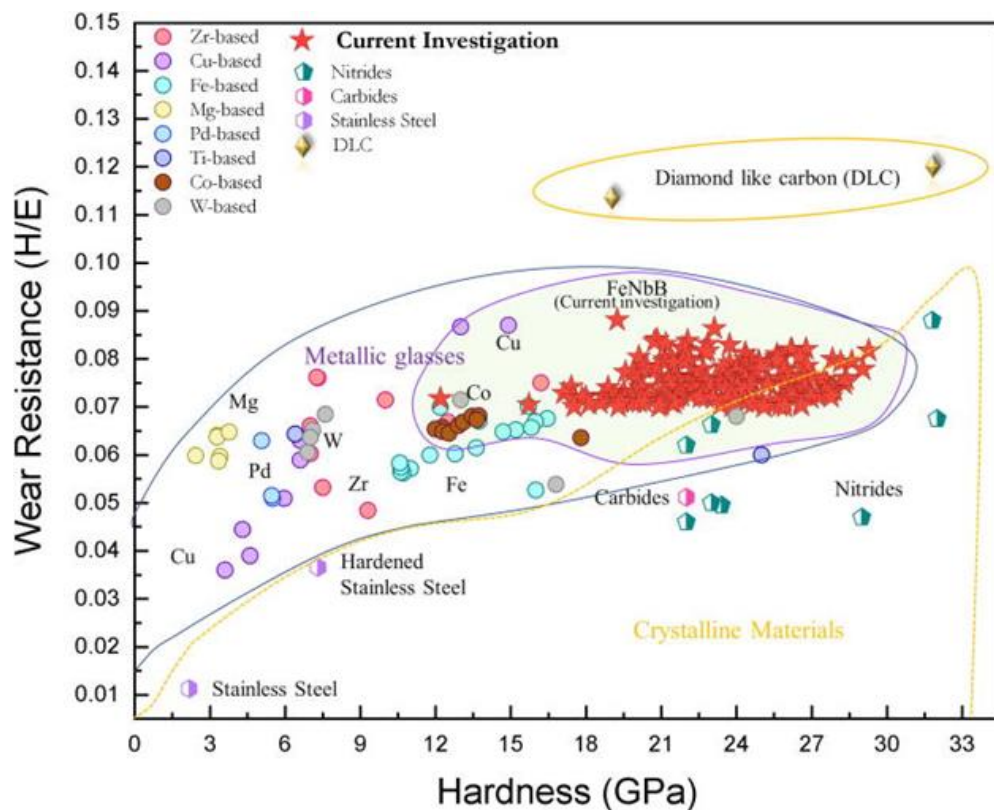


Fig. 16. The relationship between hardness and wear resistance for metallic glasses. The red stars and description “Current investigation” indicate measurements from source [173]

Nanoindentation test

The nanoindenter is a device that is used for precise hardness measurements. The device registers the changes in force (F) under the change in depth (h) of the indenter tip. Changes are measured in both the loading and unloading processes. The depth of the indent is nanoscale, and similarly, the area of indent is nanoscale, which allows one to measure the mechanical properties of exact spot on the sample, such as single crystals, segregation area, hardness changes in the heat affected zone, etc. From the obtained plot the indentation hardness (H_{IT}), the Vickers hardness (HV_{IT}) and the indentation modulus (E_{IT}) can be determined. Calculations of those values are described below. All symbols and index used in this sub-chapter and later for describing those mechanical properties are shown in the Tab. 5.

Tab. 5. Index of symbols for nanoindentation measurements

Symbol	Designations	Unit	Formula
ADO	adjust depth offset	-	-
H_{IT}	indentation hardness	MPa	$H_{IT} = F_{max}/A_p$
HV_{IT}	Vickers hardness calculated from H_{IT}	Vickers	$HV_{IT} = H_{IT} / 10.80$
F_{max}	maximum test force	N	input value if h_{max} is not set as an input value
F	test force	N	measured value
A_p	projected contact area	m ²	$A_p = 24.5 h_c^2$, for Berkovich indenter
h_c	contact depth of the indenter with the sample at F_{max}	m	$h_c = h_{max} - \epsilon F_{max} / S$
h_p	permanent indentation depth	m	measured value after releasing force
h	indentation depth under applied test force	m	measured value
h_{max}	maximum indentation depth	m	input value if F_{max} is not set as an input value
ϵ	geometric constant	-	for Berkovich indenter $\epsilon = 0.75$
S	contact stiffness	N/m	$S = dF/dh$
a	dimension of indenter used to calculate A_p	m	-
E_{IT}	indentation elastic modulus	Pa	$E_{IT} = (1 - \nu_s^2) / [1 / E_r - (1 - \nu_i^2) / E_i]$
ν_s	Poisson's ratio of sample	-	input value
ν_i	Poisson's ratio of indenter	-	input value
E_r	reduced modulus	Pa	$E_r = \sqrt{\pi}/2 * S/\sqrt{A_p}$
E_i	indenter modulus	Pa	input value

To calculate H_{IT} the maximum test force (F_{max}), it is divided by the projected contact area between the sample and the indenter (A_p) [187] of (Eq. 2)

Eq. 2. Indentation hardness formula

$$H_{IT} = F_{max}/A_p$$

A_p is calculated by knowing the value of the contact depth of the indenter (h_c) and the geometry of the used indenter. For the Berkovich indenter that was used in those measurements, A_p is calculated by the following equation [187] (Eq. 3).

Eq. 3. Formula for the contact area

$$A_p = 24.5 h_c^2$$

The contact depth of the indentation (h_c) is not the same as the maximum indentation depth (h_{max}). Oliver and Pharr have found a formula for h_c shown in Eq. 4 using the Sneddon's equation for elastic component of the displacement [187], where ϵ is a geometric constant for the specific indenter tip. For Berkovic tip, ϵ is 0,75. Contact stiffness (S) is calculated as the slope of the Eq. 5. Visualization of contact stiffness is shown in Fig. 18. The visualization of the difference between h_c and h_{max} is shown in Fig. 17.

Eq. 4. Contact depth of the indenter formula

$$h_c = h_{max} - \epsilon \frac{F_{max}}{S}$$

Eq. 5. Stiffness formula calculated from the unloading graph

$$S = \frac{dF}{dh}$$

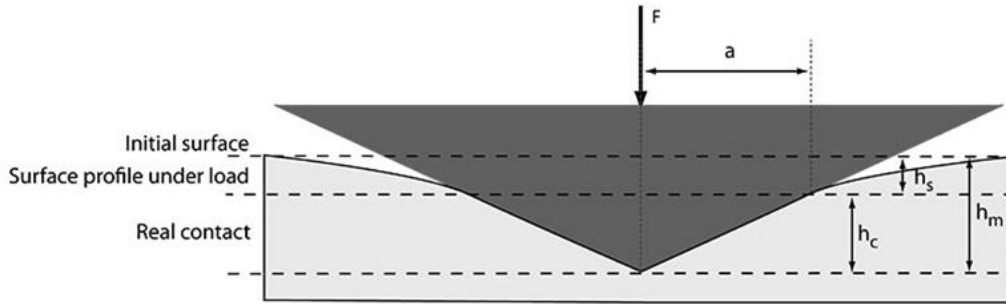


Fig. 17. The scheme of differences in indentation depths according to the Oliver and Pharr research. h_m (or h_{max})- maximum indentation depth, h_c - contact depth of the indenter, h_s - difference between h_m and h_c [188]

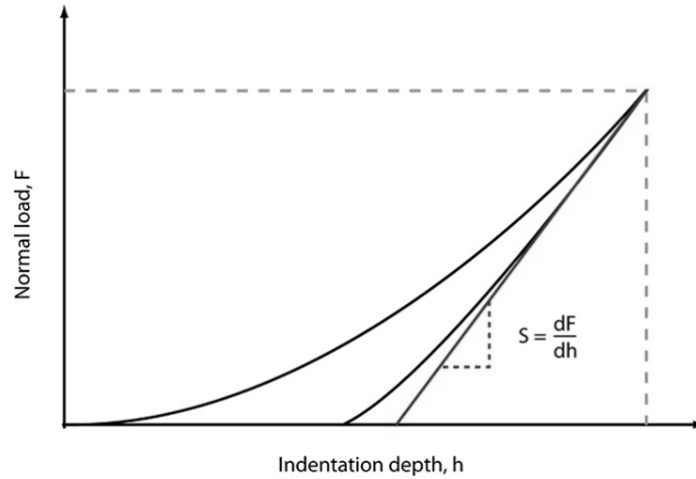


Fig. 18. Plot F (load) versus h (indentation depth) of indentation test with formula for S (stiffness) of the sample [188]

To obtain the elastic modulus of the sample (indentation modulus E_{IT}) few calculations need to be made. First, the reduced modulus (E_r) can be calculated using the Sneddon solution for the Berkovic indenter [187,189] by knowing S and A_p (Eq. 8). Next, E_r is the sum of the elastic modulus of two objects (sample E_{IT} and indenter E_i) connected in a series. This dependence gives us another equation, Eq. 9. After combining Eq. 6 and Eq. 7 the Eq. 8 is given to calculate the elastic modulus (E_{IT}) of the measured material (sample). From Eq. 8 the Poisson ratio of the indenter (ν_i) and the indenter modulus (E_i) is known (information obtained

from the indenter specification), E_r is calculated from Eq. 6. To calculate the E_{IT} , only ν_s is needed. The value of this parameter is taken from literature or other studies on the tested material.

Eq. 6. General formula for reduced modulus

$$E_r = \frac{\sqrt{\pi}}{2} \cdot \frac{S}{\sqrt{A_p}}$$

Eq. 7. Calculation of reduced modulus as a system of sample and elastic objects of the indenter

$$\frac{1}{E_r} = \frac{1 - \nu_s^2}{E_{IT}} + \frac{1 - \nu_i^2}{E_i}$$

Eq. 8. Indentation modulus formula

$$E_{IT} = \frac{1 - \nu_s^2}{\left[\frac{1}{E_r} - \frac{1 - \nu_i^2}{E_i} \right]}$$

5.1.2. Elastic modulus

The elastic modulus of the materials defines how the material reacts by changing geometrical parameters under applied external force. Common moduli that can be found to compare materials are Young's module (E) (measured as an E_{IT} by nanoindentation testing), the shear module (G or sometimes S or μ), bulk modulus (K or B) and Poisson's ratio (ν). To describe the mechanical properties of MG in this work, Young's module E and the Poisson ratio ν are reviewed. The information collected from Poisson ratio is shown in the Tab. 6. The highest Poisson's ratio among MG was reported for alloys based on platinum ($\nu = 0.42 - 0.43$) [190–192] and palladium based ($\nu = 0.40 - 0.42$) [190,192]. A low value of the Poisson ratio was recorded for MG based on calcium and magnesium, respectively, 0.305 and 0.308, 0.309 [190,192,193]. But the lowest Poisson ratio was shown by two amorphous Fe alloys: $\text{Fe}_{61}\text{Mn}_{10}\text{Cr}_4\text{Mo}_6\text{Er}_1\text{C}_{15}\text{B}_6$ $\nu = 0.286$ [194] and $\text{Fe}_{70}\text{P}_{10}\text{C}_5\text{B}_5\text{Si}_3\text{Al}_5\text{Ga}_2$ $\nu = 0.280$ [192]. Including these two alloys, Fe-based MGs achieve only values of 0.316 to 0.338 [38,190,195,196]. In article [194] data from 46 experiments were collected and fitted to the Gaussian distribution. This adjustment gives an average value of $\nu = 0.358$ (variation of 0.0136). This Poisson ratio was reported on MG based on zirconium 0.34 – 0.36 [191]. In [192] Poisson's ratio for those MGs was similar ($\nu = 0.35 - 0.37$) and [123] [120] confirmed these values for Zr-based MGs (in [193] some Zr-based MGs have even slightly higher Poisson's ratio values up to 0.39). Finally, only a few articles where elastic modules were found for Co-based alloys were measured. [171] reported for $\text{Co}_{65-x}\text{Ta}_x\text{B}_{35}$ ($x = 7 - 9$) $\nu = 0.315$, [197] $\text{Co}_{43}\text{Fe}_5\text{Cr}_{15}\text{Mo}_{14}\text{C}_{15}\text{B}_6\text{Er}_2$ $\nu = 0.331$ and [198] alloys $\text{Co}_{64}\text{Mo}_{22}\text{B}_{14}$, $\text{Co}_{59}\text{Mo}_{28}\text{B}_{13}$ respectively 0.344 and 0.301. The Poisson value chosen for both alloys in this work for the nanoindentation work were $\nu = 0.315$. The reasons are that the amount of metalloid is similar to that of and [197] have chemical elements that are also present in my alloys.

Tab. 6. Comparison of Poisson ratio for metallic glasses

Major chemical element of MG	Poisson's ratio ν	Reference
Platinum-based	0.42 - 0.43	[190–192]
Palladium-based	0.40 - 0.42	[190,192]
Zirconium-based	0.34 - 0.37	[191]
Calcium- or magnesium- based	0.30 - 0.31	[190,192,193]
Iron-based	0.30 - 0.34	[38,190,195,196]
Cobalt-based	0.30 - 0.34	[171] [197] [198]

5.1.3. Young's modules

Young's modules describing how much sample will deform along one axis, under applied force along this axis. Materials such as elastomers that have a high deformation under force have a module much lower than that of ceramics, which do not deform almost completely under applied forces. The review of Young's module of engineering materials is shown in Fig. 19. Many metallic glasses based on the same chemical element have a Young module like the crystalline alloy based on the same element. However, the value can differ due to the large number of metalloids and nonmetals compared to traditional crystalline alloys. For MG, the lowest elastic module was reported in [190] for $\text{Ca}_{65}\text{Mg}_{15}\text{Zn}_{20}$ $E = 26.42$ GPa, but it should be noted that MG based on Mg has an elastic module around 50 GPa, which is also a very low value. The highest elastic module values were reported for Co-Mo-B glassy alloys: $\text{Co}_{64}\text{Mo}_{22}\text{B}_{14}$, $\text{Co}_{59}\text{Mo}_{28}\text{B}_{13}$ respectively, 246.2 GPa, 259.0 GPa [129] and for Co-Ta-B MG: $\text{Co}_{65-x}\text{Ta}_x\text{B}_{35}$ ($x = 7 - 9$), $\text{Co}_{92-x}\text{B}_x\text{Ta}_8$ ($x = 30, 32.5, 35, 37.5$) in the range from 240.1 to 249 GPa [171] [49]. Fe-based MGs also obtain the high value of the elastic module. The elastic module values of these alloys ranges from 145 to 226 GPa [38,190,195,196]. When testing the value of elastic module, it can be found that pure elements that are the base of specific alloys have an E similar to E of those alloys [199]. Continuing the comparison, pure Ca has a Young module of value 19.6 GPa, Mg 44.7 GPa, which is not more than 25% difference between pure elements and a Young module of alloy. The elements of the Young modules based on Co are 211 GPa, B 440 GPa, Ta 185.7 GPa, Mo 324.8 GPa. In summary, alloys made from elements with a low Young module develop MG with a low Young module. Similarly, elements with high E develop MG with the highest elastic module.

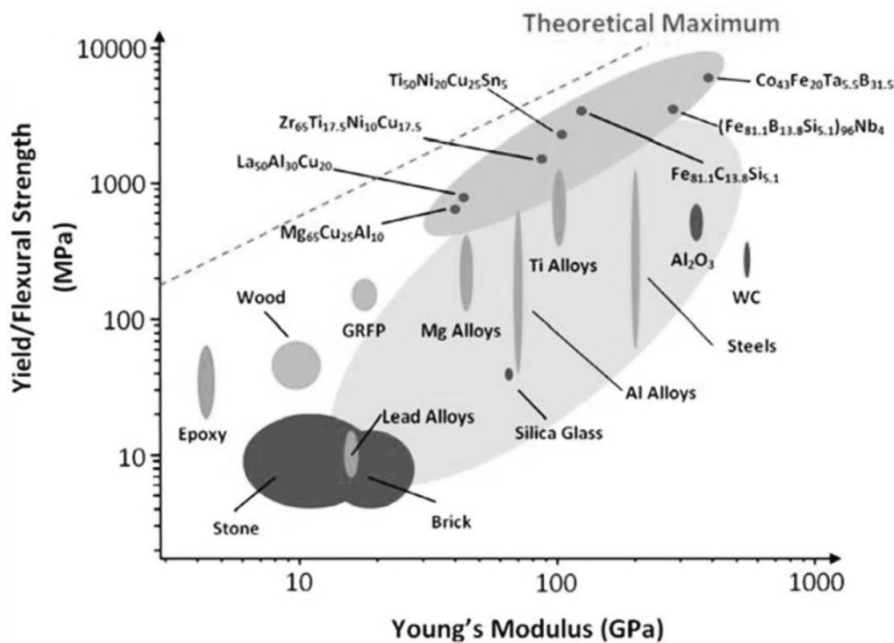


Fig. 19. Schematic representation of the yield (metals, composites and polymers) at room temperature or flexural strength (ceramics) as a function of Young's modulus. Red presents the metallic glasses and orange presents the crystalline metals. [168,200]

5.1.4. Wear resistance

Wear resistance according to [201] is the ability of the material to resist surface damage during routine usage, according to [202] one of the typical parameters to describe the tribological behavior of the material for which the sliding wear test is performed. Sliding wear occurs when two smooth surfaces slide over each other with or without lubrication. Usually

the version without lubrication (dry) test is used to measure the resistance to sliding wear. Another wear test is abrasive wear tests where the harder than tested material abrasive particles are added. As a parameter to compare the material wear resistance, the parameter named the specific wear rate W_s , the wear coefficient K , or the ratio H/E (H_c - hardness to E - young module) is used. Specific wear resistance W_s is calculated from Eq. 9, where V_w is volume loss, L sliding distance and F the normal load. The K parameter is calculated from Eq. 10. It can be noticed that K is an W_s multiplied by the hardness of the tested material. The W_s unit is mm^3/Nm meanwhile K is dimensionless.

Eq. 9. Specific wear resistance [203]

$$W_s = \frac{V_w}{LF} , \quad \left[\frac{mm^3}{Nm} \right]$$

Eq. 10. Wear coefficient, dimensionless [202]

$$K = \frac{V_w H}{LF}$$

Work [204] studied the often used H/E ratio as an index of material wear resistance. This ratio is often used to compare coating hardness [205,206]. This index predicts the wear resistance of the material based only on the two mechanical properties of the material without experimental wear test such as W_s or K . Work [204] based on a few other works including [207] shows that H and E are closely related properties of material (low E value implicates low atomic bonding of material and negatively influence the H of material) and the H/E ratio can be inconsistent for materials that are strain-free, which can be problematic for many metallic glasses which do not show plastic behavior. However, it can be seen that this ratio is used despite this inconsistency as shown in Fig. 20 [173]. Fig. 20 shows that most metallic glasses have a higher H/E ratio than traditional crystalline steels or even hardened steel and similar to carbides and nitrides (up to 0.1 ratio). This makes metallic glass an interesting material for protecting coatings application. The work [93] compared the same Fe-based amorphous coating developed by two technologies. The study shows that coatings manufactured by laser cladding compared to the ones obtained by plasma spraying show a higher wear resistance. This was related to the higher density, less cracks, and higher microhardness of the coating manufactured by laser cladding. Work [203] went further to investigate the wear resistance of metallic glasses, concluding that hardness (H), strength (σ_i), young's module (E), glass transition temperature (T_g), notch toughness (K_Q) and Poisson's ratio (ν) do correlate dependently with the wear rate of metallic glasses. The most crucial factors are the strength and toughness factors such as K_Q and ν . Second, an especially important achievement of the work is designing the index that correlates the bulk modulus (B) and ν with the wear resistance. The higher the index, the higher the strength, toughness and elastic parameters of the described material are and, in consequence, have a very high W_s of metallic glass. The correlation is shown in Fig. 20.

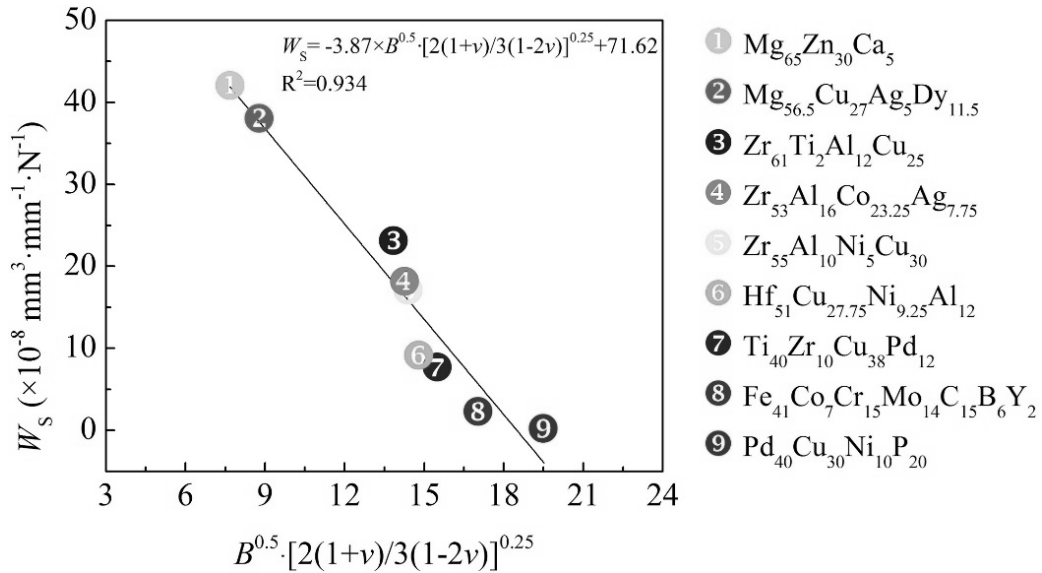


Fig. 20. Correlation between specific wear resistance (W_s) and index including bulk modulus (B), Poisson's ratio (ν) [203]

5.1.5. Strength and ductility

According to [208–211] the mechanical properties of metallic glasses are closely related to the properties of their component. Knowledge of the mechanics underlying the strength and ductility of MG is still very limited; however, several ideas will be discussed. What is known is that at low temperatures (not higher than T_g - individual for different MG) metallic glasses under applied force form and propagate nanosized shear bands [212–216]. The shear band is a 10- to 100-nm thick zone through the volume of material in which a large share of plastic deformation occurs, while the material outside the share zone remains undeformed [210]. Metallic glasses tend to form a small number of shear bands in the material under stress. The small number of shear zones leads to initiating the strain softening of the material and consequently failure of the MG with limited global plasticity despite its high strength and hardness.

To understand the place and mechanism of shear bands development, a closer look at the atomic arrangement in metallic glasses is needed. Metallic glasses, are characterize by short and medium range order of atmos. Work [167] investigated several types of atom-packages (SRO) and their pairs (MRO) found in some binary MG system. Those atoms packages called also clusters; and are characterized by more dense atoms arrangement than average atom density of whole metallic glass. Typical polyhedral clusters that work [167] found to be present in MG are shown in Fig. 21 a. These clusters are ordered by the coordination number of solute atom in center of cluster. Clusters may be responsible for SRO of atoms in MG, and the concentration of cluster creates MRO structures of MG. Typical connections found and proposed by [167] are shown in Fig. 21 b, c, d. The present clusters connections exhibit fivefold symmetry and can be noticed that part of the atoms in connected clusters are shared. Depending on the which atom is shared the connection is named face-, vortex- or edge-shared [167,210].

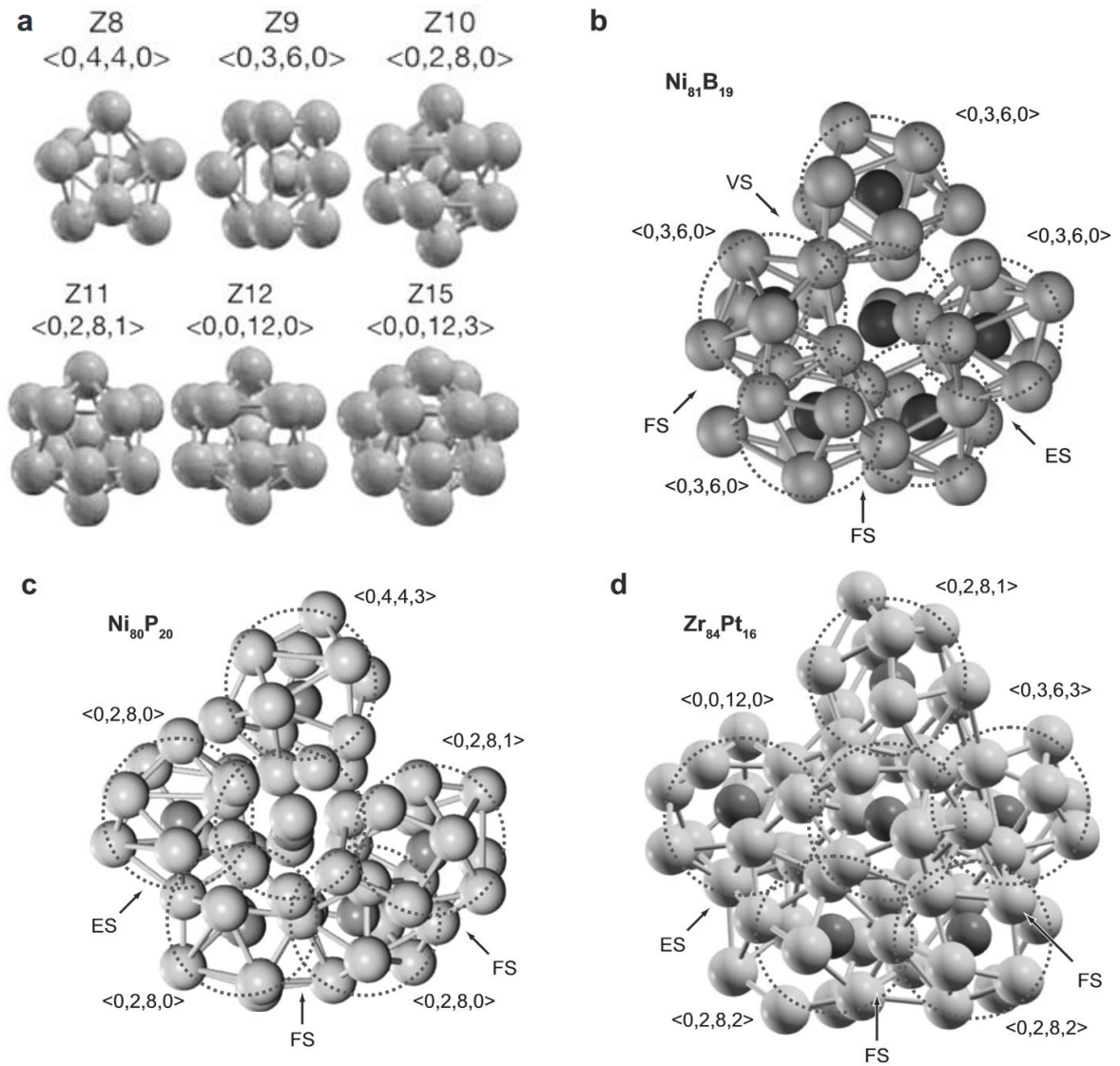


Fig. 21. **a**- typical polyhedral clusters of the *solute* atoms found in MGs- $\text{Ni}_{81}\text{B}_{19}$, $\text{Ni}_{80}\text{P}_{20}$ and $\text{Zr}_{84}\text{Pt}_{16}$. Z8, Z9 etc. represents the coordination number of solute atom (number of atoms a central atom carries as its closest neighbors [217]) [167]; **b**, **c**, **d**- presents the typical cluster connection found in $\text{Ni}_{81}\text{B}_{19}$, $\text{Ni}_{80}\text{P}_{20}$ and $\text{Zr}_{84}\text{Pt}_{16}$, respectively. Voronoi index (e.g. $\langle 0,2,8,0 \rangle$) indicate the type of cluster (delineate with red dash circles) and FS, VS, ES represent the type of atoms sharing between the clusters and stand for face-sharing, vortex- sharing and edge-sharing, respectively. The bonds between atoms in the center clusters are not shown for clarity [167]

The SRO and MRO arrangements described above do not fill the whole volume of the MG. Between the clusters, areas with lower atom density are observed, often called the empty space or free-volume. Free volume is characterized by a lower atomic coordination compared to observed dens atomic clusters [218–220]. One of the known reasons for the free volume is geometric packing frustration of atoms [221]. Free volume is especially important for the mechanical behavior of the MG because it is the prone area where the glassy structure can destabilize. Destabilization in this area occurs due to the easier possibility of inelastic relaxation of atoms by their local arrangements without significantly affecting its surroundings [222,223]. Local relaxation in free volume can occur due to applied stress to the structure (forming local shearing) or influence of temperature (above glass transition temperature). Also, the state of atoms around the free-volume can differ for the same MG due to a different

development history, i.e. the cooling rates that were used for developed MG, annealing history or applied forces [224–228].

One of the suggested parameters that can predict the ductile or brittle behavior of metallic glasses is G/B ratio (elastic shear modulus G, bulk modulus B). Work [229] by analyzed twelve MG suggested that ratio 0.41–0.43 is an critical value where the MG change behavior from ductile to brittle. Ductile MGs are those with G/B values lower than critical. But the ductile behavior can change into brittle by annealing-induced embrittlement or by a slight change in the chemical composition of the MG [229,230] (Fig. 22). Review of MG mechanical properties- hardness, Young's module and yield strength is shown in Tab. 7.

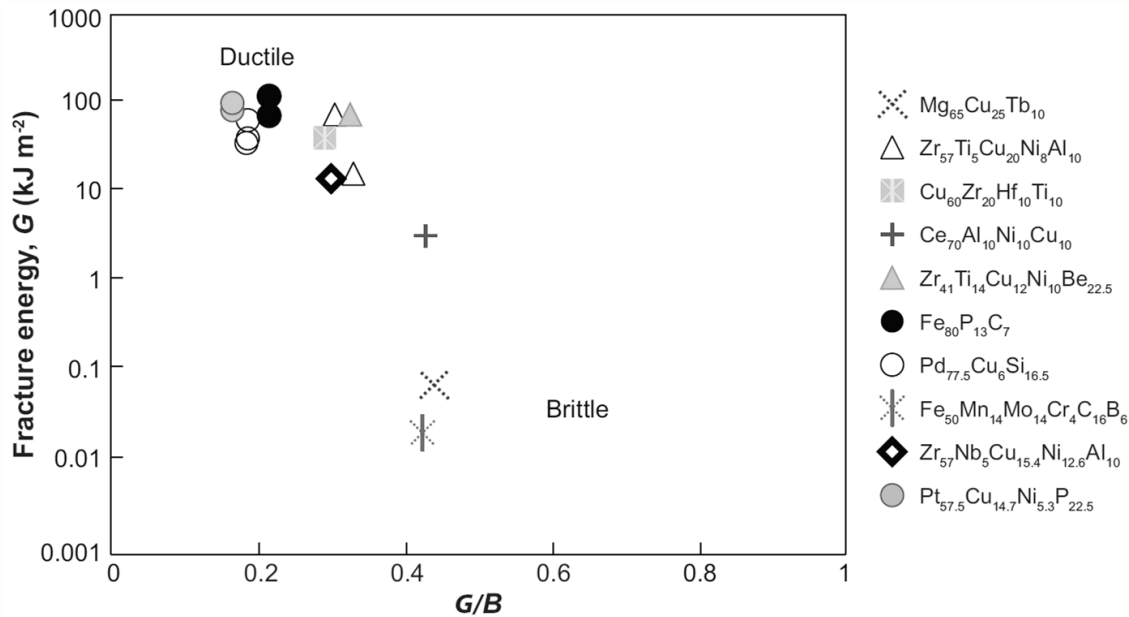


Fig. 22. Correlation of the fracture energy E with the elastic modulus ratio G/B for selected as-cast metallic glasses [210,229]

Tab. 7. Review of the mechanical properties of bulk metallic glasses [170]

Alloy	H (GPa)	E (GPa)	σ_y (GPa)	Reference
$\text{Zr}_{57}\text{Ti}_5\text{Ni}_8\text{Cu}_{20}\text{Al}_{10}$	4.6 ± 0.1	85 ± 1	1.64 ± 0.02	[170,231,232]
$\text{Hf}_{11.4}\text{Zr}_{45.6}\text{Ti}_5\text{Ni}_8\text{Cu}_{20}\text{Al}_{10}$	4.7 ± 0.1	87 ± 1	1.78 ± 0.01	[170,231,232]
$\text{Hf}_{22.8}\text{Zr}_{34.2}\text{Ti}_5\text{Ni}_8\text{Cu}_{20}\text{Al}_{10}$	5.2 ± 0.1	94 ± 1	1.80 ± 0.10	[170,231,232]
$\text{Zr}_{52.4}\text{Ti}_5\text{Ni}_{14.6}\text{Cu}_{17.9}\text{Al}_{10}$	5.0 ± 0.2	93 ± 2	1.74 ± 0.03	[170,231,232]
$\text{Hf}_{10.5}\text{Zr}_{42}\text{Ti}_5\text{Ni}_{14.6}\text{Cu}_{17.9}\text{Al}_{10}$	5.3 ± 0.1	108 ± 3	1.94 ± 0.02	[170,231,232]
$\text{Hf}_{21}\text{Zr}_{31.5}\text{Ti}_5\text{Ni}_{14.6}\text{Cu}_{17.9}\text{Al}_{10}$	5.5 ± 0.1	113 ± 2	1.85 ± 0.02	[170,231,232]
$\text{Hf}_{31.5}\text{Zr}_{21}\text{Ti}_5\text{Ni}_{14.6}\text{Cu}_{17.9}\text{Al}_{10}$	5.8 ± 0.2	110 ± 3	2.03 ± 0.03	[170,231,232]
$\text{Hf}_{42}\text{Zr}_{10.5}\text{Ti}_5\text{Ni}_{14.6}\text{Cu}_{17.9}\text{Al}_{10}$	6.0 ± 0.2	124 ± 2	2.04 ± 0.04	[170,231,232]
$\text{Hf}_{52.5}\text{Ti}_5\text{Ni}_{14.6}\text{Cu}_{17.9}\text{Al}_{10}$	6.1 ± 0.2	128 ± 4	2.09 ± 0.02	[170,231,232]
$\text{Zr}_{57}\text{Nb}_5\text{Ni}_{12.6}\text{Cu}_{15.4}\text{Al}_{10}$	4.9 ± 0.1	89 ± 1	1.74 ± 0.04	[170,231,232]
$(\text{Al}_{0.84}\text{Y}_{0.09}\text{Ni}_{0.05}\text{Co}_{0.02})_{95}\text{Sc}_5$	4.4	78	1.51	[233]
$(\text{Al}_{0.85}\text{Y}_{0.08}\text{Ni}_{0.05}\text{Co}_{0.02})_{95}\text{Sc}_5$	4	75	1.45	[233]
$\text{Co}_{78}\text{Si}_{10}\text{B}_{12}$	8.9	88	3	[234]
$\text{Cu}_{60}\text{Hf}_{25}\text{Ti}_{15}$	6.7	124	$1.92^T/2.01$	[235]
$\text{Cu}_{60}\text{Hf}_{30}\text{Ti}_{10}$	6.3	119	2	[235]
$\text{Cu}_{47.5}\text{Zr}_{47.5}\text{Al}_5$	-	87	1.55	[226]
$\text{Fe}_{80}\text{B}_{20}$	10.6	167	3.40	[234]
$\text{Fe}_{80}\text{P}_{13}\text{C}_7$	7.5	118	3.04	[234]
$\text{Fe}_{78}\text{B}_{10}\text{Si}_{12}$	8.9	118	3.33	[234]
	10.5	180	3.16	[236]

(Fe _{0.75} B _{0.2} Si _{0.05}) ₉₆ Nb ₄	11.3	190	3.82	[236]
(Fe _{0.9} C _{0.1}) _{0.75} B _{0.2} Si _{0.05}) ₉₆ Nb ₄	12.0	205	4.05	[236]
(Fe _{0.8} C _{0.2}) _{0.75} B _{0.2} Si _{0.05}) ₉₆ Nb ₄	12.2	210	4.10	[236]
(Fe _{0.7} C _{0.3}) _{0.75} B _{0.2} Si _{0.05}) ₉₆ Nb ₄	12.3	210	4.10	[236]
(Fe _{0.6} C _{0.4}) _{0.75} B _{0.2} Si _{0.05}) ₉₆ Nb ₄	12.0	210	4.07	[236]
(Fe _{0.5} C _{0.5}) _{0.75} B _{0.2} Si _{0.05}) ₉₆ Nb ₄	8.4	78	2.45	[234]
Ni ₇₈ Si ₁₀ B ₁₂	7.8	114	2.37	[43]
Ni ₄₅ Ti ₂₀ Zr ₂₅ Al ₁₀	7.6	111	2.18	[43]
Ni ₄₀ Cu ₆ Ti ₁₆ Zr ₂₈ Al ₁₀	8.4	134	2.30	[43]
Ni ₄₀ Cu ₅ Ti ₁₇ Zr ₂₈ Al ₁₀	7.8	122	2.30	[43]
Ni ₄₀ Cu ₅ Ti _{16.5} Zr _{28.5} Al ₁₀	8.1	117	2.32	[43]
Ni _{39.8} Cu _{5.97} Ti _{15.92} Zr _{27.86} Al _{9.95} Si _{0.5}	5.2	96	1.90	[237]
Zr _{41.25} Ti _{13.75} Ni ₁₀ Cu _{12.5} Be _{22.5}	5.5	-	1.69	[238]
Zr _{54.4} Cu _{25.6} Fe ₈ Al ₁₂	5.3	-	1.63	[238]
Zr ₅₈ Cu ₂₂ Fe ₈ Al ₁₂	5.1	-	1.56	[238]
Zr _{61.6} Cu _{18.4} Fe ₈ Al ₁₂	3.2	67	1.34	[234]
Pd ₈₀ Si ₂₀	5.3	108	1.46/1.78	[239,240]
Pd ₄₀ N ₄₀ P ₂₀	4.9	88	1.44/1.54	[239,240]
Pd _{77.5} Cu ₆ Si _{16.5}	-	94	1.40	[225]
Pt _{57.5} Cu _{14.7} Ni _{5.3} P _{22.5}				

σ_y - yield strength, T_c - indicates tensile yield strength

5.2. Thermal

The applications of metallic glasses are limited by their characteristic temperatures. When the MG establishes a temperature higher than T_g , the structure is no longer glassy, but it is still amorphous (without LRO of atom arrangements). The first LRO structures (nucleation of crystal) can be observed by reaching the onset of first crystallization temperature T_x . The difference between T_x and T_g (supercooled liquid region) is used for the comparison of GFA between MG (the higher ΔT_x the higher the GFA). The history of annealing MG can induce embrittlement and result in brittle behavior of before ductile MG. Work [241] studies the behavior of MG between 77 K and 0.9 T_g temperatures and shows experimentally that elastic modulus, yield stress and strain, and hardness decrease linearly in the measured temperature range.

The next important characteristic temperature, often not measured, is melt overheating. Research points out that not enough overheating can lead to unmelted particles that can then function as nucleation seeds even for an alloy cooled with very high cooling rates [242–245]. As a result, the composite structure is obtained with non-homogeneous properties. Interesting phenomena occur when the overheating is increased. Namely, higher overheating leads to trapping more free-volumes in the cooled MG which as we already acknowledge are sole of the plastic behavior of MG. Research [246] studied three metallic glasses based on Zr. The results showed that the plasticity of the MG increased with increased overheating of the melt if the cooling rates were higher than the critical cooling rates. Additionally, MG cast with higher overheating had greater resistance to crystallization, exhibited higher homogeneity, and greater plastic strain.

Characteristic temperatures of each metallic glass can differ. Change may be induced for different reasons. A slight change in the chemical composition of the alloy can change the ΔT_x . For example, one of the highest values of ΔT_x is around 90°C for Fe₄₃Cr₁₆Mo₁₆C₁₅B₁₀ MG, which can drop to a moderate value of 40°C due to changes in elements C and B concentrations [247]. The characteristic temperatures of MG can also change by changing the cooling rate

(R_c) of the solidifying alloy [248–250]. The largest changes are observed for the T_g values, which decrease with increasing R_c , while the T_x values almost do not change (therefore the supercooled region value increases). Again, this phenomenon is explained by changes in free volume [250]. With decreasing R_c in an amorphous structure, clusters start to form and the homogeneity of the local chemical compound of the alloy decreases, resulting in a higher T_g [248]. As mentioned in [248], the measured difference of the ΔT_x was 31°C between two different types of casting (with different cooling rates). As a moderate values ΔT_x usually are 40–60°C which provides enough values to establish an amorphous structure using typical manufacturing methods [251–253]. The schematic change of T_g is shown in Fig. 24. Additionally, in the discussion of the results of thermal analysis of metallic glasses, attention should be paid to heating rates used in analyzed thermal analyses because not only the cooling but also different heating rate influence on the measured characteristic temperatures.

5.3. Chemical

A characteristic of metallic glasses is the absence of structural defects, such as the grain boundaries characteristic of polycrystal structures. This absence and uniform structure provide very high corrosion resistance to some metallic glasses; however, some factors can influence their anticorrosion resistance [254]. Partial crystallization leads to the presence of the second phase, which decreases the anticorrosion properties. The passivation ability of MG can also be improved by the presence of Cr, Ni, Co, Fe, Mn to Cu (in sequence of decreasing passivation ability [255]) by increasing the content of the passive protective oxide film. Other very important factors are residual stress, surface state, and crack presentation, which can significantly reduce anticorrosion properties. Most of the tested MGs with these abilities are based on Fe [159,162], Zr [256], Ni [257], Ti [258], Al [259], Co [58,260,261] and Cu [262]. The positive influence on the anticorrosion ability of MG, the actual development technologies used and the factors that threaten corrosion resistance are shown in Fig. 23.

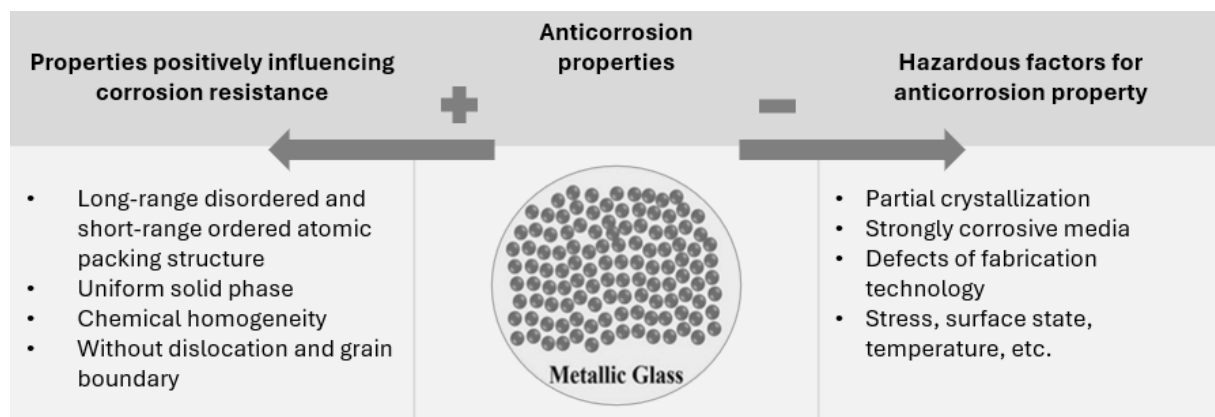


Fig. 23. Summary of factors influencing on anticorrosion properties of metallic glasses [254]

5.4. Processability

The processing of metallic glasses has its pros and cons. It is certain that the pros of metallic glasses processing are some esthetic and physical properties that can make them very attractive for possible buyers. The high hardness, wear resistance, and anticorrosion properties of MG can make the elements very durable. The ability to finish the surface to a high polish makes them esthetics attractive. The relatively novelty of the material (material

with such a different structure) can become very interesting and attractive for potential consumers. Another asset of metallic glasses is their low solidification shrinkage, which allows a very low deviation of dimension, equaling the high precision of manufactured elements. However, it should be noted that changing the cooling rates of metallic glasses (even in the supercooled region) influence the shrinkage value. Fig. 24 shows the comparison of fast, slow and very slow (crystallization occurs) cooling of the same alloy and the change in the volume of it. As can be concluded from the Fig. 24, MG cooled with higher cooling rates will be characterized by the lowest shrinkage compared to those cooled with lower cooling rates [263] [264].

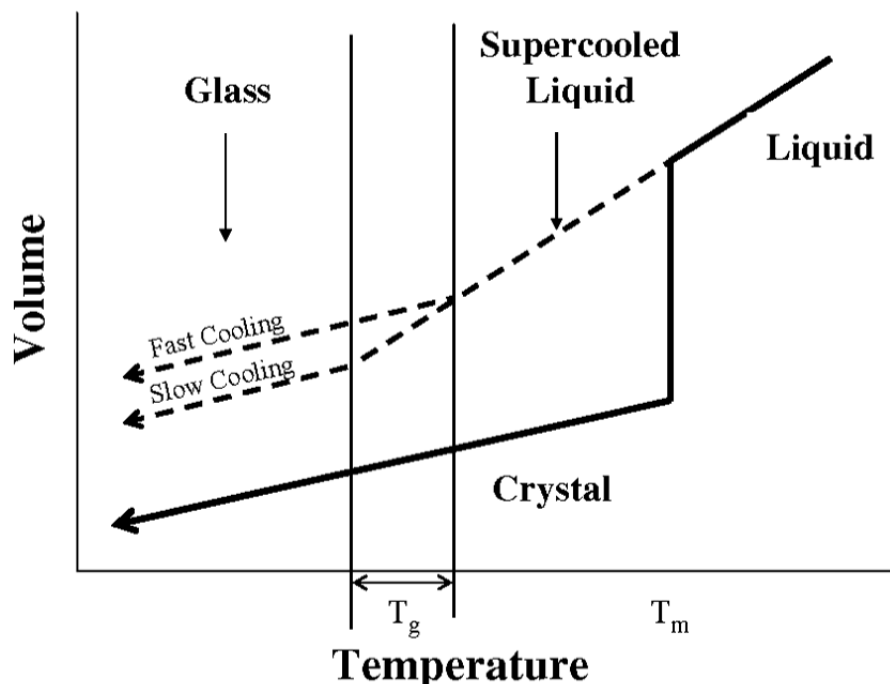


Fig. 24. Volumetric changes of alloy during cooling with different cooling rates [263]

The cons of metallic glasses include the price of developing products from MG. One of the price components of the MG is chemical elements present in their composition. MG requires a special chemical composition of the alloy, which will provide high GFA and consequently a glassy structure of the established product. Often, this special composition includes chemical elements that are more expensive than traditional chemical elements in carbon or construction steel. Especially costly MG are those containing the rare-earth elements which are often present, as shown in Fig. 5 (*Percentage of MG classified by base material (...)*). Another component of the price of MG is manufacturing technology, such as the very commonly used vacuum die casting, which has a relatively slow development rate making it expensive [168], or spraying technologies which use expensive noble gases. However, there are also technologies that are inexpensive in use, such as melt spinning, where the development rate is very high because of the continuity of the process.

6. Applications

In the paragraph above, the characteristic properties of MG such as mechanical, chemical, esthetic, and processing were described. Many of those unique properties found application in different fields of industry such as medical, sports, electronics, etc. Work [265]

groups some of the applications already in use adding economic reasons that include novelty of material, justification of the high cost of material by a high-valued durability and performance of the developed element. The analysis of metallic glass applications is shown in Tab. 8.

Tab. 8. Current and possible applications of BMGs [265]

	Application	Technical reasons	Economic reasons
SPORT	Golf clubs (commercialized)	<ul style="list-style-type: none"> - high strength - high σ_y/E, σ_y^2/E 	A, B, C, D, E
	Edges for sport goods (skis, skates)	<ul style="list-style-type: none"> - high hardness - wear and corrosion resistance - high σ_y/E - ability to be sharpened 	A, B, C, D, E
MEDICINE	Knives for ophthalmology (commercialized)	<ul style="list-style-type: none"> - high hardness - wear and corrosion resistance - high σ_y^3/E^2 	A, B, E
	Dental materials	<ul style="list-style-type: none"> - high strength - hardness - wear and corrosion resistance - castability - abilities for surface finishing 	B, C, E
MECHANICAL	Precision mechanical elements	<ul style="list-style-type: none"> - high strength - high hardness - wear and corrosion resistance - good abilities for surface finishing 	A, B, C, E
	Machinery structural material (high performance springs)	<ul style="list-style-type: none"> - high σ_y^2/E, - high fatigue strength - high workability 	
ELECTRONICS	Materials for digital master discs	<ul style="list-style-type: none"> - wear resistance - no grain structure 	C, E
ART	Wires for musical instruments	<ul style="list-style-type: none"> - high strength - high workability 	C, E
	Jewelry (Pd and Pt-based alloys)	<ul style="list-style-type: none"> - high hardness - wear and corrosion resistance - luster, precious metal content 	C, D, E

Market indicators: A- cost of material constitutes small part of the price; B- performance is highly valued; C- cost of failure is modest; D- fashion and “novelty” are welcomed; E- market does not require large volumes of material. σ_y - yield strength, E- elastic modulus

In the sport industry, MG found application, for example in golf clubs due to the very high elastic limit that provides low energy loss while playing golf [33]. Work [266] shows that Zr-based MG compared to traditional use of crystalline materials helped establish a high coefficient of restitution (which is the square root of the ratio of the final kinetic energy to the

initial kinetic energy). Additionally, at the same time, Zr-based MG provides very high mechanical properties: tensile strength of 1700 MPa, impact fracture toughness 130 kJ/m² and Young's modulus of 81 GPa, which makes this material perfect for sports equipment.

The medical industry found the use of metallic glass for super sharp knives due to their high wear and corrosion resistance, high hardness and ratio σ_y^3/E^2 which able to form and sustain sharp edges [265]. Knives manufactured from MG glasses can either be made from a bulk element or done from commercial stainless steel with MG coating. Fig. 25 shows knives manufactured from BMG and with MG film and a comparison of commercial knife edge and BMG edge [267,268]. A sharper knife with lower roughness provides a cleaner slice and better wound healing [269]. Similar, high mechanical properties and chemical resistance to corrosion and castability make BMG suitable material for dental purposes, such as implants, stents, fillers, surgery sutures. However, all biomedical applications must meet other requirements such as being nontoxic and noncancer. Work [268] classified MG suitable for biomedical purposes and division into nonbiodegradable including: Ti-based, Zr-based, Fe-based MG; and biodegradable: Mg-based, Ca-based, Zn-based, and Sr-based BMGs.

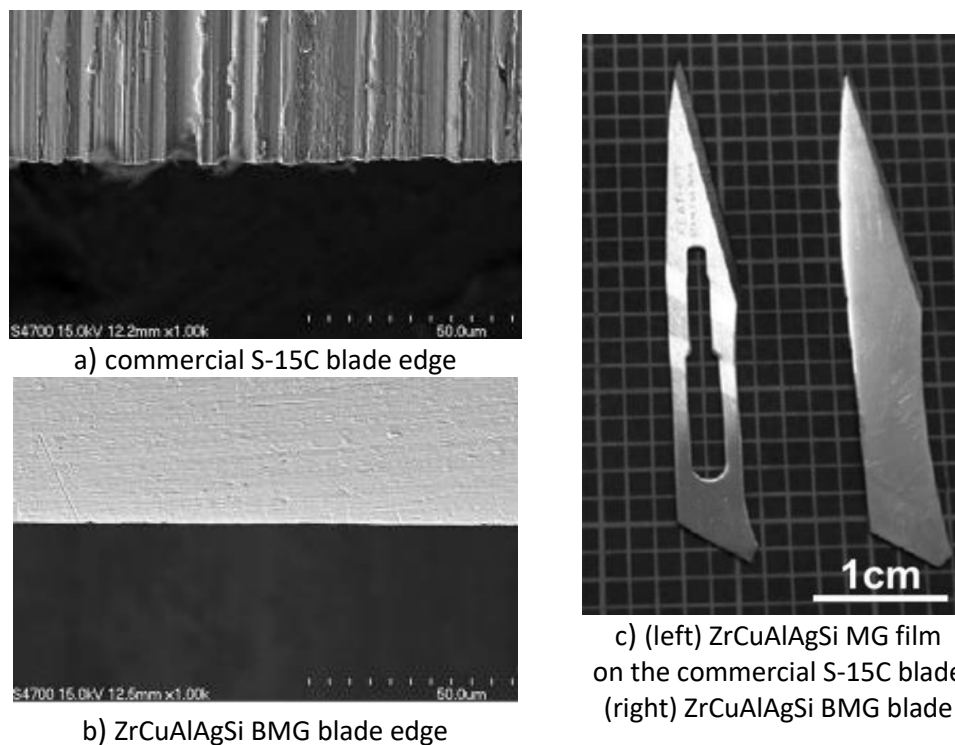


Fig. 25. Use of MG in surgical knives[267,268]

Due to the high cost of the material, combined with the very high mechanical properties, MG in machine building finds its place in micro and nano electromechanics, often found under the name of MEMS and NEMS (micro-/ nano- electromechanical system). MEMS and NEMS do not require a large amount of material, which reduces the cost of finished electromechanics while providing all the advantages of MG such as excellent mechanical properties and very low surface roughness. The tribological properties of MG thin films are promising for applications in NEMS and MEMS [270]. Furthermore, the isotropic and magnetic properties of MG enable them to be used for sensing and detection purposes [271]. One of the successful MEMS examples is the micro solenoid fluxgate sensor established from a multilayer Fe-based amorphous core (commercially available 2605S Metglas) [272]. Other successfully developed MEMS is an actuator with a conical spring of 7.6 μm thickness

developed from $\text{Pd}_{76}\text{Cu}_7\text{Si}_{17}$ MG with a long stroke of $200\text{ }\mu\text{m}$ [273]. An example of developed MEMS is shown in Fig. 26.

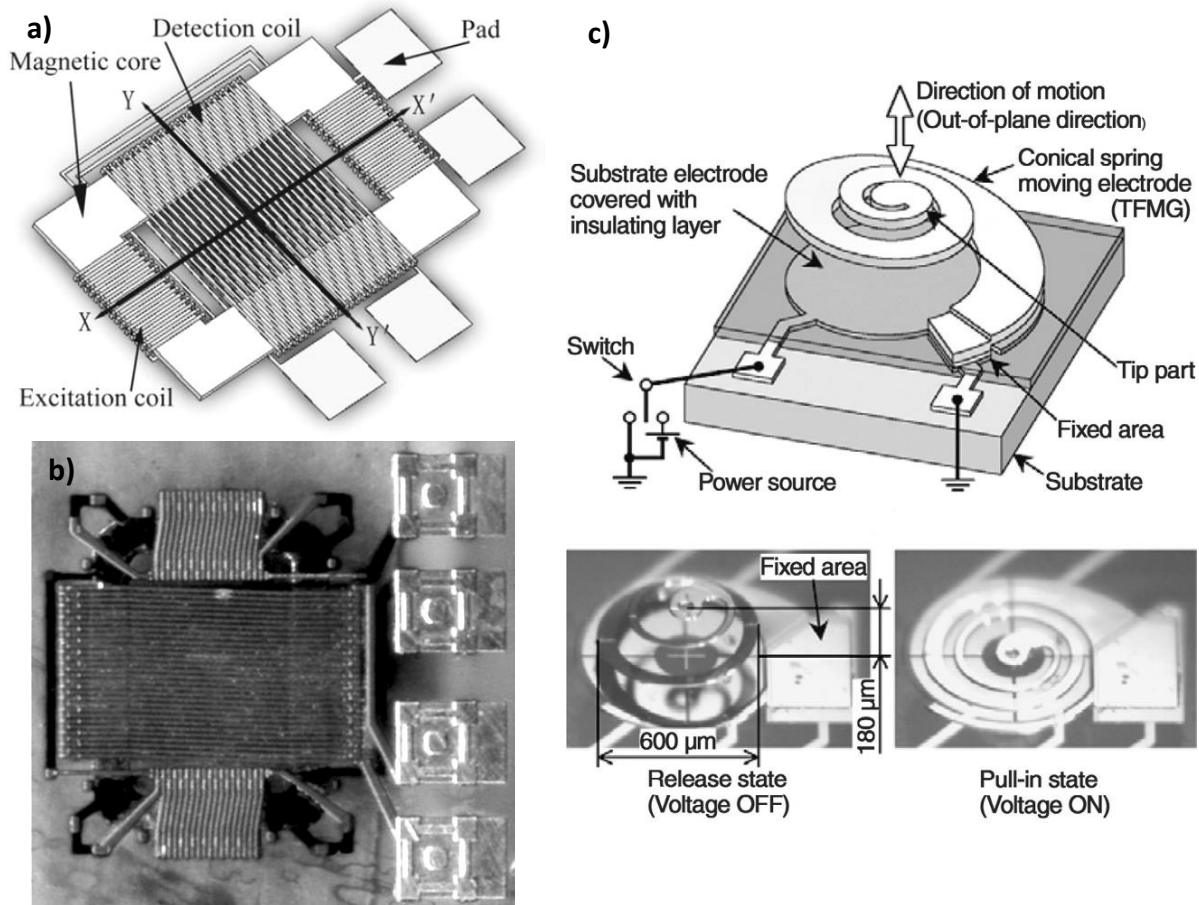


Fig. 26. Fluxgate sensor with Fe-based MG core a) schematic view b) development sensor [272]; c) Conical spring actuator developed with $\text{Pd}_{76}\text{Cu}_7\text{Si}_{17}$ metallic glass [273]

Work [274] presents the smallest developed and commercialized geared-motor in size of 9.9 mm length and 1.5 mm diameter (Fig. 27). As a material, the Zr-based BMG was used developed by the casting technics. The developed gear was able to carry torque around 20 times higher than the conventional vibration motor with a diameter of 4 mm used in cell phones or other electric devices. Beside vibration motors, the mechanism was tested for commercialization in precision optics, micro pumps, etc. [86].

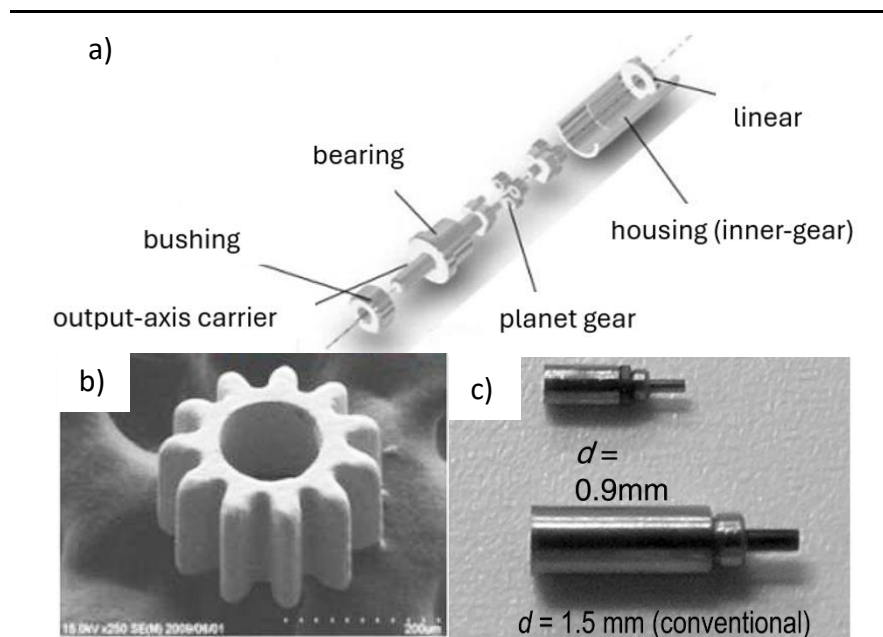


Fig. 27. Smallest geared-motor made of Zr-based MG a) schematic view of gear, b) MG gear c) assembled geared-motor- the smallest $d = 0.9$ mm, and the conventional $d = 1.5$ mm [86]

7. Co-based metallic glasses

7.1. Classification and properties

Cobalt-based alloys with high glass-forming ability are a very wide group of metallic glasses. Common alloying elements for cobalt-based alloys with high glass-forming ability include metallic tantalum, iron, niobium, molybdenum, and metalloids such as boron, carbon, silicon, and phosphorus, which means that Co-based alloys are mostly metal-metalloid types. Binary systems are rarely present in Co-based alloys, but ternary alloys are quite common like $\text{Co}_{61}\text{Nb}_8\text{B}_{31}$, $\text{Co}_{59}\text{Ta}_6\text{B}_{35}$, $\text{Co}_{64}\text{Mo}_{22}\text{B}_{14}$ etc. [275,276]. A more complicated system has up to six elements like $[(\text{Co}_{0.535}\text{Fe}_{0.1}\text{Ta}_{0.055}\text{B}_{0.31})_{0.98}\text{Mo}_{0.02}]_{98}\text{Si}_2$ [277]. The most popular chemical elements that can be found in Co-based MG are marked in the Fig. 28. As for other metallic glasses, the addition of metalloids and nonmetals such as C, B, P, Si [50] to enhance the glass-forming ability of Co-based metallic glasses. Work [50] tests the perfect ratio of C to B that will provide a wide range of supercooled regions. The result shows that adding boron to Co-Cr-Mo-C-B alloy in an amount twice less than the amount of carbon will secure ΔT_x on level of 100°C , which is one of the highest values among MG. Similar research that studied the proper ratio of B to C [278] for Co-based Co-Cr-Mo-C-B MG is 1:1. This ratio allowed to establish the fully amorphous samples with the highest recorded ΔT_x for the Co-based MG. The value is equal to $111 \pm 5^\circ\text{C}$ while the low values of ΔT_x is usually at the level of $30\text{--}40^\circ\text{C}$ [279] and moderate around 60°C [280]. Other parameters indicating GFA such as a D_c for a Co-based MG can reach a value of 4.5 mm for CoMoPB alloys [281] or even 5.0 or 5.5 mm for the CoFeNiBSiNb alloys [282,283].

<div><div>Nonmetal</div><div>Alkali Metal</div><div>Alkaline Earth Metal</div><div>Transition Metal</div></div> <div><div>Lanthanide</div><div>Actinide</div><div>Metalloid</div><div>Post-Transition Metal</div></div> <div><div>Halogen</div><div>Noble Gas</div><div><div>* Solid</div><div>** Liquid</div><div>*** Gas</div></div></div>																		<div><div>Helium</div><div>He</div><div>***</div><div>4.003</div><div>2</div></div>																
<div><div>Hydrogen</div><div>H</div><div>***</div><div>1.008</div><div>1</div></div>																	<div><div>Neon</div><div>Ne</div><div>***</div><div>20.18</div><div>10</div></div>																	
<div><div>Lithium</div><div>Li</div><div>*</div><div>6.941</div><div>3</div></div>	<div><div>Beryllium</div><div>Be</div><div>*</div><div>9.012</div><div>4</div></div>																	<div><div>Boron</div><div>B</div><div>*</div><div>10.81</div><div>5</div></div>	<div><div>Carbon</div><div>C</div><div>*</div><div>12.01</div><div>6</div></div>	<div><div>Nitrogen</div><div>N</div><div>***</div><div>14.01</div><div>7</div></div>	<div><div>Oxygen</div><div>O</div><div>***</div><div>16.00</div><div>8</div></div>	<div><div>Fluorine</div><div>F</div><div>***</div><div>19.00</div><div>9</div></div>	<div><div>Argon</div><div>Ar</div><div>***</div><div>39.95</div><div>18</div></div>											
<div><div>Sodium</div><div>Na</div><div>*</div><div>22.99</div><div>11</div></div>	<div><div>Magnesium</div><div>Mg</div><div>*</div><div>24.31</div><div>12</div></div>																	<div><div>Aluminium</div><div>Al</div><div>*</div><div>26.98</div><div>13</div></div>	<div><div>Silicon</div><div>Si</div><div>*</div><div>28.09</div><div>14</div></div>	<div><div>Phosphorus</div><div>P</div><div>*</div><div>30.97</div><div>15</div></div>	<div><div>Sulfur</div><div>S</div><div>*</div><div>32.07</div><div>16</div></div>	<div><div>Chlorine</div><div>Cl</div><div>***</div><div>35.45</div><div>17</div></div>	<div><div>Krypton</div><div>Kr</div><div>***</div><div>83.80</div><div>36</div></div>											
<div><div>Potassium</div><div>K</div><div>*</div><div>39.10</div><div>19</div></div>	<div><div>Calcium</div><div>Ca</div><div>*</div><div>40.08</div><div>20</div></div>	<div><div>Scandium</div><div>Sc</div><div>*</div><div>44.96</div><div>21</div></div>	<div><div>Titanium</div><div>Ti</div><div>*</div><div>47.87</div><div>22</div></div>	<div><div>Vanadium</div><div>V</div><div>*</div><div>50.94</div><div>23</div></div>	<div><div>Chromium</div><div>Cr</div><div>*</div><div>52.00</div><div>24</div></div>	<div><div>Manganese</div><div>Mn</div><div>*</div><div>54.94</div><div>25</div></div>	<div><div>Iron</div><div>Fe</div><div>*</div><div>55.84</div><div>26</div></div>	<div><div>Cobalt</div><div>Co</div><div>*</div><div>58.93</div><div>27</div></div>	<div><div>Nickel</div><div>Ni</div><div>*</div><div>58.69</div><div>28</div></div>	<div><div>Copper</div><div>Cu</div><div>*</div><div>63.55</div><div>29</div></div>	<div><div>Zinc</div><div>Zn</div><div>*</div><div>65.39</div><div>30</div></div>	<div><div>Gallium</div><div>Ga</div><div>*</div><div>69.72</div><div>31</div></div>	<div><div>Germanium</div><div>Ge</div><div>*</div><div>72.63</div><div>32</div></div>	<div><div>Arsenic</div><div>As</div><div>*</div><div>74.92</div><div>33</div></div>	<div><div>Selenium</div><div>Se</div><div>*</div><div>78.96</div><div>34</div></div>	<div><div>Bromine</div><div>Br</div><div>***</div><div>79.90</div><div>35</div></div>	<div><div>Xenon</div><div>Xe</div><div>***</div><div>131.29</div><div>54</div></div>																	
<div><div>Rubidium</div><div>Rb</div><div>*</div><div>85.47</div><div>37</div></div>	<div><div>Strontium</div><div>Sr</div><div>*</div><div>87.62</div><div>38</div></div>	<div><div>Yttrium</div><div>Y</div><div>*</div><div>88.91</div><div>39</div></div>	<div><div>Zirconium</div><div>Zr</div><div>*</div><div>91.22</div><div>40</div></div>	<div><div>Niobium</div><div>Nb</div><div>*</div><div>92.91</div><div>41</div></div>	<div><div>Molybdenum</div><div>Mo</div><div>*</div><div>95.94</div><div>42</div></div>	<div><div>Technetium</div><div>Tc</div><div>*</div><div>[98]</div><div>43</div></div>	<div><div>Ruthenium</div><div>Ru</div><div>*</div><div>101.07</div><div>44</div></div>	<div><div>Rhodium</div><div>Rh</div><div>*</div><div>102.91</div><div>45</div></div>	<div><div>Palladium</div><div>Pd</div><div>*</div><div>106.42</div><div>46</div></div>	<div><div>Silver</div><div>Ag</div><div>*</div><div>107.87</div><div>47</div></div>	<div><div>Cadmium</div><div>Cd</div><div>*</div><div>112.41</div><div>48</div></div>	<div><div>Indium</div><div>In</div><div>*</div><div>114.82</div><div>49</div></div>	<div><div>Tin</div><div>Sn</div><div>*</div><div>118.71</div><div>50</div></div>	<div><div>Antimony</div><div>Sb</div><div>*</div><div>121.76</div><div>51</div></div>	<div><div>Tellurium</div><div>Te</div><div>*</div><div>127.60</div><div>52</div></div>	<div><div>Iodine</div><div>I</div><div>*</div><div>126.90</div><div>53</div></div>	<div><div>Xenon</div><div>Xe</div><div>***</div><div>131.29</div><div>54</div></div>																	
<div><div>Caesium</div><div>Cs</div><div>*</div><div>132.91</div><div>55</div></div>	<div><div>Barium</div><div>Ba</div><div>*</div><div>137.33</div><div>56</div></div>	<div><div>LANTHANIDE</div><div>▼</div></div>	<div><div>Hafnium</div><div>Hf</div><div>*</div><div>178.49</div><div>72</div></div>	<div><div>Tantalum</div><div>Ta</div><div>*</div><div>180.95</div><div>73</div></div>	<div><div>Tungsten</div><div>W</div><div>*</div><div>183.84</div><div>74</div></div>	<div><div>Rhenium</div><div>Re</div><div>*</div><div>186.21</div><div>75</div></div>	<div><div>Osmium</div><div>Os</div><div>*</div><div>190.23</div><div>76</div></div>	<div><div>Iridium</div><div>Ir</div><div>*</div><div>192.22</div><div>77</div></div>	<div><div>Platinum</div><div>Pt</div><div>*</div><div>195.08</div><div>78</div></div>	<div><div>Gold</div><div>Au</div><div>*</div><div>196.97</div><div>79</div></div>	<div><div>Mercury</div><div>Hg</div><div>**</div><div>200.59</div><div>80</div></div>	<div><div>Thallium</div><div>Tl</div><div>*</div><div>204.38</div><div>81</div></div>	<div><div>Lead</div><div>Pb</div><div>*</div><div>207.2</div><div>82</div></div>	<div><div>Bismuth</div><div>Bi</div><div>*</div><div>208.98</div><div>83</div></div>	<div><div>Polonium</div><div>Po</div><div>*</div><div>[209]</div><div>84</div></div>	<div><div>Astatine</div><div>At</div><div>*</div><div>[210]</div><div>85</div></div>	<div><div>Radon</div><div>Rn</div><div>***</div><div>[222]</div><div>86</div></div>																	
<div><div>Francium</div><div>Fr</div><div>*</div><div>[223]</div><div>87</div></div>	<div><div>Radium</div><div>Ra</div><div>*</div><div>[226]</div><div>88</div></div>	<div><div>ACTINIDES</div><div>▼</div></div>	<div><div>Rutherfordium</div><div>Rf</div><div>*</div><div>[267]</div><div>104</div></div>	<div><div>Dubnium</div><div>Db</div><div>*</div><div>[268]</div><div>105</div></div>	<div><div>Seaborgium</div><div>Sg</div><div>*</div><div>[269]</div><div>106</div></div>	<div><div>Bohrium</div><div>Bh</div><div>*</div><div>[270]</div><div>107</div></div>	<div><div>Hassium</div><div>Hs</div><div>*</div><div>[269]</div><div>108</div></div>	<div><div>Meitnerium</div><div>Mt</div><div>*</div><div>[278]</div><div>109</div></div>	<div><div>Darmstadtium</div><div>Ds</div><div>*</div><div>[281]</div><div>110</div></div>	<div><div>Roentgenium</div><div>Rg</div><div>*</div><div>[281]</div><div>111</div></div>	<div><div>Copernicium</div><div>Cn</div><div>*</div><div>[285]</div><div>112</div></div>	<div><div>Nihonium</div><div>Nh</div><div>*</div><div>[286]</div><div>113</div></div>	<div><div>Flerovium</div><div>Fl</div><div>*</div><div>[289]</div><div>114</div></div>	<div><div>Moscovium</div><div>Mc</div><div>*</div><div>[289]</div><div>115</div></div>	<div><div>Livermorium</div><div>Lv</div><div>*</div><div>[293]</div><div>116</div></div>	<div><div>Tennessee</div><div>Ts</div><div>*</div><div>[294]</div><div>117</div></div>	<div><div>Oganesson</div><div>Og</div><div>***</div><div>[294]</div><div>118</div></div>																	
<div><div>Lanthanum</div><div>La</div><div>*</div><div>138.91</div><div>57</div></div>																		<div><div>Cerium</div><div>Ce</div><div>*</div><div>140.12</div><div>58</div></div>	<div><div>Praseodymium</div><div>Pr</div><div>*</div><div>140.91</div><div>59</div></div>	<div><div>Neodymium</div><div>Nd</div><div>*</div><div>144.24</div><div>60</div></div>	<div><div>Promethium</div><div>Pm</div><div>*</div><div>[145]</div><div>61</div></div>	<div><div>Samarium</div><div>Sm</div><div>*</div><div>150.36</div><div>62</div></div>	<div><div>Europium</div><div>Eu</div><div>*</div><div>151.96</div><div>63</div></div>	<div><div>Gadolinium</div><div>Gd</div><div>*</div><div>157.25</div><div>64</div></div>	<div><div>Terbium</div><div>Tb</div><div>*</div><div>158.93</div><div>65</div></div>	<div><div>Dysprosium</div><div>Dy</div><div>*</div><div>162.50</div><div>66</div></div>	<div><div>Holmium</div><div>Ho</div><div>*</div><div>164.93</div><div>67</div></div>	<div><div>Erbium</div><div>Er</div><div>*</div><div>167.26</div><div>68</div></div>	<div><div>Thulium</div><div>Tm</div><div>*</div><div>168.93</div><div>69</div></div>	<div><div>Ytterbium</div><div>Yb</div><div>*</div><div>173.04</div><div>70</div></div>	<div><div>Lutetium</div><div>Lu</div><div>*</div><div>174.97</div><div>71</div></div>			
<div><div>Actinium</div><div>Ac</div><div>*</div><div>[227]</div><div>89</div></div>	<div><div>Thorium</div><div>Th</div><div>*</div><div>232.04</div><div>90</div></div>	<div><div>Protactinium</div><div>Pa</div><div>*</div><div>231.04</div><div>91</div></div>	<div><div>Uranium</div><div>U</div><div>*</div><div>238.03</div><div>92</div></div>	<div><div>Neptunium</div><div>Np</div><div>*</div><div>[237]</div><div>93</div></div>	<div><div>Plutonium</div><div>Pu</div><div>*</div><div>[244]</div><div>94</div></div>	<div><div>Americium</div><div>Am</div><div>*</div><div>[243]</div><div>95</div></div>	<div><div>Curium</div><div>Cm</div><div>*</div><div>[247]</div><div>96</div></div>	<div><div>Berkelium</div><div>Bk</div><div>*</div><div>[247]</div><div>97</div></div>	<div><div>Californium</div><div>Cf</div><div>*</div><div>[251]</div><div>98</div></div>	<div><div>Einsteinium</div><div>Es</div><div>*</div><div>[252]</div><div>99</div></div>	<div><div>Fermium</div><div>Fm</div><div>*</div><div>[257]</div><div>100</div></div>	<div><div>Mendelevium</div><div>Md</div><div>*</div><div>[258]</div><div>101</div></div>	<div><div>Nobelium</div><div>No</div><div>*</div><div>[259]</div><div>102</div></div>	<div><div>Lawrencium</div><div>Lr</div><div>*</div><div>[262]</div><div>103</div></div>																				

Fig. 28. Most popular chemical elements present in Co-based metallic glasses marked with red frame [284]

The addition of Fe for Co-based MG helps to enhance the magnetic properties of the material, such as particularly saturation magnetization. The addition of an iron can enhance the mechanical strength of an alloy and at the same time make iron cost effective [285]. Work [58] showed that Ni has a positive influence on the mechanical strength of Co-based MG, increasing its amount from 15% to 30% (by substituting Co) increased the compressive strength by 19%, however, the plasticity decreases significantly from 2.3 to 1.0%. The compressive strength of the Co-based alloy can reach up to 6000 MPa, making them one of the highest values among MG. This high value was obtained in [186] by the proper ratio of Co, W, and B in a ternary Co-based alloy. $\text{Co}_{63}\text{W}_{21}\text{B}_{16}$ composition results in the highest compressive strength of an alloy while still having 1.3% plastic strain and the tested rods were fully amorphous alloy with D_c at a level of 2.0 mm and ΔT_x equal to 75°C. However, still high values of strength were also obtained in the ternary alloy where W was substituted by Mo. Exemplary, $\text{Co}_{64}\text{Mo}_{22}\text{B}_{14}$ alloy showed the 2 mm D_c and the compressive strength of 5250 MPa, while the plasticity was very high - 4.1% plastic strain. In addition, the alloy had a very high density of 9.18 g/cm³ [198]. A good review of the typical compressive strength of Co-based alloys with a high glass-forming ability was done in work [286]. The visual presentation of the review is shown in Fig. 29, the Co-based alloys are grouped on the graph by the presents of chemical elements. The mentioned ternary Co-Mo(W)-B alloys exhibit high compressive strain values in comparison to the Co-Ta-B alloys. However, Co-based alloys that show the highest D_c are typical based on Co-Fe-B-Si-Nb [286].

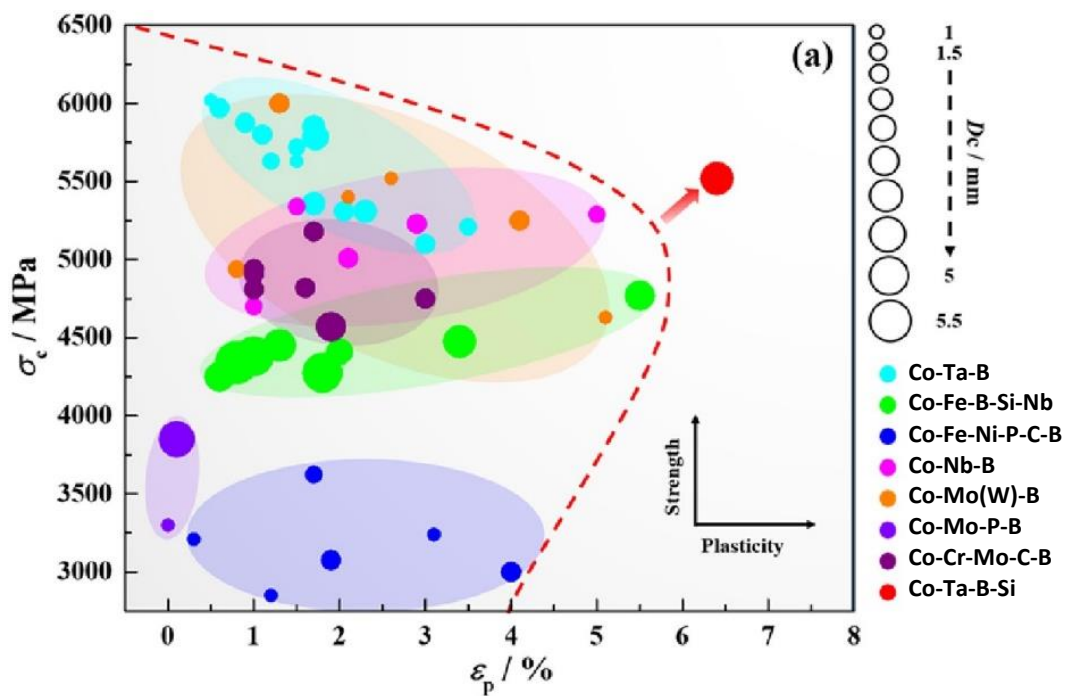


Fig. 29. Review of Co-based alloys with high glass-forming ability showing the relationship between D_c (critical diameter), compressive strength, and plastic strain [286]

To enhance the plasticity of MG, some research uses a minor addition of Cu [287,288]. Exemplary, Cu microdosing in the alloy based on Co-Fe, apart from influencing plasticity, increased D_c from 2 to 4 mm [66]. The optimal amount of Cu for the GFA was 0.6 at%. Another effect of the addition of Cu was the reduction of the amount of oxygen that dissolves in the obtained Co-Fe alloy. In [289] it was confirmed that 2 at.% Cu addition to Co-based MG wires increased their mechanical properties such as fracture strength, fracture strength, tensile strain, the values were 3725 MPa, 4250 MPa and 2.7%, respectively.

Elements that can enhance the corrosion resistance of Co-based alloys are Ni [58], Mo, and Cr [290]. Furthermore, the base element-cobalt itself shows high corrosion resistance [291,292]. Work [58] tested the resistance to corrosion of $\text{Co}_{51}\text{Ni}_{20}\text{Mo}_9\text{P}_{14}\text{B}_6$ at solutions of 3.5% NaCl and 1 M HCl. The results confirm the very good corrosion resistance of the alloy because the value of the corrosion current density (i_{corr}) was at the level of 10^{-7} A/cm^2 for both solutions. The described results of potentiodynamic corrosion tests are shown in Fig. 30. Cr addition to fully Co-Si-B-Nb-Cu MG in an amount of 8% elevates the corrosion resistance of the alloy while still ensuring the amorphous structure of it. The i_{corr} was reduced from 10^{-6} to 10^{-13} A/cm^2 at the 1 M H_2SO_4 solution [290]. The curves obtained in that research are shown in Fig. 31.

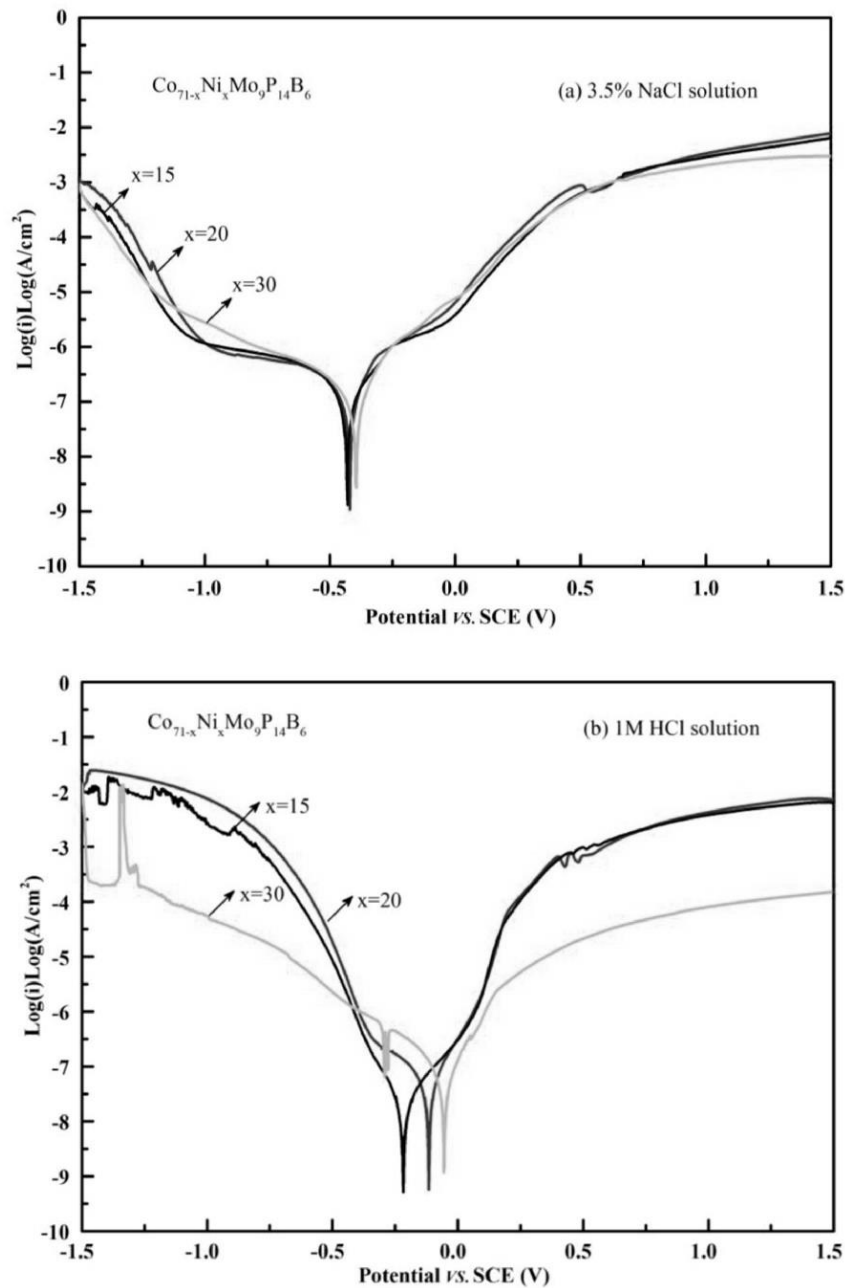


Fig. 30. Potentiodynamic polarization curves of the $\text{Co}_{71-x}\text{Ni}_x\text{Mo}_9\text{P}_{14}\text{B}_6$ ($x = 15, 20, 30 \text{ at.}\%$) obtained at room temperature in 3.5 wt.% NaCl solution (top) and 1 M HCl solution (bottom) [58]

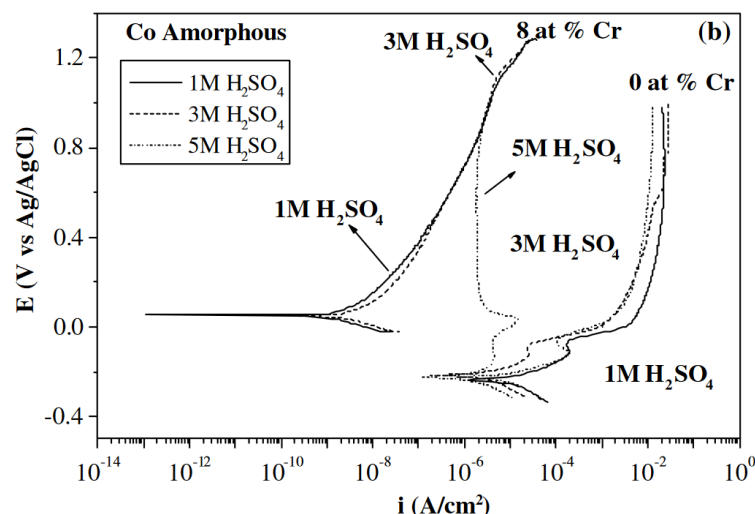


Fig. 31. Anodic potentiodynamic polarization curves for $\text{Co}_{73.5-x}\text{Si}_{13.5}\text{B}_9\text{Nb}_3\text{Cu}_1\text{Cr}_x$ ($x=0, 8$) at different concentrations of H_2SO_4 [290]

In addition to non-metals and metalloids, rare earth elements such as Gd or Y have also been reported to have a positive influence on GFA and soft magnetic properties of Co-based MG [46]. In work [293] binary alloy Co-B increased the D_c from less than 1 mm to 2 mm and ΔT_x establish 50°C by adding 3.5 at.% of Y and subtracting 20% of Co from Fe. Work [294] also indicates the positive influence of rare earth elements on the magnetic properties and GFA ability of Co-based MG. However, it shows the superiority of Er over Y.

7.2. Manufacturing and applications

The good GFA of Co-based alloys allows different shape samples to be developed for research. Most work on Co-based metallic glasses focusing on BMG was developed with casting method, like plates, rods (Fig. 32 a), and other simple shapes, which is shown in the literature review from Tab. 9. Co-based ribbons have been successful obtained by melt spinning processes [295–298]. The powder form of the high GFA Co-based alloy was also obtained by gas atomization [299] (Fig. 32 b), which was then used to develop an amorphous coating by laser cladding (Fig. 32 c). However, researchers are still working on the use of Co-based metallic glasses to prepare coating by thermal spraying methods and to develop BMG by additive manufacturing which will be investigated in this thesis.

Tab. 9. Review of the literature (state-of-the-art)

Alloy	Form	Technology of development	Index
CoTaB	rods	injection casting	[300]
	powder	gas-atomization	[278]
	coating	laser-cladding from powder	[278]
CoNbB	rods	casting	[301]
CoMoB	rods	copper mold casting	[176]
CoCrMoCB	rods	copper mold casting with water-cooling	[50]
CoFeTaB	rods	casting	[302]
CoFeBSiNb	rods	copper mold casting	[303]
	ribbons	copper roller melt-spinning	[304]
CoFeBSiP	ribbons	copper roller melt-spinning,	[305]
	rods	copper mold casting method in air	

CoFeYB	ribbons rods	melt spinning copper mold casting under the argon atmosphere	[293]
CoFeMoPB	rods	casting (J-quenching technique)	[306]

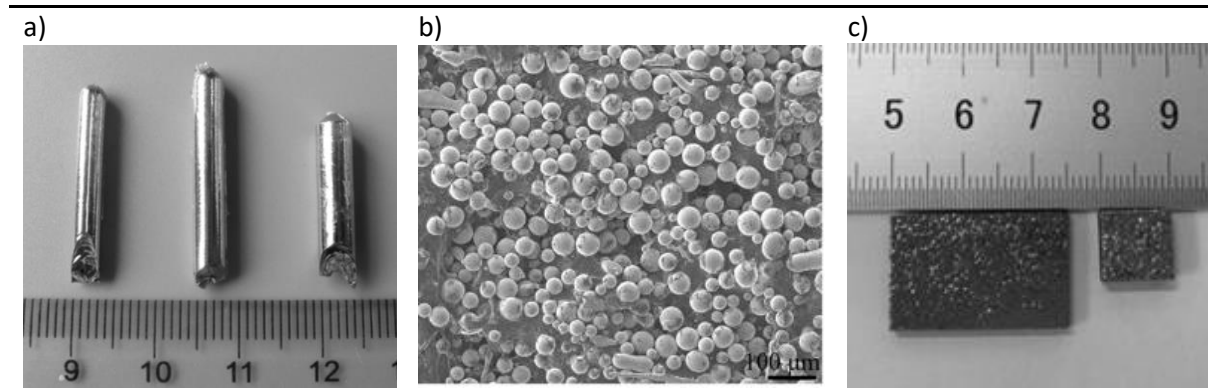


Fig. 32. Fully amorphous Co-based metallic glasses with different shapes. a) Cast rods with diameters of 3.5 mm, 4 mm and 4.5 mm CoFeNiBSiNb [283], b) gas atomized CoTaB powder used to develop c) Co-based MG coatings [278]

Co-based alloys are worth looking closer at their properties and doing research to use them in thermal spraying technologies and additive manufacturing. For example, a Co-based amorphous layer developed by laser cladding can develop maximum microhardness on a very high level about 1100-1200 HV [307–309] (value at the top of the layer). In addition, these coatings exhibit very good high-temperature wear resistance (compared to plasma arc spray welding coating) [309] and better corrosion resistance in a solution of 3.5 wt.% NaCl than steel H13 [178]. The layers obtained had a thickness of 230–250 μm [309], and were amorphous in 81% [308] and 92% [307] of volume. The hardness of the Co-based MG coating deposited by laser coating at work [310] establishes a hardness of up to 14.9 GPa. MGs based on cobalt are distinguished by their very high hardness; thus, MGs are widely applied as protection coatings for gas turbines or valves. Even harder Co-based MGs were obtained by casting rods of (CoFe)YB [293]. The rods establish 1336 HV (100 g load, dwell time 10 s) and in [311] CoNiTaB even 1410 HV (load 5 N, dwell time 10 s dwell time). The hardness of Co-based alloys compared to other MG based on different chemical elements are shown in Fig. 33 what again confirms their one of the highest hardness among MG.

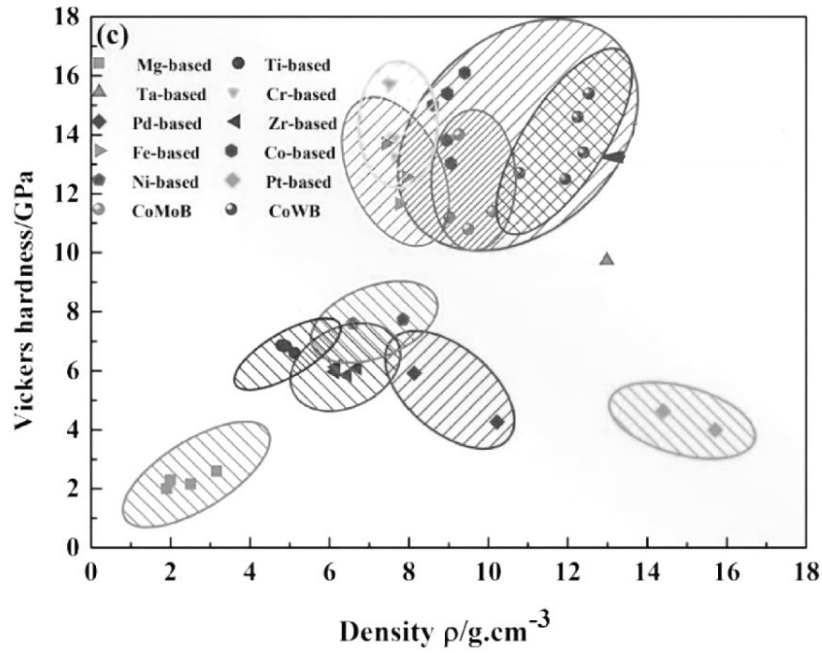


Fig. 33. Correlation between hardness and density for metallic glasses [174–186]

Considering that Co is a natural ferromagnetic material with a magnetic moment of 1.7–1.75 μ_B . Moreover, this element is characterized by a stronger spin-orbit coupling than pure iron, and is extremely important during the design of materials for practical applications, i.e., small inductor footprints or transformers [312,313]. CoFeSiB soft magnetic alloys are excellent candidates for such applications because of their high electrical resistivity. The most popular soft magnetic Co-based alloy is a material called Vitrovac and its modifications [314,315] which are characterized by relatively low coercivity, high saturation magnetization, low eddy current, and high magnetic permeability. Co-based alloys were found to reduce Barkhausen jumps in the magnetic field in toroidal samples from $\lambda_s = 30 \cdot 10^{-6}$ for Fe₈₄B₁₆ to $\lambda_s = 10^{-6}$ for Co₇₀Fe₅Si₁₅B₁₀ [316]. Recently, Nosenko et al. [317] have shown that selective Cr addition and optimal thermal treatment could decrease saturation induction, which is extremely important in the perspective application of Co-based alloys as supersensitive fluxgate sensors. At present, alloys with excellent magnetic properties are used in the form of metallic ribbons (melt spinning technic) which find application as a core of transformers [318,319].

IV. RESEARCH METHODS

1. Research plan

To confirm the hypothesis, the research plan was established and shown in Fig. 34. The first step involved the selection of two alloys that will follow several restrictions and alloying them into a master alloy. Next, the master alloy was used to make the castings (the conventional form of MG) and for obtaining powders. Next, powders were used to obtain coatings by atmospheric plasma spraying and bulk samples by selective laser melting.

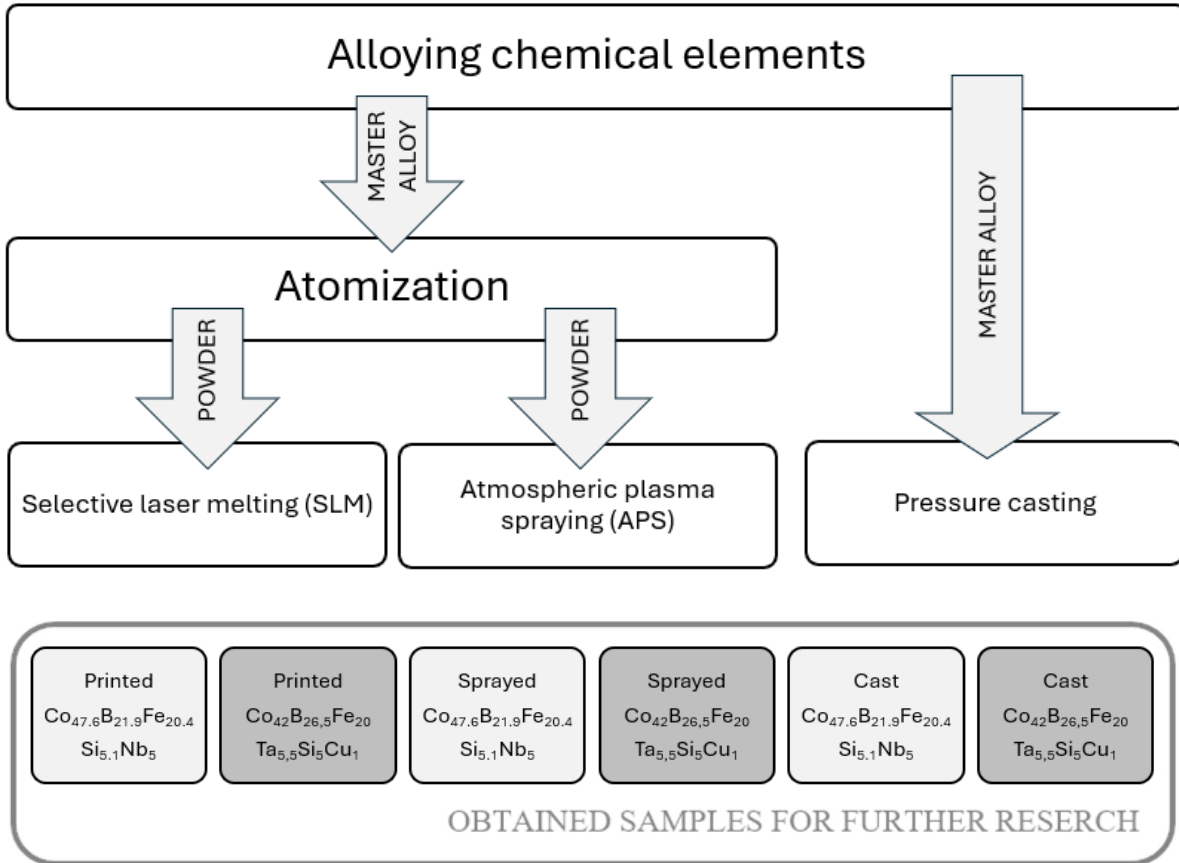


Fig. 34. Research plan for Ph.D. thesis for obtaining samples for further test

The samples were then characterized by different tests and analysis. The microstructure of all samples was analyzed by digital microscopy, scanning electron microscopy (SEM), and X-ray diffraction. Additional differential thermal analysis was used to describe characteristic temperatures in the analysis. Finally, to describe the mechanical properties of the samples the nanoindentation test was performed. For clear characterization of each form of the alloys, the research was grouped in chapters according to the technologies used:

- *Atomized powders*, p. 64,
- *Cast plates*, p.65,
- *Selective laser melting bulk samples*, p. 66,
- *Plasma sprayed coatings*, p. 67.

The visual presentation of the performed testes is shown in Fig. 35. In addition to the above-mentioned analysis, for the sample prepared by plasma spraying, additional tests were

performed that included measurements of wear resistance and roughness of the surface. For samples manufactured by selective laser melting, additionally density measurements and scanning transition electron microscopy were done. Also, selective laser melting technology was studied in two stages because of the lack of any previous test of this technology for printing alloys with high glass forming ability based on cobalt, which was a huge innovation but at the same time required extended research. Other important corrections of the research plan involve developing additional cast samples from the CoBFeTaSiCu alloys due to the high crystallization of the developed and researched plates. The additional cast samples were obtained by melt spinning in the form of ribbons which next were tested with the same testes as described in the previous paragraph (digital microscopy, SEM, XRD, and nanoindentation).

In the work the **symbols for samples** will be used. For the powder used for SLM the fraction symbol is '**20-50 μm** ', for larger fraction used for APS the symbol is '**50-80 μm** '. The SLM samples (**bulk samples**) are marked **PA_WB**, where **A** is the value of the **laser power** used for the sample and **B** represents the **scanning speed**. Samples developed with APS are marked as **CoNb_X** or **CoTa_X**, respectively for the alloy $\text{Co}_{47.6}\text{B}_{21.9}\text{Fe}_{20.4}\text{Si}_{5.1}\text{Nb}_5$ and $\text{Co}_{42}\text{B}_{26.5}\text{Fe}_{20}\text{Ta}_{5.5}\text{Si}_5\text{Cu}_1$. The **X** represents the **spraying distance** used for developing coatings.

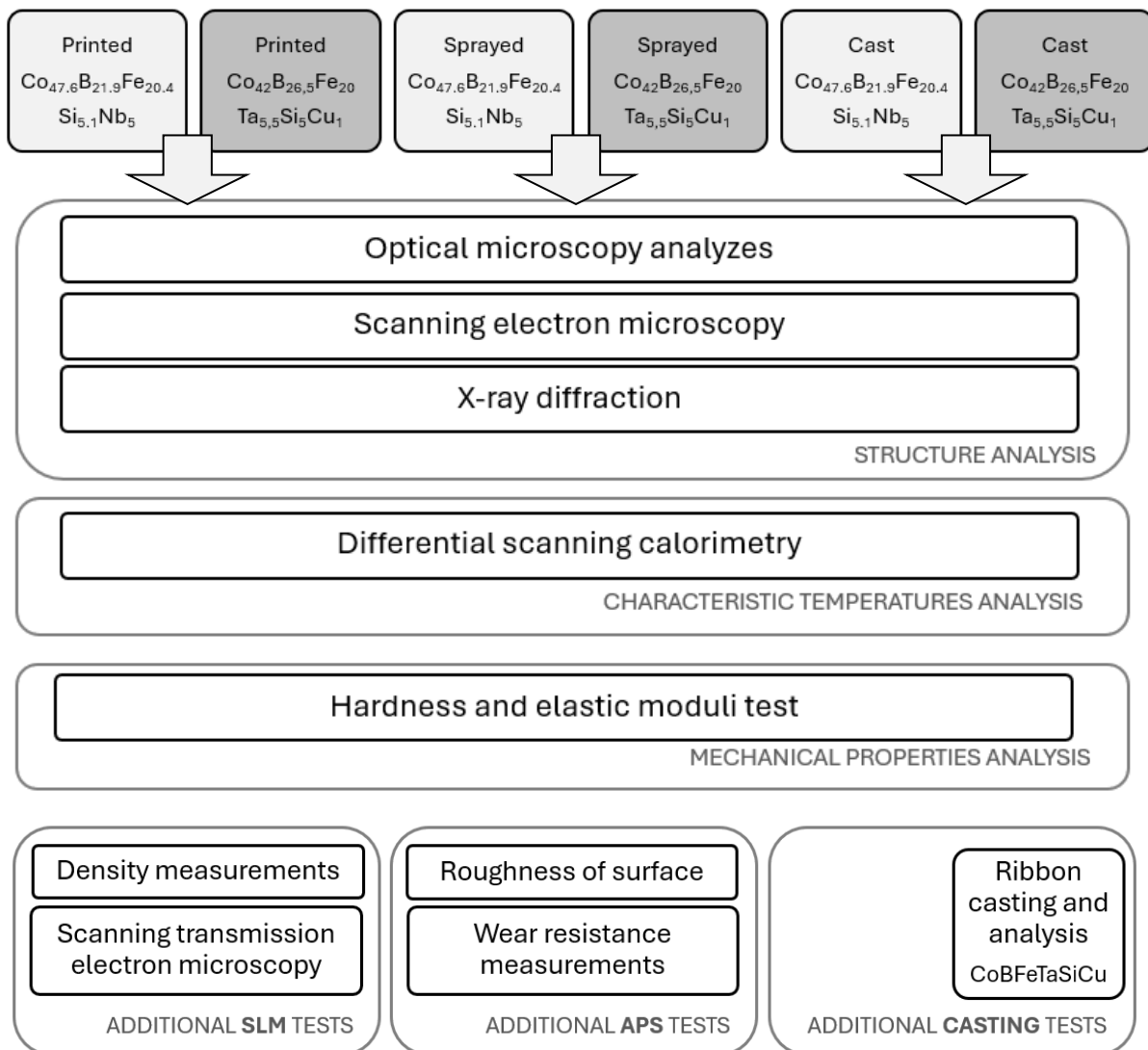


Fig. 35. Analysis performed on all forms of samples obtained from $\text{Co}_{47.6}\text{B}_{21.9}\text{Fe}_{20.4}\text{Si}_{5.1}\text{Nb}_5$ and $\text{Co}_{42}\text{B}_{26.5}\text{Fe}_{20}\text{Ta}_{5.5}\text{Si}_5\text{Cu}_1$ in this thesis

In the *Discussion* chapter, all forms of Co-based alloys were summarized, and the most characteristic properties were shown. To confirm the hypothesis, the properties of SLM bulk samples and APS coatings were also compared to the properties of cast materials in the subchapter *Technologies comparison*. For $\text{Co}_{47.6}\text{B}_{21.9}\text{Fe}_{20.4}\text{Si}_{5.1}\text{Nb}_5$ the reference samples were a cast plate, while for $\text{Co}_{42}\text{B}_{26.5}\text{Fe}_{20}\text{Ta}_{5.5}\text{Si}_5\text{Cu}_1$ the reference sample to compare was a cast ribbon, as mentioned above. Additionally, in the subchapter *Alloys comparison*, these two alloys with high GFA were included. The graph representing properties comparisons is shown in Fig. 36. In the last chapter *Conclusions*, the final confirmation of the PhD thesis was described, and the main conclusions were highlighted.

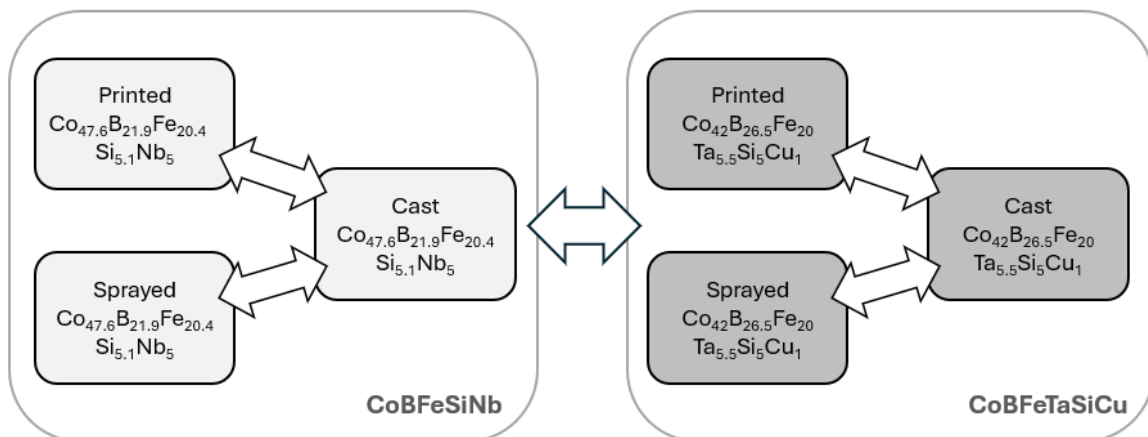


Fig. 36. Graph showing the properties comparison (marked as an arrows) done in the *Discussion* chapter in this thesis

2. Alloys selection

To choose alloys on which the Ph.D. work was based, a literature review was carried out. Because of the number variation of the amorphous alloys, the morphological analysis was performed. The literature review was held by searching specific phrases such as metallic glasses, amorphous metals or high glass forming ability, on well-known science articles bases, namely <https://www.sciencedirect.com/> and <https://scholar.google.com/>. The alloys researched from the articles were then filtered by four criteria that are shown in Fig. 37.

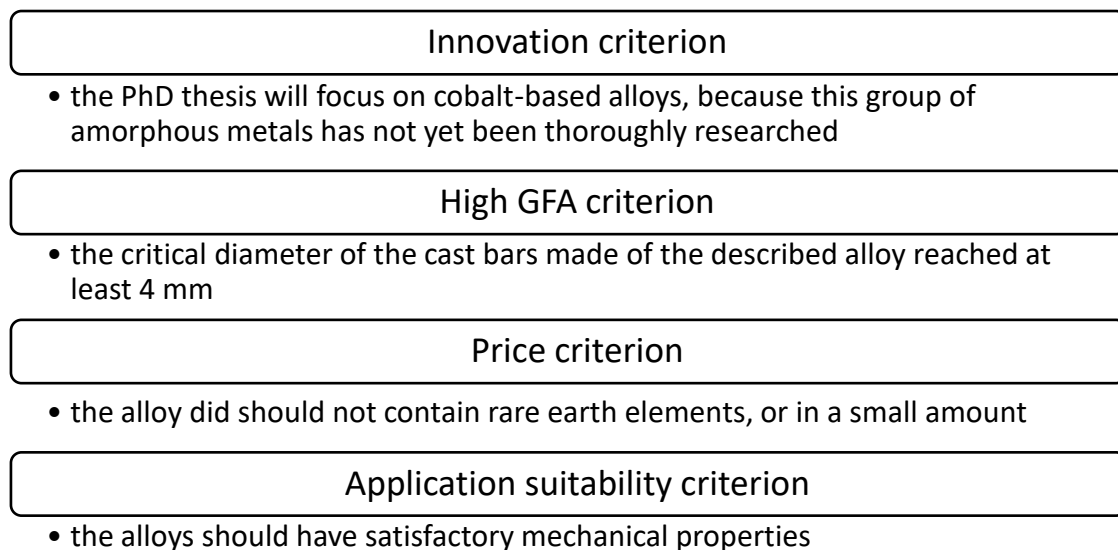


Fig. 37. Criteria for the alloys that will be investigated in the thesis

Alloys that met the criteria mentioned in Fig. 37. were found in eight items of the literature, which are presented in the Tab. 10. The material selected based on these articles is $[(\text{Co}_{0.7}\text{Fe}_{0.3})_{0.68}\text{B}_{0.219}\text{Si}_{0.051}\text{Nb}_{0.05}]_{100}$ (other name $\text{Co}_{47.6}\text{B}_{21.9}\text{Fe}_{20.4}\text{Si}_{5.1}\text{Nb}_5$) (number 4 in Tab. 10) and $\text{Co}_{42}\text{B}_{26.5}\text{Fe}_{20}\text{Ta}_{5.5}\text{Si}_5\text{Cu}_1$ (number 13 in Tab. 10). These alloys exhibit the highest critical diameters of the alloys found, respectively, 5,5 and 6 mm.

Tab. 10. Review of the literature of Co-based alloys with high glass-forming ability

No.	Ref.	Published	Chemical composition	Critical diameter [mm]
1	[320]	2012-07-01	CoFeBSiNb $\text{Co}_{47}\text{Fe}_{20.9}\text{B}_{21.2}\text{Si}_{4.6}\text{Nb}_{6.3}$	4
2			CoFeBSiNbGa $[\text{Co}_{47}\text{Fe}_{20.9}\text{B}_{21.2}\text{Si}_{4.6}\text{Nb}_{6.3}]_{98}\text{Ga}_2$	4
3	[99]	2018-03-15	CoFeBSiNbCu $[(\text{Co}_{0.7}\text{Fe}_{0.3})_{0.68}\text{B}_{0.219}\text{Si}_{0.051}\text{Nb}_{0.05}]_{100-0.5}\text{Cu}_{0.5}$	4.5
4			CoFeBSiNb $[(\text{Co}_{0.7}\text{Fe}_{0.3})_{0.68}\text{B}_{0.219}\text{Si}_{0.051}\text{Nb}_{0.05}]_{100}$	5.5
5			CoFeBSiNbCu $[(\text{Co}_{0.7}\text{Fe}_{0.3})_{0.68}\text{B}_{0.219}\text{Si}_{0.051}\text{Nb}_{0.05}]_{100-0.1}\text{Cu}_{0.1}$	5.5
6	[303]	2010-10-01	CoFeBSiNb $\text{Co}_{46}\text{Fe}_{20}\text{B}_{22.5}\text{Si}_{5.5}\text{Nb}_6$	4.5
7			CoFeBSiNb $\text{Co}_{46}\text{Fe}_{20}\text{B}_{23}\text{Si}_5\text{Nb}_6$	4
8	[321]	2012-04-01	CoFeBSiNb $(\text{Co}_{0.7}\text{Fe}_{0.3})_{68}\text{B}_{21.9}\text{Si}_{5.1}\text{Nb}_5$	5.5
9	[283]	2011-06-01	CoFeNiBSiNb $(\text{Co}_{0.6}\text{Fe}_{0.3}\text{Ni}_{0.1})_{67}\text{B}_{22.7}\text{Si}_{5.3}\text{Nb}_5$	4.5
10	[322]	2010-08-01	CoFeBSiNb $(\text{Co}_{0.942}\text{Fe}_{0.058})_{67}\text{Nb}_5\text{B}_{22.4}\text{Si}_{5.6}$	4
11	[323]	2006-05-01	CoFeBSiNb $[(\text{Co}_{0.6}\text{Fe}_{0.4})_{0.75}\text{B}_{0.2}\text{Si}_{0.05}]_{96}\text{Nb}_4$	4
12	[276]	2015-05-02	CoFeBSiTaCu $\text{Co}_{42.5}\text{Cu}_{0.5}\text{Fe}_{20}\text{Ta}_{5.5}\text{B}_{26.5}\text{Si}_5$	5
13			CoFeBSiTaCu $\text{Co}_{42}\text{Cu}_1\text{Fe}_{20}\text{Ta}_{5.5}\text{B}_{26.5}\text{Si}_5$	6
14			CoFeBSiTaCu $\text{Co}_{41.5}\text{Cu}_{1.5}\text{Fe}_{20}\text{Ta}_{5.5}\text{B}_{26.5}\text{Si}_5$	5
15	[324]	2019-02-01	CoFeBSiNb $(\text{Fe}_{0.5}\text{Co}_{0.5})_{72-x}\text{B}_{20}\text{Si}_4\text{Nb}_4$	3
16			CoFeBSiNbCu $(\text{Fe}_{0.5}\text{Co}_{0.5})_{72-x}\text{B}_{20}\text{Si}_4\text{Nb}_4\text{Cu}_{0.3}$	4
17			CoFeBSiNbCu $(\text{Fe}_{0.5}\text{Co}_{0.5})_{72-x}\text{B}_{20}\text{Si}_4\text{Nb}_4\text{Cu}_{0.4}$	3
18			CoFeBSiNbCu $(\text{Fe}_{0.5}\text{Co}_{0.5})_{72-x}\text{B}_{20}\text{Si}_4\text{Nb}_4\text{Cu}_{0.7}$	3
19			CoFeBSiNbCu $(\text{Fe}_{0.5}\text{Co}_{0.5})_{72-x}\text{B}_{20}\text{Si}_4\text{Nb}_4\text{Cu}_1$	3
20	[325]	2014-02-07	FeCoSiBNbCu $\{[(\text{Fe}_{0.5}\text{Co}_{0.5})_{0.75}\text{Si}_{0.05}\text{B}_{0.20}]_{96}\text{Nb}_4\}_{99.5}\text{Cu}_{0.5}$	2
21	[326]	2007-01-01	FeCoBSiNbCu $\{[(\text{Fe}_{0.5}\text{Co}_{0.5})_{0.75}\text{B}_{0.2}\text{Si}_{0.05}]_{96}\text{Nb}_4\}_{99.5}\text{Cu}_{0.5}$	2

Based on the mentioned criteria, $\text{Co}_{47.6}\text{B}_{21.9}\text{Fe}_{20.4}\text{Si}_{5.1}\text{Nb}_5$ was selected. According to the literature, it provides high glass forming ability, which was measured by $\Delta T = 42^\circ\text{C}$ and by the critical diameter of 5.5 mm [99,321]. The alloy was developed for studies in the form of rods by copper mold casting. Both articles [99,321] show very small plasticity of the rods, the compressive plastic strain was at a level of 0.8%, however, the compressive strength was very high and was set at around 4.3 - 4.4 GPa. In further description, the shortened composition of the alloy is also used, which is CoBFeSiNb . The exact atomic and weight percentages of the CoBFeSiNb chemical elements are shown in the Tab. 11.

Tab. 11. Chemical composition of the alloy CoBFeSiNb

Chemical element					
	Cobalt	Iron	Boron	Silicon	Niobium
% at.	47.60	20.40	21.90	5.10	5.00
% wt.	58.58	23.79	4.94	2.99	9.70

% at. - atomic percentage, % wt. - weight percentage

The second selected alloy is $\text{Co}_{42}\text{B}_{26.5}\text{Fe}_{20}\text{Ta}_{5.5}\text{Si}_5\text{Cu}_1$ according to Yazici et al. [276] has a critical diameter of the cast rod equal to 6 mm. The glass transition temperature (T_g) of this alloy was reported at the 623°C level and ΔT (the difference between T_g and T_x) at 48°C [276]. Similar alloys were also successfully cast on rods or ribbons in other works [327,328], where the reported T_g was similar [10-12], but the ΔT was slightly higher in [12]. The hardness of Vickers measured under a load of 2.94 N for 15 s was 1204 HV and the compressive strength 3.9 GPa. For further description, the shortened composition of the alloy is also used, which is CoBFeTaSiCu. The exact atomic and weight percentages of the CoBFeTaSiCu chemical elements are shown in the Tab. 12.

Tab. 12. Chemical composition of the alloy CoBFeTaSiCu

	Chemical elements					
	Cobalt	Iron	Boron	Silicon	Copper	Tantalum
% at.	42.00	20.00	26.50	5.00	1.00	5.50
% wt.	48.75	22.00	5.64	2.77	1.25	19.60

% at. - atomic percentage, % wt. - weight percentage

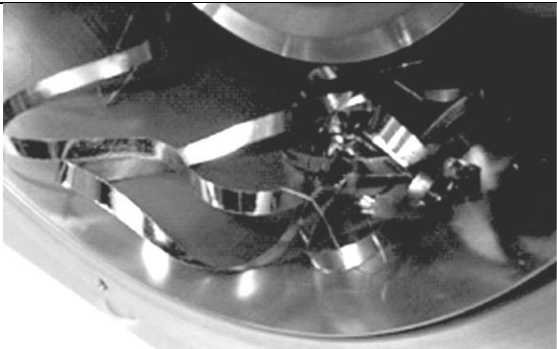
3. Manufacturing processes

3.1. Casting

For describing and comparing the properties of CoBFeSiNb and CoBFeTaSiCu and its possibility to form amorphous/ nanocrystal structures by 3D printing and thermal spraying, the reference sample was obtained by a more traditional and older method of developing metallic glasses, casting. The alloys $\text{Co}_{47.6}\text{B}_{21.9}\text{Fe}_{20.4}\text{Si}_{5.1}\text{Nb}_5$ and $\text{Co}_{42}\text{B}_{26.5}\text{Fe}_{20}\text{Ta}_{5.5}\text{Si}_5\text{Cu}_1$ were cast onto plates by pressure die casting. For die casting, mater alloys were melted by induction furnace and then cast under argon pressure into water-cooled die copper forms. The shaped plates obtained were 30 x 10 x 1 mm. The schematic illustration of die casting was shown in Fig. 8 b).

As mentioned, for CoBFeTaSiCu alloy the additional casting process was conducted, namely melt spinning. In that process, the master alloy was melted by inductors of 5 kW power and cast into ribbons by continuously pouring the melted alloy onto a cooled rotating wheel. The rotation speed of the wheel was 20 mm/s. The whole process was conducted under the argon atmosphere. The next ribbons were cut into shorter samples for planned research. The parameters used in the process and the example of ribbon obtained by the melt spinning are shown in the Tab. 13.

Tab. 13. a) parameters of the casting of ribbons by melt spinning, b) the example of ribbons developed by similar parameters by the same casting set [329]

a)	Parameter	Value	b)
	roller speed	20 mm/s	
	vacuum	$7 \cdot 10^{-2}$ mbar	
	working pressure	500 mbar	
	distance between crucible-roller	0,3 mm	
	injection pressure	400 mbar	
	diameter of Cu wheel	20 mm	

3.2. Atomization process

To obtain the powders of $\text{Co}_{47.6}\text{B}_{21.9}\text{Fe}_{20.4}\text{Si}_{5.1}\text{Nb}_5$ and $\text{Co}_{42}\text{B}_{26.5}\text{Fe}_{20}\text{Ta}_{5.5}\text{Si}_5\text{Cu}_1$ the master alloy was first developed by alloying pure chemical elements and chemical compounds into homogeneous master alloys with the use of an induction furnace. All elements had very high purity, as shown in Tab. 14. Next, the alloys were cast inside a vacuum chamber into bars. The bars obtained were sandblasted to eventually remove scale or contaminants. The furnace used for the alloying process is shown in Fig. 38.

Tab. 14. Components used to manufacture Co-based alloys

Chemical element or compound	Pureness of pure element [%]	Concentration of another element
Cobalt	99,99	-
	99,9	-
Iron	99,99	-
	99,97	-
Boron	99,9	-
Silicon	99,99	-
Niobium	99,95	-
CoB17%	-	B - 83%
FeSi25%	-	Si - 75,4%
FeB18%	-	Fe - 82%
FeNb65%	-	Nb - 35%



Fig. 38. Vacuum induction furnace VIM-LAB 50-60 used for alloying and casting for later atomization

The master alloys were gas atomized to obtain material in the form of powder for thermal spraying and 3D printing. In this work, alloy powders were obtained by gas atomization. For this purpose, the cast bars of the master alloys were melted inside a vacuumed crucible by an induction furnace connected to the atomization chamber. Then, a thin stream of melted alloy was released to flow from a hole on the bottom of the crucible. In that stream, the jet of argon under 30 bar of pressure was headed. The gas jet sprayed the stream into small, mostly spherical particles. The particles in the process are cooled at a very high cooling rate, which prevents crystallization from occurring for alloys with high GFA. The schematic illustration of the atomization process is shown in Fig. 39 a), and the temperatures at which the master alloys were heated before releasing the liquid alloy stream are shown in Fig. 39 b).

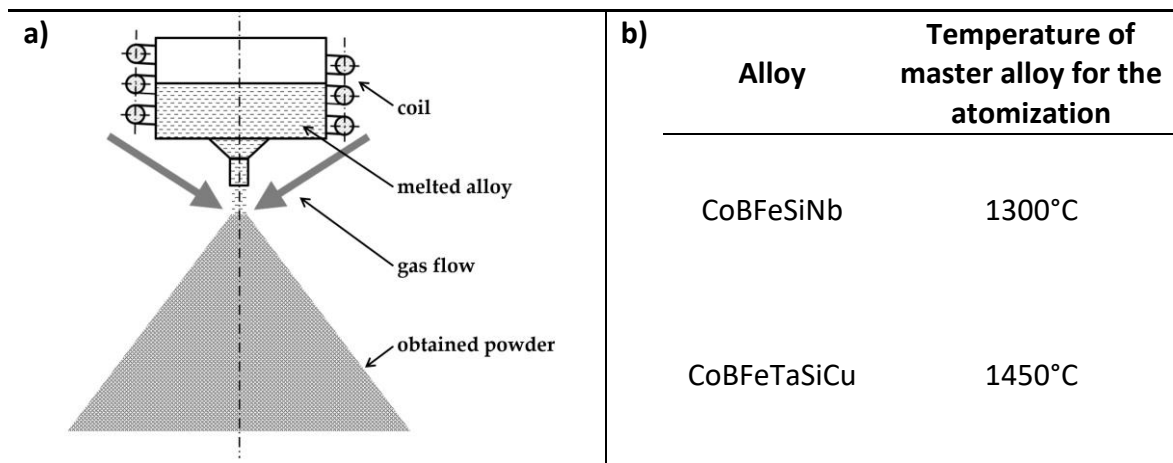


Fig. 39. a) Schematic illustration of the atomization process [330] b) highest alloy temperatures in the atomization process to obtain a homogeneous liquid state

After atomization, the powders were sieved to the desired fraction in the pre-selected manufacturing processes. For plasma spraying, the range of sizes can be wide from 10 to 100 μm however, for atmospheric plasma spraying applied in this work, the fraction 50-80 μm was used [331,332]. For laser powder-bed fusion processes such as SLM used in this work, the typical feedstock size is between 20 and 50 μm and that fraction was used in this thesis [333]. A larger fraction (up to 100 μm) can be used for other flame spray techniques; however, these

are not a concern in this work [331,332]. The devices used for sieving and the fraction of powders obtained are shown in Fig. 40.


	Size of fractions	Purpose
	0-20 μm	Fine powder, not used
	20-50 μm	SLM printing
	50-80 μm	Atmospheric plasma spraying
	80-100 μm	Scraps including irregular-shaped particles

Fig. 40. Vortex mixer for powder fraction segregation Fritsch Analysette 3 Pro with sets of sieves and the fraction purpose in this work

3.3. Selective laser melting

To select the parameters for printing $\text{Co}_{47.6}\text{B}_{21.9}\text{Fe}_{20.4}\text{Si}_{5.1}\text{Nb}_5$ and $\text{Co}_{42}\text{B}_{26.5}\text{Fe}_{20}\text{Ta}_{5.5}\text{Si}_5\text{Cu}_1$ with SLM technologies, a literature review was performed. The literature review includes analyses of Fe-based alloys successfully printed by SLM that were similar to Co-based alloys chosen for this thesis. The similarities include chemical composition, feedstock size, and characteristic temperatures. The collected literature concerned four manuscripts [117,133,334,335] and the parameters that were used to print them are shown in the Tab. 15. In the same table, the range of parameters values used in this thesis is also listed. More detailed information on selecting the parameters is described below.

Tab. 15. Review of parameters of Fe-based alloys printing with high glass-forming ability [117,133,334,335]

Parameters		Literature	In this thesis	Unit
ED	energy density	17 - 106	16 - 82	J/mm^3
P	laser power	60 - 100	55 - 95	W
v	scanning speed	350 - 1800	600 - 1800	mm/s
H	layer thickness	25 - 40	25	μm
h	scanning hatch distance	80 - 200	77	μm

To verify the wide range of parameters to test, based on the literature review, the matrix of preliminary parameters was established (the first stage of the printing experiment). Furthermore, the mentioned matrix in the preliminary stage of the experiment was the same for $\text{Co}_{47.6}\text{B}_{21.9}\text{Fe}_{20.4}\text{Si}_{5.1}\text{Nb}_5$ and $\text{Co}_{42}\text{B}_{26.5}\text{Fe}_{20}\text{Ta}_{5.5}\text{Si}_5\text{Cu}_1$. The parameters that were changing were the scanning speed and the laser power. To limit the number of sets of parameters, the scanning speed in the experiment was changed with a step of 200 mm/s (600, 800, 1000, 1200, 1400, 1600, and 1800 mm/s) and the laser power with 20 W (55, 75, 95 W). The rest of the parameters were constant, that is, the hatch spacing $h = 77 \mu\text{m}$, and the layer thickness $H = 25 \mu\text{m}$. For a further detailed description of the experiment, volumetric energy density (ED) was introduced, which connects all the parameters mentioned above. The formula for ED is

shown in Eq. 11 and the calculated values are put into the matrix of parameters shown in the Tab. 16.

Eq. 11. Energy density formula: P- laser power [W], v- scanning speed [mm/s], h- hatch spacing [mm], H- layer thickness [mm]

$$ED = \frac{P}{v \cdot h \cdot H} \quad , \quad \left[\frac{J}{mm^3} \right]$$

Tab. 16. Matrix of preliminary parameters for SLM printing [336]

Energy density [J/mm ³]		Scanning speed v [mm/s]						
		600	800	1000	1200	1400	1600	1800
Laser power P [W]	55	47.6	35.7	28.6	23.8	20.4	17.9	15.9
	75	64.9	48.7	39.0	32.5	27.8	24.4	21.6
	95	82.3	61.7	49.4	41.1	35.3	30.8	27.4

To ensure low humidity, the feedstock was dried at 50°C for 4 hours. An mLab Concept Laser printer with an argon atmosphere was used in this work for SLM printing bulk samples Fig. 41 a). The oxygen level was always lower than 0.5%. The scanning pattern used for printing was straight lines with a changing direction for 90° with each layer as shown in Fig. 41 b).

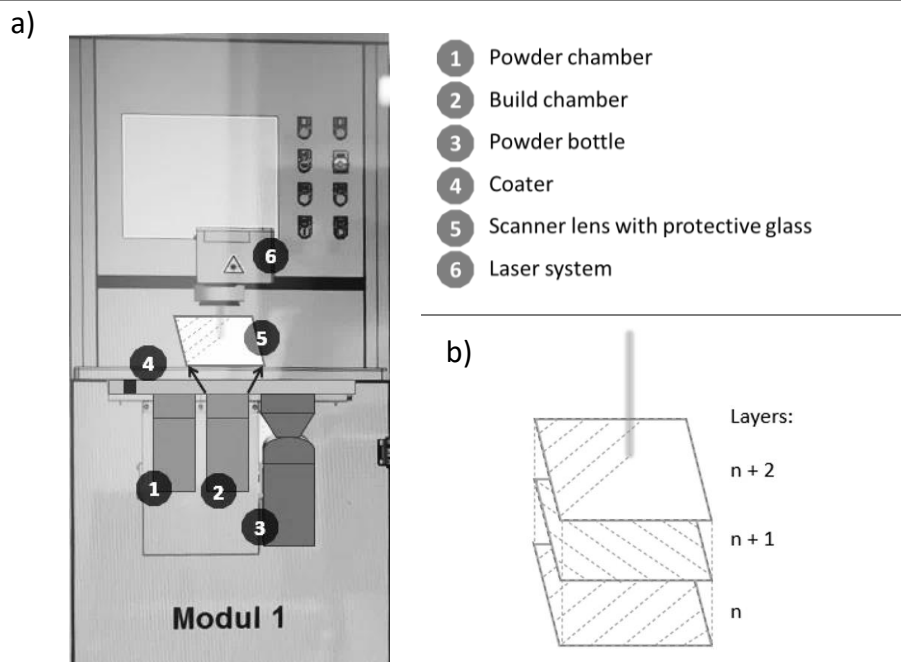


Fig. 41. a) mLab Concept Laser printer, b) schematic illustration of scanning strategy [336]

After printing, samples were cut from the base using an electrical discharge machine and cross sections prepared using abrasive techniques including sandpapers and polishing with diamond paste. To clear the samples, an ultrasonic cleaner filled with ethanol was used and the samples were dried with an air blower. The prepared samples were validated macroscopically, and the cross sections were observed by digital microcopy (VHX-6000 Keyence). The validation led to the narrowing of the parameter matrix by limiting the ED to successfully develop samples by SLM printing. However, to explore more proper sets of parameters in the second stage, the scanning speed and laser power steps were reduced with restriction of the ED range. Furthermore, the parameter matrix for the second stage of an experiment was different for each alloy due to the different preliminary printing results for

$\text{Co}_{47.6}\text{B}_{21.9}\text{Fe}_{20.4}\text{Si}_{5.1}\text{Nb}_5$ and $\text{Co}_{42}\text{B}_{26.5}\text{Fe}_{20}\text{Ta}_{5.5}\text{Si}_5\text{Cu}_1$. The ED limitation for the $\text{Co}_{47.6}\text{B}_{21.9}\text{Fe}_{20.4}\text{Si}_{5.1}\text{Nb}_5$ ranged from 39 to 68 J/mm³, the laser power was changed from 45 to 75 W (step 5 W) and the scanning speed was changed from 500 to 800 mm/s (step 100 mm/s). For $\text{Co}_{42}\text{B}_{26.5}\text{Fe}_{20}\text{Ta}_{5.5}\text{Si}_5\text{Cu}_1$ ED ranged from 41 to 50 J/mm³, so the laser power changed from 60 to 95 W (step 5 W) and scanning speed from 700 to 1200 mm/s (step 100 mm/s). The parameters matrixes used for the second stage of printing $\text{Co}_{47.6}\text{B}_{21.9}\text{Fe}_{20.4}\text{Si}_{5.1}\text{Nb}_5$ and $\text{Co}_{42}\text{B}_{26.5}\text{Fe}_{20}\text{Ta}_{5.5}\text{Si}_5\text{Cu}_1$ are shown in the Tab. 17.

Tab. 17. The second stage parameters for SLM printing a) $\text{Co}_{47.6}\text{B}_{21.9}\text{Fe}_{20.4}\text{Si}_{5.1}\text{Nb}_5$, b) $\text{Co}_{42}\text{B}_{26.5}\text{Fe}_{20}\text{Ta}_{5.5}\text{Si}_5\text{Cu}_1$ [336]

Legend		a) $\text{Co}_{47.6}\text{B}_{21.9}\text{Fe}_{20.4}\text{Si}_{5.1}\text{Nb}_5$						b) $\text{Co}_{42}\text{B}_{26.5}\text{Fe}_{20}\text{Ta}_{5.5}\text{Si}_5\text{Cu}_1$						
<div>highest</div>	<div>Laser power P [W]</div>	ED [J/mm ³]	Scanning speed v (mm/s)				ED [J/mm ³]	Scanning speed v (mm/s)						
			500	600	700	800		700	800	900	1000	1100	1200	
		45	46.8				60	44.5						
		50	51.9	43.3			65	48.2	42.2					
55		57.1	47.6			70		45.5						
60		62.3	51.9	44.5		75		48.7	43.3					
65		67.5	56.3	48.2	42.2	80			46.2	41.6				
70			60.6	51.9	45.5	85			49.1	44.2				
75			64.9	55.7	48.7	90				46.8	42.5			
lowest							95				49.4	44.9	41.1	
not tested														

ED restriction

39 < ED < 68 J/mm³

ED restriction

41 < ED < 50 J/mm³

3.4. Atmospheric plasma spraying

The manufacture of $\text{Co}_{47.6}\text{B}_{21.9}\text{Fe}_{20.4}\text{Si}_{5.1}\text{Nb}_5$ and $\text{Co}_{42}\text{B}_{26.5}\text{Fe}_{20}\text{Ta}_{5.5}\text{Si}_5\text{Cu}_1$ by atmospheric plasma spraying (APS) was carried out with a Praxair cathode-anode SG-100 plasma torch mounted on an industrial 6-axis Fanuc robot. As a plasmatic gas, argon was used, which ensures low heat transfer from the plasma jet to the feedstock and is easily ionized. The flow of the argon was 8 standard liter per minute. Plasma power was set at 22 kW. The spraying distance (distance between the end of the plasma torch and the substrate) for $\text{Co}_{47.6}\text{B}_{21.9}\text{Fe}_{20.4}\text{Si}_{5.1}\text{Nb}_5$ and $\text{Co}_{42}\text{B}_{26.5}\text{Fe}_{20}\text{Ta}_{5.5}\text{Si}_5\text{Cu}_1$ was set at three values, which are 90, 100 and 110 mm. The distance was changed by manipulating the length of the holder. The feedstock used for $\text{Co}_{47.6}\text{B}_{21.9}\text{Fe}_{20.4}\text{Si}_{5.1}\text{Nb}_5$ and $\text{Co}_{42}\text{B}_{26.5}\text{Fe}_{20}\text{Ta}_{5.5}\text{Si}_5\text{Cu}_1$ coating deposition was 50 µm to 80 µm and was radial supply to the plasma jet with a rate of 15 g/min. Camera footage of powder distribution in the plasma jet is shown in Fig. 42 a). As substrates, stainless steel disks were used. To increase the bond strength of the deposited powder, the substrates were sandblasted and then cleaned with ethanol. The substrates were mounted on the rotating holder as shown in Fig. 42 b). For temperature observation of the samples, the SensorThermal infrared camera was used. And to decrease the temperature of the deposited coating, an additional air blow was used.

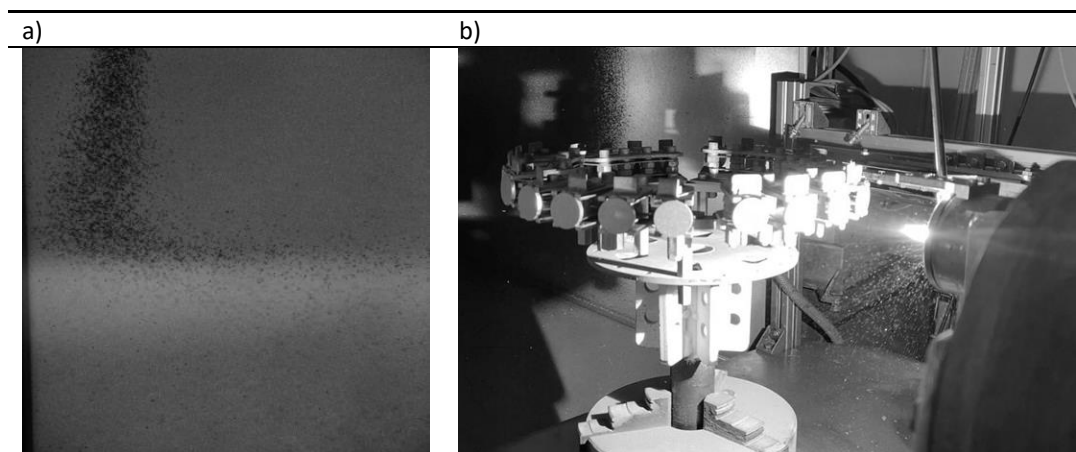


Fig. 42. Atmospheric plasma spraying a) image of feedstock feeding into the plasma jet and b) image of coating development by spraying samples mounted on a rotational holder

4. Samples analysis

For all samples, in addition to macroscopic or surface analysis, cross sections were prepared by cutting the samples with an electrical discharge machine (BMG) or circular saw. Next, the surface was prepared for further observation using abrasive techniques, including grinding with sandpaper and polishing with diamond paste (lowest size of paste 1 μm). To clean the samples, an ultrasonic cleaner filled with ethanol and an air blower were used. Furthermore, to analyze the powders, the particles were cast in epoxy resin and then grinded and polished as in the other samples described above. All measurements and observations listed below were made for samples manufactured from $\text{Co}_{47.6}\text{B}_{21.9}\text{Fe}_{20.4}\text{Si}_{5.1}\text{Nb}_5$ and $\text{Co}_{42}\text{B}_{26.5}\text{Fe}_{20}\text{Ta}_{5.5}\text{Si}_5\text{Cu}_1$.

4.1. Atomized powders

The research carried out on the powder particles included the following:

- Scanning electron microscopy with topographic contrast (SE) of whole particles

Powder fractions 20–50 μm and 50–80 μm were analyzed in the form of whole particles glued by carbon tape with SEM using topographic contrast (SEM Tescan Vega). The acceleration voltage of the electrons for analysis was set at 20 kV, the working distance was set to 15 mm. Based on the five images, the analysis of size and shape of the particles was conducted by counting the number of non-spherical particles divided by the number of all observed particles and multiplied by 100%. The analysis included elongated and flattened-shaped particles. The circularity (sphericity) of the sample was conducted as a ratio of ratio the circumference of a circle (of equivalent area to the measured particle) and the perimeter of the particle itself [337].

- Liquid particle size analysis (PSA)

Powder fractions 20–50 μm and 50–80 μm were analyzed by liquid (at water) PSA with the Anton Parr particle size analyzer PSA 1190, Anton Paar GmbH, 8054 Graz, Austria. Obscuration of all measurements was established between 8 and 12%. Before measurements were made, ultrasound dispersions of the powders were performed for 30 s. The reconstruction mode was Fraunhofer.

- Scanning electron microscopy with energy dispersive spectroscopy (EDS) module with material and topographic contrast (BSE and SE) of cross sections

Visual and chemical composition analysis of the obtained particles were performed by SEM Tescan Vega with an energy-dispersive spectroscopy module with material and topographic contrast. The acceleration voltage of the electrons for analysis was set at 20 V, the working distance was set to 15 mm. For this research, a cross section of powder particles was used.

- X-ray diffraction (XRD)

The amorphous state of the alloys and the validation of the presence of the crystalline phase was investigated by XRD using the Rigaku Ultima IV diffractometer with Cu K α irradiation ($\lambda = 1.5406 \text{ \AA}$). The X-ray scanning range was 25–95° 2 θ with a step of 0.05°.

- Differential thermal analysis (DTA)

To measure the characteristic temperatures of the alloys, DTA was performed, such as the temperature of glass transition (T_g), crystallization (T_x), melting point (T_m) and liquidus temperature (T_l). For this test, the STA 449 F3 Jupiter with the NETZSCH factory thermal analyzer was used. The samples were analyzed by heating them at room temperature to 1300°C with a heating rate of 40°C/min.

- Nanoindentation

Hardness and the elastic module were measured with an Anton Paar Tester NHT3 on the STeP 4 platform with Berkovich-type tip, calibrated before measurements on a fused silica sample. Measurements were taken at room temperature, the applied load was set at a level of 35 mN, a pause of 30 s was observed, and the load and unload rate were 70 mN/min. The distance between the indentations was at least 3 times the width of the indent. The number of measurements was at least 15. The calculations of the hardness and elastic module were performed using the Oliver and Pharr method [338].

4.2. Cast plates

The research carried out on the CoBFeSiNb and CoBFeTaSiCu plates (and CoBFeTaSiCu ribbons), included:

- Scanning electron microscopy

Fractures and cross sections of cast samples were investigated by SEM with SE and BSE contrast. The acceleration voltage of the electrons for analysis was set at 20 V, the working distance was set to 15 mm. The observation was made to determine the type of sample fracture and the possible presence of emptiness, impurities, or a second phase. Cross sections were prepared according to the description above and the fractures were made by bending the plates mounted on a four-point holder.

- X-ray diffraction

Plates were also tested with XRD using the Rigaku Ultima IV Diffractometer with Cu K α irradiation ($\lambda = 1.5406 \text{ \AA}$). The range of X-ray scanning was 25–95° 2 θ with a step of 0.05°.

- Differential scanning calorimetry (DSC)

To establish the precise glass transition (T_g) and the crystallization temperature (T_x), DSC was performed on the DSC822 Mettler Toledo thermal analyzer. The samples were heated to 700°C from room temperature, the heating rate was 40°C/min.

- Nanoindentation

The hardness of plate was measured in the cross-section by an Anton Paar Tester NHT3 on the STeP 4 platform with Berkovich type tip, calibrated before measurements on fused silica samples. Measurements were taken at room temperature, the applied load was set at a level of 35 mN, a pause of 30 s was observed, and the load and unload rate were 70 mN/min. The distance between the indentation was at least 3 times the width of the indentation. The number of indents was at least 15. The calculations of the hardness and the elastic module were performed using the Oliver and Pharr method [338].

4.3. Selective laser melting bulk samples

As was described above, the SLM process was done in two stages to establish the best set of parameters to print $\text{Co}_{47.6}\text{B}_{21.9}\text{Fe}_{20.4}\text{Si}_{5.1}\text{Nb}_5$ and $\text{Co}_{42}\text{B}_{26.5}\text{Fe}_{20}\text{Ta}_{5.5}\text{Si}_5\text{Cu}_1$. As indicators of the best sets, the porosity rate, the presence of the second phase, and the number of cracks or fractures were validated. Furthermore, to validate the conclusions of the conducted study, six samples of CoBFeSiNb and three of CoBFeTaSiCu from the second stage of an experiment were tested with additional measurements listed below. The chosen samples represented the whole range of ED of the second stage of an experiment, e.g., the highest, medium and lowest ED. Finally, the set of parameters for $\text{Co}_{47.6}\text{B}_{21.9}\text{Fe}_{20.4}\text{Si}_{5.1}\text{Nb}_5$ and the set for $\text{Co}_{42}\text{B}_{26.5}\text{Fe}_{20}\text{Ta}_{5.5}\text{Si}_5\text{Cu}_1$ was selected as the best for manufacturing by SLM.

- The first stage of a printing experiment (preliminary studies) included the following:
 - Digital microscopic observation

All successfully printed samples from the first stage of an experiment were analyzed with a digital microscope VHX-6000 Keyence. The analysis was performed on the prepared cross section.

- Second stage of printing (all samples) included:
 - Digital microscopic observation

Samples from the second-stage experiment were analyzed with digital microscopy like those from the first stage using the VHX-6000 Keyence microscope.

- Density of samples measurements using the Archimedes method

The density of samples of the samples from the second printing stage was measured using the Archimedes method with a scale (Radwag AS 60/220.X2 PLUS). As the liquid for the measurements, ethanol was used with purity of 99%.

- Additional measurements on six samples of CoBFeSiNb and three of CoBFeTaSiCu , included:
 - Scanning electron microscopy

Cross sections of selected samples were observed by SEM (Tescan Vega 3) with topography contrast to validate their structure, including cracks and porosity. The acceleration voltage of the electrons for analysis was set at 20 V, the working distance was set to 15 mm.

- X-ray diffraction

Extended analysis included X-ray diffractometry (Bruker AXS, D8 DISCOVER) with a Cobalt radiation lamp $\text{WL} = 1,78897$. The range of X-ray scanning was $25\text{--}95^\circ 2\theta$ with a step of 0.05° .

- Nanoindentation

The nanohardness and elastic modulus were calculated by the nanoindentation test performed with an Anton Pharr NHT3 nanoindenter with a Berkovich-type tip. Like for cast plates, measurements were taken at room temperature, and the applied load was set at a level of 35 mN, a pause 30 s, and the load and unloading rate were 70 mN/min. The distance between the indentation was at least 3 times the width of the indentation. The number of indents was at least 15. The calculations of the hardness and the elastic module were performed using the Oliver and Pharr method [338].

- Sample (one) with the best set of parameters included:
 - Scanning transmission electron microscopy (STEM) with an energy-dispersive spectroscope

The best sample was tested with scanning transmission electron microscopy (ThermoFisher Themis G2 200 kV) with a Ceta™ camera (bright-field observations), Fischione high-angle annular dark-field STEM detector as well as ChemiSTEM™ energy-dispersive spectroscope.

- Differential scanning calorimetry

To establish the precise glass transition (T_g) and the crystallization temperature (T_x), DSC was performed on the DSC822 Mettler Toledo thermal analyzer. The samples were heated to 700°C from room temperature, the heating rate was 40°C/min.

4.4. Plasma sprayed coatings

Tests that were done on plasma sprayed coatings:

- Scanning electron microscopy with topography contrast of the surface

The surface topography was observed with SEM (Tescan Vega 3). Topographic contrast was used to observe the deformation of the deposited powder and eventual contamination.

- Roughness measurements

The roughness of the coatings was measured by the MarSurf PS 10 profilometer, each sample was tested at least 5 times, the length of the measurement profile by device was 15 mm. The measured parameters were R_a , the arithmetical average value of all absolute distances of the roughness profile from the center line within the measuring length, and R_z , the average maximum peak to valley height of five consecutive sampling lengths within the measuring length [339–341].

- Digital microscopic observation of the cross section and thickness measurement

The prepared cross sections of the samples were observed with the VHX-6000 Keyence digital microscope. Each coating was measured in 20 places to calculate the average thickness. Furthermore, analyses of particles deformation and potential delamination were done.

- Porosity analysis performed on scanning electron microscopy images

Cross-section of selected samples were observed using SEM (Tescan Vega 3) with topography contrast to determine the amount of porosity in the coating. Each coating was photographed at least five times, and the porosity was calculated with the ImageJ graphic program.

- X-ray diffraction

Evaluation of the crystal phase absence was done with X-ray diffractometer with Bruker AXS, D8 DISCOVER, Cobalt radiation lamp WL= 1,78897. The range of X-ray scanning was 25–90° 2θ with a step of 0.05°.

- Differential scanning calorimetry

To establish the precise glass transition (T_g) and the crystallization temperature (T_x), DSC was performed on the DSC822 Mettler Toledo thermal analyzer. The samples were heated to 700°C from room temperature, the heating rate was 40°C/min.

- Nanoindentation

The nanohardness and elastic modulus were calculated by the nanoindentation test performed with an Anton Pharr NHT3 nanoindenter with a Berkovich-type tip. Measurements were taken at room temperature, and the applied load was set at a level of 35 mN, a pause of 30 s, and the load and unload rate were 70 mN/min. The distance between the indentation was at least 3 times the width of the indentation. The number of indents was at least 15. The calculations of the hardness and the elastic module were performed using the Oliver and Pharr method [338].

- Wear resistance measurement

Wear resistance was tested with an Rtec MFT-5000 tribometer. Sliding wear without lubrication was performed with the ball-on-disk method. The counter-body used was a 6 mm diameter WC-Co ball. The applied load was constant at the level of 20 N, the sliding speed 0.1 m/s on the distance of 500 m. The counter body was moving clockwise on the circle with 3 mm diameter (R_w). Value of the specific wear resistance was calculated with equation shown in chapter *State of art*, and the V_w (volume loss) was calculated using the Eq. 12. The area of the wear track (A) was measured in at least eight cross-sections of each sample using the digital microscope VHX-6000 Keyence.

Eq. 12. Volume loss of wear track formula [342]

$$V_w = 2\pi R_w A , \quad \left[\frac{mm^3}{Nm} \right]$$

V. RESULTS

1. CoBFeSiNb results

In this chapter, the results for $\text{Co}_{47.6}\text{B}_{21.9}\text{Fe}_{20.4}\text{Si}_{5.1}\text{Nb}_5$ are presented. The chapter is organized by the forms of the developed samples, which were obtained using atomization, casting, selective laser melting, and atmospheric plasma spraying. The atomization section includes results for the powder used in SLM and APS processes. The casting process section provides data for the reference sample to which alternative technologies were compared.

1.1. CoBFeSiNb atomized powder

1.1.1. General view of material

After atomization and segregation, two fractions of the material were tested. In Fig. 43 the two fractions are shown. The smaller fraction 20-50 μm was used for SLM printing and the larger fraction 50-80 μm for APS. Most of the particles were spheric-shaped, but elongated or flat particles were also observed in the whole volume of powder. The particle shape analysis done on SEM images show the 10-15% number of non-spherical particles in both fractions.

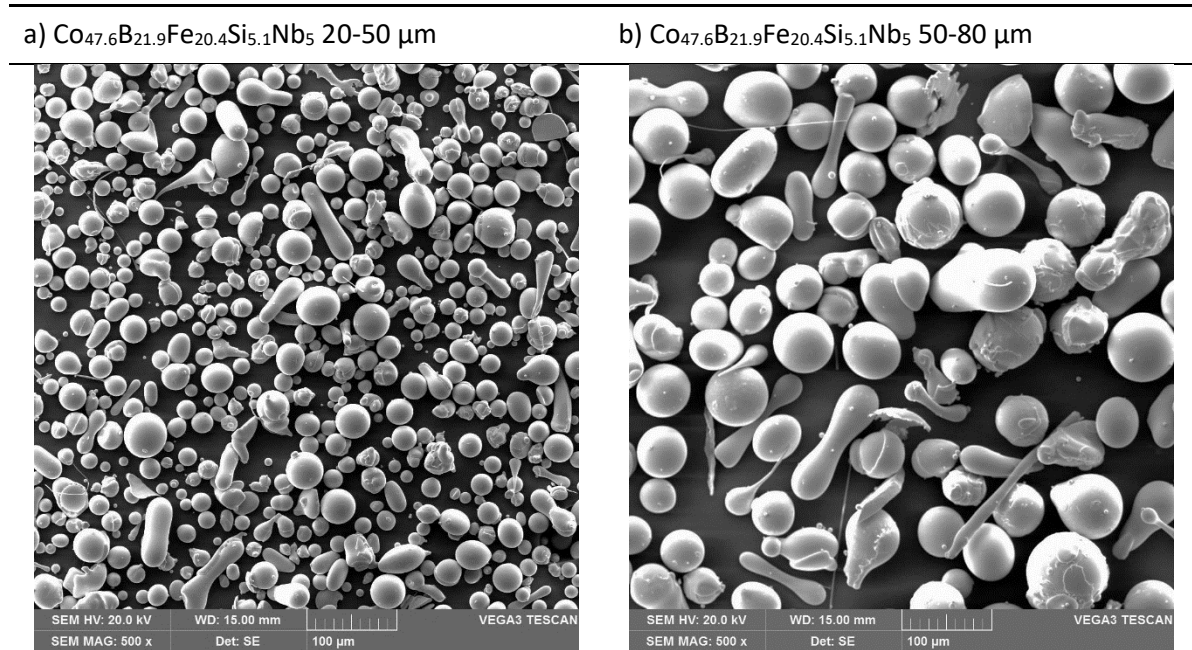


Fig. 43. SEM powder images of $\text{Co}_{47.6}\text{B}_{21.9}\text{Fe}_{20.4}\text{Si}_{5.1}\text{Nb}_5$

1.1.2. Liquid particle size analysis

The particle size analysis shows a Gaussian distribution with positive (right) skewness of the powder sizes of $\text{Co}_{47.6}\text{B}_{21.9}\text{Fe}_{20.4}\text{Si}_{5.1}\text{Nb}_5$. The results of the particle size analysis showed that 50% of the particle size (D50) for 20–50 μm granulation had a diameter less than or equal to 31.4 μm and D50 for 50–80 μm to 59.2 μm . The particle size analysis plots are shown in Fig. 44.

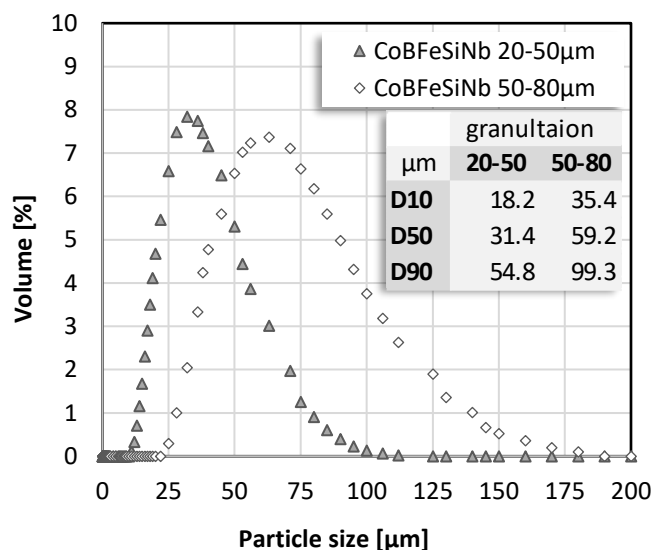


Fig. 44. Particle size analysis of $\text{Co}_{47.6}\text{B}_{21.9}\text{Fe}_{20.4}\text{Si}_{5.1}\text{Nb}_5$ [330]

1.1.3. Scanning electron microscopy

Scanning electron microscopy images of cross-section of the 20-50 and 50-80 μm powder fractions show very low percentages of porosity particles- not higher than 4%. The EDS analysis of cross-section particles shows the steady level of chemical elements. The example of the described analysis and image of the analyzed metallographic section of the particles are shown in Fig. 45.

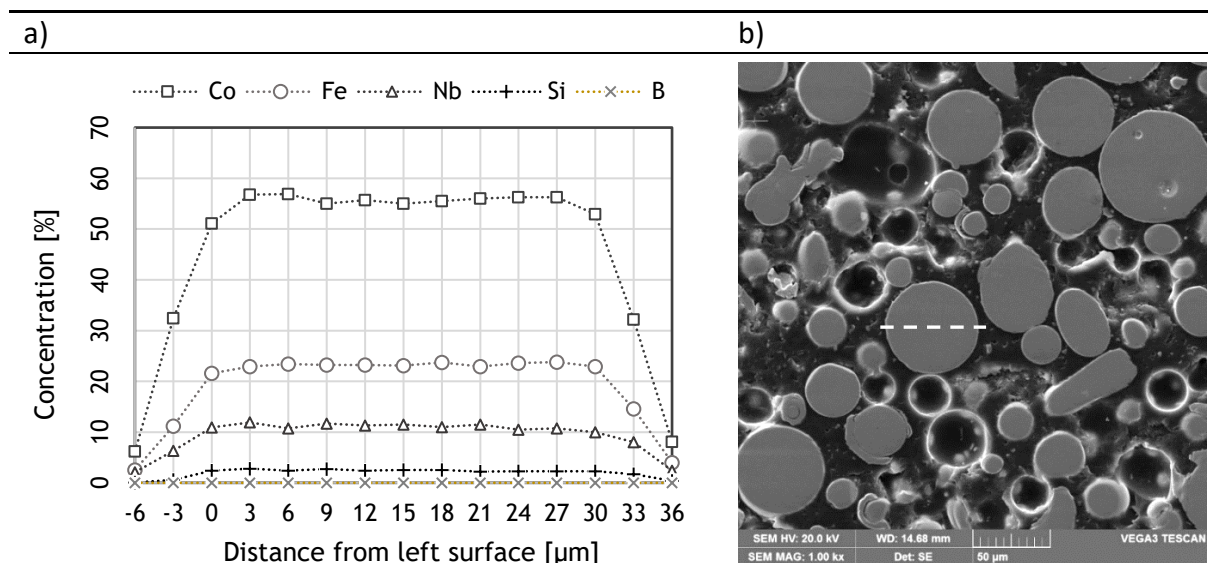


Fig. 45. Example of a) EDS analysis of chemical composition homogeneity and b) SEM image of the analyzed metallography section of $\text{Co}_{47.6}\text{B}_{21.9}\text{Fe}_{20.4}\text{Si}_{5.1}\text{Nb}_5$. White dotted line shows the analyzed particle

1.1.4. X-ray diffraction

X-ray diffraction of $\text{Co}_{47.6}\text{B}_{21.9}\text{Fe}_{20.4}\text{Si}_{5.1}\text{Nb}_5$ did not show any diffraction peaks, which indicates no long-range atom order. However, the amorphous halo peak was observed and had a maximum at $46^\circ 2\theta$. The plot of XRD is shown in Fig. 46.

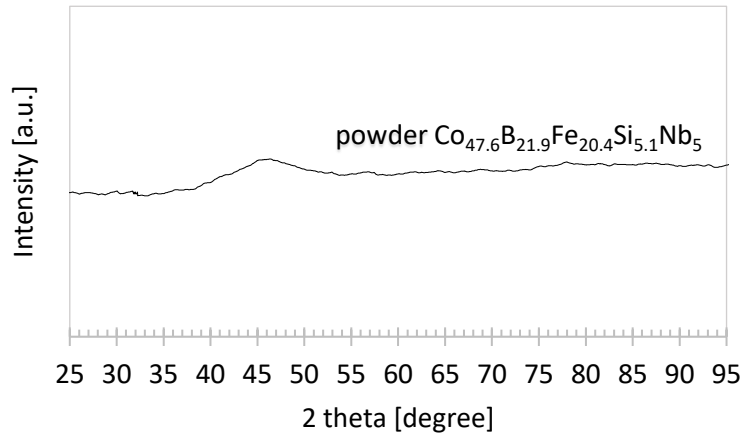


Fig. 46. X-ray diffractogram of CoBFeSiNb alloy in form of powder

1.1.5. Differential thermal analysis

Conducted DTA (Fig. 47) of the CoBFeSiNb alloy shows the existence of the glass transition (T_g) which is at 598°C. Exothermic peaks were observed. The onset of the first was at 656°C (T_x). The last peak with two maxima was endothermic and corresponded to the melting temperature (T_m) – the onset was at 1074°C.

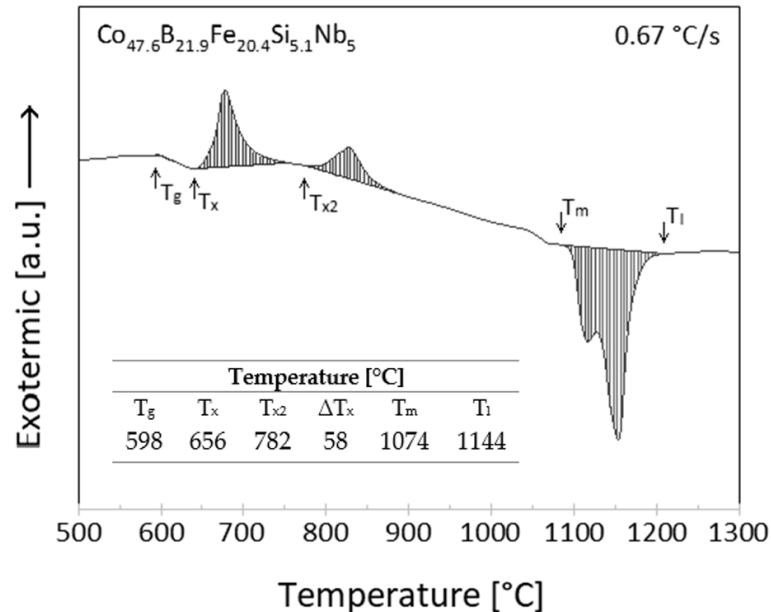


Fig. 47. Differential thermal analysis of $\text{Co}_{47.6}\text{B}_{21.9}\text{Fe}_{20.4}\text{Si}_{5.1}\text{Nb}_5$ powder

1.1.6. Nanoindentation

The mean hardness value of the 50-80 μm powder was 14.8 GPa. Lack of E_{IT} value contributes to the characteristics of the powder nanoindentation measurements. The test powder had to be embedded in the epoxy resin to make metallographic cross-sections. Epoxy resin significantly affects elastic modulus measurements. This phenomenon also influences hardness testing, albeit to a lesser extent, making hardness measurement results more suitable for indicative purposes. Nanoindentation results are shown in Tab. 18.

Tab. 18. Results of the nanoindentation test of $\text{Co}_{47.6}\text{B}_{21.9}\text{Fe}_{20.4}\text{Si}_{5.1}\text{Nb}_5$

	50-80 μm	
Parameter Unit	H_{IT} [GPa]	E_{IT} [GPa]
Mean	14.8	x
Standard deviation	0.8	x
Coefficient of variation [%]	5.1	x

H_{IT} - indentation hardness, x- not measured

1.2. CoBFeSiNb cast plate

1.2.1. General view of material

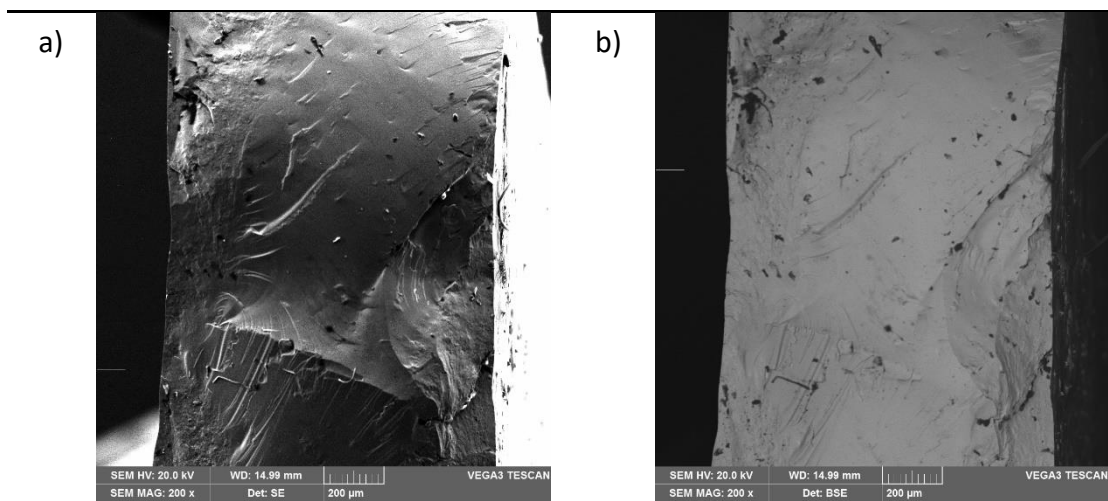
The cast plate was not cracked and had a typical shiny glassy surface. Additionally, voids were observed on the surface of the cast. The example of the cast plate is shown in Fig. 48.



Fig. 48. Cast plate of $\text{Co}_{47.6}\text{B}_{21.9}\text{Fe}_{20.4}\text{Si}_{5.1}\text{Nb}_5$

1.2.2. Scanning electron microscopy

The SEM SE observation (Fig. 49 a) shows the presence of mixed hackle zone with mirror surfaces. BSE contrast (Fig. 49 b) shows the absence of second face in the form of crystallization, however, the casting impurities were observed. The cast plate was solid, without porosity inside the cast and visible cracks. The observation of the cross-section of $\text{Co}_{47.6}\text{B}_{21.9}\text{Fe}_{20.4}\text{Si}_{5.1}\text{Nb}_5$ plate confirmed the absence of second-phase (Fig. 49 c, d).



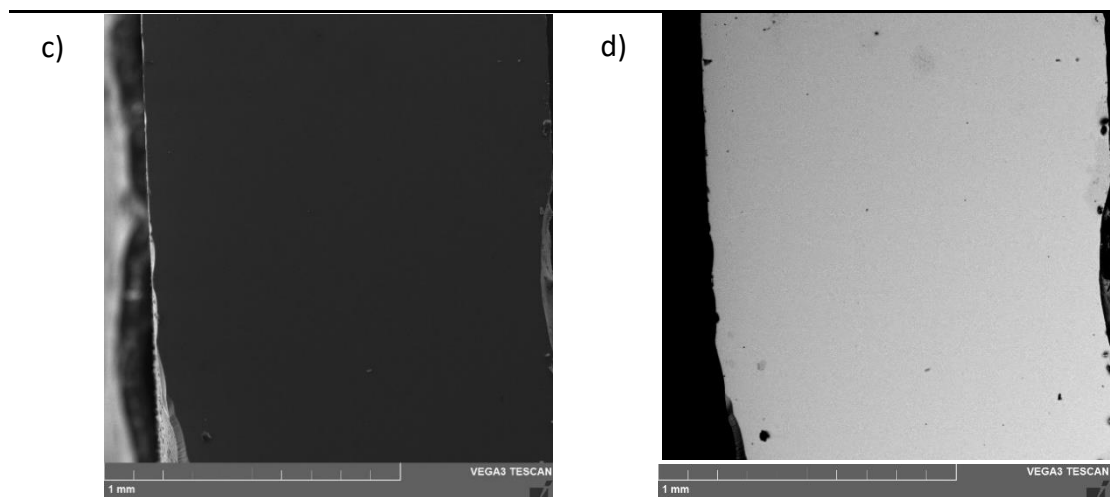


Fig. 49. SEM of cast plate images with topographic (a, c) and material contrast (b, d). Image of the fracture (a, b) and cross-section (c, d)

1.2.3. X-ray diffraction

The X-ray diffractogram of $\text{Co}_{47.6}\text{B}_{21.9}\text{Fe}_{20.4}\text{Si}_{5.1}\text{Nb}_5$ is shown in Fig. 50. No crystallization peaks were observed, and the amorphous halo has the highest intensity around 46° 2 theta.

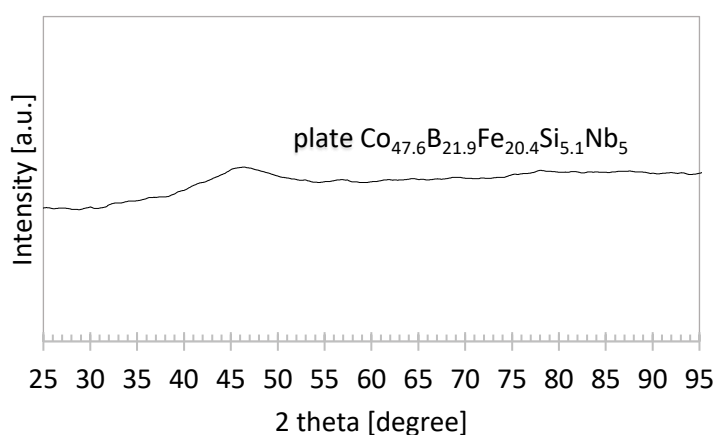


Fig. 50. X-ray diffractogram of $\text{Co}_{47.6}\text{B}_{21.9}\text{Fe}_{20.4}\text{Si}_{5.1}\text{Nb}_5$ plate

1.2.4. Differential scanning calorimetry

The differential thermal analysis plot of the $\text{Co}_{47.6}\text{B}_{21.9}\text{Fe}_{20.4}\text{Si}_{5.1}\text{Nb}_5$ plate shows a presence of T_g at 577°C and a sharp exothermal peak with onset at 618°C , which makes difference between the temperatures of 41°C . The DSC analysis is shown in Fig. 51.

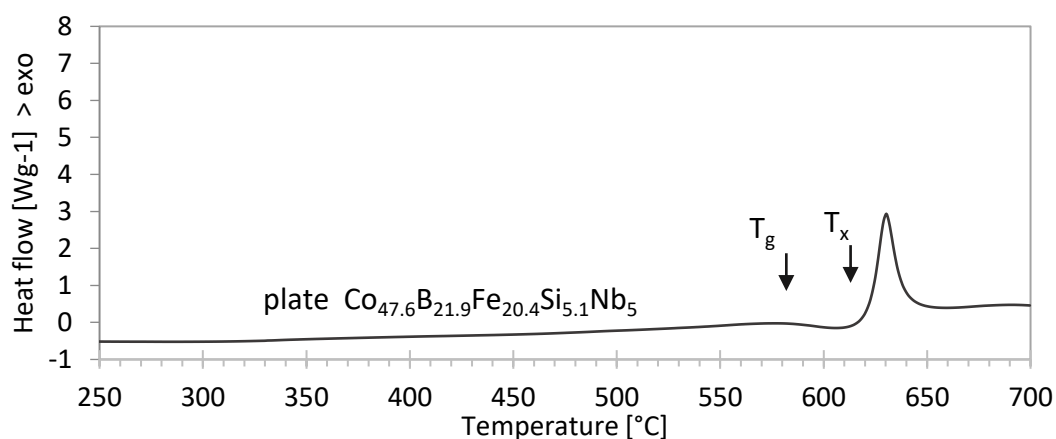


Fig. 51. Differential scanning calorimetry of cast plate of $\text{Co}_{47.6}\text{B}_{21.9}\text{Fe}_{20.4}\text{Si}_{5.1}\text{Nb}_5$

1.2.5. Nanoindentation

The hardness of the plate was 15.6 GPa and elastic module 222.8 GPa. Nanoindentation results of the plate are shown in Tab. 19. The example of indents is shown in Fig. 52.

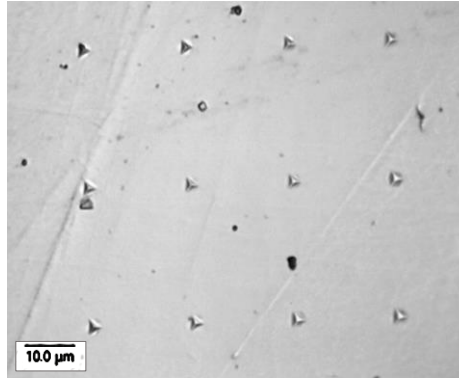


Fig. 52. Example of indents done by nanohardness testing

Tab. 19. Results of the nanoindentation test of $\text{Co}_{47.6}\text{B}_{21.9}\text{Fe}_{20.4}\text{Si}_{5.1}\text{Nb}_5$

Plate CoBFeSiNb		
Parameter Unit	H_{IT} [GPa]	E_{IT} [GPa]
Mean	15.6	222.8
Standard deviation	1.5	12.4
Coefficient of variation [%]	9.6	5.6

H_{IT} - indentation hardness, E_{IT} - indentation elastic module

1.3. CoBFeSiNb selective laser melting printed BMG

1.3.1. The first stage of printing

Macroscopic observations of CoBFeSiNb showed that samples from the 75 W series and most of the 95 W series were manufactured successfully, while samples from the 55 W series were mostly not developed successfully. The microscopic images of samples printed from preliminary parameters are shown in Fig. 53. Samples whose cross-sections were not shown in the Fig. 53. were destroyed in the process of printing or abrasive preparation. The P95_v600 sample (laser energy $P = 95$ W, scanning speed $v = 600$ mm/s) (left bottom corner of Fig. 53) was manufactured with the highest energy density (ED) of all experiments. The cross-section of the sample is not shown because in the process of printing the sample cracked and deformed, leading to the destruction of the sample. Samples with a next lower ED (e.g. P75_v600, P95_v800) were developed successfully. Furthermore, samples from this group have lower porosity compared to the sample in the middle of the table. Moving to the right of the table, more porous structures were observed with higher areas of only partially melted powder particles. Samples from the right-top of the (high scanning speed combined with low laser power) were developed in the printing process, however, were destroyed in the abrasive process of sample preparation. This destruction was caused by the lack of joining of the feedstock (e.g., sample P55_v1800).

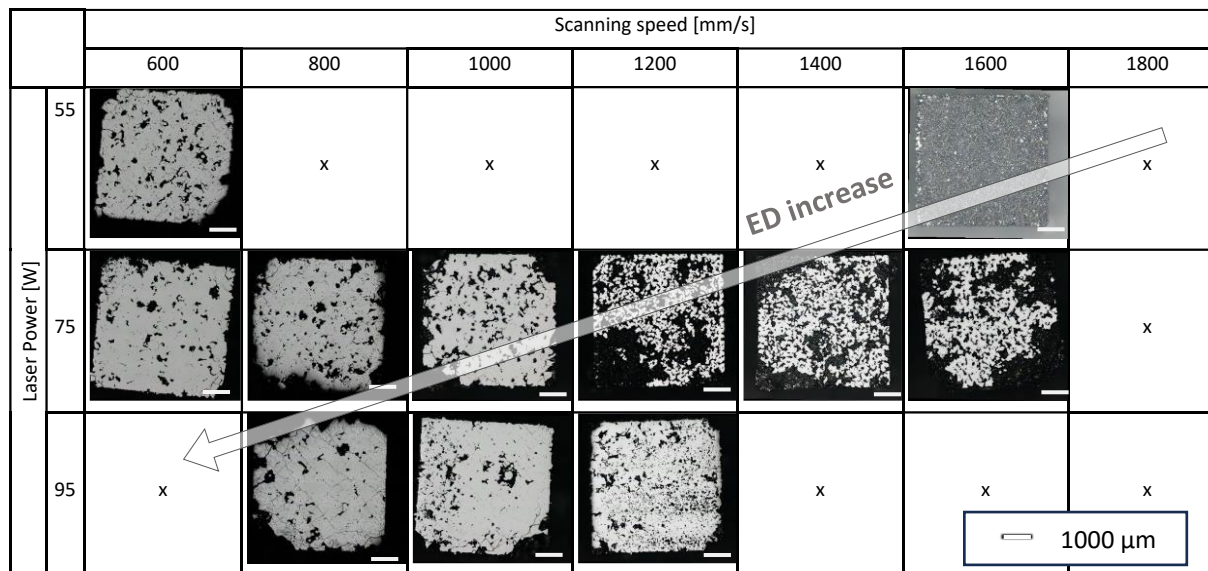


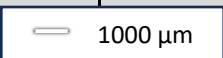
Fig. 53. Results of the first-stage printing of $\text{Co}_{47.6}\text{B}_{21.9}\text{Fe}_{20.4}\text{Si}_{5.1}\text{Nb}_5$, x- sample destroyed in the process

The above analysis leads to limiting the value of ED from 39 to 68 J/mm³. Samples with ED less than 39 J/mm³ exhibit the lack of fusion, and those with ED greater than 68 J/mm³ were destroyed in the process. This range of ED was used to establish the second stage experiment parameters.

1.3.2. The second stage of printing

The selected ED range (from 39 to 68 J/mm³) for the second stage of an experiment with a denser matrix of parameters (compared to the first stage of the experiment) led to the successful printing of all samples. The metallographic cross-sections of the samples are shown in Tab. 20. The lowest porosity was observed for samples P65_v500. All samples from this experiment exhibit cracked structures and voids. In addition, detachments of the material were observed in the corner. All samples had a cracked structure; cracks were lined in two directions, both parallel to the diagonals of the observed surfaces of the samples. The number of cracks was similar for all samples. Some of the cracks crossed the observed voids.




Tab. 20 Microstructure of the second printing stage of $\text{Co}_{47.6}\text{B}_{21.9}\text{Fe}_{20.4}\text{Si}_{5.1}\text{Nb}_5$. Digital microscopy

I.Nb		Scanning speed v (mm/s)			
		500	600	700	800
Laser power P [W]	45		 1000 μm		smaller voids, larger number
	50				
	55			ED increase	
	60				
	65				
	70	larger voids, smaller number			
	75				

The observed voids in samples across the table had different shapes and sizes. The observed voids were divided into three categories: type A are symmetric, round, with diameter less than 20 μm , type B have a wide scale of size, irregular, rounded edges, often elongated, type C have a wide size scale, rectangular or triangular shapes with sharp edges. The schematic visualization of this classification is shown in Tab. 21. Type A voids were observed in all samples in a similar amount. Sample P45_v500 (left top corner of Tab. 20) has the highest number of voids that were dispersed throughout the observed area. Most of them were type B, mostly small sizes (50-200 μm) and several medium sizes (above 200 μm). In images of P50_v600, P50_v500, P55_v600, P55_v500, P65_v500, P70_v800, and P75_v800 small and medium type B voids can also be observed (visually, these samples are on the diagonal from top-left to bottom-right and above that diagonal in Tab. 20). It can be observed

that from the right top to the left bottom of the table the voids become larger (eventually even larger than 200 μm) while the total area of the voids decreased. The lowest number of voids was observed in sample P65_v500. Only a few large and small type B voids were observed. The C type voids were also observed in all samples; however, most of them were at the corners or edges of the samples. If voids of type C were observed inside samples, then they were always observed with mixed B type voids at the bottom of them. In particular, the samples on the bottom left of Tab. 20 show a larger number of C type voids.

Tab. 21. Types of voids in the SLM samples

Type of porosity	A	B	C
Visualization			
Description	Symmetric, round, with diameter less than 20 μm	Irregular, rounded edges, often elongated, a wide scale of size	Rectangular or triangular shapes with sharp edges, a wide size scale

1.3.3. Density of samples

The samples densities measured by the Archimedes method are shown in the Tab. 22. The correlation between the density of samples and energy density can be seen. Samples with a higher energy density have a higher physical density. The highest density was measured for P65_v500, P60_v500, and P75_v600, which also had the highest energy density. The lowest density was observed for samples P45_v500, P50_v600, P60_v700, and P65_v800.

Tab. 22. The second stage of the printing of $\text{Co}_{47.6}\text{B}_{21.9}\text{Fe}_{20.4}\text{Si}_{5.1}\text{Nb}_5$ samples a) density of samples and c) calculated energy density (ED). Values are marked with color showing from the highest to lowest values b)

a)					
Laser power P [W]	Density [g/cm ³]	Scanning speed v (mm/s)			
		500	600	700	800
	45	7.2			
	50	7.3	7.3		
	55	7.4	7.3		
	60	7.5	7.4	7.3	
	65	7.6	7.5	7.4	7.3
	70		7.5	7.5	7.3
	75		7.5	7.5	7.4
b)					
highest					
lowest					
not tested					
c)					
Laser power P [W]	ED [J/mm ³]	Scanning speed v (mm/s)			
		500	600	700	800
	45	46.8			
	50	51.9	43.3		
	55	57.1	47.6		
	60	62.3	51.9	44.5	
	65	67.5	56.3	48.2	42.2
	70		60.6	51.9	45.5
	75		64.9	55.7	48.7

1.3.4. Scanning electron microscopy

For detailed observation, six samples representing the entire range of energy density were chosen (Fig. 54). SEM images of those six samples revealed the correlation between energy density and density of samples. Samples with higher ED had mostly C type voids with sharp edges. Samples with lower ED exhibit mostly B type voids with irregular large sizes ($> 50 \mu\text{m}$). Additionally, samples with lower density and ED had many unmelted particles, e.g. sample P60_v700. Porosity of B type was observed in all samples as small round voids. In the densest sample (P65_v500) a closer look on large voids of type C shows the characteristic of

typical brittle fractures with sharp edges. Void type C shows several hackle zones with hackle ridges and mist areas. Fractures are aligned along an observed grid of cracks on the surface of the sample. Some of the A type voids are crossed by the cracks. Cracks developed in all samples as an irregular grid pattern with a spacing between neighboring parallel cracks of 350-550 μm .

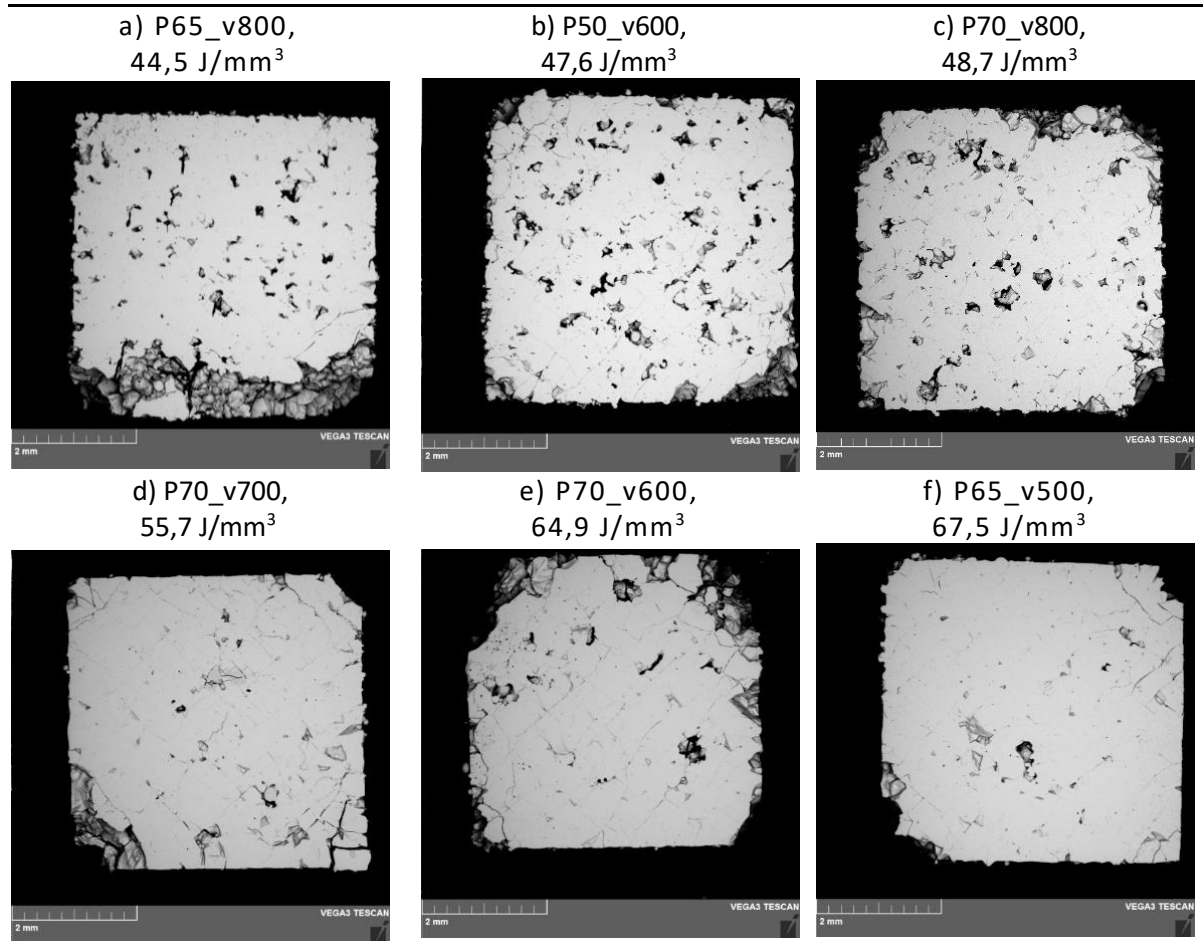


Fig. 54. SEM images of six selected samples from the second stage of $\text{Co}_{47.6}\text{B}_{21.9}\text{Fe}_{20.4}\text{Si}_{5.1}\text{Nb}_5$ printing, in the description the laser power, scanning speed and energy destiny used for manufacturing samples

1.3.5. X-ray diffraction

The X-ray diffraction of six selected samples did not show any crystallization peaks. The plot of X-ray diffraction was smooth and for all samples the amorphous halo was observed. Additionally, the maximum intensity was at the same angle, namely at about $45^\circ 2\theta$. The results are shown in Fig. 55.

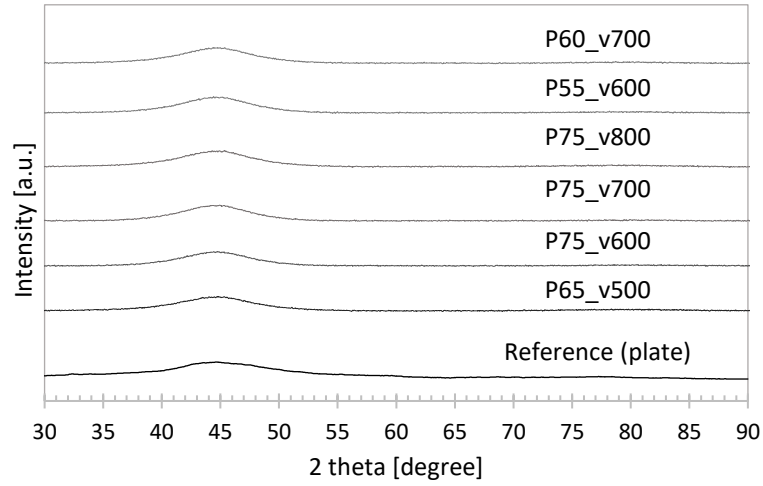


Fig. 55. X-ray diffractograms of BMG of $\text{Co}_{47.6}\text{B}_{21.9}\text{Fe}_{20.4}\text{Si}_{5.1}\text{Nb}_5$

1.3.6. Nanoindentation

The nanohardness value of the samples shown in Fig. 54 ranges between 13.8 and 15.2 GPa (Fig. 56 a). The elastic modulus ranges from 185 to 200 GPa (Fig. 56 b).

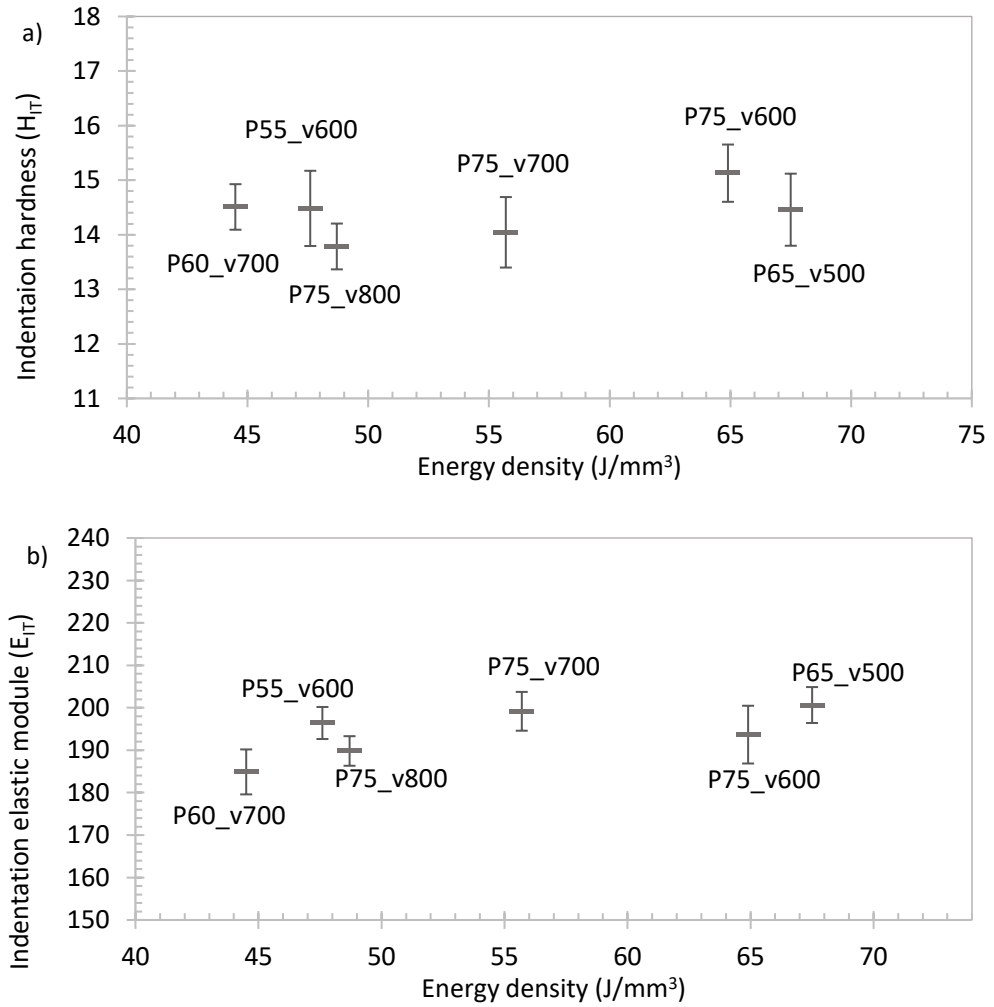


Fig. 56. Nanoindentation analysis of $\text{Co}_{47.6}\text{B}_{21.9}\text{Fe}_{20.4}\text{Si}_{5.1}\text{Nb}_5$ a) hardness, b) elastic module

The sample P65_v500 had the highest density of samples (Archimedes density measurements) and the lowest porosity (SEM analyze) while preserving the fully amorphous structure (XRD analyze). This set of parameters was chosen to be researched more extensively. The detailed nanohardness is shown below (Tab. 23). The hardness of the P65_v500 sample was 14.5 GPa and elastic module 200.6 GPa.

Tab. 23. Results of the nanoindentation test of $\text{Co}_{47.6}\text{B}_{21.9}\text{Fe}_{20.4}\text{Si}_{5.1}\text{Nb}_5$

P65_v500		
Parameter	H_{IT}	E_{IT}
Unit	[GPa]	[GPa]
Mean	14.5	200.6
Standard deviation	1.4	8.5
Coefficient of variation [%]	9.1	4.2

H_{IT} - indentation hardness, E_{IT} - indentation elastic module

1.3.7. Differential scanning calorimetry

The DSC of $\text{Co}_{47.6}\text{B}_{21.9}\text{Fe}_{20.4}\text{Si}_{5.1}\text{Nb}_5$ of sample P65_v500 showed the presence of a characteristic inflection point of the curve that corresponds to a glass transition temperature equal to 595°C. An exothermal peak was also observed. The peak was characteristic for the phase transition and had an onset at 645°C. The plot of DSC is shown in Fig. 57.

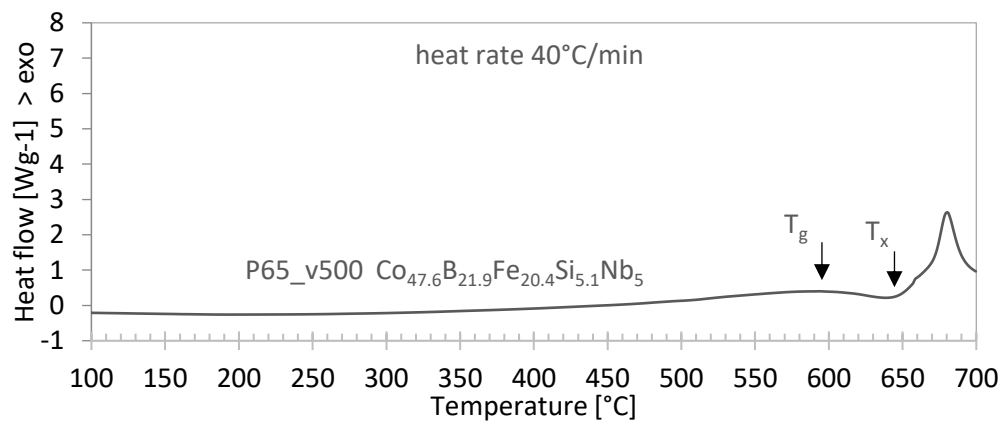


Fig. 57. Different scanning calorimetry of SLM sample of $\text{Co}_{47.6}\text{B}_{21.9}\text{Fe}_{20.4}\text{Si}_{5.1}\text{Nb}_5$

1.3.8. Scanning transmission electron microscopy

The results of energy-dispersive spectroscopy of the P65_v500 sample conducted with scanning transmission electron microscopy are shown in Fig. 58. b)-f). Analyzed area concerned up to $4\ \mu\text{m}^2$ and focus on the crack as shown in the reference image in Fig. 58 a). The result of the mapping shows no segregation in the solid area or near the analyze crack. Additionally, no segregation (homogeneity) of the elements is confirmed by the diffraction pattern of the tested sample (Fig. 58 g). The diffraction pattern had the form of circles without any single bright spots, which is characteristic for an amorphous structure.

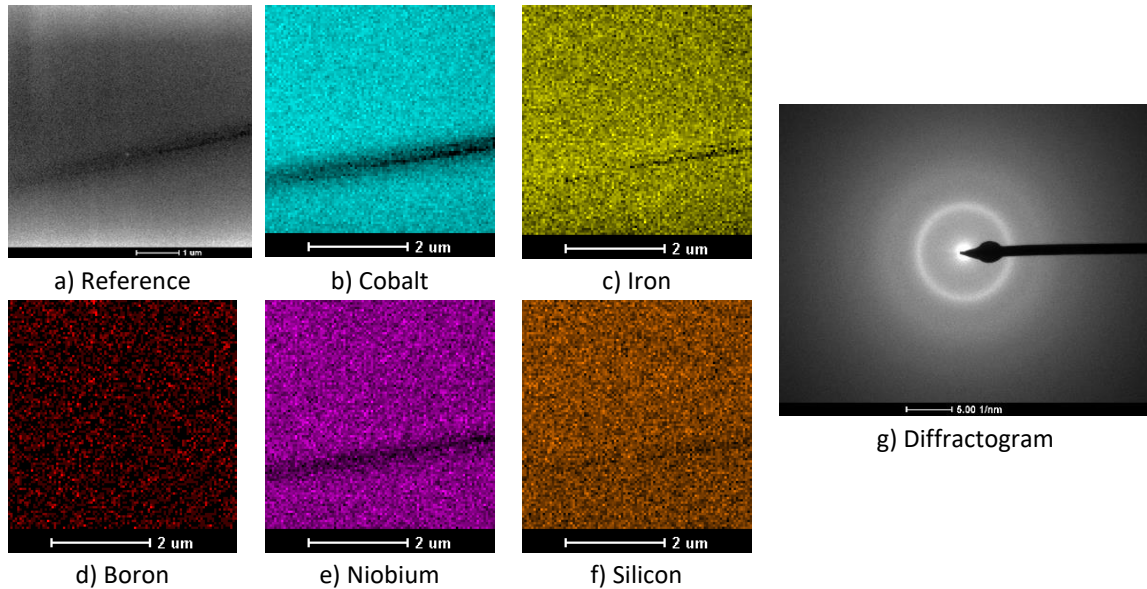


Fig. 58. Analysis of the $\text{Co}_{47.6}\text{B}_{21.9}\text{Fe}_{20.4}\text{Si}_{5.1}\text{Nb}_5$ P65_v500 BMG sample developed by SLM a)-f) energy dispersive spectroscopy (EDS) map conduct with scanning transmission electron microscopy (STEM), g) TEM, selected area electrons diffraction (SAED) pattern

1.4. CoFeSiNb atmospheric plasma sprayed coatings

1.4.1. General view of material

All three spraying distances allowed for the successful deposition of the powder onto the coatings. In Fig. 59 a view of the sample is shown. All samples developed from CoFeSiNb powder, macroscopically looked similar, and had a rough surface.

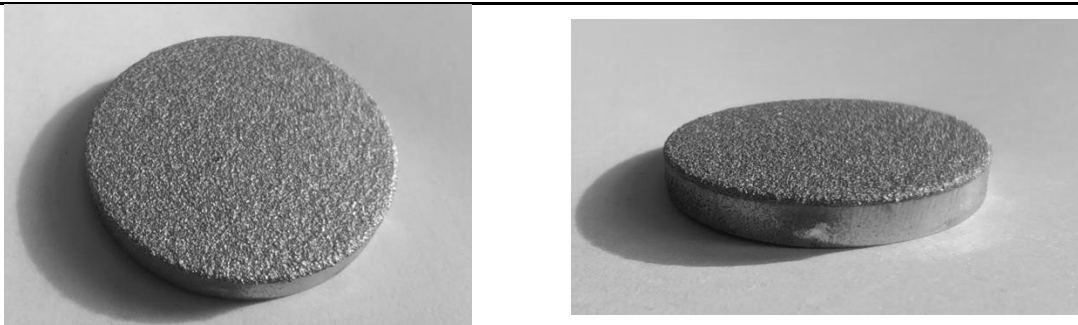
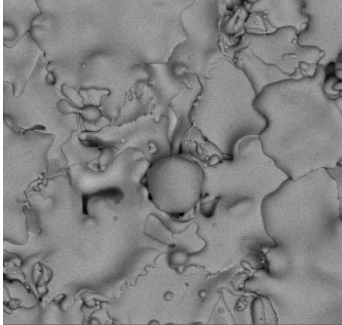
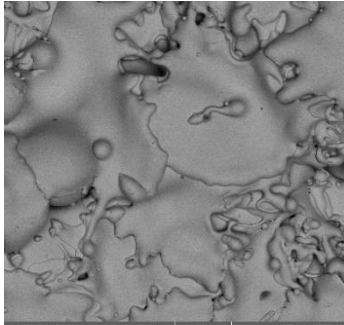
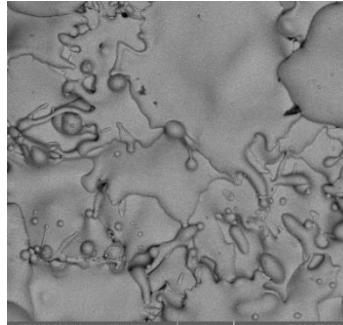
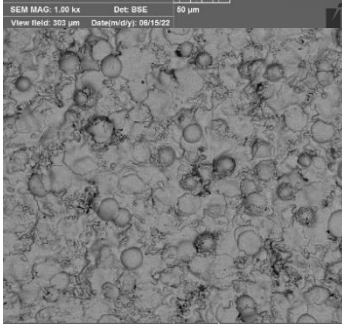
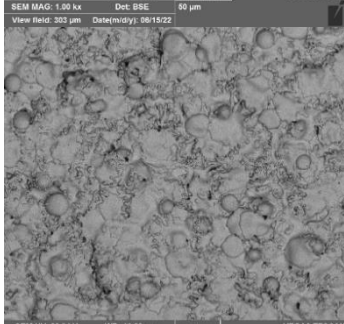
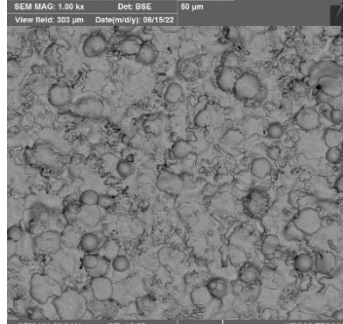
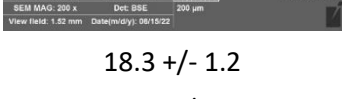
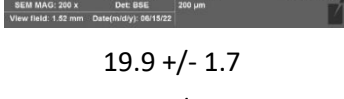
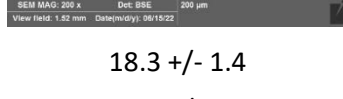


Fig. 59. Macroscopic image of the CoFeSiNb coating developed by atmospheric plasma spraying, disk in diameter of 30 mm

1.4.2. SEM surface observation and roughness

The surfaces of the CoFeSiNb plasma sprayed samples visually look similar. Characteristic flat, with high surface splats representing good plasma spraying parameters were mixed with only partially deformed powder particles spherical-shaped. The roughness of the coatings sprayed with 90, 100 and 110 mm had similar values. The image of the surfaces of the samples and the roughness analysis are shown in the Tab. 24.

Tab. 24. Surface of atmospheric plasma sprayed samples of $\text{Co}_{47.6}\text{B}_{21.9}\text{Fe}_{20.4}\text{Si}_{5.1}\text{Nb}_5\%$ at

Spraying distance [mm]	90	100	110
SEM surface images			
			
			
R_a [μm]	18.3 +/- 1.2	19.9 +/- 1.7	18.3 +/- 1.4
R_z [μm]	106.5 +/- 8.5	119.7 +/- 12.4	117.3 +/- 13.9

1.4.3. Thickness and porosity analysis

Examples of cross-section images of the plasma-sprayed coating captured with digital microscope is shown in Fig. 60. This observation was used to measure the average thickness for the samples that have a similar value. The thickness of the coatings oscillates between 345-380 μm . Additionally, the cross-section observation reveals several defects such as delimitation between particles and between coating and the substrate.

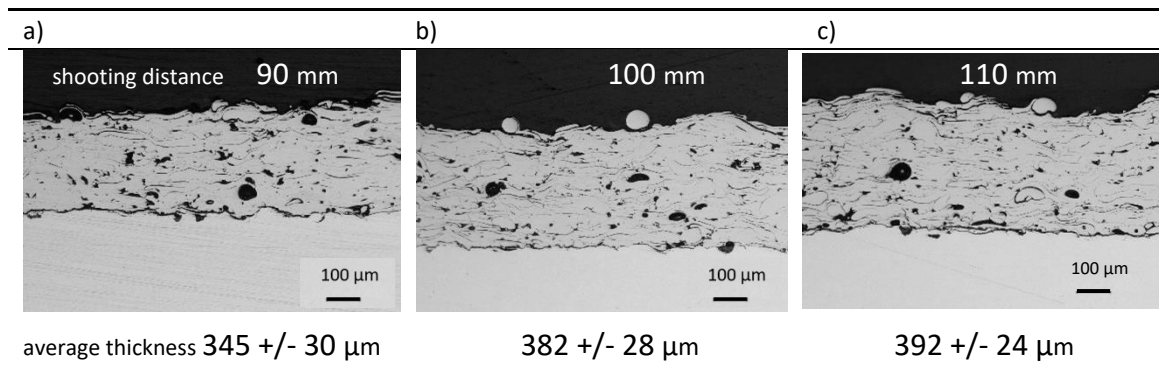
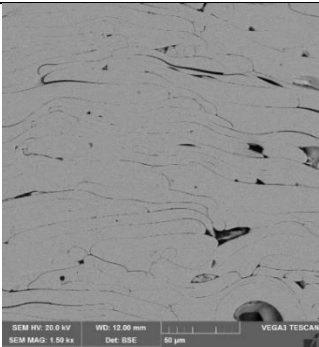
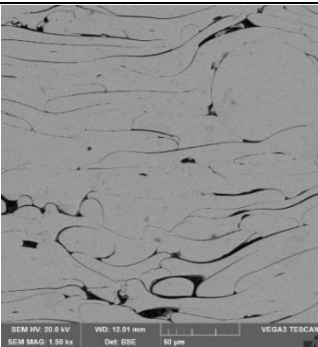
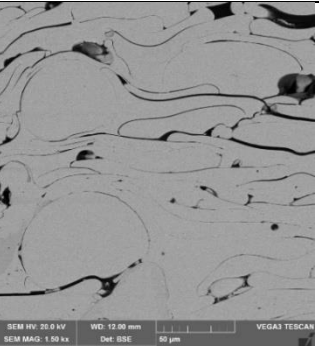


Fig. 60. APS coatings of $\text{Co}_{47.6}\text{B}_{21.9}\text{Fe}_{20.4}\text{Si}_{5.1}\text{Nb}_5$ developed with different spraying distances

Next, the defects refer to porosities inside the coatings, which were analyzed based on the SEM captured ten images. The observed porosity ranged from 6.4% to 9.3% for samples sprayed with the lowest distance (90 mm) to the highest distance (110 mm). This change can indicate that the spraying distance has an influence on the densities of the coatings. The exact

values of porosities and the examples of images used for porosity analysis are shown in Tab. 25.

Tab. 25. Porosity analysis based on the SEM images of plasma sprayed coatings of $\text{Co}_{47.6}\text{B}_{21.9}\text{Fe}_{20.4}\text{Si}_{5.1}\text{Nb}_5\%$ at

Spraying distance [mm]	90	100	110
SEM images			
Porosity [%]	6.4	8.6	9.3
Standard deviation [% points]	0.8	1.1	0.8

The following text presents a comparison of coatings developed using spraying distances of 90 mm and 110 mm. In the SEM imaging, material contrast analysis revealed no signs of crystallization; however, numerous imperfections were registered and are detailed in the images shown in Fig. 61. The images illustrate the differences between the coatings developed at the shortest and longest spraying distances. Notably, delamination between the splats is evident in all samples. In the coatings obtained at a spraying distance of 90 mm, the unmelted particles are relatively small. In contrast, the coatings developed at 110 mm exhibit a wide range of unmelted particle sizes. Additionally, porosity is mostly observed in the samples obtained with a spraying distance of 110 mm.

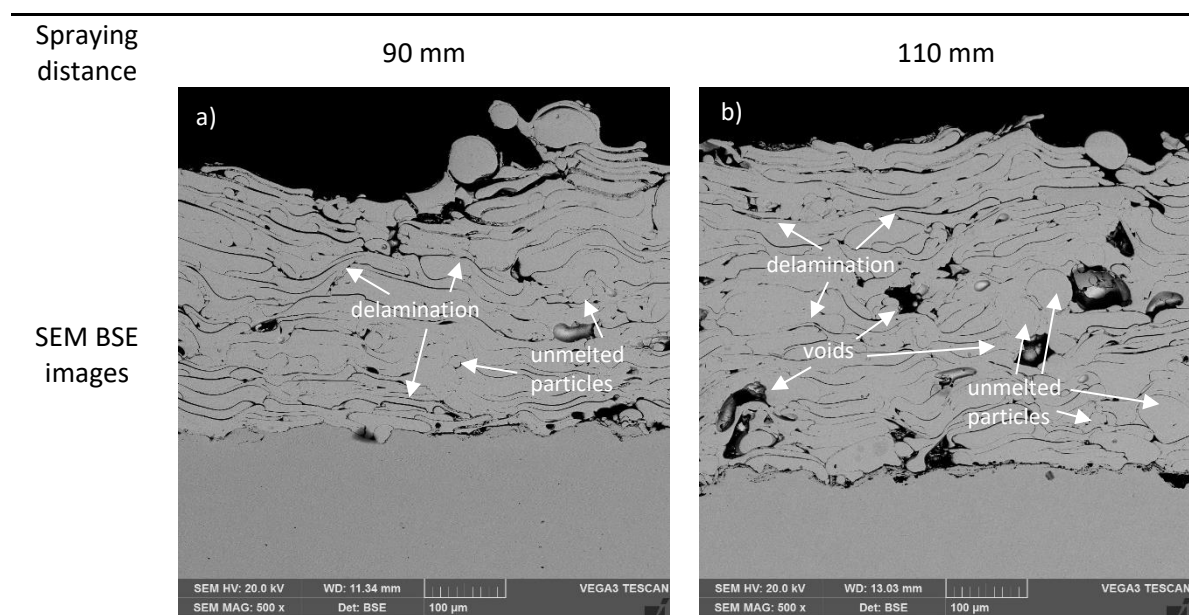


Fig. 61. Comparison of cross-section of the atmospheric plasma sprayed coatings of $\text{Co}_{47.6}\text{B}_{21.9}\text{Fe}_{20.4}\text{Si}_{5.1}\text{Nb}_5$ with spraying distance a) 90 mm and b) 110 mm

1.4.4. X-ray diffraction

The X-ray diffraction analyze did not show any peaks that could indicate the presence of the crystal phase. However, the typical amorphous halo is also absent, indicating that some segregation of chemical elements could occur. The plot of XRD is shown in Fig. 62.

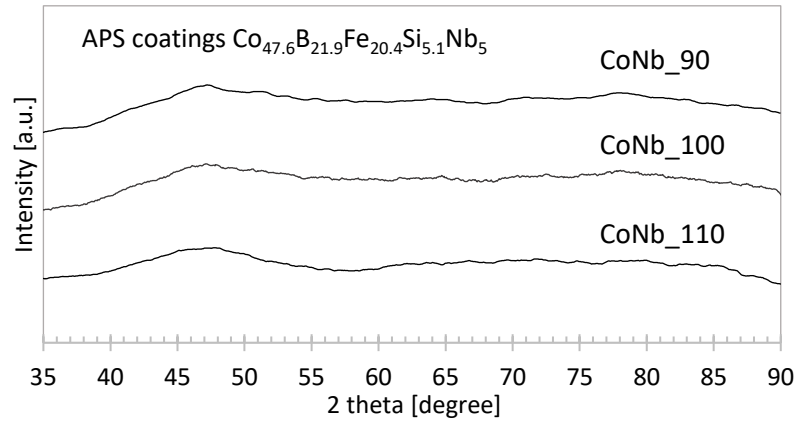


Fig. 62. X-ray diffractogram of plasma sprayed $\text{Co}_{47.6}\text{B}_{21.9}\text{Fe}_{20.4}\text{Si}_{5.1}\text{Nb}_5$

1.4.5. Differential scanning calorimetry

The DSC of the plasma sprayed coatings from $\text{Co}_{47.6}\text{B}_{21.9}\text{Fe}_{20.4}\text{Si}_{5.1}\text{Nb}_5$ showed the presence of a characteristic inflection point of the plot that corresponds to a glass transition temperature equal to 608°C . An exothermal peak was also observed. The peak was characteristic for the phase transition and had an onset at 650°C . The plot of DSC is shown in Fig. 63.

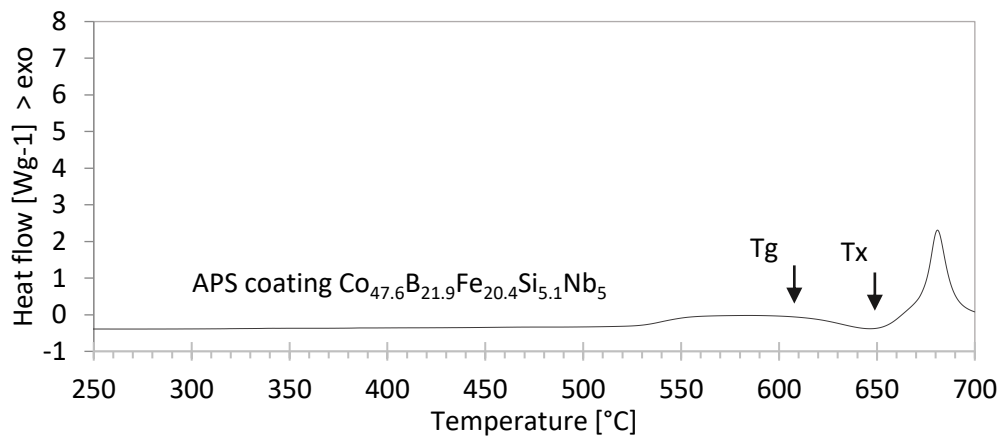


Fig. 63. Differential scanning calorimetry of plasma sprayed $\text{Co}_{47.6}\text{B}_{21.9}\text{Fe}_{20.4}\text{Si}_{5.1}\text{Nb}_5$

1.4.6. Nanoindentation test

The hardness of all coatings had a similar hardness value of around 14.0 - 14.5 GPa. The indentation elastic module differs between the samples only in the standard deviation range and was in the range of 194.7 to 221.2 GPa. The mentioned values are shown in Tab. 26.

Tab. 26. Nanoindentation results of CoBFeSiNb coating developed via atmospheric plasma spraying

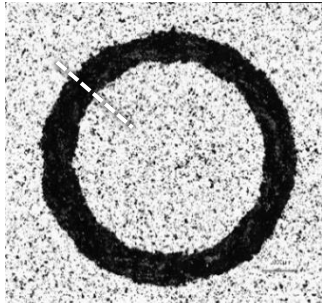
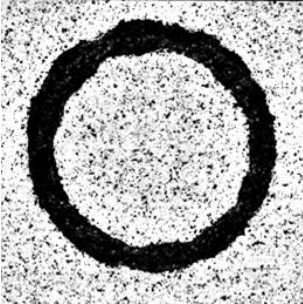
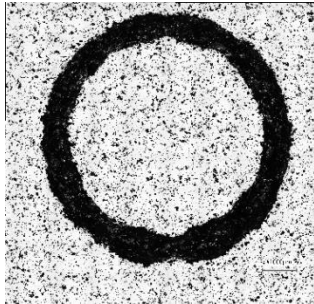
	CoNb_90		CoNb_100		CoNb_110	
Parameter Unit	H _{IT} (GPa)	E _{IT} (GPa)	H _{IT} (GPa)	E _{IT} (GPa)	H _{IT} (GPa)	E _{IT} (GPa)
Mean	14.2	213.7	14.5	194.7	14.2	221.2
Standard deviation	0.8	14.0	0.5	7.6	0.4	8.4
Coefficient of variation [%]	5.4	6.6	3.3	3.9	2.7	3.8

H_{IT}– indentation hardness, E_{IT}– indentation elastic module

1.4.7. Wear resistance measurement

Samples after the performed tests are shown in Tab. 27. The trace of ball on disk contact is irregular for all the samples. Due to this irregularity, the standard deviation of the cross-section area of the trace is high - around 20% of the mean value. Likewise, the average values of area of the cross-section area of the wear trace are similar for all samples and is on the level from $10 \cdot 10^3$ to $12 \cdot 10^3 \mu\text{m}^2$. The exact values of the areas are shown in Tab. 27, below the digital images. According to Eq. 4. the value of volume loss was calculated and then used in Eq. 2. to calculate specific wear resistance.

Tab. 27. Surface of atmospheric plasma sprayed samples after wear test of Co_{47.6}B_{21.9}Fe_{20.4}Si_{5.1}Nb₅ %at

Spraying distance [mm]	90	100	110
Digital surface image			
Mean [μm^2]*	10974	10185	11721
Standard deviation [μm^2]	2018	2136	2596
Coefficient of variation [%]	18	21	22

* Mean area value of the cross section of the wear trace, the white dashed line shows the example of a cross section. Diameter of wear trace 6 mm

Using the equation from *State of art* and *Research methods* chapters and the values of mean area of the cross sections from the Tab. 27, the specific wear resistances of the atmospheric plasma spray samples were calculated. The results are shown in Fig. 64. The value of W_s did not differ with the spraying distance of the APS. The value oscillates between 1.92 and $2.07 \cdot 10^{-5} \text{ mm}^3/\text{Nm}$ with a standard deviation of around $0.2 \cdot 10^{-5} \text{ mm}^3/\text{Nm}$.

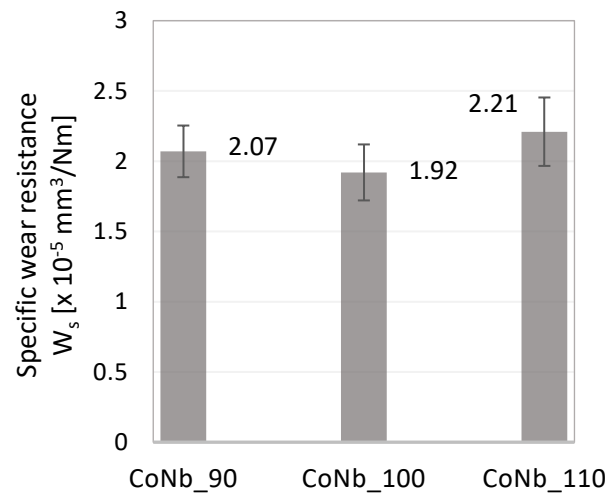


Fig. 64. Specific wear resistance of atmospheric plasma sprayed CoFeSiNb alloy with high glass forming ability

2. CoBFeTaSiCu results

In this chapter, the results for $\text{Co}_{42}\text{B}_{26.5}\text{Fe}_{20}\text{Ta}_{5.5}\text{Si}_5\text{Cu}_1$ are presented. The chapter is organized similarly to the chapter presenting the results of the first alloy, specifically by the forms of the samples obtained. The forms of $\text{Co}_{42}\text{B}_{26.5}\text{Fe}_{20}\text{Ta}_{5.5}\text{Si}_5\text{Cu}_1$ samples include powders, plates, ribbons, bulk SLM samples, and coatings. The reference sample for this alloy was a cast ribbon.

2.1. CoBFeTaSiCu atomized powder

2.1.1. General view of material

In Fig. 65 the two fractions of powder particles of $\text{Co}_{42}\text{B}_{26.5}\text{Fe}_{20}\text{Ta}_{5.5}\text{Si}_5\text{Cu}_1$ are shown. A smaller fraction of 20-50 μm was used for SLM printing and the larger fraction of 50-80 μm for APS. Most of the particles were spheric in shape, but around 8% of elongated particles were also observed in the whole volume of powder.

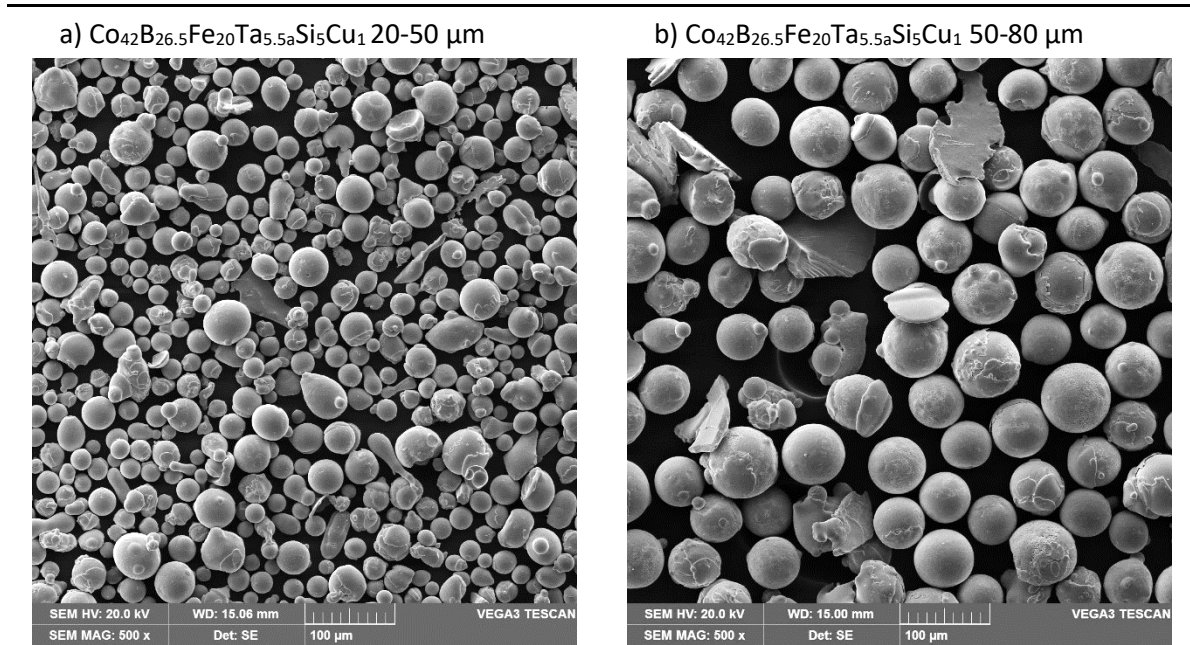


Fig. 65. SEM powder images of $\text{Co}_{42}\text{B}_{26.5}\text{Fe}_{20}\text{Ta}_{5.5}\text{Si}_5\text{Cu}_1$

2.1.2. Liquid particle size analysis

Particle size analysis of $\text{Co}_{42}\text{B}_{26.5}\text{Fe}_{20}\text{Ta}_{5.5}\text{Si}_5\text{Cu}_1$ shows a Gaussian distribution with positive (right) skewness of the powder size. The results of the particle size analysis showed that 50% of the particle size (D50) for 20–50 μm granulation had a diameter less than or equal to 29.43 μm and D50 for 50–80 μm to 63.50 μm . The particle size analysis plots are shown in Fig. 66.

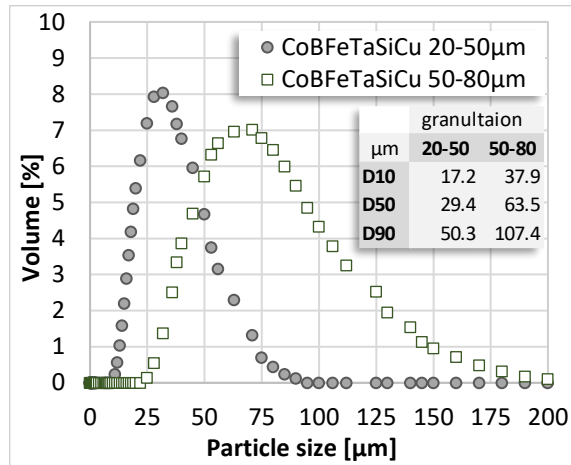


Fig. 66. Particle size analysis of $\text{Co}_{42}\text{B}_{26.5}\text{Fe}_{20}\text{Ta}_{5.5}\text{Si}_5\text{Cu}_1$ [330]

2.1.3. Scanning electron microscopy

Scanning electron microscopy images of the cross section of the 20-50 and 50-80 μm powder fractions show low percentage of the porosity particles not higher than 3.5%. The EDS analysis of cross-section shows that the maximum differences of Co was 7.6% and around 5% for Fe and Ta. For the rest of the elements, the difference was less than a 2.5% difference between the maximum and minimum concentrations. The described analysis and images of the analyzed metallographic section of the particles are shown in Fig. 67.

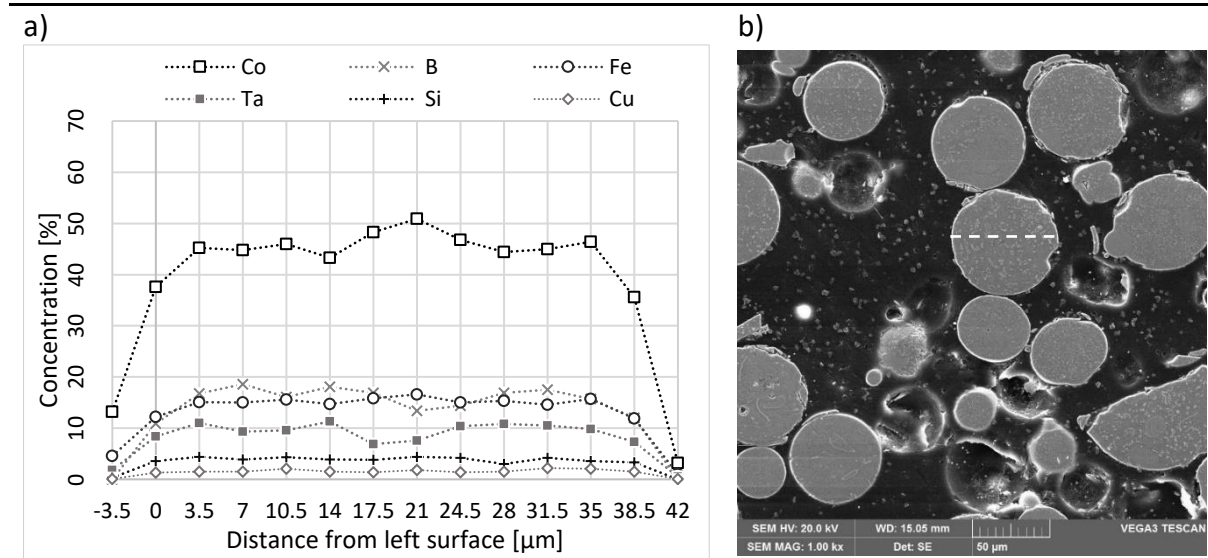


Fig. 67. Example of a) EDS analysis of the homogeneity of the chemical composition and b) SEM image of the metallography section analyzed of $\text{Co}_{42}\text{B}_{26.5}\text{Fe}_{20}\text{Ta}_{5.5}\text{Si}_5\text{Cu}_1$. White-dotted line shows the analyzed particle

2.1.4. X-ray diffraction

The X-ray diffraction of $\text{Co}_{42}\text{B}_{26.5}\text{Fe}_{20}\text{Ta}_{5.5}\text{Si}_5\text{Cu}_1$ shows several peaks that implied the presence of a crystal phase. However, the peaks are not intense, suggesting that crystallization occurs only partially in the powder. The amorphous halo can be also observed around $44-45^\circ$ 2θ . The XRD pattern of powder in the as-atomized state corresponds to $(\text{Co}, \text{Fe})_2\text{B}$ and TaB_2 . The plot is shown in Fig. 68.

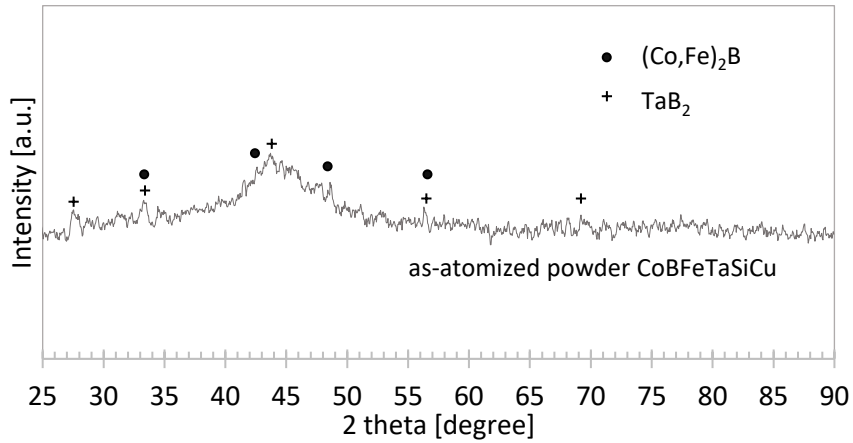


Fig. 68. X-ray diffractogram of $\text{Co}_{42}\text{B}_{26.5}\text{Fe}_{20}\text{Ta}_{5.5}\text{Si}_5\text{Cu}_1$ powder

2.1.5. Differential thermal analysis

The DTA analysis of $\text{Co}_{42}\text{B}_{26.5}\text{Fe}_{20}\text{Ta}_{5.5}\text{Si}_5\text{Cu}_1$ did not show the presence of the inflection characteristic for glass transition. However, three exothermic peaks were observed, and the first of them has an onset at 595°C. The endothermic peak occurred at 1069°C (T_m). The DTA plot is shown in Fig. 69.

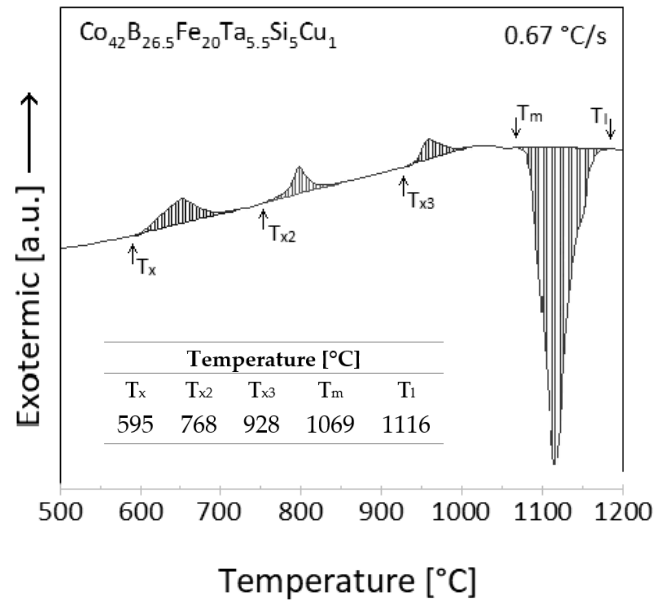


Fig. 69. Differential thermal analysis of $\text{Co}_{42}\text{B}_{26.5}\text{Fe}_{20}\text{Ta}_{5.5}\text{Si}_5\text{Cu}_1$

2.1.6. Nanoindentation

The hardness of the powder was 16.8 GPa. Lack of E_{IT} value regards to the characteristic of the powder nanoindentation measurements. The test powder had to be embedded in the epoxy resin to make metallographic cross-sections. This epoxy influences the elastic module measurements, resulting in invalid values. Measurements are shown in Tab. 28.

Tab. 28. Results of the nanoindentation test of $\text{Co}_{42}\text{B}_{26.5}\text{Fe}_{20}\text{Ta}_{5.5}\text{Si}_5\text{Cu}_1$

	Powder	
Parameter Unit	H_{IT} [GPa]	E_{IT} [GPa]
Mean	16.8	x
Standard deviation	0.1	x
Coefficient of variation [%]	6.5	x

H_{IT} - indentation hardness, E_{IT} - indentation elastic module

2.2. CoBFeTaSiCu cast plate

2.2.1. General view of material

The cast plate of $\text{Co}_{42}\text{B}_{26.5}\text{Fe}_{20}\text{Ta}_{5.5}\text{Si}_5\text{Cu}_1$ severely cracked during the cooling process inside the copper die. The surface of the plate combined shiny areas with darker zones. The cracks had a shiny surface typical of a brittle fracture. The image of the cast plates is shown in Fig. 70.

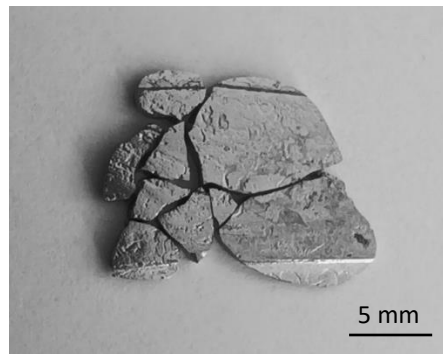


Fig. 70. Cast plate of $\text{Co}_{42}\text{B}_{26.5}\text{Fe}_{20}\text{Ta}_{5.5}\text{Si}_5\text{Cu}_1$ image

2.2.2. Scanning electron microscopy

In the cross section, the large precipitation can easily be seen (Fig. 71 a). Using the material contrast on the SEM the precipitations are observed as white areas. Closer magnification shows that plate was crystallized through the whole volume and the dendrites of another phase can also be observed (Fig. 71 b). The EDS analysis (Fig. 71 c) shows that white perceptions, both larger in size of several micrometers and smaller in size, have increased concentration of Ta and decreased Co and Fe.

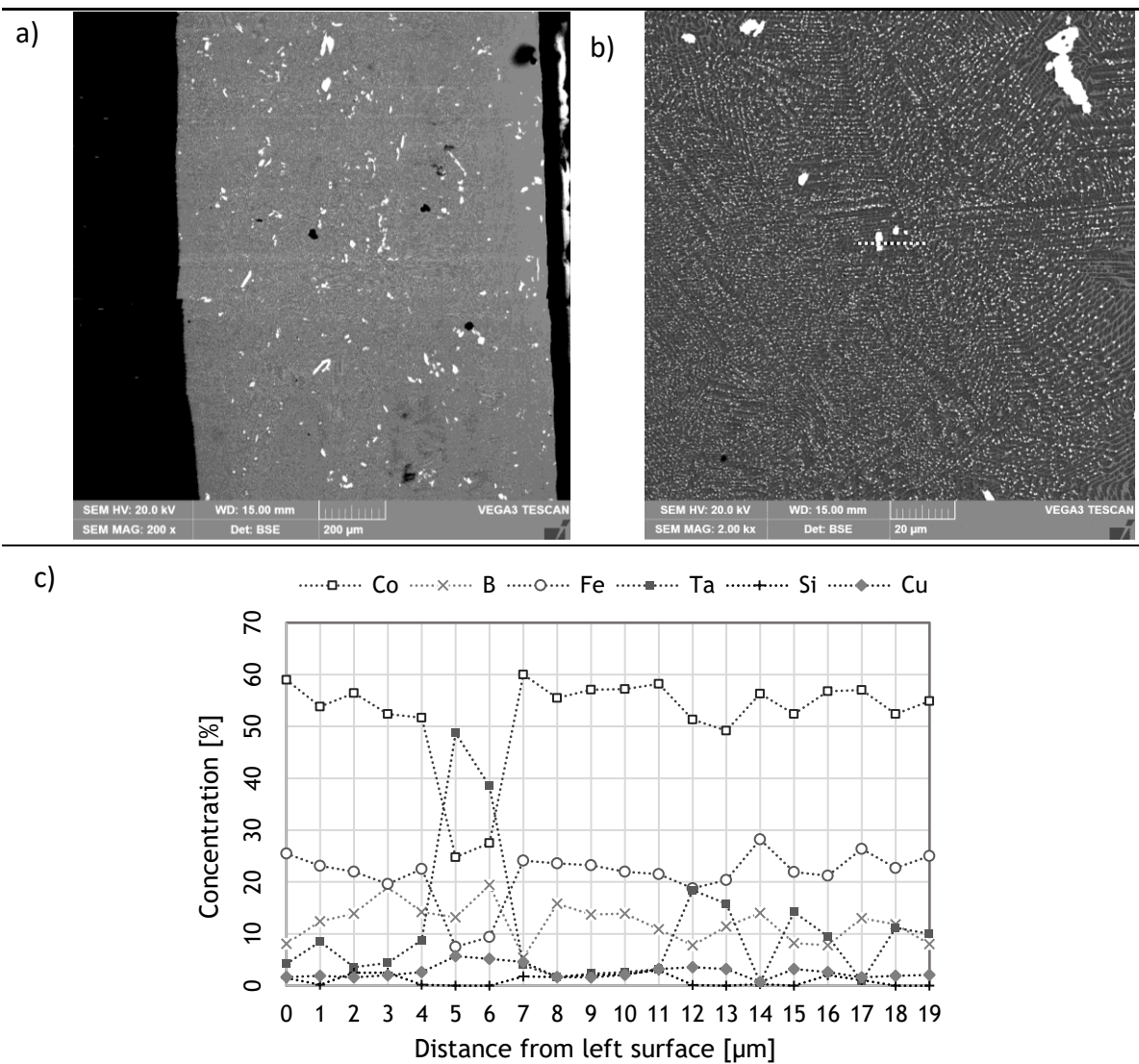


Fig. 71. SEM images of cast plate with EDS analysis of line marked with white dotted line

2.2.3. X-ray diffraction

The X-ray diffractogram of CoBFeTaSiCu shows the intense peaks indicating the presence of a crystal phase and no amorphous halo. The peaks patterns of CoBFeTaSiCu plate correspond to $(\text{Co, Fe})_2\text{B}$, and TaB_2 are shown in Fig. 72.

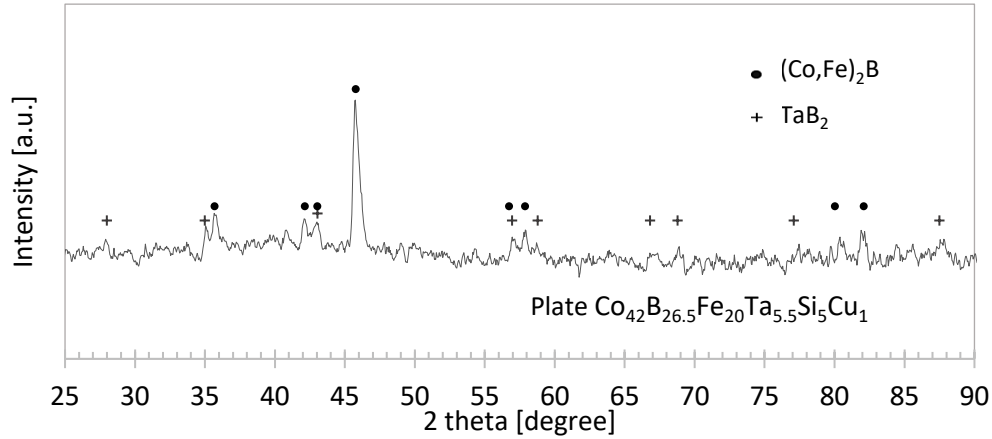


Fig. 72. X-ray diffractogram of $\text{Co}_{42}\text{B}_{26.5}\text{Fe}_{20}\text{Ta}_{5.5}\text{Si}_5\text{Cu}_1$ plate

2.2.4. Differential scanning calorimetry

The differential thermal analysis plot of the $\text{Co}_{42}\text{B}_{26.5}\text{Fe}_{20}\text{Ta}_{5.5}\text{Si}_5\text{Cu}_1$ plate confirmed the crystallization of the whole volume of the sample, the peaks corresponding to crystallization were absent (Fig. 73). However, the DSC of ribbon was also conducted, and the results showed the inflection of the plot correlating to T_g at 615°C , and sharp exothermal peak corresponding to crystallization at 665°C (Fig. 73).

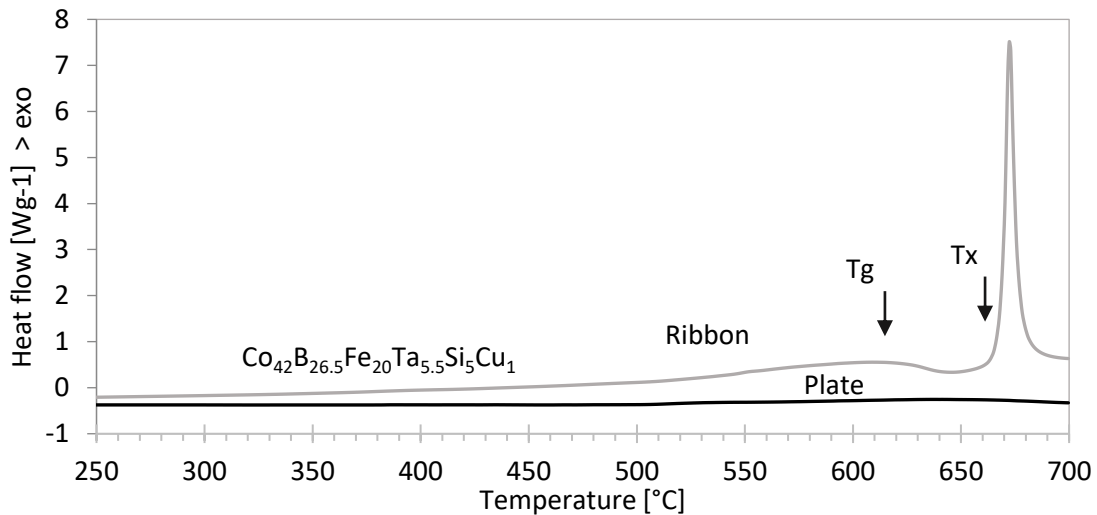


Fig. 73. Differential thermal analysis of cast plate

2.2.5. Nanoindentation

The hardness of the plate was 15.7 GPa and elastic module 322.5 GPa. The results are shown in Tab. 29.

Tab. 29. Results of the nanoindentation test of $\text{Co}_{42}\text{B}_{26.5}\text{Fe}_{20}\text{Ta}_{5.5}\text{Si}_5\text{Cu}_1$

Parameter Unit	Plate CoBFeTaSiCu	
	H_{IT} [GPa]	E_{IT} [GPa]
Mean	15.7	322.5
Standard deviation	1.3	28.0
Coefficient of variation [%]	8.2	8.7

H_{IT} - indentation hardness, E_{IT} - indentation elastic module

2.3. CoBFeTaSiCu cast ribbon

2.3.1. General view of material

The cast ribbon of $\text{Co}_{42}\text{B}_{26.5}\text{Fe}_{20}\text{Ta}_{5.5}\text{Si}_5\text{Cu}_1$ is shown in Fig. 74. The surface of the sample from both sides is shiny. No visible cracks.

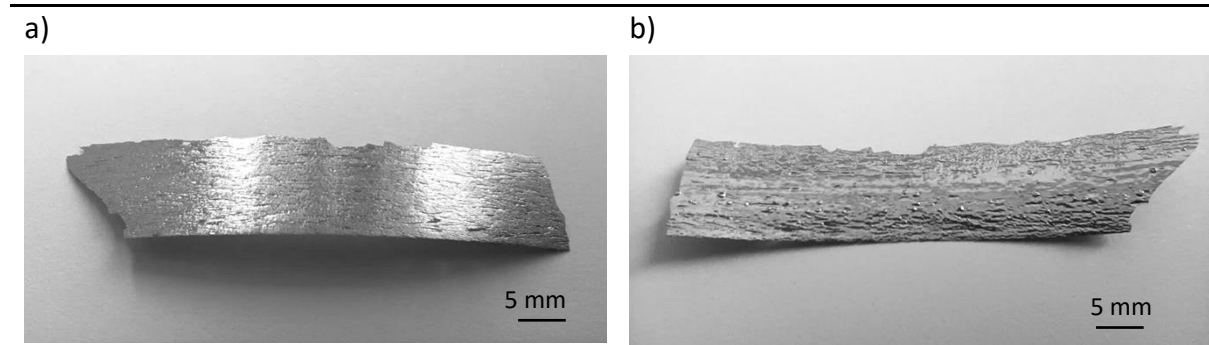


Fig. 74. $\text{Co}_{42}\text{B}_{26.5}\text{Fe}_{20}\text{Ta}_{5.5}\text{Si}_5\text{Cu}_1$ ribbon, surface view from the wheel (a) and from the top (b)

2.3.2. Scanning electron microscopy

The SEM images of fracture of $\text{Co}_{42}\text{B}_{26.5}\text{Fe}_{20}\text{Ta}_{5.5}\text{Si}_5\text{Cu}_1$ ribbon is shown in Fig. 75. BSE analysis shows the absence of second phase. The fracture surface shows typical for the metallic glasses mixed type of hackle zone and the smooth area.

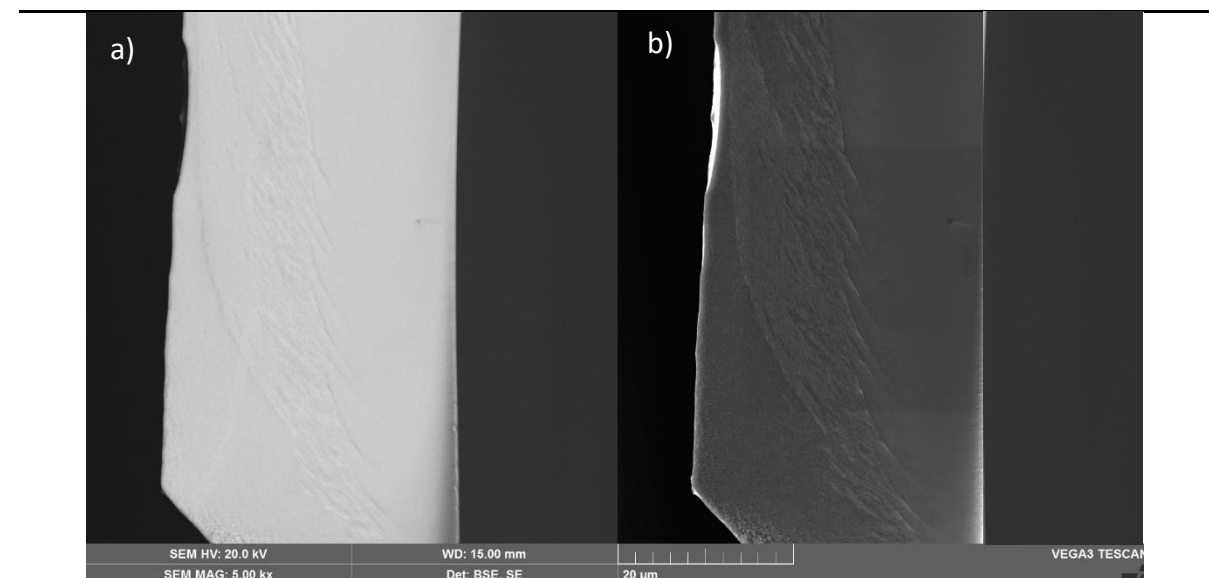


Fig. 75. SEM images of $\text{Co}_{42}\text{B}_{26.5}\text{Fe}_{20}\text{Ta}_{5.5}\text{Si}_5\text{Cu}_1$ ribbon with BSE a) and SE b) contrast

2.3.3. X-ray diffraction

The X-ray diffractogram of CoBFeTaSiCu ribbon shows an amorphous halo around $45^\circ 2\theta$. No other peaks were observed on XRD plot which is shown in Fig. 76.

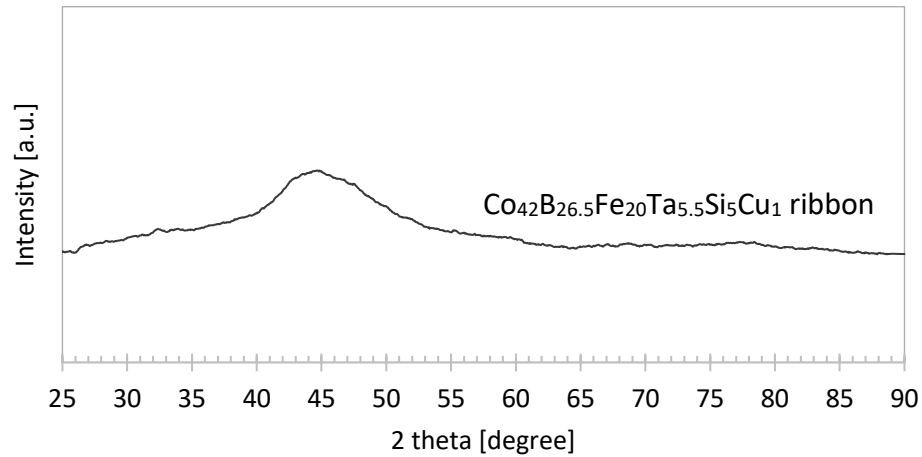


Fig. 76. X-ray diffractogram of Co₄₂B_{26.5}Fe₂₀Ta_{5.5}Si₅Cu₁ ribbon

2.3.4. Nanoindentation

The hardness of the plate was 15.1 GPa and elastic module 190.1 GPa.%. The results are shown in Tab. 30.

Tab. 30. Results of the nanoindentation test of Co₄₂B_{26.5}Fe₂₀Ta_{5.5}Si₅Cu₁

Ribbon CoBFeTaSiCu		
Parameter	H _{IT}	E _{IT}
Unit	[GPa]	[GPa]
Mean	15.1	190.1
Standard deviation	1.4	8.3
Coefficient of variation [%]	9.3	4.4

H_{IT} - indentation hardness, E_{IT} - indentation elastic module

2.4. CoBFeTaSiCu selective laser melting printed BMG

2.4.1. First stage of printing

General view

Macroscopic view of the printed Co₄₂B_{26.5}Fe₂₀Ta_{5.5}Si₅Cu₁ sample is shown in Fig. 77. Most of the samples from the 55 W and 75 W series seem to have developed successfully reaching a cuboid shape. The 95 W series had mainly destroyed samples. In some samples, the chipping of the material at the corners can be observed, as in the sample P75_v1800.

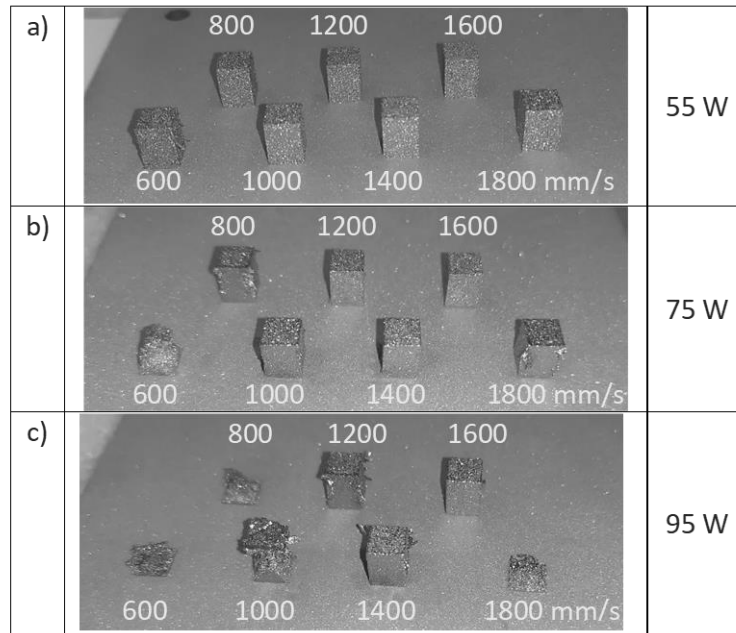
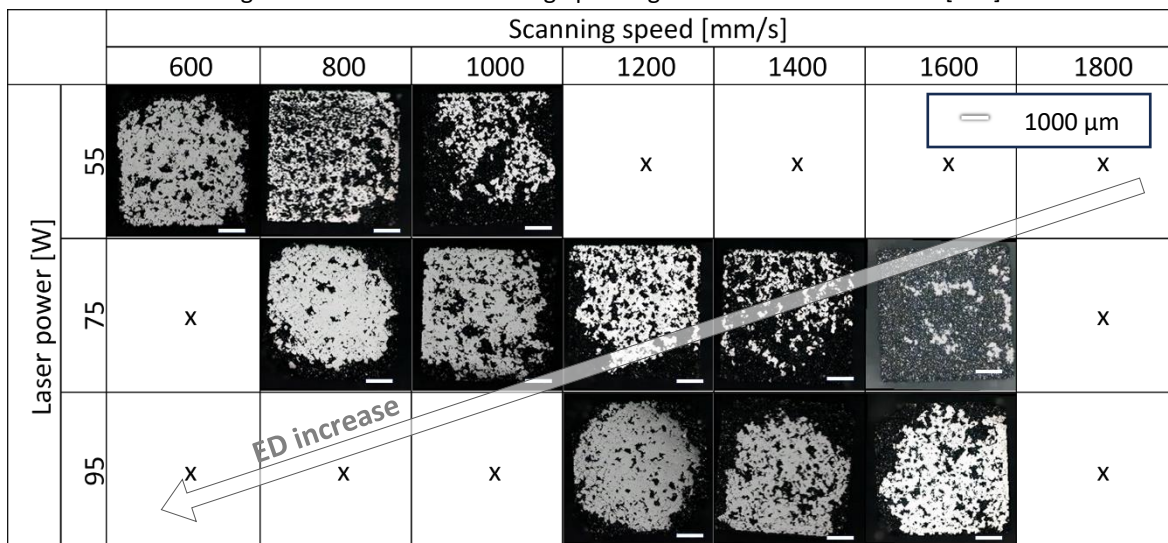


Fig. 77. Macro image of $\text{Co}_{42}\text{B}_{26.5}\text{Fe}_{20}\text{Ta}_{5.5}\text{Si}_5\text{Cu}_1$ samples (5 x 5 x 7 mm) from the first stage of an experiment. Laser power used for printing a) 55 W, b) 75 W, and c) 95 W [336]

Digital microscopic observation

In a cross-section view in Fig. 78 can be observed that most samples that had a clean external cuboid shape without any deformation have an inside defect of a lack of fusion. The effect of lack-of-fusion was manifested during cross section preparation as the removal of loosely bonded particles. Poor bonding was characteristic for the samples with the lowest ED (right upper corner of Fig. 78). Too high ED also failed at developing samples e.g. parameters P95_v600, P95_v800, P95_v1000, P75_v600 (left bottom corner of Fig. 78). The rest of the samples exhibit high porosity and presence of cracks. Analysis of the cross-section from this stage of printing leads to choosing the narrower range of the energy density for the second stage which is from 41 to 50 J/mm^3 .

Fig. 78. Results of the first-stage printing of $\text{Co}_{42}\text{B}_{26.5}\text{Fe}_{20}\text{Ta}_{5.5}\text{Si}_5\text{Cu}_1$ [336]



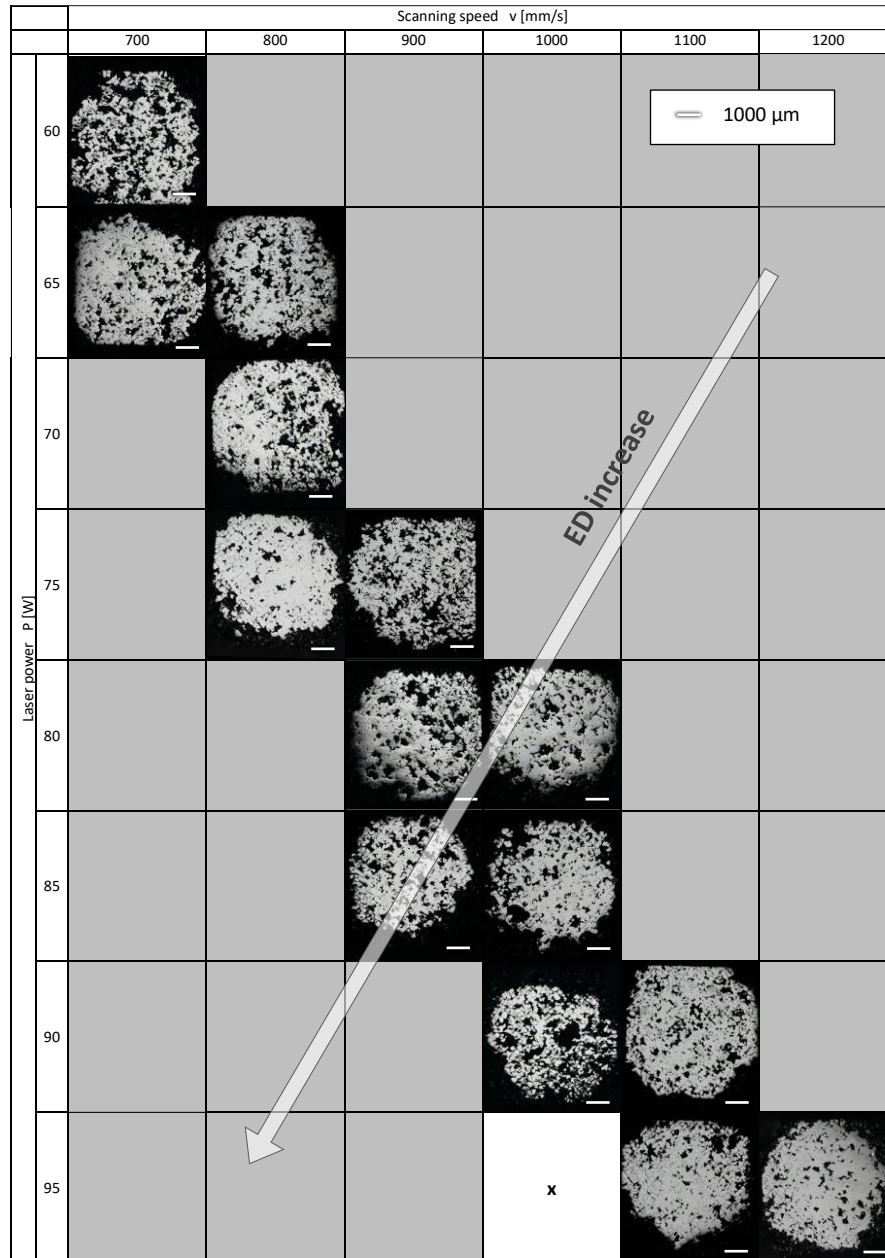
x- sample destroyed in the process

2.4.2. The second stage of printing

Digital microscopic observation

In this stage the scanning speed was changed by 100 mm/s and the laser power by 5 W. The rest of parameters, such as hatch spacing, layer thickness, and feedstock size, remain the same. The choice of range of energy density for a second stage experiment led to the manufacturing of all the samples (Tab. 31), except for P95_v1000 samples which had the highest ED. However, the P85_v900 sample with only 0.3 J/mm³ (0.6%) lower ED was successfully developed. Macroscopic observation of this sample showed a detachment of the corners, which occurred during the printing process. However, in the sample with the second-lowest energy, the corners also chipped off, but to a lesser extent. All samples exhibit a grid of cracks through the sample and a chipped corner that fractured during abrasive preparation of samples. The porosity takes a large area of all samples; the highest value of porosity area was observed for the P60_v700 and for the P90_v1000 sample, which had the ED 44.5 and 46.8 J/mm³, respectively, which are middle values for the second stage of the printing experiment. The lowest porosity area was observed for P75_v800, P95_v1100, and P95_v1200. The first two mentioned samples (P75_v800, P95_v1100) also had a middle value of ED while the last sample (P95_v1200) had the lowest ED, which led to discussion not only about the value of ED but also the influence of scanning speed and laser power, which will be taken in next chapter.

Tab. 31 Microstructure of the second printing stage of $\text{Co}_{42}\text{B}_{26.5}\text{Fe}_{20}\text{Ta}_{5.5}\text{Si}_5\text{Cu}_1$. Digital microscopy



x- sample destroyed in process, gray areas- parameters not tested

Density of samples measurements by the Archimedes method

To evaluate the porosity presence in the entire volume of samples (not only based on cross-section observation) Archimedes density calculations were performed. To check whether the density of samples is related to ED in the Tab. 32 matrix of values of both parameters are shown. The highest density of samples was observed for the P85_v900, P90_v1000, and P95_v1100 sample, which is 7.72, 7.70 and 7.69 g/mm^3 , respectively. These samples had the highest value of laser power and high energy density compared to the whole tested matrix. However, the samples P65_v700 and P75_v800 also had a high ED, but the density has a lower value of 7.56 and 7.59 g/mm^3 , respectively. Similarly, the lowest density was observed for the sample with relatively low laser power and medium or low ED- P60_v700 and P65_v800 7.37 and 7.42 g/mm^3 , respectively. These results coincide only partially with microscopic observation, which can have a few causes which will be discussed in the *Discussion* chapter.

Tab. 32. The second stage of the printing of $\text{Co}_{42}\text{B}_{26.5}\text{Fe}_{20}\text{Ta}_{5.5}\text{Si}_5\text{Cu}_1$ samples a) density of samples and c) calculated energy density (ED) [336]. Values are marked with color scale b)

a)

Density [g/cm ³]		Scanning speed v (mm/s)					
		700	800	900	1000	1100	1200
Laser power P [W]	60	7.4					
	65	7.6	7.4				
	70		7.5				
	75		7.6	7.6			
	80			7.6	7.5		
	85			7.7	7.6		
	90				7.7	7.6	
	95				x	7.7	7.6

highest

lowest

not tested

b)

c)

ED [J/mm ³]		Scanning speed v (mm/s)					
		700	800	900	1000	1100	1200
Laser power P [W]	60	44.5					
	65	48.2	42.2				
	70		45.5				
	75		48.7	43.3			
	80			46.2	41.6		
	85			49.1	44.2		
	90				46.8	42.5	
	95				49.4	44.9	41.1

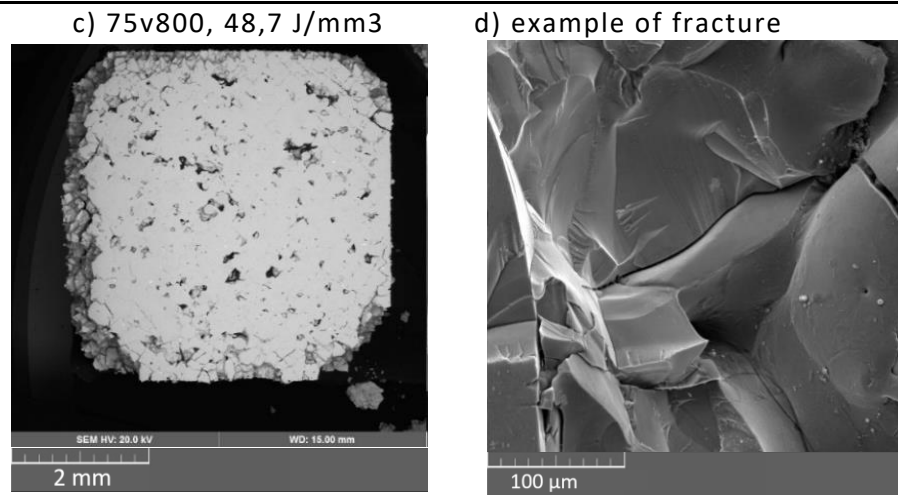


Fig. 79. SEM images of three chosen samples from the second stage of the printing of CoBFeTaSiCu (a-c) and example X-ray diffraction

XRD of samples with low, medium, and high energy density is shown in Fig. 80. Each of the samples tested exhibits a similar XRD plot with peaks in similar 2θ angles. In addition, the intensity of the peaks is similar for those three samples. Additional quantitative analyzes of the crystal phase (the Rietveld method) provided the amount of crystal phase 48%, 57%, and 54% for with sample P80_v1000 (low ED), P95_v1100 (medium ED), and P75_v800 (high ED), respectively. The pattern of XRD for printed $\text{Co}_{42}\text{B}_{26.5}\text{Fe}_{20}\text{Ta}_{5.5}\text{Si}_5\text{Cu}_1$ alloy correspondences to $\text{Co}_5\text{Si}_2\text{B}$ and TaB_2 phases.

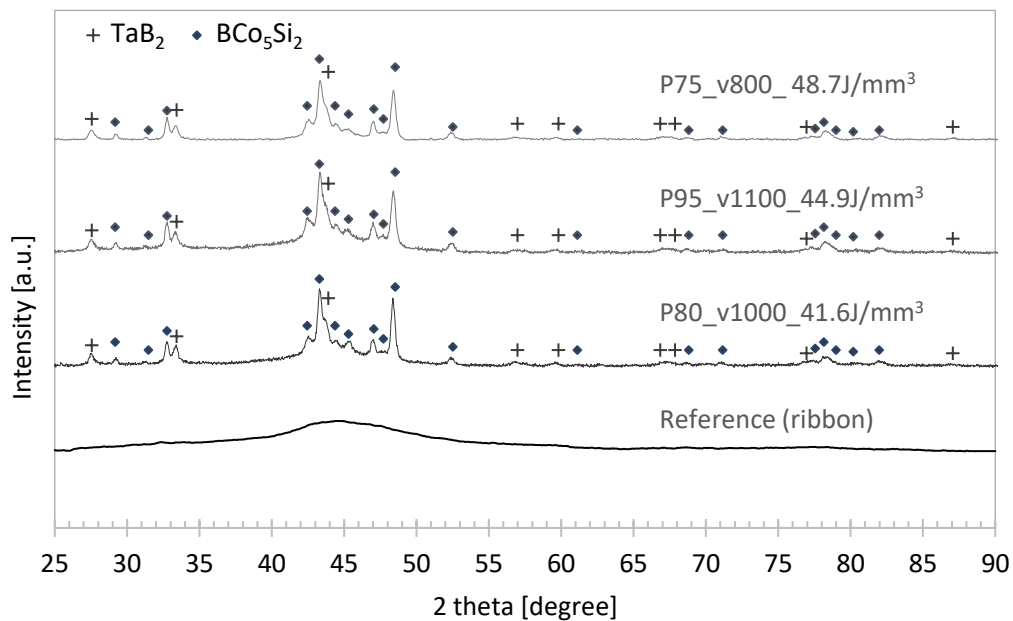


Fig. 80. X-ray diffractograms of $\text{Co}_{42}\text{B}_{26.5}\text{Fe}_{20}\text{Ta}_{5.5}\text{Si}_5\text{Cu}_1$ SLM samples

Nanoindentation

The nanoindentation results of P80_v1000, P95_v1100, and P75_v800 samples are shown in Tab. 33. Hardness ranges between 18.0 and 17.6 GPa. The elastic modulus ranges from 211.1 to 225.4 GPa. The differences in the hardness and elastic module values between samples are not significant and are in the range of standard deviation. Exact values are shown in Tab. 33.

Tab. 33. Results of the nanoindentation test of $\text{Co}_{42}\text{B}_{26.5}\text{Fe}_{20}\text{Ta}_{5.5}\text{Si}_5\text{Cu}_1$

	P80_v1000		P95_v1100		75W_800m/s	
Parameter Unit	H_{IT} (GPa)	E_{IT} (GPa)	H_{IT} (GPa)	E_{IT} (GPa)	H_{IT} (GPa)	E_{IT} (GPa)
Mean	17.9	211.1	17.6	223.1	18.0	225.4
Standard deviation	0.6	6.7	0.8	18.6	0.8	10.9
Coefficient of variation [%]	3.4	3.2	4.4	8.3	4.2	4.8

H_{IT} - indentation hardness, E_{IT} - indentation elastic module

Scanning electron microscopy and nanoindentation of 75W_800m/s

After conducting analysis on samples printed with different sets of parameters, sample P75_v800 was selected for more detailed measurements. This sample had a relatively good density (the lowest amount of porosity), correlated with fewer fracture materials on the observed surface and lowest fractures on corners of the sample. Detailed SEM observation revealed the grid of cracks on the surface of the P75_v800 sample. The cracks form a perpendicular grid, where the average distance between the closest parallel cracks was around 215 μm (Fig. 81 a). The higher magnification of the observed surface also showed the agglomerates of nanoscale precipitations, and several microscopic precipitations observed as brighter spots in SEM images with material contrast (Fig. 81 b). Precipitations crystallized in agglomerates in amorphous matrix, however, no regularity of those areas was observed and no connection with the grid of cracks was observed. The topography contrast (Fig. 81 c) showed that these precipitations seem to be above the rest of the observed surface. This suggests a higher hardness of precipitation than the rest of the matrix. An additional nanohardness test of the second phase confirmed its very high hardness, which was 24 GPa and the elastic module 320 GPa; for each value the standard deviation was at a level of $\pm 10\%$. EDS analyzes showed the concentrations of tantalum and boron in the described precipitations.

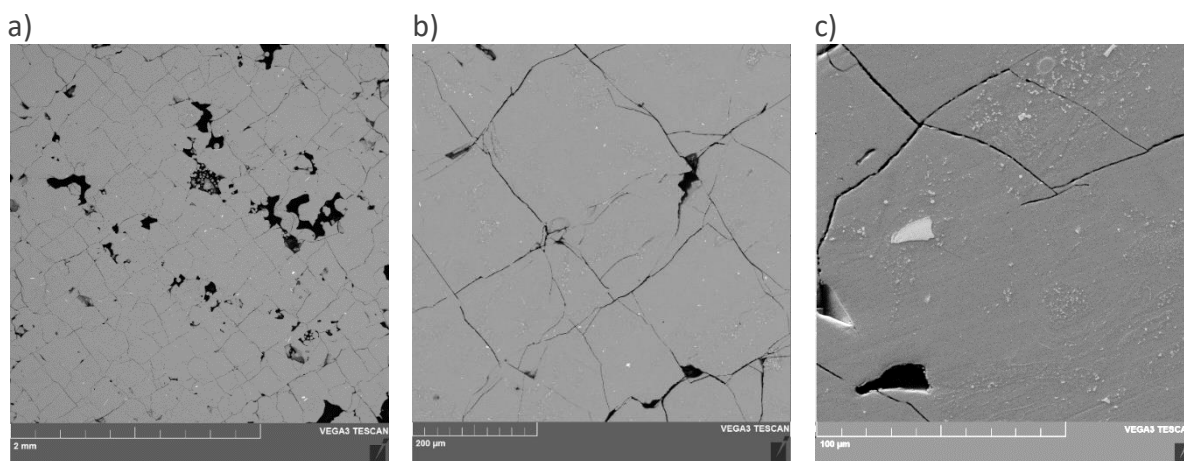


Fig. 81. SEM sample P75_v800 a) BSE contrast, x100, b) BSE contrast, x500, c) SE contrast, x1000

Differential scanning calorimetry

The DSC of $\text{Co}_{42}\text{B}_{26.5}\text{Fe}_{20}\text{Ta}_{5.5}\text{Si}_5\text{Cu}_1$ did not show the presence of T_g but an exothermic peak was registered with onset at 660°C . The mention plot is shown in Fig. 82.

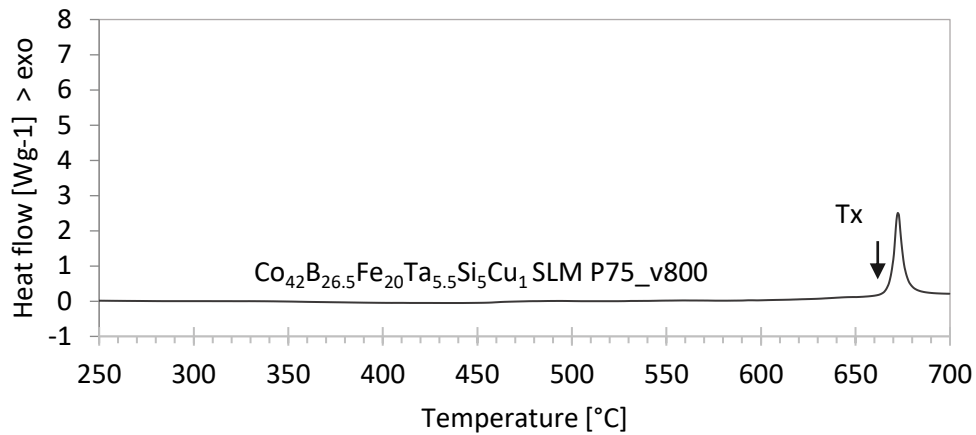


Fig. 82. Different scanning calorimetry of $\text{Co}_{42}\text{B}_{26.5}\text{Fe}_{20}\text{Ta}_{5.5}\text{Si}_5\text{Cu}_1$

Scanning transmission electron microscopy with an energy-dispersive spectroscope

Transmission electron microscopy (TEM) diffractograms are shown in Fig. 83 b) and c). The reference image is shown in Fig. 83 a). The tested lamella shows the homogeneous matrix with darker precipitations aligned in two lines. Diffractograms of the homogeneous area confirmed a fully amorphous structure by forming characteristic circles, while diffractograms of the area with precipitations exhibited mixed amorphous phase with the crystal phases observed as regular bright reflexes.

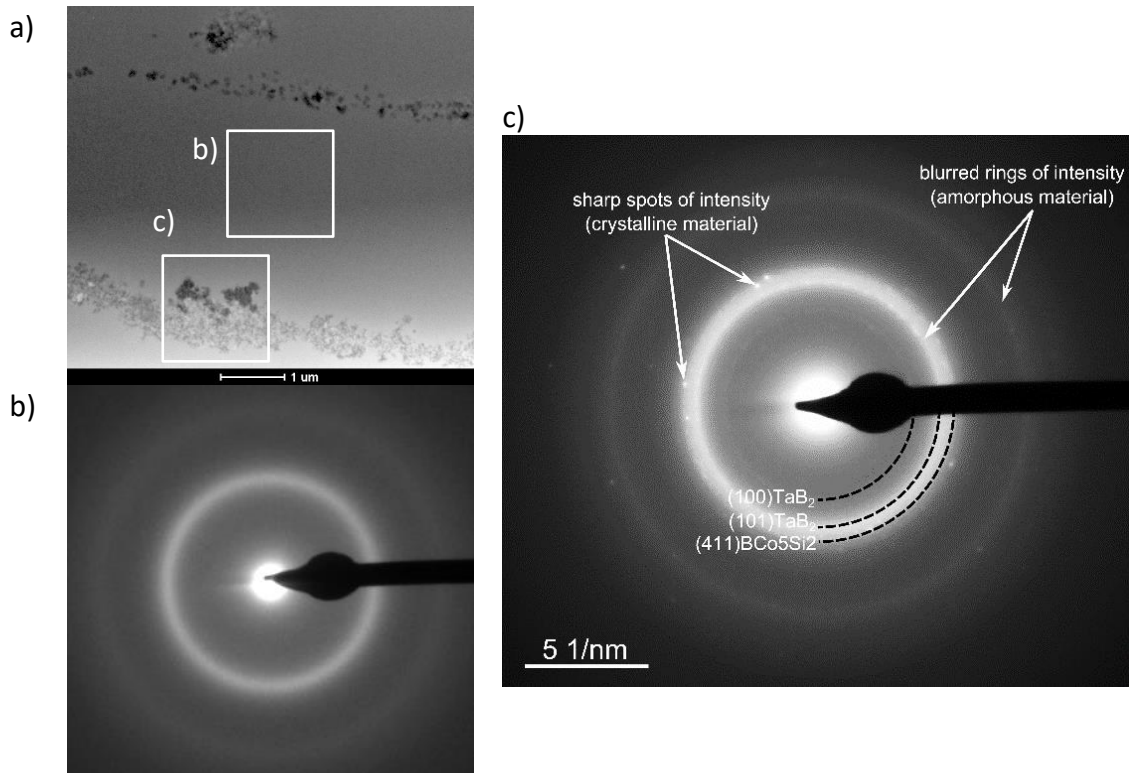


Fig. 83. Transmission electron microscopy (TEM) diffraction images of a) reference b) amorphous regions c) composite region

The results of energy-dispersive spectroscopy of the P75_v800 sample conducted with scanning transmission electron microscopy are shown in Fig. 84 a-f. The analyzed area (Fig. 84 g) concerned up to $4\ \mu\text{m}^2$ and it is the same as observed for the diffraction pattern in Fig. 83. The distribution of boron was homogeneous in the entire observed area, while the other chemical elements such as cobalt, iron, tantalum, silicon and copper were homogeneous only in the amorphous matrix. The precipitation mentioned above crystallized in line shows the concentration of three elements, namely tantalum, silicon, and copper. The remaining three elements (cobalt, boron, and iron) show absence in those precipitation.

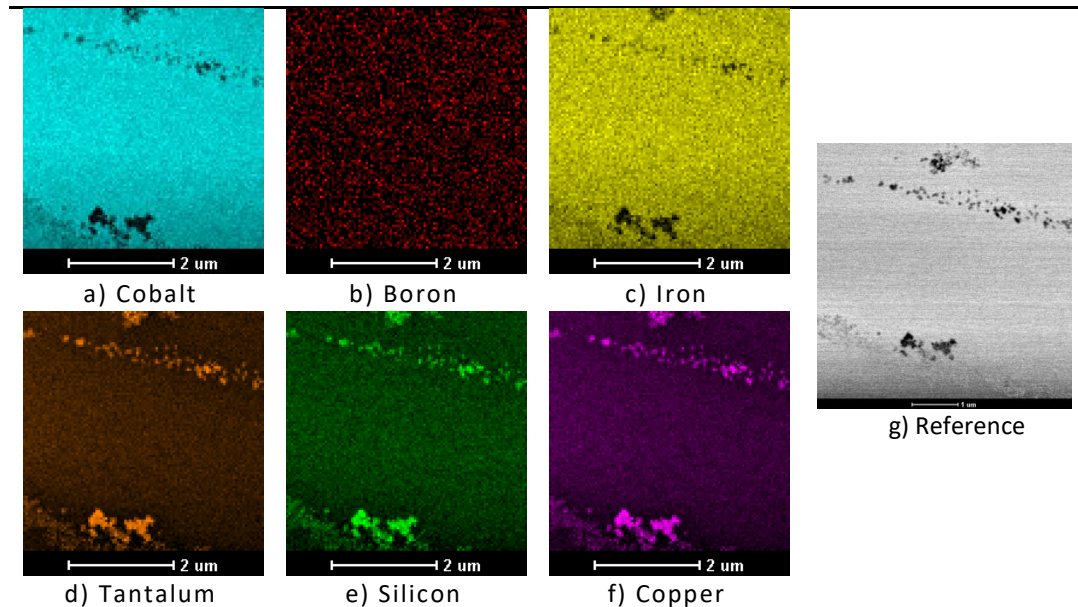


Fig. 84. Analysis of $\text{Co}_{42}\text{B}_{26.5}\text{Fe}_{20}\text{Ta}_{5.5}\text{Si}_5\text{Cu}_1$ P75_v800 BMG sample developed by SLM a)-f) energy dispersive spectroscopy (EDS) map conduct with scanning transmission electron microscopy (STEM), g) reference image

2.5. CoFeTaSiCu atmospheric plasma sprayed coating

2.5.1. General view of material

All three spraying distances used for plasma spraying allowed for the successful coatings deposition. In a Fig. 85 view of the sample prepared for wear resistance test is shown. All samples developed from CoFeTaSiCu powder, macroscopically looked similar, and show visible voids on the samples surfaces.

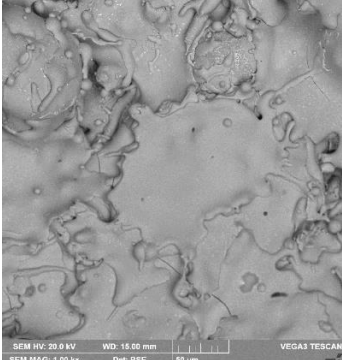
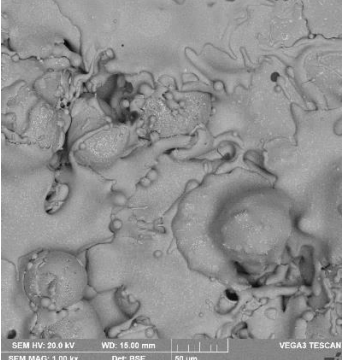
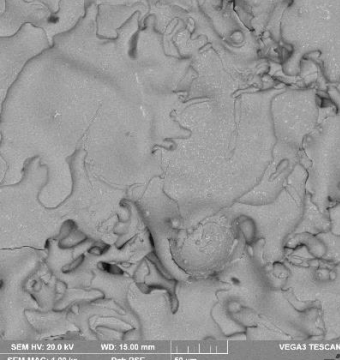
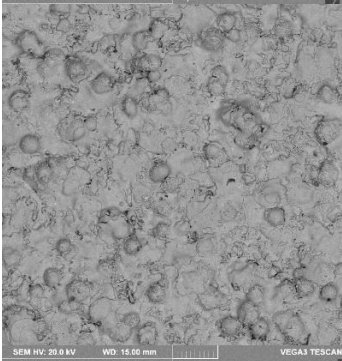
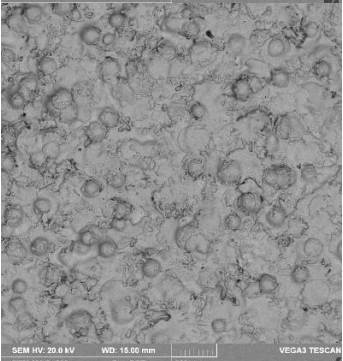
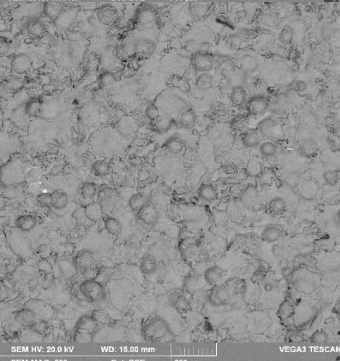


Fig. 85. Macroscopic image of the CoFeTaSiCu coating developed by atmospheric plasma spraying with polished surface (diameter 30 mm)

2.5.2. Surface view and roughness

The surfaces of the $\text{Co}_{42}\text{B}_{26.5}\text{Fe}_{20}\text{Ta}_{5.5}\text{Si}_5\text{Cu}_1$ plasma sprayed samples visually look similar. On the surface, both flat powder particles in the form of splats and more spherical particles that were only partially deformed during the depositing process could be observed. The roughness of the coatings sprayed with 90, 100 and 110 mm had similar values. The images of the surfaces of the samples and the roughness analysis are shown in the Tab. 34.

Tab. 34. Surface of atmospheric plasma sprayed samples $\text{Co}_{42}\text{B}_{26.5}\text{Fe}_{20}\text{Ta}_{5.5}\text{Si}_5\text{Cu}_1$

Spraying distance [mm]	90	100	110
SEM surface images			
			
R_a [μm]	17.1 +/- 1.1	16.5 +/- 1.3	16.7 +/- 1.0
R_z [μm]	101.6 +/- 3.1	100.3 +/- 8.9	98.5 +/- 4.5

2.5.3. Thickness and porosity analysis

An example of cross-section images of the plasma-sprayed coating captured with digital microscopy is shown in Fig. 86. This observation was used to measure the average thickness of the coatings. The results showed that the average thickness of the coatings was similar for all samples and oscillated between 320-360 μm. Additionally, the cross-section observation reveals defects such as delamination between particles and between the coating and the substrate and high porosity.

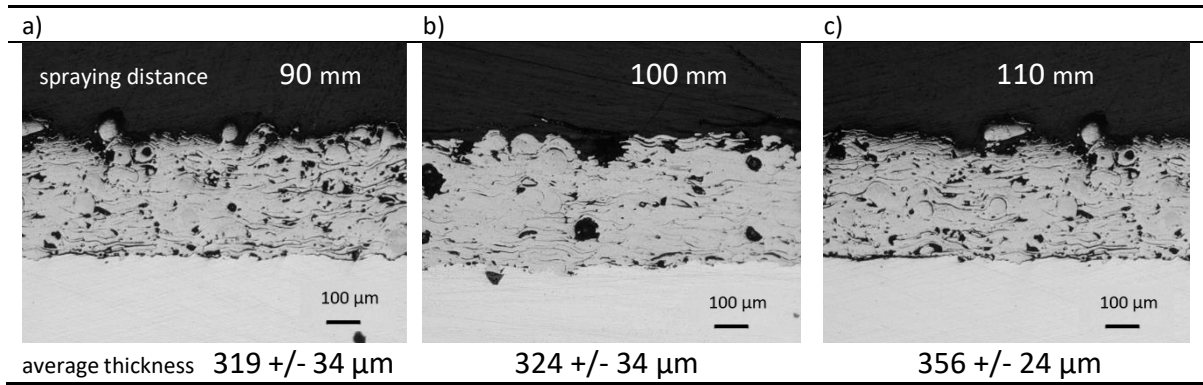


Fig. 86. Plasma spraying coatings of $\text{Co}_{42}\text{B}_{26.5}\text{Fe}_{20}\text{Ta}_{5.5}\text{Si}_5\text{Cu}_1$ developed with different spraying distance

The percentage of porosity observed in the coatings was analyzed based on the ten SEM captured images. For $\text{Co}_{42}\text{B}_{26.5}\text{Fe}_{20}\text{Ta}_{5.5}\text{Si}_5\text{Cu}_1$ coatings, it ranged from 8.5% to 11.2%. The samples sprayed with the lowest spraying distance obtained the lowest percentage of porosity, while samples with the larger distance also had a higher percentage of porosity. The exact measured values and examples of images used for porosity analysis are shown in Tab. 35.

Tab. 35. Porosity analyzed based on the SEM images of plasma sprayed coatings $\text{Co}_{42}\text{B}_{26.5}\text{Fe}_{20}\text{Ta}_{5.5}\text{Si}_5\text{Cu}_1$

Spraying distance [mm]	90	100	110
SEM images			
Porosity [%]	8.5	9.1	11.2
Standard deviation [% points]	0.5	0.6	0.9

2.5.4. X-ray diffraction

The X-ray diffraction analysis shows the presence of $(\text{Co}, \text{Fe})_2\text{B}$ and TaB_2 . The typical amorphous halo is absent. The plot of XRD is shown in Fig. 87.

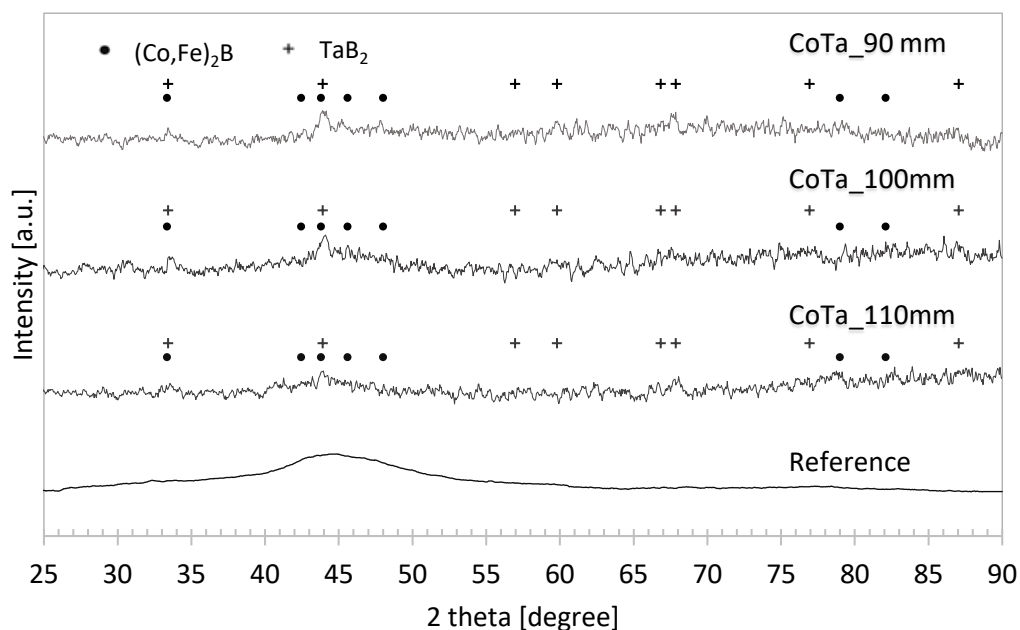


Fig. 87. X-ray diffractograms of plasma sprayed $\text{Co}_{42}\text{B}_{26.5}\text{Fe}_{20}\text{Ta}_{5.5}\text{Si}_5\text{Cu}_1$

2.5.5. Differential scanning calorimetry

The DSC of the coating showed the presence of an exothermal peak that has an onset at 590°C. The plot is shown in Fig. 88.

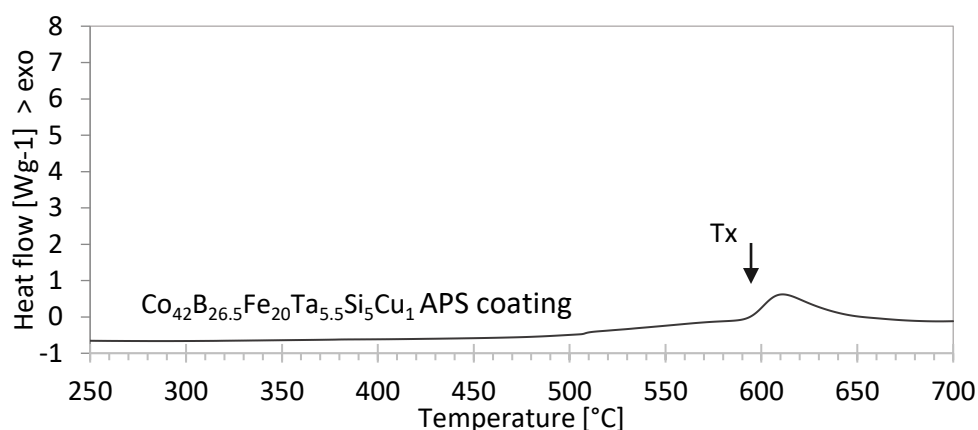


Fig. 88. Differential scanning calorimetry of plasma sprayed $\text{Co}_{42}\text{B}_{26.5}\text{Fe}_{20}\text{Ta}_{5.5}\text{Si}_5\text{Cu}_1$

2.5.6. Nanoindentation test

The hardness of all coatings had a similar hardness value in the range of 14.0 - 14.4 GPa. The indentation elastic module differs between the samples only in the standard deviation range and was in the range of 198.2 to 214.8 GPa. The values are shown in Tab. 36.

Tab. 36. Nanoindentation results of $\text{Co}_{42}\text{B}_{26.5}\text{Fe}_{20}\text{Ta}_{5.5}\text{Si}_5\text{Cu}_1$ coating developed via atmospheric plasma spraying

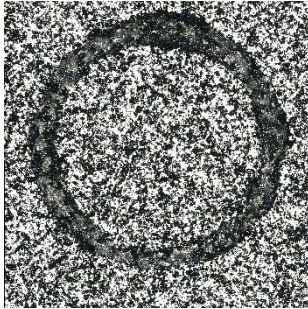
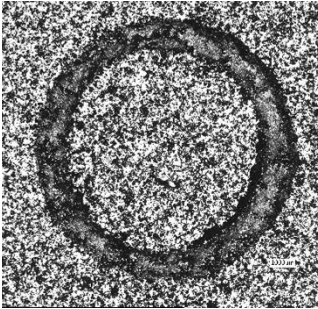
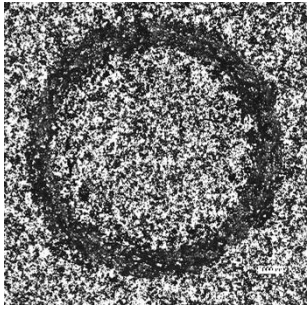
	CoTa_90		CoTa_100		CoTa_110	
Parameter	H_{IT}	E_{IT}	H_{IT}	E_{IT}	H_{IT}	E_{IT}
Unit	(GPa)	(GPa)	(GPa)	(GPa)	(GPa)	(GPa)
Mean	14.0	198.2	14.4	214.8	14.1	209.6
Standard deviation	0.9	14.5	0.9	11.1	1.1	14.2
Coefficient of variation [%]	6.4	7.3	6.1	5.2	8.1	6.8

H_{IT} - indentation hardness, E_{IT} - indentation elastic module

2.5.7. Wear resistance test

Samples after the test performed are shown in Tab. 37. The trace of ball on disk contact is irregular for all the samples. The cross-section area of the wear was on level of $10.0\text{--}10.2 \cdot 10^3 \mu\text{m}^2$.

Tab. 37. Surface of atmospheric plasma sprayed samples after wear test $\text{Co}_{42}\text{B}_{26.5}\text{Fe}_{20}\text{Ta}_{5.5}\text{Si}_5\text{Cu}_1$ % at

Spraying distance [mm]	90	100	110
Digital surface image			
Mean [μm^2]*	10001	10174	9969
Standard deviation [μm^2]	1868	1543	1322
Coefficient of variation [%]	19	15	13

* Mean area value of the cross section of the wear trace. The diameter of the trace equals 6 mm

Using the equation from *State of art* and *Research methods* chapters and the values of mean area of the cross sections from the Tab. 37, the specific wear resistances of the atmospheric plasma spray samples were calculated. The results are shown in Fig. 89. The value of W_s did not differ with changing the spraying distance of the APS. The value oscillates between 1.88 and $1.92 \cdot 10^{-5} \text{ mm}^3/\text{Nm}$ with a maximum standard deviation of $0.2 \cdot 10^{-5} \text{ mm}^3/\text{Nm}$.

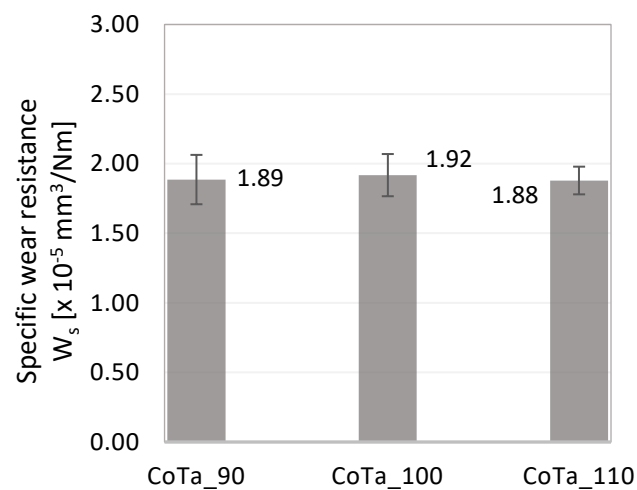


Fig. 89. Specific wear resistance of atmospheric plasma sprayed CoBFeTaSiCu alloy with high glass forming ability

VI. DISCUSSION

1. CoFeSiNb discussion

In this chapter, the discussion of the presented result from the previous chapter will be conducted. In this sub-chapter, all forms of the alloy $\text{Co}_{47.6}\text{B}_{21.9}\text{Fe}_{20.4}\text{Si}_{5.1}\text{Nb}_5$ are discussed starting from a powder used as feedstock for SLM and APS, then the reference cast plate, and next the bulk and coating samples obtained by SLM and APS, respectively.

1.1. CoFeSiNb atomized powder

The obtained powder has a typical amount of non spherical shaped particles for gas-atomized technic [343–345]. On the surface of the powder for fraction used for APS (50–80 μm) and SLM (20–50 μm) there was no visible presence of second phase in the SEM observation. The obtained powder has a typical Gaussian-like distribution for gas-atomized technic. No anomalies were observed [346]. For both fractions, positive (right) skewness was observed, suggesting that the D50 (median) is higher than the mean value of the powder sizes. Limiting the powder distribution sizes from D10 to D90 (deciles), the actual fraction sizes of feedstock are 18.2 - 54.8 μm for fraction used for SLM and 35.4 - 99.3 μm for APS. Powders 20–50 μm and 50–80 μm show low porosity, which is desired for SLM and APS. Homogeneity- the steady level of chemical elements across the particle- shows the lack of second phase in the powder. Very high homogeneity and no signs of oxidation increase the chance of obtaining the amorphous state of BMG and coatings [346].

An amorphous halo on the XRD plot indicates the presence of only SRO atmos. The structure is amorphous. Characteristic inflection of the DTA plot for a glass transition shows that powders in as-atomized state are fully amorphous and have a glassy state. The second, more intense, peak indicates the temperature of the first crystallization measured as an onset of this peak. The difference between the T_g and T_x is a popular measure of GFA, namely ΔT_x . For CoFeSiNb powder ΔT_x is 58°C. For alloys with the same composition, measured with the same heating rate (40°C/min) in work [321] and [99], the characteristic temperatures were the same, as shown in the Tab. 38. High ΔT_x points out a high disorder of atoms arrangement, which is usually obtained by a higher cooling speed while cooling from the liquid to the solid state. In Tab. 38 alloys with the same and similar chemical compositions to $\text{Co}_{47.6}\text{B}_{21.9}\text{Fe}_{20.4}\text{Si}_{5.1}\text{Nb}_5$ are listed. All presented alloys showed similar values of the characteristic temperatures.

Tab. 38. Thermal analysis of alloys like $\text{Co}_{47.6}\text{B}_{21.9}\text{Fe}_{20.4}\text{Si}_{5.1}\text{Nb}_5$

Form	Alloy (at.%)	T_g [°C]	T_x [°C]	ΔT_x [°C]	D_c [mm]	Reference
powder	$\text{Co}_{47.6}\text{B}_{21.9}\text{Fe}_{20.4}\text{Si}_{5.1}\text{Nb}_5$	598	656	58	x	this work
rod	$\text{Co}_{47.6}\text{B}_{21.9}\text{Fe}_{20.4}\text{Si}_{5.1}\text{Nb}_5$	580	635	55	5.5	[321]
rod	$\text{Co}_{47.6}\text{B}_{21.9}\text{Fe}_{20.4}\text{Si}_{5.1}\text{Nb}_5$	580	623	43	5.5	[99]
rod	$\text{Co}_{46}\text{Fe}_{20}\text{B}_{23}\text{Si}_5\text{Nb}_6$	599	654	55	4.5	[303]
ribbon	$\text{Co}_{47}\text{Fe}_{20.9}\text{B}_{21.2}\text{Si}_{4.6}\text{Nb}_{6.3}$	584	638	54	4	[320]
rod	$\text{Co}_{47}\text{Fe}_{20.9}\text{B}_{21.2}\text{Si}_{4.6}\text{Nb}_{6.3}$	584	639	55	4	[320]
rod	$[(\text{Co}_{0.6}\text{Fe}_{0.4})_{0.75}\text{B}_{0.2}\text{Si}_{0.05}]_{96}\text{Nb}_4$	549	592	43	4	[347]

x- not tested

Summary $\text{Co}_{47.6}\text{B}_{21.9}\text{Fe}_{20.4}\text{Si}_{5.1}\text{Nb}_5$ atomized powder

- SEM SE, BSE, EDS, XRD and DTA results unanimously indicate the amorphous and glassy state of powder
 - $T_g = 598^\circ\text{C}$, $T_x = 656^\circ\text{C}$, $\Delta T_x = 58^\circ\text{C}$
 - $H_{IT} = 14.8$ GPa
 - From XRD the halo peak has maximum at $46^\circ 2\theta$ (Cu $K\alpha$ irradiation)
 - 10-15% elongated particles
-

Obtained powder in sizes of $18.2 - 54.8 \mu\text{m}$ and $35.4 - 99.3 \mu\text{m}$ has a fully amorphous structure what was confirmed by the XRD, SEM and DTA results. The factors contributing to the amorphous state of the cast are:

- a) High glass forming ability of the $\text{Co}_{47.6}\text{B}_{21.9}\text{Fe}_{20.4}\text{Si}_{5.1}\text{Nb}_5$
 - the literature review showed that the D_c (5.5 mm) and ΔT_x (55°C) of alloy is high what was confirmed by the DTA results of the powder. That indicated that $\text{Co}_{47.6}\text{B}_{21.9}\text{Fe}_{20.4}\text{Si}_{5.1}\text{Nb}_5$ has a good glass forming ability
- b) Homogenization of the alloy before atomization process
 - the absence of the second phase indicates that the alloy was correctly homogenized in the alloying process and then fully melted before the atomization process.
- c) The cooling rate of atomization
 - the typical cooling rate of atomization is from 10^5 to $4.2 \cdot 10^3^\circ\text{C/s}$ [348], which ensure enough R_c to form amorphous structure from alloy with good GFA [349].

1.2. CoBFeSiNb cast plate

The discussion presented below concerns the casting of $\text{Co}_{47.6}\text{B}_{21.9}\text{Fe}_{20.4}\text{Si}_{5.1}\text{Nb}_5$ plate which is the reference sample for comparison with the innovative technologies for MG such as SLM and APS. The reference sample should be fully amorphous and show the typical mechanical properties for Co-based MG.

The cast plate has a shiny surface which is typical for the glassy state of the material, no cracks suggest that the residual thermal stress did not exceed the mechanical strength of the material. The cast plate is fully amorphous, there was no sight of second phase during SEM observation. Additionally, sample in which occurred crystallization tend to be very brittle and usually fractures in the process of cooling due to very high thermal stress driven by very high cooling rates needed to obtain amorphous structure [229]. Amorphous halo on the XRD plot indicate the presence only of SRO atmos. The characteristic inflection on the graph of DSC for a glass transition shows that the plate is fully amorphous and has a glassy structure. The second, more intense exothermic peak indicates the temperature of the first crystallization measured as an onset of this peak. The ΔT_x for CoBFeSiNb plate in this thesis equals 43°C . This value is exactly the same as for cast rods in work [99], also the T_g and T_x are almost the same. This confirms a similar combination of the casting condition (overheating, cooling rate [248]) and the purity of the chemical elements used for alloying in this thesis and in the mentioned work [99]. Because the described cast plate of $\text{Co}_{47.6}\text{B}_{21.9}\text{Fe}_{20.4}\text{Si}_{5.1}\text{Nb}_5$ is the reference sample, the hardness measurements for further form of the alloy will be refer to these values.

Summary Co_{47.6}B_{21.9}Fe_{20.4}Si_{5.1}Nb₅ cast plate

- SEM SE, BSE, EDS, XRD and DSC results unanimously indicate the amorphous and glassy state of plate
 - $T_g = 577^\circ\text{C}$, $T_x = 620^\circ\text{C}$, $\Delta T_x = 43^\circ\text{C}$
 - $H_{IT} = 15.6 \text{ GPa}$, $E_{IT} = 222.8 \text{ GPa}$
 - From XRD the halo peak has maximum at $46^\circ 2\theta$ (Cu K α irradiation)
-

The obtained cast is fully amorphous. The condition of casting and chemical composition allowed to suppress the crystallization leading to development of a plate that will be a reference samples for other technologies. Amorphous state of plate indicates that:

- a) High glass forming ability of the tested alloy
- the literature review showed that the D_c (5.5 mm) and ΔT_x (55°C) of alloy is high what indicates that Co_{47.6}B_{21.9}Fe_{20.4}Si_{5.1}Nb₅ has a good glass forming ability, which was confirmed
- b) Homogenization of the alloy before pouring into dies
- the absence of the second phase indicates that the alloy was correctly homogenized in liquid state before pouring into the dies.
- c) The cooling rate of pressure die casting
- the typical cooling rate of pressure die casting is from 10^2 to 10^3°C/s [350,351], which ensure enough R_c to form amorphous structure from alloy with good GFA [349].

1.3. CoBFeSiNb selective laser melting printed BMG

1.3.1. The first stage of printing

The ED was limited from 39 to 68 J/mm³ for developing Co_{47.6}B_{21.9}Fe_{20.4}Si_{5.1}Nb₅ by selective laser melting, supplies enough energy to establish connection of particles (lower limitation), and not lead to destruction through the thermal stress (upper limitation). ED values greater than 68 J/mm³ result in destroying the sample in the printing process. The thermal stress is generated during the solidification of the feedstock. After laser scan, at the top of the solidifying layer, tensile stress is generated, while at the bottom of the layer, the compression stress occurs as a result of the restriction of the neighboring layer [135,352]. If the residual stress exceeds the plastic strength, it leads to plastic deformation or brittle fracture for the alloys with limited plasticity, which is characteristic for the most Co-based metallic glasses [134]. The residual stress can accumulate during the manufacturing of the subsequent sample layers and be released in form of cracks later in the process.

The higher ED means a higher supply of thermal energy to the sample what lead to a increased volume of molten material. When the material starts cooling the shrinkage is larger and the residual stress is higher. That is why in samples with ED higher than 68 J/mm³ the problem of cracking and fracturing was more severe leading to destruction of them, as was observed for sample P95_v600. For samples with ED lower than 39 J/mm³ the particle joining problem occurred. Too low ED does not provide enough heat to sufficiently melt the layer of powder. If the offset of laser next scanning is too high for a set low ED, the molten pool does not fill the space between subsequent laser tracks leading to lack of joining in the whole

sample. Examples of those samples are P55_v1800, P55_v1600 and P75_v1800 which were not successfully developed in the process or were destructed in the abrasive preparation process.

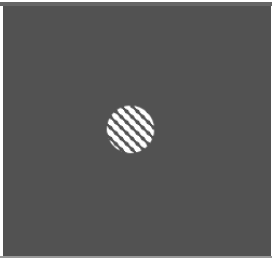


1.3.2. The second stage of printing

The types of porosity that were observed in samples from the second stage of an experiment were divided into three categories and showed in the Tab. 21. *Types of voids in the SLM samples* in chapter *Results*. The shape of A-type porosity indicates that its origin is a trapped gas and in the literature is called hydrogen or metallurgic porosity [44]. To reduce the possibility of metallurgic porosity, the feedstock should be dried before printing, and the atmosphere used for printing should be good quality. No significant difference in metallurgic porosity in the samples with ED between 39 and 68 J/mm³ shows that changing the parameters in that range does not influence the metallurgic porosity.

The shape of B type voids indicates the problem of not having enough filling of the layers with molten alloy. These types of voids are called lack-of-fusion porosity [126,353,354]. In the observations, it was shown that the number of these voids is larger for samples with a lower ED (closer to ED 39 J/mm³). A lower ED can lead to a thinner molten pool, which can be not wide enough for the set hatch distance. Furthermore, the literature showed the problem of a phenomenon called the balling effect, which is observed for low ED values. The balling effect is the result of breaking the continuity of the molten pool while scanning the material with the laser. The broken molten pool forms characteristic spherical shapes that minimize surface tension and surface energy for solidifying material [133,355,356]. In the article [357] the additional analyses of correlating ED with balling effect shows that samples with ED equal or lower ED than 23.8 J/mm³ shows the most intensified balling effect of the laser track. The same research showed the second type of laser track instability – fluctuating width when the ED was too high. In this case the ED was equal or higher than 82.3 J/mm³.

The shape and surface of the C-type porosity show that it has a secondary origin. The observed voids are fractures originated from severe cracks that were present in all samples. The number of fractures increased with ED. When the ED is higher, the residual stress amount in the developed sample increases, resulting in a higher cracks density [358]. The cracked material that fell off during the abrasive preparation is then observed as a fracture. The cracking problem can also be intensified by the impurities that can be present in the samples with lower ED despite the low residual stress in the samples. The impurities contribute to the stress accumulation due to the lack of continuity of the material. The impurity can be a second phase or a void. The second phase was not detected for the discussed MG, but the voids were observed and described above. The shape of the void influences the rate of stress accumulation. The pointy ending lack-of-fusion porosity tends to accumulate the stress and be notches in which the cracks start. The spherical shape of the metallurgic porosity does not influence stress accumulation so strongly, which is confirmed by the lack of metallurgic pores crossed by the observed cracks in the samples, while for the lack-of-fusion voids, many cracks and fractures were observed. These conclusions match the often observed mix of C-type voids with B-type (fractures and the lack-of-fusion porosity, respectively). The described analysis of type of voids observed for SLM process is shown in the Tab. 39.

Tab. 39. Types of voids in the SLM samples

Type of voids	Metallurgic (A type)	Lack-of-fusion (B type)	Fracture (C type)
Visualization			
Shapes	Symmetric, round, with diameter less than 20 μm	Irregular, rounded edges, often elongated, a wide scale of size	Rectangular or triangular shapes with sharp edges, a wide size scale
Origin	Trapped gas	Lack of material filling the layer	Fracture of the material caused by cracking
Cause	<ul style="list-style-type: none"> - poorly dried feedstock - low quality atmosphere, vacuum in the printing chamber 	<ul style="list-style-type: none"> - not fully melted layers of feedstock- to thin laser track to set hatch distance - balling effects - lack of stability of melt pool due to too combination of printing parameters (to low ED) - not even distribution of feedstock on printing layers (because of magnetization of power or due to defect of roller geometry) 	<ul style="list-style-type: none"> - too high thermal stress - low plasticity of the material leading to critical cracking of the material (low free volume, embrittlement caused due to the influence of HAZ etc.) - type of scanning pattern causing higher residual stress
Place of presence	Homogeneity in whole volume of samples	On the border of neighboring laser tracks	Parallel to the laser tracks

Density of samples analyzes shows the tendency for higher density with a higher ED used to develop the sample. The higher ED allows to lower the number of lack-of-fusion porosity, which influences the overall porosity of the sample represented as the higher density of samples. The correlation between density of samples and energy density is shown in the Fig. 90.

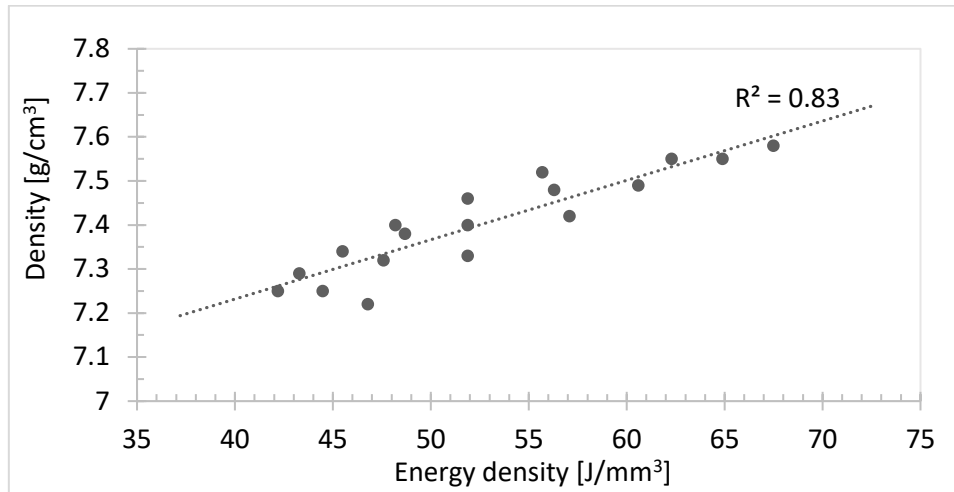


Fig. 90. Correlation between density of samples and energy density in the CoBFeSiNb samples printed with SLM

The SEM analysis of six samples representing the entire ED tested range confirmed the previous observation. Samples with lower ED show a high problem with lack-of-fusion porosity. Samples with high ED have only a singular lack-of-fusion porosities; however, the fracture occurred due to higher thermal stress from the higher amount of heat delivered. By comparison, the best sample, i.e., with lowest porosity and the best inner structure, seems to be the sample with the highest ED from restricted range by the first stage of printing which is P65_v500 (ED = 67,5 J/mm³). Study shows that ED range restrictions from the first stage of printing do not result in crystallization in any of the sample. The amorphous halo was presented in all samples and peaks at the same angle. Porosity and its origin change across the samples, the nanohardness and elastic modulus do not show significant differences between the samples even between 44.5 and 67.5 J/mm³. This observation matches the XRD observation that does not show any difference between the samples. The P65_v500 sample showed H_{IT} 15% lower than for the CoBFeSiNb plate, the E_{IT} was 35% lower. The decrease in these values could be the result of the influence of HAZ on the samples developed. Repeating thermal cycles below T_g can lead to relaxation of the structure and decrease the hardness of the sample [241].

The characteristic inflection on the plot of the DSC for a glass transition shows that the sample P65_v500 developed with 67.5 J/mm³ has a glassy phase. The ΔT_x is equal to 42°C, like for the CoBFeSiNb plate. However, value of T_g and T_x are higher of about 20°C. Articles [248–250] showed that for MG developed with different R_c in the glassy state range tend to have the same T_x value while T_g fluctuated - for lower R_c , the T_g was higher. TEM diffraction and STEM with EDS analysis confirm all before results that the P65_v500 samples have fully amorphous structure. Furthermore, no segregation of chemical elements was detected, indicating that mainly SRO structures are present in the Co_{47.6}B_{21.9}Fe_{20.4}Si_{5.1}Nb₅ SLM samples.

Summary Co_{47.6}B_{21.9}Fe_{20.4}Si_{5.1}Nb₅ BMG SLM

- SEM, XRD, STEM and DSC confirm the fully amorphous state, no segregation of chemical elements and the presence of glassy state
 - T_g equal 598°C and T_x equal 640°C
 - H_{IT} = 14.5 GPa, E_{IT} = 200.6, GPa
-

Manufacturing $\text{Co}_{47.6}\text{B}_{21.9}\text{Fe}_{20.4}\text{Si}_{5.1}\text{Nb}_5$ by SLM resulted in a fully amorphous material with a glassy state called BMG. The samples exhibited major cracking problems and a minor lack-of-fusion porosity, which was significantly reduced by adjusting the parameters of printing, such as laser power and scanning speed. The cracking problem is a known topic for researchers testing BMG based on Co-based alloys or based on other chemical elements [359,360]. The cracking occurs due to the very high thermal stress occurring during rapid solidification of the melt pool obtained with the high-density energy beam of the laser. In the literature to reduce that cracking problem, in addition to lowering the number of lack-of-fusion porosity (which can be indicators of releasing stress by initializing the crack), the change of scanning pattern or addition of the second plastic phase to BMG is proposed. The most promising results seem to be obtained for the chessboard scanning pattern, which can significantly reduce residual stress even twice according to [133]. Another researched option for reducing the cracking issue is the addition of ductile phase into MG which leads to developing the BMGC (bulk metallic glass composite). As the result the second, ductile phase with much lower plastic strength plasticity deforms absorbing the stress what suppress the eventual cracks. However, obtaining such structure is demanding using SLM. The most important conclusion about developing a BMG sample by SLM from $\text{Co}_{47.6}\text{B}_{21.9}\text{Fe}_{20.4}\text{Si}_{5.1}\text{Nb}_5$ is that the ED should be between 44.5 and 67.5 J/mm³. Additionally, the samples showing the best structure were developed with laser power 65 W, scanning speed 500 mm/s, layer thickness at 25 μm , hatch distance set at 77 μm from a powder 18.2 to 54.8 μm . The ΔT_x of the BMG obtained by SLM had values like those obtained by the reference method (casting). The hardness of the printed samples is 15% lower than the hardness of the plate, and the elastic modulus lower by 35%. Obtaining the first glassy structure of BMG Co-based with SLM is a novelty and is a great success of this Ph.D. study. The factors that influence the amorphous state of the alloy are:

- a) High glass forming ability of the tested alloy
 - obtained by the atomization fully amorphous powder and ΔT_x (42°C) of alloy indicates that $\text{Co}_{47.6}\text{B}_{21.9}\text{Fe}_{20.4}\text{Si}_{5.1}\text{Nb}_5$ have a good glass-forming ability what was confirmed by fully amorphous samples.
- b) Homogenization of the feedstock
 - absence of second phase in the powder was a positive indicator that obtaining BMG could be fully amorphous.
- c) The cooling rate of SLM
 - the cooling rate of SLM ranges from 10^4 to 10^7 °C/s [73–76] such high R_c ensures a very rapid solidification of molten pool because typically the 10^2 to 10^4 °C/s is needed for developing the MG.

1.4. CoBFeSiNb atmospheric plasma sprayed coating

The discussion concerns the coatings developed by the APS technology from $\text{Co}_{47.6}\text{B}_{21.9}\text{Fe}_{20.4}\text{Si}_{5.1}\text{Nb}_5$ alloy. Samples shows a typical rough surface for a thermal spraying [361,362], which gives no suggestion if the material is in glassy or crystallized state like it was possible for the cast plate. The surfaces of the CoBFeSiNb plasma sprayed samples visually are similar. The R_a : R_z values oscillate around 1:6, and similar values can be obtained after machining, making them moderate [363]. Characteristic flat, high surface splats representing good plasma spraying parameters were mixed with only partially deformed spherical-shaped

powder particles. Different behavior of the feedstock deposition may have origin in a wide size distribution. Used feedstock has diameters from 35.4 to 99.3 μm while the D50 was 59.2 μm . Particles with smaller diameter tend to accelerate more in the plasma jet and establish the maximum velocity earlier than the large particles. Additionally, the temperature of the smaller particles lowers much quicker with increasing distance from the plasma nozzle than for particles with higher diameter [364]. If the particles do not have enough kinetic or thermal energy the deposition rate of them may be low and it will be observed as a partial deformed particles while particles deposited with high enough energy will form splats [137]. The roughness of the coatings sprayed with 90, 100 and 110 mm had similar value, which suggests that changing the stand off distance from 90 to 110 mm does not influence much the deposition of the CoBFeSiNb by APS process. Coatings developed with lower values of the spraying distance showed lower porosity and a visibly smaller number of undeformed particles deposited (not melted in the process). During reducing the spraying distance from 110 to 90 mm, the porosity was reduced by 30%. Research [365] confirms that particles deposited with higher energy form the coating with lower porosity. In the above work, the higher energy was obtained by the higher power of plasma, while in this work the higher energy of particles seems to be connected to kinetic energy of particles which is increased by reducing the spraying distance. In mentioned work [364] the most sensitive to the loss of kinetic energy are the smaller particles which at the same time can be easier to melt properly in the plasma jet and form a coating with lower voids [153,366].

Absence of peaks on the XRD diffractogram confirms the SEM BSE observation. No second phase was observed for all coating developed by the atmospheric plasma spraying from $\text{Co}_{47.6}\text{B}_{21.9}\text{Fe}_{20.4}\text{Si}_{5.1}\text{Nb}_5$. The characteristic inflection point responding to T_g was equal to 620°C and the onset of the exothermic peak was at 650°C. That means the ΔT_x has a smaller value than for a casted plate of about 10°C, which suggests the higher order of atom arrangement in the coating than in the cast plate, however, the presence of the T_g confirms the presence of the glassy state of the material. Articles [248–250] showed that MG developed with the smaller R_c tend to have the same T_x value, while T_g fluctuated to higher values.

The H_{IT} of the coating was lower than the hardness of the plate by 9% and E_{IT} was 4.1% lower. The decrease of those value might be the result of the repeating cycles of heating the coating by deposition the partial or fully melted particles. The repeating thermal cycles below the T_g can lead to relaxation of the structure and decreasing the hardness of the coating [241].

The wear resistance of the coating has a moderate value. Changes in spray distance did not show an influence on wear rate in the tested range. The similar rate for Fe-based MG was established in [153]. The wear rate of $\text{Fe}_{43}\text{Cr}_{16}\text{Mo}_{16}\text{C}_{10}\text{B}_5\text{P}_{10}$ for the coating obtained from the powder D50 was equal to 66 μm for the same sliding distance, the same sliding velocity as in this thesis and twice the smaller load (10 N) was equal to $2.0 \cdot 10^{-5} \text{ mm}^3/\text{Nm}$. Other observations in the same work showed that reducing the size of the feedstock significantly reduced the porosity and the wear rate of the developed coating. For example, when the feedstock size was increased from D50 66 to 33 μm the wear rate decreased by around $1.0 \cdot 10^{-5} \text{ mm}^3/\text{Nm}$. Furthermore, when the feedstock size increased (D50 84 μm) the wear rate also increased to $2.5 \cdot 10^{-5} \text{ mm}^3/\text{Nm}$. Additionally, the change in the sliding speed also changed the value of the wear rate (a larger speed resulted in a larger wear rate even if the load was the same). Other literature testing of wear resistance using the ball-on-disk method with similar test parameters was done for the Zr-based alloy [367] [368]. In those works, the wear rate was 10 times higher than for the Co-based alloy tested in this work. To increase the

wear resistance of the coating (reduced the wear rate) in addition to the increase in its hardness, which the Co-based alloys already show, the plasticity could be improved. Research [369] showed that two MG coatings with the same hardness at the level around 540 HV showed different wear rates, which was associated with their mechanical behavior under the applied load by the sliding ball. The Cu-based MG coating that had a greater plasticity compared to the Ti-base coating showed a significantly lower wear rate. The plasticity of the Cu-based MG coating led to plastic deformation instead of fractures (which dominated in the Ti-based MG) in the contacted area of the ball, which led to slower wear of the coating.

Summary Co_{47.6}B_{21.9}Fe_{20.4}Si_{5.1}Nb₅ APS

- SEM, XRD and DSC confirm the fully amorphous state, no segregation of chemical elements and the presence of glassy state
 - T_g equal 577°C and T_x equal 620°C
 - $H_{IT} = 14.2$ GPa, $E_{IT} = 213.7$, GPa
 - Specific wear rate around $2.0 \cdot 10^{-5}$ mm³/Nm
-

The manufacture of Co-based MG coatings by the APS process was carried out successfully. The obtained coating showed a fully amorphous state with the presence of glassy structure. The issue that occurred in the coatings concerns the delamination that was observed in the volume of the samples. Changing the spraying distance positively affects the reduction in the porosity of the coating. However, it did not influence the hardness or the specific wear rate of them. A further improvement of the coating could include tests with smaller feedstock and enhancement of the plasticity of Co-based alloys. The fully amorphous state with the glassy structure of the coatings can lead to certain conclusions:

- a) High glass forming ability of the tested alloy
 - obtained by atmospheric plasma spraying samples were fully amorphous and ΔT_x equaled 43°C, which indicates that Co_{47.6}B_{21.9}Fe_{20.4}Si_{5.1}Nb₅ have a good glass-forming ability.
- b) Homogenization of the feedstock
 - the absence of a second phase in the powder was a positive indicator that the APS coating could be fully amorphous.
- c) The cooling rate of APS is high
 - the cooling rate of APS ranges from 10⁵-10⁷°C/s [144], such high R_c ensure a rapid solidification of molten feedstock because typically the 10² to 10⁴ C/s is needed for developing the MG. Additionally, the heat supplied by the deposited particles and the plasma jet (high enough spraying distance) did not lead to crystallization of coating.

2. Comparison of CoBFeSiNb samples

In this subchapter the summary of all forms of $\text{Co}_{47.6}\text{B}_{21.9}\text{Fe}_{20.4}\text{Si}_{5.1}\text{Nb}_5$ are collected and used for discussion about the hypothesis tested in this work. Fig. 91 shows the stage of comparison that the hypothesis concerns.

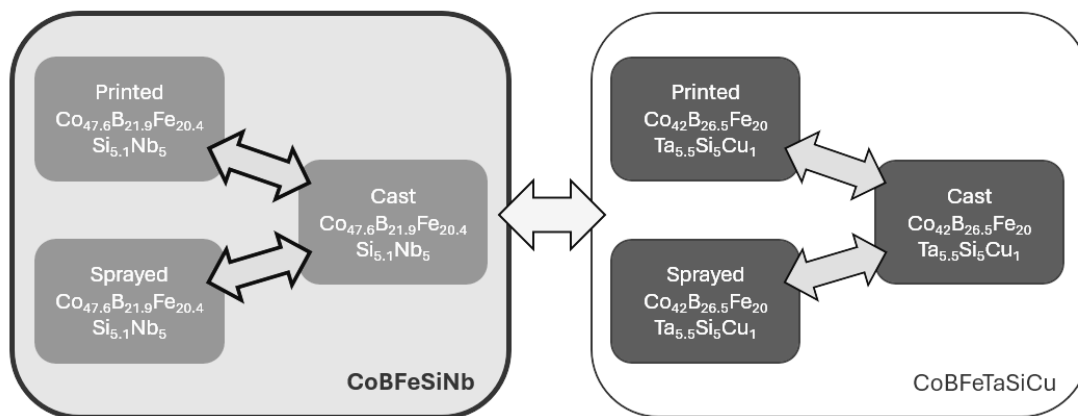


Fig. 91. Visualization of the conducted comparison of $\text{Co}_{47.6}\text{B}_{21.9}\text{Fe}_{20.4}\text{Si}_{5.1}\text{Nb}_5$

The first Ph.D. hypothesis constitutes the possibility that amorphous or amorphous nanocrystal structures can be developed by thermal spraying or by printing technologies from an alloy based on cobalt. No plasma spraying or SLM technologies were used for that purpose, which makes this an interesting topic for this research. The extensive studies and experiments confirmed the hypothesis presented, leading to the statement that Co-based alloys can be successfully developed into coating or bulk samples by method technologies and preserve not only the amorphous structure with nanocrystals but also the fully amorphous structure. That achievement was obtained for a $\text{Co}_{47.6}\text{B}_{21.9}\text{Fe}_{20.4}\text{Si}_{5.1}\text{Nb}_5$ (% at) alloyed from a pure chemical element and transformed into powder form by the gas atomization process. The powder form also showed a fully amorphous structure, and the publication of the properties of such a powder was also one of the first on a certain topic, which also makes it innovative research.

The second Ph.D. hypothesis states that it is possible to obtain the mechanical properties of newly developed form of the Co-based alloy in an amorphous/ amorphous with nanocrystal with values like those obtained by the traditional method of developing amorphous alloys, which is casting. The research showed that for the $\text{Co}_{47.6}\text{B}_{21.9}\text{Fe}_{20.4}\text{Si}_{5.1}\text{Nb}_5$ the decrease of hardness was registered comparing the new technologies to the casting. The decrease in hardness contributed to relaxation of the amorphous structure under heat transfer from SLM or APS processes without phase transformation. However, the difference in hardness is at the level of up to 9% for H_{IT} . These values are confirmation of the hypothesis that the Co-based alloy with fully amorphous structure developed with APS and SLM can have mechanical properties such as hardnesses on a level like those developed with casting.

For $\text{Co}_{47.6}\text{B}_{21.9}\text{Fe}_{20.4}\text{Si}_{5.1}\text{Nb}_5$ both scientific hypotheses were confirmed leading to valuable results for the mechanical engineering discipline and a valuable source of information for further studies concerning Co-based MG, especially for AM use. The collection of the most important and useful information is collected in Tab. 40.

Tab. 40. Summary of $\text{Co}_{47.6}\text{B}_{21.9}\text{Fe}_{20.4}\text{Si}_{5.1}\text{Nb}_5$ development technologies analysis

form	technology	T_g [°C]	T_x [°C]	ΔT_x [°C]	Structure	H_{IT} [GPa]	change	E_{IT} [GPa]	change	utility
plate	pressure die casting	577	618	41	amorphous glassy	15.6	ref	222.8	ref	solid structure no porosities size limitation
bulk	selective laser melting	595	645	50	amorphous glassy	14.5	-7.1%	200.6	-10.0%	cracked structure some fracture and porosities no size limitation
coating	atmospheric plasma spraying	608	650	42	amorphous glassy	14.2	-9.0%	213.7	-4.1%	delimitations porosities
powder	gas-atomization	598	656	58	amorphous glassy	14.8	-5.1 %	x	x	proper for AM and thermal spraying

3. CoBFeTaSiCu discussion

3.1. CoBFeTaSiCu atomized powder

The obtained powders of $\text{Co}_{42}\text{B}_{26.5}\text{Fe}_{20}\text{Ta}_{5.5}\text{Si}_5\text{Cu}_1$ have a typical Gaussian-like distribution for gas-atomized technology. No anomalies were observed [346]. For both fractions the positive (right) skewness was observed what suggest the D50 (median) is higher than the mean value of the powder sizes. Limiting the powder distribution sizes from D10 to D90 (deciles) the actual fraction sizes are 17.2 - 50.3 μm for fraction used for SLM, and 37.9 - 107.4 μm for APS. The obtained powders have a typical amount of non spherical shaped particles like for gas-atomized method [343–345]. On the surface of the powder for both fractions 50-80 μm and 20-50 μm the signs of second phase were observed. The SEM analysis of powders 20-50 μm and 50-80 μm showed low porosity what is desired for SLM and APS [370–372]. The fluctuation of chemical elements level across the particle done by the EDS analyses indicates that the local segregation in the powder took place. This observation is confirmed by cross-section images, where the presence of the second phase is visible in the form of white precipitation on the grey matrix. The phase is rich in tantalum and boron. The XRD analysis confirmed the SEM observation. The crystallization in the powder particles occurred. However, the crystals are suspended in the amorphous structure what is represented by the amorphous halo (SRO of atoms arrangements). The patterns of XRD show that the observed precipitations are $(\text{Co}, \text{Fe})_2\text{B}$ and TaB_2 . Alloys with similar chemical compositions also showed the presence of $(\text{Co}, \text{Fe})_2\text{B}$ [276,373] and TaB_2 [374]. Absence of inflection points on the DTA curve indicate absence of the glassy phase in the $\text{Co}_{42}\text{B}_{26.5}\text{Fe}_{20}\text{Ta}_{5.5}\text{Si}_5\text{Cu}_1$ powder, however the SEM observation results and the presence of amorphous halo on the XRD plot suggest presence of partially amorphous structure (SRO and MRO). Studies of the alloy with the same chemical composition in work [276], in form of cast rods, showed the presence of the T_g at 623°C. In this research the heating rate for the calorimetry test was set at 20°C/min what is twice smaller than in this thesis. The T_x measured in the [276] was 671°C what gives 48°C difference of T_x to this study. Such a high difference of the T_x onset can be the result of the inherited higher segregation of chemical elements in the tested powder than in rods from [276]. Collected values of characteristic temperatures for the powder and similar alloys are shown in Tab. 41.

The pre-segregated chemical elements in tested powder are corelated to lower free volume in the material and the higher amount of formed clusters and the presence of already nucleated crystal, which makes them prone to the further phase transition from amorphous to LRO structures [247,250]. Obtaining full amorphous structure from non fully amorphous powder requires strict conditions of manufacturing them. Research [375] confirms the possibility of obtaining fully amorphous structure by SLM printing using not fully amorphous powder. The value of measured nanohardness will be disused in the next chapter.

Tab. 41. Thermal analysis of $\text{Co}_{42}\text{B}_{26.5}\text{Fe}_{20}\text{Ta}_{5.5}\text{Si}_5\text{Cu}_1$

Form	Alloy	T_g [°C]	T_x [°C]	ΔT_x [°C]	D_c [mm]	Reference
powder	$\text{Co}_{42}\text{B}_{26.5}\text{Fe}_{20}\text{Ta}_{5.5}\text{Si}_5\text{Cu}_1$	-	595	-	x	this work
rod	$\text{Co}_{42}\text{B}_{26.5}\text{Fe}_{20}\text{Ta}_{5.5}\text{Si}_5\text{Cu}_1$	623	671	48	6	[276]
rod	$\text{Co}_{43}\text{B}_{31.5}\text{Fe}_{20}\text{Ta}_{5.5}$	637	709	72	2	[328] [175]
rod	$\text{Co}_{59}\text{B}_{33}\text{Ni}_2\text{Ta}_6$	347	685	38	2.5	[311]

‘x’ not measured, ‘-’ no data

Summary $\text{Co}_{42}\text{B}_{26.5}\text{Fe}_{20}\text{Ta}_{5.5}\text{Si}_5\text{Cu}_1$ powder

- SEM SE, BSE, EDS, XRD and DTA results indicate the presence of crystal precipitation phase in the amorphous matrix and absence of glassy state. The precipitations are $(\text{Co}, \text{Fe})_2\text{B}$ and TaB_2 .
- $T_x = 595^\circ\text{C}$, T_g not detected.
- $H_{IT} = 16.8$ GPa.
- From XRD the halo peak, maximum at $44\text{--}45^\circ 2\theta$ (Cu K α irradiation).
- 8% of elongated particles.

Obtained powders in sizes of $17.2 - 50.3 \mu\text{m}$ and $37.9 - 107.4 \mu\text{m}$ have an amorphous structure with nano precipitation of $(\text{Co}, \text{Fe})_2\text{B}$ and TaB_2 what was confirmed by the XRD, SEM and DTA results. Mention fractions were used respectively, for developing bulk samples and coatings. The factors contributing to the mixed structure of the powder are:

- Homogenization of the alloy before atomization process
 - the presence of Ta_2B in the powder can be the result of not fully homogenization of the alloy before atomization. This phase has a very high melting temperature above 2000°C which was not excited in the atomization process [376]. Additionally, the presence of crystals in the melt can increase the heterogeneous crystallization of other phases such a detected $(\text{Co}, \text{Fe})_2\text{B}$.
- The cooling rate of atomization
 - the typical cooling rate of atomization is from 10^5 to $4.2 \cdot 10^3^\circ\text{C/s}$ [348], which ensure enough R_c to form amorphous structure from alloy with good GFA [349].

3.2. CoBFeTaSiCu cast plate

The cracking of $\text{Co}_{42}\text{B}_{26.5}\text{Fe}_{20}\text{Ta}_{5.5}\text{Si}_5\text{Cu}_1$ cast plate indicates the presence of high thermal stress in the process of instant cooling. The non-shiny (mat) surface and the cracked structure suggest that the crystallization in the sample took place. However, on the very surface of the cast some shiny parts were observed, which indicates the presence of amorphous phase in the place where the colling speed was the highest, namely, the contact place of solidifying alloy with the copper die. According to [377] the cracking in crystalized sample occurs due to their lower fracture strength than the typical fully amorphous MG. In the tested Zr-based and Pd-based alloy the percentage of crystal phase in the amorphous matrix that significantly reduced the fracture strength was at level of 7% or more. Additionally, work [378] point out

that beside the lower fracture toughness of the crystal phase which can easily fracture under high thermal stress during high cooling rates, the reduction of the free volume in the amorphous matrix can occur what can lead to its embrittlement [379].

The SEM observation of cross-section of the fragments of the cast plate did not show the cracked structure, only the white precipitations were present similar to ones in the powder. The EDS analyses showed the increased presents of Ta and B, while the number of all other elements decreases. The Ta-B rich crystalline phases smaller than micrometer are homogenously present in the whole volume of sample but the larger ones in sizes from several micrometers to even 20 μm could be also observed. It is proposed that those large precipitations are the results of not fully homogeneous liquid alloy before the casting process in which the tantalum borides preserved solid form while the small precipitation are the effect of not high enough R_c of the process. Beside the Ta-B phase, the whole structure shows the presence of dendrites observed as a darker area. The XRD analyses confirmed the SEM observation, no amorphous halo indicates the absence or very low volume of amorphous phase. The observed sharp peaks indicate the presence of only LRO atoms forming the $(\text{Co}, \text{Fe})_2\text{B}$ and TaB_2 phases. Those phases were also detected in powder, however the in the plate these peaks are much more intense, and the number of peaks is higher in the same measured range of 2 theta angle. Alloys with similar chemical compositions showed the presence of $(\text{Co}, \text{Fe})_2\text{B}$ [276,373] and TaB_2 [374]. No presence of peaks on DSC plot confirmed the absence of the amorphous phase, also no presence of T_{x1} that was registered up to 750°C for powder suggest that the alloy in form of plate is fully crystalized.

Values of nanoindentation test need to be discussed by comparison with results obtained with similar parameters. The hardness of the plate seems to be like the hardness of the powder while the elastic modulus is very high. That high value is probably owe to the tantalum borides present in the whole volume of plate which show were high values of elastic modulus [380,381].

Summary $\text{Co}_{42}\text{B}_{26.5}\text{Fe}_{20}\text{Ta}_{5.5}\text{Si}_5\text{Cu}_1$ plate

- SEM SE, BSE, EDS, XRD and DSC results indicate the absence of neither glassy nor amorphous state of the plate.
 - The detected phases are $(\text{Co}, \text{Fe})_2\text{B}$ and TaB_2 .
 - T_g , T_x not detected.
 - $H_{IT} = 15.7 \text{ GPa}$, $E_{IT} = 322.5 \text{ GPa}$
-

Casting of the plate from $\text{Co}_{42}\text{B}_{26.5}\text{Fe}_{20}\text{Ta}_{5.5}\text{Si}_5\text{Cu}_1$ alloy resulted in fully crystalline structure what eliminated it to be the reference sample to which the samples developed via SLM and APS will be compared to. The detected phases were $(\text{Co}, \text{Fe})_2\text{B}$ and TaB_2 . Factors that combined could result in the crystal state of plates are:

- a) Not high enough glass forming ability of the tested alloy
 - literature review showed that the D_c and ΔT_x of alloy are high, in conclusions the $\text{Co}_{42}\text{B}_{26.5}\text{Fe}_{20}\text{Ta}_{5.5}\text{Si}_5\text{Cu}_1$ should have a good glass-forming ability. However, the presence of not melted and homogenized Ta_2B in master alloy can lead to doubt if the chemical composition of tested alloy is not reduced in Ta and B. This reduction of those elements in cast alloy could lead to different GFA than state in the literature.

- b) Not fully homogenized alloy before pouring into dies
 - this could result in heterogeneous crystallization which happens easier than in fully homogeneous structure. The heterogeneous crystallization usually happens faster than from nucleus in homogeneous volume because the presence of impurities (unmelted Ta-B particles in this work) reduced the energy needed to form critical nucleus [382]. Research showed that presence of the unmelted particle can lead to crystallization of the alloy even when the R_c is very high [242–245].
- c) The cooling rate of pressure die casting is too small to develop amorphous structure
 - the typical cooling rate of pressure die casting is from 10^2 to 10^3 °C/s [350,351], which is high enough to form amorphous structure from an alloy with a good GFA [349]. Also, in this work the confirmation of the good R_c is successfully using the same technology the same devices and copper die to develop the fully amorphous CoBFeSiNb plates, leading to the conclusion that the issue of developing fully amorphous structure of $\text{Co}_{42}\text{B}_{26.5}\text{Fe}_{20}\text{Ta}_{5.5}\text{Si}_5\text{Cu}_1$ concerns the mentioned above reasons like to low GFA of developed alloy in this work.

3.3. CoBFeTaSiCu cast ribbon

The shiny surface of the $\text{Co}_{42}\text{B}_{26.5}\text{Fe}_{20}\text{Ta}_{5.5}\text{Si}_5\text{Cu}_1$ ribbon suggests the amorphous state of the sample. Absence of cracks suggests that the residual stress occurred during the solidification does not exceed the mechanical strength of the material. The SEM images of fracture of $\text{Co}_{42}\text{B}_{26.5}\text{Fe}_{20}\text{Ta}_{5.5}\text{Si}_5\text{Cu}_1$ ribbon show typical mixed type surface that contains smooth area called a mirror area and the typical hackle zone that can also be called river pattern or fish scale pattern. This mixed type of fracture indicates the absence of second phase and the glassy structure of the ribbon [329,383]. The smooth area corresponds to a brittle fracture while the fish pattern presents the single shear bands corresponding to a very low plasticity present in very hard MG.

The XRD analysis confirmed the SEM observation. The amorphous halo on the XRD plot indicates the presence of amorphous structure and no other peaks show the absence of the second phase. The DSC analyses showed typical inflection for transition from glassy state to non glassy state in the heating process. The value of T_g is close to the value that was register in literature for this alloy which is 623°C [276]. The ΔT_x value from this thesis is 50°C and matches to value from the [276] where the ΔT_x is 48°C. Those values suggested that there is possibility to obtain amorphous structure from alloy $\text{Co}_{42}\text{B}_{26.5}\text{Fe}_{20}\text{Ta}_{5.5}\text{Si}_5\text{Cu}_1$ by other manufacturing technologies. Furthermore, the absence of the Ta_2B phase indicates the proper homogenization of the alloy before pouring it into the wheel where the material solidifies in the melt-spinning technology used.

The hardness of the ribbon is much lower than the hardness of the fully crystallized plate and partial crystallized powder which has the highest hardness. Highest hardness for the samples with nano-crystallization like in powder form of alloy in literature is attributed to hardening by a solid solution or interaction between phases boundaries (amorphous and crystal)[328,384,385]. Hardness of the plate, which is fully crystallized, correspond to the hardness changes during annealing of the Fe-based MG [386]. After the first increase of the hardness by the annealing of the sample, the value starts to decrease to finally drops below the initial value. In work [386] the decrease of hardness in later stage of annealing is connected

to the increased of the grain size. The changes described in $\text{Co}_{42}\text{B}_{26.5}\text{Fe}_{20}\text{Ta}_{5.5}\text{Si}_5\text{Cu}_1$ alloy are shown in Tab. 42.

Tab. 42. Hardness comparison of CoBFeTaSiCu

	H_{IT} (GPa)	change	E_{IT} (GPa)	change	structure
Powder	16.8	+11.3%	x	x	amorphous + crystal
Plate	15.7	+4.6%	322.5	+69.7%	fully amorphous
Ribbon	15.1	0	190	0	amorphous and glassy

Summary of $\text{Co}_{42}\text{B}_{26.5}\text{Fe}_{20}\text{Ta}_{5.5}\text{Si}_5\text{Cu}_1$ ribbon

- SEM SE, BSE, EDS, XRD and DSC results indicate the absence of second phase and the glassy state of the ribbon
- $T_g = 615^\circ\text{C}$, $T_x = 665^\circ\text{C}$
- $H_{IT} = 15.1$ GPa, $E_{IT} = 190.1$ GPa

The results of ribbon tested confirm its amorphous and glassy state. For those reasons the reference sample to which the SLM and APS results will be compared to validate the hypothesis of the PhD in later chapter. Discussing the same issues that were debated for the $\text{Co}_{42}\text{B}_{26.5}\text{Fe}_{20}\text{Ta}_{5.5}\text{Si}_5\text{Cu}_1$ plate, the ribbon form prepared by the melt spinning had a fully amorphous structure what indicates that:

- High enough glass forming ability of the tested alloy
 - the $\text{Co}_{42}\text{B}_{26.5}\text{Fe}_{20}\text{Ta}_{5.5}\text{Si}_5\text{Cu}_1$ has a high enough glass forming ability to form homogeneous, glassy structure by the melt spinning technologies
- Good homogenization of the alloy before pouring into the wheel
 - alloy was homogenized properly and formed a structure that does not show the presence of Ta_2B phase, which was observed for all the previous tested form of alloy (powder and plate)
- Cooling rate for the melt spinning is high enough to form the glassy structure
 - R_c for melt spinning according to [387] ranges from $4 \cdot 10^4$ to 10^6 $^\circ\text{C/s}$ which was high enough to form fully amorphous and glassy structure from $\text{Co}_{42}\text{B}_{26.5}\text{Fe}_{20}\text{Ta}_{5.5}\text{Si}_5\text{Cu}_1$ alloy.

3.4. CoBFeTaSiCu selective laser melting printed BMG

3.4.1. The first stage of printing

Macroscopic observation of the $\text{Co}_{42}\text{B}_{26.5}\text{Fe}_{20}\text{Ta}_{5.5}\text{Si}_5\text{Cu}_1$ sample from the first stage of the printing showed that high laser power (95 W) causes degradation of the samples. In addition, the small scanning speed has similar results. The samples of series 75 W and 55 W did not show macroscopic defects; however, the macroscopic observation revealed that samples with ED smaller than 41 J/mm^3 did not have enough joining of the feedstock. Too low ED does not supply enough heat to melt enough area on the laser track. If the offset of the

next laser track is larger than the width of the melt pool, the joining problem occurs. In addition to the lack of joining, in voids partial melted feedstock can be observed. Samples with energy greater than 50 J/mm³ were also destroyed in the printing process due to excess energy. Higher ED means a higher supply of thermal energy to the sample that implies a higher volume of melt pool. When the materials start to cool, the shrinkage increases and the residual stress increases [358].

3.4.2. The second stage of printing

The Co₄₂B_{26.5}Fe₂₀Ta_{5.5}Si₅Cu₁ samples from the second stage of printing, restricted by the ED from the results from the first stage, show the cracking problem and porosity. Those phenomena were present in all samples, but to different extents. The same three types of voids were detected for the first alloy (Co_{47.6}B_{21.9}Fe_{20.4}Si_{5.1}Nb₅) and are described in the Tab. 39. Types of observed voids are lack-of-fusion porosity, metallurgic porosity and fractures. Lack-of-fusion porosity was present in all samples, but the highest number was present in samples with low ED, like sample P80_v1000. Metallurgic pores were detected in all samples, but in very small amounts and rarely were crossed by cracks, which led to the conclusion that the argon atmosphere was of good quality (no impurities, e.g., H₂O) and the powder was sufficiently dried before printing. Fractures connected with higher heat input were mostly detected in samples with highest ED- P95_v1000, P85_v900, and P75_v800. Density of sample analyzes show a tendency for higher values with a higher ED used to develop the sample. Higher ED lets the number of lack-of-fusion porosity decreases, which positively influences the value of the density. Some samples, however, do not follow the described tendency. This disorder is caused by a cracking problem of samples that can influence the density of samples measurements using the Archimedes method.

The analysis of selected samples representing the tested range of ED (low, medium, and high ED) confirms the previous expectations. The sample with the highest ED showed more fractures due to the higher thermal stress due to the higher amount of heat delivered. Meanwhile, the sample with low ED shows a larger problem with lack-of-fusion porosity. By comparison, the best sample, i.e., with lowest porosity and the best inner structure, seems to be the sample with the second highest ED from restricted range by the first stage of printing, which is P75_v800 (ED = 48,7 J/mm³).

The XRD analysis showed the phase Co₅Si₂B which was not detected in other form of the alloy in this thesis, but was present in the MG with similar chemical composition [388,389]. The second crystal phase detected in BMG was Ta₂B, observed also in powder and the plate form of the CoBFeTaSiCu alloy. The similar amount of crystal phase in the samples from 41 to 49 J/mm³ indicates that in this range of the ED does not influence the degree of crystallization. It also shows that SLM process still maintains the Ta₂B phase present in the feedstock while the Co₅Si₂B phase was developed.

The hardness of the BMG is 19% higher than for ribbon, the elastic modulus is also 19% higher. Hardening of the amorphous material by the nano-crystallization is a mechanism of hardening by a solid solution or by the interaction between phases boundaries (amorphous and crystal) [328,384,385]. Crystallization led to an increase in the overall hardness of the BMGC. Additionally, the very high hardness of crystalized Ta₂B may also increase the average measured hardness of the prints [374,381].

Analyses of the SEM image P75_v800 sample showed the nanosized Ta₂B precipitation in whole volume of the sample, suggesting the problem of the crystallization similar that was observed in the powder form of CoBFeTaSiCu. However, crystallization occurred in half of the volume of the material, and the precipitations are mostly nanoscale. Some of the larger Ta₂B were large enough to be tested with nanoindentation. The hardness of them was higher than the hardness of the powder or ribbon, which could increase the average hardness of the material. The absence of inflection or exothermal peaks on the DSC plot confirmed that the material was not in a glassy state, and at least the first crystallization observed for the reference material (ribbon) had already occurred.

The diffraction patterns obtained by TEM confirmed the result from XRD of the presence of both amorphous and crystal phases. The EDS mapping of elements suggests the segregation of Cu, Ta and Si. Those elements were observed in other studies as a combination of phases such as: Cu₃Si+Si+TaSi₂, Cu+TaSi₂+Ta₅Si₃ or Cu+Ta₃Si+Ta [390]. The tendency of tantalum segregation [391,392] and silicon segregation in the iron-based crystal structures were confirmed by previous research [63]. The observed copper segregation could be the result of the substitutions of atoms in TaB₂ in the form of a solid solution or the copper on the EDS mapping can be overrepresented by the secondary fluorescence of the copper grid to which the tested samples were attached.

The observed parallel cracks in the cross-sections of BMG were distanced between for about 215 µm what makes it three times of the hatching distance (77 µm). This behavior can be interpreted as the accumulation of thermal stress that increases with the next thermal cycle as the next layer tracks are develop [358]. The accumulation of stress leads to exceeding the yield strength of an alloy, leading to the development of a crack. According to [134] the shortening of the laser track can reduce the development of cracks. To do so, the researchers propose to use the chessboard scanning pattern [133], where the laser track can be shorter than the proposed critical length, which for the FeCrMoCB alloy of [134] was equal to 650 µm. When the length of the laser track for this alloy was reduced from 650 to 400 µm the measured residual stress was reduced twice (from 572 to 285 MPa).

Summary Co₄₂B_{26.5}Fe₂₀Ta_{5.5}Si₅Cu₁ SLM

- SEM, XRD, STEM and DSC results indicate the presence of crystal phase (Ta₂B and Co₅Si₂B) on level of around 50%, which are perceptions in the amorphous matrix (STEM)
 - Absence of T_g and T_x
 - H_{IT} = 18.0 GPa, E_{IT} = 225.4 GPa
-

Manufacturing of Co₄₂B_{26.5}Fe₂₀Ta_{5.5}Si₅Cu₁ by SLM resulted in developing BMG composites with nano and micro crystals of Ta₂B and Co₅Si₂B. The samples exhibited large problems with cracking and the lack-of fusion porosity. It was shown by the literature that crystal phase in the amorphous matrix above some percentage increase the cracking problem which is indicated by the thermal stress that occurs during the development of the samples. Lack-of-fusion porosity was connected to the too high hatch spacing combined with not enough wide molten pool and the feedstock problem which showed the magnetization properties what reduced the continuity of the powder layer before the melting. Most important conclusion about developing a BMG sample by SLM from Co₄₂B_{26.5}Fe₂₀Ta_{5.5}Si₅Cu₁ is

that the ED should be between 41 and 50 J/mm³. Additionally, the samples showing the best structure were developed with laser power 75 W, scanning speed 800 mm/s, layer thickness at 25 µm, hatch distance was set at 77 µm from a powder 17.2 - 50.3 µm.

The crystallization of the SLM samples was at level around 50% what makes the material the BMGC (bulk metallic glass composite), where the reinforcement is the crystals suspended in the amorphous matrix. Such high crystallization led to mention problems with cracking, increased hardness of the material and embrittlement. Three factors that were discussed previously for plate form which in crystallization also occurred conclude:

- a) Not high enough glass forming ability of the tested alloy
 - Literature review showed that the D_c and ΔT_x of $\text{Co}_{42}\text{B}_{26.5}\text{Fe}_{20}\text{Ta}_{5.5}\text{Si}_5\text{Cu}_1$ are high, in conclusions the alloy should have a good glass-forming ability. However, the DSC analysis of the prints showed the absence of T_g indicating that alloy could have lowered glass forming ability.
- b) Not fully homogenized alloy before melting by the laser
 - the powder showed the segregation of chemical elements in form of precipitations however the literature study showed that even the non-fully-amorphous feedstock after melting by laser beam in the SLM process can form an amorphous structure [375].
- c) The cooling rate of SLM might be too small to develop amorphous structure
 - the cooling rate of the SLM process ranges from 10^4 to 10^7 °C/s [37,117–119]. However, for alloys with not high enough glass-forming ability the segregation could be observed for SLM technologies. The phenomena occurring in SLM process that leading to segregation might be the thermocapillary flow [393] or Marangoni effect [131–133] that took place in the molten pool or the HAZ [394,395]. The surface tension gradients along with temperature gradients of the melt pool leads to the radial flow of the melt (from the center to the edges of the pool) or create a loop flow inside the melt pool, respectively thermocapillary flow and Marangoni effect. Both effects can lead to segregation of chemical element in the molten pool [134]. Those two phenomena are not able to lead to crystallization in SLM due to mention very high cooling rates of the process but later influence of the heat of the next scanning (HAZ) may lead to crystallization what was shown in [394,395].

3.5. CoBFeTaSiCu atmospheric plasma sprayed coating

The macroscopic view of the $\text{Co}_{42}\text{B}_{26.5}\text{Fe}_{20}\text{Ta}_{5.5}\text{Si}_5\text{Cu}_1$ coatings developed via APS is typical for thermal spraying and had a developed, rough surface [361,362]. Such a surface gives no suggestion if the material is in a glassy or crystallized state as it was possible for the other manufactured forms of $\text{Co}_{42}\text{B}_{26.5}\text{Fe}_{20}\text{Ta}_{5.5}\text{Si}_5\text{Cu}_1$. The surfaces of the CoBFeTaSiCu plasma sprayed samples are visually similar. The $R_a:R_z$ values oscillate around 1:6, and similar values can be obtained after machining, making them moderate [363]. The characteristics flat with high surface splats observed on the surface representing good plasma spraying parameters, while observed only partially deformed spherical-shaped powder particles suggest to low energy supplied for those particles. Different behaviors of feedstock deposition may have an origin in a wide range of particle sizes. The feedstock used has diameters from 37.9 to 107.4 µm, while the D50 was 63.50 µm. Particles with smaller diameter tend to accelerate more in the plasma jet and establish the maximum velocity earlier than the large particles.

Furthermore, the temperature of the smaller particles drops much faster with increasing distance from the plasma nozzle [364]. If the particles do not have enough kinetic or thermal energy, they will not be deposited or will be deposited with only partial deformation observed as a particle deformed. Particles that had enough energy melt in the plasma jet and in the deposition process form the splat [137]. The roughness of the coatings sprayed with 90, 100 and 110 mm had similar values, which suggests that a change in the spraying distance in the mentioned range does not influence the deposition of CoBFeTaSiCu by the APS process. On the surface of the coating, the presence of micro precipitation can be observed, suggesting that the process of crystallization occurred. However, precipitations observed in the partial deformed particles have an origin in the partial crystallized powder, which showed the presence of a second phase. Because of not fully melting of those particles, the crystallization from the as-atomized state was preserved in the particles deformed particles.

Coatings developed with lower values of the spraying distance showed lower porosity and. With a change in the spraying distance from 110 to 90 mm, porosity was reduced by 24%. Research [365] establishes that particles deposited with higher energy form a coating with lower porosity. In the above work, the higher energy was obtained by the higher power of plasma, whereas in this work, the higher energy of particles is connected to the kinetic energy of particles. The higher kinetic energy of the particles could also be obtained by reducing the spraying distance, which was done in this work. In work [364] the most sensitive to loss of kinetic energy are the smaller particles, which at the same time can be easier to melt properly in the plasma jet and form a coating with lower voids [153,366]. Bright precipitations observed by SEM on the surface of the splats and undeformed particles are also visible in the whole volume of the coating, as was shown by the cross-section observation. Precipitations are regular for most of the splats and undeformed particles; however, on some of the splats (long and flat), precipitations do not occur or show only the few visible precipitations. Splats are particles that fully melt in the spray process. This melting enables a process of rapid solidification to take place and suppresses crystallization, which leads to the presence of an amorphous phase with only minor crystallization. Meanwhile, partial melting of particles resulted in supplying extra thermal heat to already present nanocrystals in the feedstock leading to growth of the second phase. The XRD analyses confirmed the SEM observation, no amorphous halo indicates the absence or low volume of amorphous phase (thin splats). The observed peaks indicate the presence of only LRO structures forming the $(\text{Co, Fe})_2\text{B}$ and TaB_2 phases. Those phases were also detected in powder. Alloys with similar chemical compositions that showed the presence of $(\text{Co, Fe})_2\text{B}$ are [276,373] and TaB_2 [374]. The DSC analyses did not show inflection typical for transition from glassy state to non glassy state in the heating process. However, the exothermic peak presents the crystallization at 590°C , which confirms the presence of some amorphous phase in the plasma sprayed coating from an $\text{Co}_{42}\text{B}_{26.5}\text{Fe}_{20}\text{Ta}_{5.5}\text{Si}_5\text{Cu}_1$.

The H_{IT} of the coating was lower than the hardness of the ribbon by 7% and E_{IT} was 4% higher. According to research done on the Fe-based alloy [328,384–386] first crystallization in the amorphous structure should result in the increasing the hardness while in this work the hardness decreased. As was observed, the structure of the coatings is highly heterogeneous. The presence of strongly crystallized areas and some with only several precipitations mixed with amorphous matrix and the presence of porosity result in the lowering the initial hardness of the material comparing both to the powder form and the ribbon form of the $\text{Co}_{42}\text{B}_{26.5}\text{Fe}_{20}\text{Ta}_{5.5}\text{Si}_5\text{Cu}_1$.

The wear resistance of the coating has a moderate value. Changes in spray distance did not show an influence on wear rate in the tested range. The similar rate for Fe-based MG ($\text{Fe}_{43}\text{Cr}_{16}\text{Mo}_{16}\text{C}_{10}\text{B}_5\text{P}_{10}$) was established in [153]. In most of the other research the wear rate is much higher what was shown in the [203]. The highest wear rate was reported for Mg-based MG (around $40 \cdot 10^{-5} \text{ mm}^3/\text{Nm}$), Zr-based MG reported 10 times larger wear rate. The MG that showed the best wear resistance, so the lowest wear rate was reported for Pd-based MG ($\text{Pd}_{40}\text{Cu}_{30}\text{Ni}_{10}\text{P}_{20}$).

Summary $\text{Co}_{42}\text{B}_{26.5}\text{Fe}_{20}\text{Ta}_{5.5}\text{Si}_5\text{Cu}_1$ coatings
<ul style="list-style-type: none"> • SEM, XRD and DSC show high crystallization with some amorphous phase • T_x equal 590°C • $H_{IT} = 14 \text{ GPa}$, $E_{IT} = 198, \text{ GPa}$ • Specific war rate around $1.9 \cdot 10^{-5} \text{ mm}^3/\text{Nm}$

The obtained coatings showed strong crystallization of the deposited feedstock; however, DSC and SEM showed the presents of some amount of amorphous phase. The coating shows a high problem of poor joining of the splats and high content of only partial deformed particles. The porosity problem was also notable, but reduction of the spraying distance influences the reduction of porosity positively. Nevertheless, the specific wear rate of coatings was very high. The observed issues and imperfections of coating in the plasma spaying may be resolved by better homogenization of the feedstock and use of smaller size of the feedstock. The crystallization that occurs might be the result of:

- Not high enough glass forming ability of the tested alloy
 - like discussed above the literature review showed that the D_c and ΔT_x of alloy are high, which should result in a good glass-forming ability of $\text{Co}_{42}\text{B}_{26.5}\text{Fe}_{20}\text{Ta}_{5.5}\text{Si}_5\text{Cu}_1$. However, the crystallization occurred strongly in the APS samples.
- Not fully homogenized feedstock before the plasma spraying
 - the powder showed the segregation of chemical elements in form of precipitations. However, in the atmospheric plasma spraying the feedstock should be melted completely in the plasma jet so this should not be considered.
- The cooling rate of APS is too low
 - the cooling rate of APS can ranges up to $10^5 - 10^7^\circ\text{C/s}$ [144], such high R_c could ensure a rapid solidification of molten feedstock and establish an amorphous structure even for alloys with moderate glass forming ability. However, in this work the melting did not occur for man feedstock showing that the even if the cooling was high enough then still the not melting enough let to inherit the crystallization that was present in feedstock and additionally led to grew of the crystallization phase.

4. Comparison of CoBFeTaSiCu samples

In this subchapter the summary of all forms of $\text{Co}_{42}\text{B}_{26.5}\text{Fe}_{20}\text{Ta}_{5.5}\text{Si}_5\text{Cu}_1$ are collected and used for discussion about the hypothesis tested in this work. Fig. 92 shows the stage of comparison that the hypothesis concerns. Summarizing the discussion results of the Co-based alloy namely the $\text{Co}_{42}\text{B}_{26.5}\text{Fe}_{20}\text{Ta}_{5.5}\text{Si}_5\text{Cu}_1$ the hypothesis will be validated.

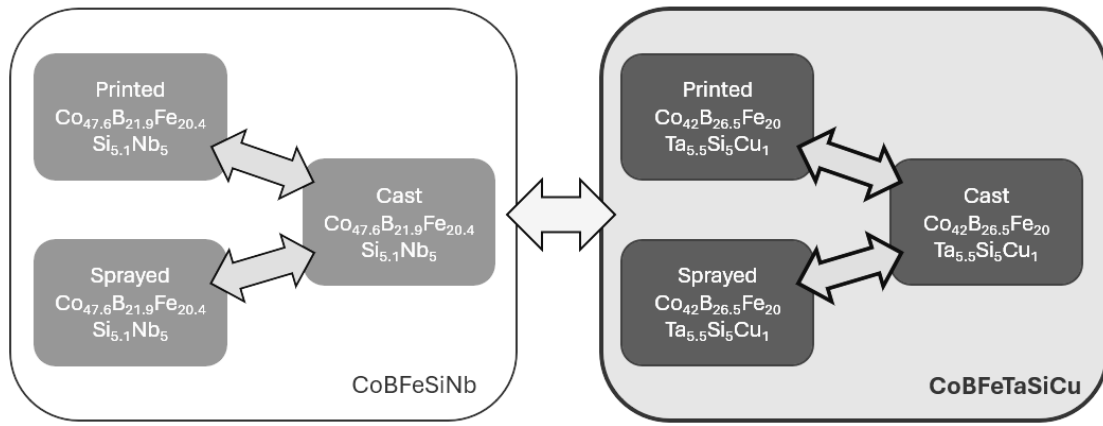


Fig. 92. Visualization of the conducted comparison of $\text{Co}_{42}\text{B}_{26.5}\text{Fe}_{20}\text{Ta}_{5.5}\text{Si}_5\text{Cu}_1$

The first Ph.D. hypothesis constitutes the possibility that amorphous or amorphous nanocrystal structures can be developed by thermal spraying or by printing technologies from an alloy based on cobalt. For the alloy $\text{Co}_{42}\text{B}_{26.5}\text{Fe}_{20}\text{Ta}_{5.5}\text{Si}_5\text{Cu}_1$, an amorphous structure with both nanoscale and microscale crystallization was successfully achieved using SLM. The work establishes the parameters that enable this and points to further steps to improve the quality of the prints and reduce crystallization. These steps include better homogenization of the feedstock, reducing the hatch distance, and changing the scanning pattern for the prints. The second technology from the thermal spraying group showed mediocre results. The samples showed many defects; however, one sample relevant to this hypothesis revealed that the coating was mostly crystallized, which did not support the hypothesis for the experiments conducted on $\text{Co}_{42}\text{B}_{26.5}\text{Fe}_{20}\text{Ta}_{5.5}\text{Si}_5\text{Cu}_1$. Nevertheless, like the results from SLM, improving feedstock quality is expected to significantly enhance outcomes. In this case, along with better homogenization, reducing the particle size of the feedstock may also help decrease crystallization and lower porosity.

The second Ph.D. hypothesis states that it is possible to obtain mechanical properties of new BMG and coatings from the Co-based alloy that are like those obtained by traditional methods of developing amorphous alloys, which is casting. For $\text{Co}_{42}\text{B}_{26.5}\text{Fe}_{20}\text{Ta}_{5.5}\text{Si}_5\text{Cu}_1$, challenges arose even during casting, leading to the use of a method that ensures a high cooling rate, specifically melt spinning. The obtained ribbons had fully amorphous structures and served as reference samples. The SLM technology led to obtaining a hardened structure due to nano and micro crystallization processes in the whole volume of the amorphous phase. The hardness of the obtained BMGs was not at a similar level as the cast ribbons- the hardness of prints was much higher. Similarly, the elastic modulus of BMG was increased for related reasons. APS technologies resulted in nearly complete crystallization, which reduced material hardness. For atmospheric plasma spraying (APS) technologies, almost full crystallization led to a decrease in the hardness of the material; however, the elastic modulus remained at a similar level. Thus, obtaining a similar level of mechanical properties for $\text{Co}_{42}\text{B}_{26.5}\text{Fe}_{20}\text{Ta}_{5.5}\text{Si}_5\text{Cu}_1$ alloy was not successfully achieved, leading to a lack of confirmation of the hypothesis for this material.

For $\text{Co}_{42}\text{B}_{26.5}\text{Fe}_{20}\text{Ta}_{5.5}\text{Si}_5\text{Cu}_1$, both scientific hypotheses were rejected. However, the results obtained have greatly improved our understanding of printing and spraying methods and provided valuable insights into partially crystalline MGs, including changes in structure and mechanical properties. A summary of the most important information is presented in Tab. 43.

Tab. 43. Summary of $\text{Co}_{42}\text{B}_{26.5}\text{Fe}_{20}\text{Ta}_{5.5}\text{Si}_5\text{Cu}_1$ development technologies analysis

Form	technology	T_g [°C]	T_x [°C]	ΔT_x [°C]	Structure	H_{IT} [GPa]	change	E_{IT} [GPa]	change	utility
Ribbon	melt-spinning	615	665	50	amorphous and glassy	15.1	ref	190.1	ref	solid structure no porosities size limitation
bulk	selective laser melting	x	660	x	half amorphous-half crystal	18.0	+19.2%	225.4	+18.6%	cracked structure very high hardness fracture and porosities no size limitation
coating	atmospheric plasma spraying	x	590	x	fully crystallized areas and amorphous + micro-crystals areas	14.0	-7%	198.2	+4%	delimitations porosities strong crystallization
powder	gas-atomization	x	595	x	amorphous + nano-crystals	16.8	+11.3%	x	x	Proper for SLM need more homogenization
plate	pressure die casting	x	x	x	fully crystallized	15.7	+4.6%	322.5	+69.7%	Very brittle very high elastic module

5. Comparison of CoBFeSiNb to CoBFeTaSiCu

Comparison conduct in this subchapter are shown in Fig. 93. This subchapter compares the two alloys that were disused in this work.

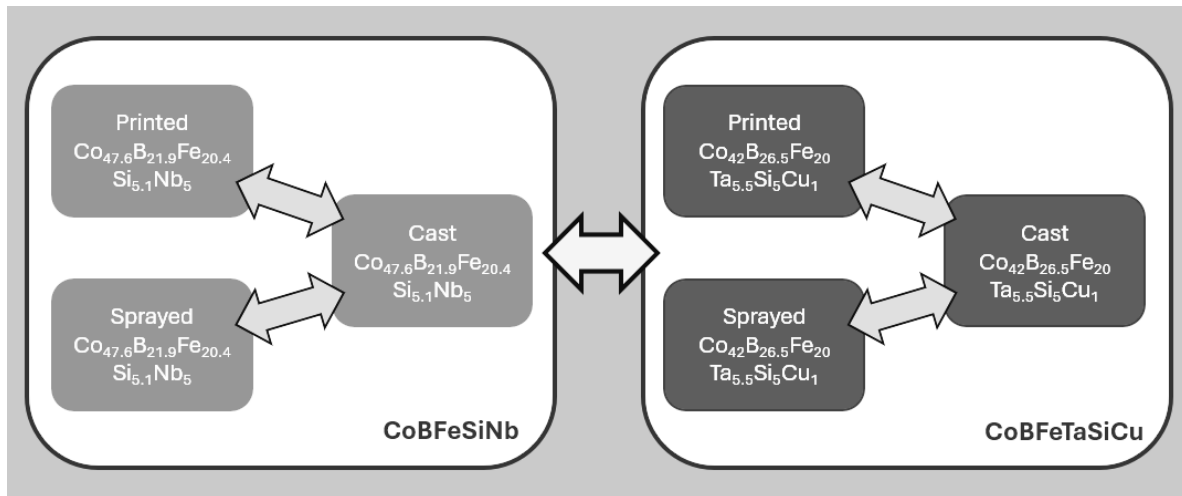
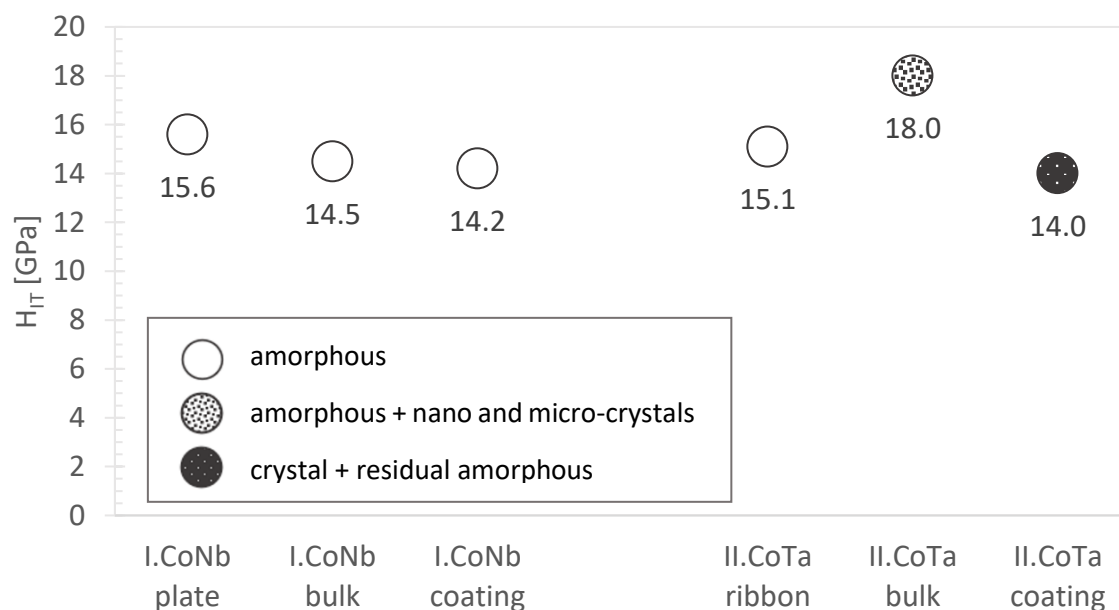


Fig. 93. Visualization of the conducted comparison between $\text{Co}_{47.6}\text{B}_{21.9}\text{Fe}_{20.4}\text{Si}_{5.1}\text{Nb}_5$ and $\text{Co}_{42}\text{B}_{26.5}\text{Fe}_{20}\text{Ta}_{5.5}\text{Si}_5\text{Cu}_1$

Two alloys tested in this work with potentially high glass forming ability based on cobalt presented two different behaviors using the same development technology such as casting, selective laser melting or atmospheric plasma spraying. The first alloy of $\text{Co}_{47.6}\text{B}_{21.9}\text{Fe}_{20.4}\text{Si}_{5.1}\text{Nb}_5$ presented much higher glass forming ability leading to manufacturing fully amorphous sample with each mentioned technology while the second alloy $\text{Co}_{42}\text{B}_{26.5}\text{Fe}_{20}\text{Ta}_{5.5}\text{Si}_5\text{Cu}_1$ showed the issue with homogenization and therefore with suppressing the crystallization in the amorphous matrix. However, both alloys showed typical brittle behavior with only a few shear bands represented in the fracture images and the very high hardness, elastic module and wear resistance. The summary of hardness changes in for the Co-based alloys developed with different technology is shown in the Tab. 44. I.CoNb and II.CoTa represent $\text{Co}_{47.6}\text{B}_{21.9}\text{Fe}_{20.4}\text{Si}_{5.1}\text{Nb}_5$ and $\text{Co}_{42}\text{B}_{26.5}\text{Fe}_{20}\text{Ta}_{5.5}\text{Si}_5\text{Cu}_1$, respectively.



Tab. 44. Indentation hardness and structure of samples developed by casting, SLM and APS from alloy $\text{Co}_{47.6}\text{B}_{21.9}\text{Fe}_{20.4}\text{Si}_{5.1}\text{Nb}_5$ (I.CoNb) and $\text{Co}_{42}\text{B}_{26.5}\text{Fe}_{20}\text{Ta}_{5.5}\text{Si}_5\text{Cu}_1$ (II.CoTa)

VII. CONCLUSIONS

This work contributed to the knowledge about developing metallic glasses from cobalt-based alloys with modern technologies like additive manufacturing- the SLM, and with thermal spraying- APS. The thesis proves that it is possible to obtain fully amorphous structure with good mechanical properties by the mentioned technologies from the $\text{Co}_{47.6}\text{B}_{21.9}\text{Fe}_{20.4}\text{Si}_{5.1}\text{Nb}_5$ alloy. Further research on the topic of metallic glasses should concern:

- Development of research on 3D printing, including SLM studies with changes in scanning strategy and scanning distance for cobalt-based alloys with high ability to reduce the cracking problem.
- Development of research on thermal spraying, including plasma spraying using powder fractions below 50 μm for cobalt-based alloys with a high glass forming ability to reduce the porosity of the obtained coatings.
- Analysis and development of methods for manufacturing cobalt-based alloys with high glass forming ability containing refractory chemical elements (for example, tantalum).
- Analysis of the compressive strength of samples developed by the SLM method from cobalt-based alloys with a high glass forming ability.

Besides confirmation of both hypotheses for $\text{Co}_{47.6}\text{B}_{21.9}\text{Fe}_{20.4}\text{Si}_{5.1}\text{Nb}_5$ the dissertation establishes scientific (S1, S2 etc.) and unitary (U1, U2 etc.) conclusion from research the Co-based alloys with ability to form amorphous or glassy structure:

- (S1) It is possible to obtain the amorphous structure of a Co-based alloy, specifically $\text{Co}_{47.6}\text{B}_{21.9}\text{Fe}_{20.4}\text{Si}_{5.1}\text{Nb}_5$, by selective laser melting and atmospheric plasma spraying. The fully amorphous structure of the $\text{Co}_{47.6}\text{B}_{21.9}\text{Fe}_{20.4}\text{Si}_{5.1}\text{Nb}_5$ alloy developed using selective laser melting technology was maintained when the energy density ranged from 39 to 68 J/mm^3 . In the case of atmospheric plasma spraying, all samples were amorphous within the tested range of parameters.
- (S2) The optimal energy density for selective laser melting processing to achieve a fully amorphous structure while minimizing porosity for $\text{Co}_{47.6}\text{B}_{21.9}\text{Fe}_{20.4}\text{Si}_{5.1}\text{Nb}_5$ was 67.5 J/mm^3 .
- (S3) Reducing the energy density in the selective laser melting process of developing $\text{Co}_{47.6}\text{B}_{21.9}\text{Fe}_{20.4}\text{Si}_{5.1}\text{Nb}_5$ and $\text{Co}_{42}\text{B}_{26.5}\text{Fe}_{20}\text{Ta}_{5.5}\text{Si}_5\text{Cu}_1$ leads to an increase in the porosity of samples. Increasing the ED leads to more fractures in prints.
- (S4) Manufacturing the $\text{Co}_{47.6}\text{B}_{21.9}\text{Fe}_{20.4}\text{Si}_{5.1}\text{Nb}_5$ alloy through various rapid solidification processes, such as selective laser melting, atmospheric plasma spraying, and casting, while maintaining the amorphous structure of the obtained material, leads to variations in its mechanical properties (namely hardness and elastic modulus). The values can differ by up to 10%, with the pressure-cast material serving as the reference.
- (S5) Crystallization at a level of 50% of the alloy $\text{Co}_{42}\text{B}_{26.5}\text{Fe}_{20}\text{Ta}_{5.5}\text{Si}_5\text{Cu}_1$ printed by selective laser melting resulted in a hardness increase of 19% ($H_{IT} = 18 \text{ GPa}$) compared to the fully amorphous samples obtained by melt spinning casting.
- (S6) Not fully homogenized compounds of $\text{Co}_{42}\text{B}_{26.5}\text{Fe}_{20}\text{Ta}_{5.5}\text{Si}_5\text{Cu}_1$ (especially the high-temperature tantalum) lead to a decrease in the glass-forming ability of the alloy, which was observed in the cast plates, printed samples by selective laser melting, and atmospheric plasma spraying.
- (S7) To obtain samples from $\text{Co}_{42}\text{B}_{26.5}\text{Fe}_{20}\text{Ta}_{5.5}\text{Si}_5\text{Cu}_1$ with low glass-forming ability by selective laser melting, the energy density should range from 41 to 50 J/mm^3 . Such energy ensures the obtained sample. Lower energy leads to a lack of joining between the powder

particles, and higher energy density leads to severe fracturing of samples, leading to destruction.

- (S8) Atmospheric plasma spraying of $\text{Co}_{42}\text{B}_{26.5}\text{Fe}_{20}\text{Ta}_{5.5}\text{Si}_5\text{Cu}_1$ and $\text{Co}_{47.6}\text{B}_{21.9}\text{Fe}_{20.4}\text{Si}_{5.1}\text{Nb}_5$ leads to the development of coatings with a very low abrasive wear rate (approximately $2.0 \cdot 10^{-5} \text{ mm}^3/\text{Nm}$).
- (U1) To produce elements from Co-based alloys with a tendency to form amorphous structures, the energy density should be optimized by setting an upper limit to suppress crystallization, reduce fractures and a lower limit to reduce the number of porosities.
- (U2) To obtain samples with the lowest porosity while still maintaining the amorphous structure, the alloy $\text{Co}_{47.6}\text{B}_{21.9}\text{Fe}_{20.4}\text{Si}_{5.1}\text{Nb}_5$ should be developed with an energy density of 67.5 J/mm^3 . This can be achieved by setting the laser power at 65 W, scanning speed at 500 mm/s, layer thickness at 25 μm , and spacing between tracks at 77 μm .
- (U3) To increase the processability of $\text{Co}_{42}\text{B}_{26.5}\text{Fe}_{20}\text{Ta}_{5.5}\text{Si}_5\text{Cu}_1$ to obtain a fully amorphous structure, the tantalum must be fully melted and homogenized with other chemical compounds in the alloy. In other cases, manufacturing samples by SLM from $\text{Co}_{42}\text{B}_{26.5}\text{Fe}_{20}\text{Ta}_{5.5}\text{Si}_5\text{Cu}_1$ with tantalum precipitation requires using a narrow range of energy density. Samples developed within this range still show problems with large porosity and around presents of crystal phase in the amorphous matrix.
- (U4) The high glass-forming ability of the alloy $\text{Co}_{47.6}\text{B}_{21.9}\text{Fe}_{20.4}\text{Si}_{5.1}\text{Nb}_5$ allows it to process it by different technologies such as selective laser melting, atmospheric plasma spraying, gas-atomization or vacuum casting, while still maintaining a fully amorphous structure. While alloy $\text{Co}_{42}\text{B}_{26.5}\text{Fe}_{20}\text{Ta}_{5.5}\text{Si}_5\text{Cu}_1$ due to high temperature tantalum shows the lowered glass forming ability and processability into solid structures.
- (U5) Co-based alloys with the ability to form amorphous structures are suitable for developing anti wear coatings, namely high wear resistance coatings, using atmospheric plasma spraying.
- (U6) The $\text{Co}_{47.6}\text{B}_{21.9}\text{Fe}_{20.4}\text{Si}_{5.1}\text{Nb}_5$ powders obtained by argon-atomization of the 20-50 μm fraction can be implemented in industrial applications such as 3D printing and thermal spraying.

Finally, I would like to express my sincere gratitude to my supervisors Prof. Wirginia Pilarczyk and PhD Aleksandra Małachowska, for their invaluable guidance and support throughout my research. Their insights have been *essential* in shaping this thesis. I also extend my appreciation to all my fellow researchers, colleagues and reviewers that helped in the process of becoming a young scientist. The journey of working on the PhD for the last 5 years surely made me a new person. Enlightened, more experienced and gave me an opportunity and space for growth.

1. Pilarczyk, W. *Struktura i Właściwości Masywnych Szkielek Metalicznych w Stanie Po Wytworzeniu i Po Procesie Spawania Laserowego*; Wydawnictwo Politechniki Śląskiej, 2017;
2. Stoica, M. *Fe-Based Bulk Metallic Glasses: Understanding the Influence of Impurities on Glass Formation*; Springer, 2017; ISBN 978-3-658-17018-9.
3. Suryanarayana, C.; Inoue, A. *Bulk Metallic Glasses*; CRC Press, 2011; ISBN 978-1-4398-5969-8.
4. Prajapati, A.; Rajpurohit, S. *FORMATION AND APPLICATIONS OF SINGLE CRYSTAL MATERIAL*; 2017;
5. Gell, M.; Duhal, D.N.; Gupta, D.K.; Sheffler, K.D. Advanced Superalloy Airfoils. *JOM* **1987**, 39, 11–15, doi:10.1007/BF03258033.
6. Haubold, T. Nanocrystalline Materials – Structure and Properties. In *Magnetic Properties of Fine Particles*; Dormann, J.L., Fiorani, D., Eds.; North-Holland Delta Series; Elsevier: Amsterdam, 1992; pp. 67–75.
7. Suryanarayana, C.; Inoue, A. Iron-Based Bulk Metallic Glasses. *Int. Mater. Rev.* **2013**, 58, 131–166, doi:10.1179/1743280412Y.0000000007.
8. Lan, S.; Zhu, L.; Wu, Z.; Gu, L.; Zhang, Q.; Kong, H.; Liu, J.; Song, R.; Liu, S.; Sha, G.; et al. A Medium-Range Structure Motif Linking Amorphous and Crystalline States. *Nat. Mater.* **2021**, 20, 1347–1352, doi:10.1038/s41563-021-01011-5.
9. Shechtman, D.; Blech, I.; Gratias, D.; Cahn, J.W. Metallic Phase with Long-Range Orientational Order and No Translational Symmetry. *Phys. Rev. Lett.* **1984**, 53, 1951–1953, doi:10.1103/PhysRevLett.53.1951.
10. Glotzer, S. Quasicrystals: The Thrill of the Chase. *Nature* **2019**, 565, 156–158, doi:10.1038/d41586-019-00026-y.
11. Wan, Z.; Xu, Q.; Li, H.; Zhang, Y.; Ding, Y.; Wang, J. Efficient Co@CoO Core-Shell Nanocrystals as Catalysts for Visible-Light-Driven Water Oxidation. *Appl. Catal. B Environ.* **2017**, 210, doi:10.1016/j.apcatb.2017.03.056.
12. Ye, Z.; Zhang, F.; Sun, Y.; Mendelev, M.; Ott, R.; Park, E.; Besser, M.; Kramer, M.; Zejun, D.; Wang, C.; et al. Discovery of a Metastable Al₂₀Sm₄ Phase. *Appl. Phys. Lett.* **2015**, 106, 101903, doi:10.1063/1.4914399.
13. Kumar, A.; Nayak, S.K.; Bijalwan, P.; Dutta, M.; Banerjee, A.; Laha, T. Optimization of Mechanical and Corrosion Properties of Plasma Sprayed Low-Chromium Containing Fe-Based Amorphous/Nanocrystalline Composite Coating. *Surf. Coat. Technol.* **2019**, 370, 255–268, doi:10.1016/j.surfcoat.2019.05.010.
14. Bindi, L.; Yao, N.; Lin, C.; Hollister, L.S.; Andronicos, C.L.; Distler, V.V.; Eddy, M.P.; Kostin, A.; Kryachko, V.; MacPherson, G.J.; et al. Natural Quasicrystal with Decagonal Symmetry. *Sci. Rep.* **2015**, 5, 9111, doi:10.1038/srep09111.
15. Busch, R. The Thermophysical Properties of Bulk Metallic Glass-Forming Liquids. *JOM* **2000**, 52, 39–42, doi:10.1007/s11837-000-0160-7.
16. Sohn, S.; Xie, Y.; Jung, Y.; Schroers, J.; Cha, J.J. Tailoring Crystallization Phases in Metallic Glass Nanorods via Nucleus Starvation. *Nat. Commun.* **2017**, 8, 1980, doi:10.1038/s41467-017-02153-4.
17. Pawlik, P. *Rola składu chemicznego i procesu wytwarzania w kształtowaniu właściwości magnetycznych masywnych amorficznych i nanokrystalicznych stopów żelaza*; Wydawn. Wydz. Inżynierii Procesowej, Materiałowej i Fizyki Stosowanej Politechniki Częstochowskiej, 2011; ISBN 978-83-87745-04-2.
18. Zheng, Q.; Zhang, Y.; Montazerian, M.; Gulbitten, O.; Mauro, J.C.; Zanolto, E.D.; Yue, Y. Understanding Glass through Differential Scanning Calorimetry. *Chem. Rev.* **2019**, 119, 7848–7939, doi:10.1021/acs.chemrev.8b00510.
19. Turnbull, D. Under What Conditions Can a Glass Be Formed? *Contemp. Phys.* **1969**, 10, 473–488, doi:10.1080/00107516908204405.
20. Inoue, A. High Strength Bulk Amorphous Alloys with Low Critical Cooling Rates (<I>Overview</I>). *Mater. Trans. JIM* **1995**, 36, 866–875, doi:10.2320/matertrans1989.36.866.
21. Mondal, K.; Murty, B.S. On the Parameters to Assess the Glass Forming Ability of Liquids. *J. Non-Cryst. Solids* **2005**, 351, 1366–1371, doi:10.1016/j.jnoncrysol.2005.03.006.
22. Yuan, Z.-Z.; Bao, S.-L.; Lu, Y.; Zhang, D.-P.; Yao, L. A New Criterion for Evaluating the Glass-Forming Ability of Bulk Glass Forming Alloys. *J. Alloys Compd.* **2008**, 459, 251–260, doi:10.1016/j.jallcom.2007.05.037.
23. Lu, Z.P.; Liu, C.T. A New Glass-Forming Ability Criterion for Bulk Metallic Glasses. *Acta Mater.* **2002**, 50, 3501–3512, doi:10.1016/S1359-6454(02)00166-0.
24. Phys. Rev. Lett. 91, 115505 (2003) - Glass Formation Criterion for Various Glass-Forming Systems Available online: <https://journals.aps.org/prl/abstract/10.1103/PhysRevLett.91.115505> (accessed on 23 August 2023).
25. Du, X.H.; Huang, J.C.; Liu, C.T.; Lu, Z.P. New Criterion of Glass Forming Ability for Bulk Metallic Glasses. *J. Appl. Phys.* **2007**, 101, 086108, doi:10.1063/1.2718286.
26. Chen, Q.; Shen, J.; Zhang, D.; Fan, H.; Sun, J.; McCartney, D.G. A New Criterion for Evaluating the Glass-Forming Ability of Bulk Metallic Glasses. *Mater. Sci. Eng. A* **2006**, 433, 155–160, doi:10.1016/j.msea.2006.06.053.
27. Evaluation of Glass-Forming Tendency by Means of DTA | SpringerLink Available online: <https://link.springer.com/article/10.1007/BF01690134> (accessed on 23 August 2023).

28. Fan, G.J.; Choo, H.; Liaw, P.K. A New Criterion for the Glass-Forming Ability of Liquids. *J. Non-Cryst. Solids* **2007**, *353*, 102–107, doi:10.1016/j.jnoncrysol.2006.08.049.
29. Kim, J.-H.; Park, J.S.; Lim, H.K.; Kim, W.T.; Kim, D.H. Heating and Cooling Rate Dependence of the Parameters Representing the Glass Forming Ability in Bulk Metallic Glasses. *J. Non-Cryst. Solids* **2005**, *351*, 1433–1440, doi:10.1016/j.jnoncrysol.2005.03.020.
30. Long, Z.; Wei, H.; Ding, Y.; Zhang, P.; Xie, G.; Inoue, A. A New Criterion for Predicting the Glass-Forming Ability of Bulk Metallic Glasses. *J. Alloys Compd.* **2009**, *475*, 207–219, doi:10.1016/j.jallcom.2008.07.087.
31. Suryanarayana, C.; Seki, I.; Inoue, A. A Critical Analysis of the Glass-Forming Ability of Alloys. *J. Non-Cryst. Solids* **2009**, *355*, 355–360, doi:10.1016/j.jnoncrysol.2008.12.009.
32. Klement, W.; Willens, R.H.; Duwez, P. Non-Crystalline Structure in Solidified Gold–Silicon Alloys. *Nature* **1960**, *187*, 869–870, doi:10.1038/187869b0.
33. Dong, Y.; Wunderlich, R.; Biskupek, J.; Cao, Q.P.; Wang, X.D.; Zhang, D.X.; Jiang, J.Z.; Fecht, H.-J. Co Content Effect on Elastic Strain Limit in ZrCuNiAlCo Bulk Metallic Glasses. *Scr. Mater.* **2017**, *137*, 94–99, doi:10.1016/j.scriptamat.2017.05.007.
34. Zhou, Z.; Shang, Y.; Yang, Y. A Critical Review of the Machine Learning Guided Design of Metallic Glasses for Superior Glass-Forming Ability. *J. Mater. Inform.* **2022**, *2*, 2, doi:10.20517/jmi.2021.12.
35. Pilarczyk, W. Preparation and Characterization of Zr-Based Bulk Metallic Glasses in Form of Plate. *J. Alloys Compd.* **2014**, *615*, S132–S135, doi:10.1016/j.jallcom.2014.01.037.
36. Zhou, K.; Liu, Y.; Pang, S.; Zhang, T. Formation and Properties of Centimeter-Size Zr–Ti–Cu–Al–Y Bulk Metallic Glasses as Potential Biomaterials. *J. Alloys Compd.* **2016**, *656*, 389–394, doi:10.1016/j.jallcom.2015.09.254.
37. Ouyang, D.; Li, N.; Xing, W.; Zhang, J.; Liu, L. 3D Printing of Crack-Free High Strength Zr-Based Bulk Metallic Glass Composite by Selective Laser Melting. *Intermetallics* **2017**, *90*, 128–134, doi:10.1016/j.intermet.2017.07.010.
38. Lewandowski, J.J.; Gu, X.J.; Shamimi Nouri, A.; Poon, S.J.; Shiflet, G.J. Tough Fe-Based Bulk Metallic Glasses. *Appl. Phys. Lett.* **2008**, *92*, 091918, doi:10.1063/1.2890489.
39. Alvarez, K.L.; Baghbaderani, H.A.; Martín, J.M.; Burgos, N.; Ipatov, M.; Pavlovic, Z.; McCloskey, P.; Masood, A.; Gonzalez, J. Novel Fe-Based Amorphous and Nanocrystalline Powder Cores for High-Frequency Power Conversion. *J. Magn. Magn. Mater.* **2020**, *501*, 166457, doi:10.1016/j.jmmm.2020.166457.
40. Li, H.X.; Lu, Z.C.; Wang, S.L.; Wu, Y.; Lu, Z.P. Fe-Based Bulk Metallic Glasses: Glass Formation, Fabrication, Properties and Applications. *Prog. Mater. Sci.* **2019**, *103*, 235–318, doi:10.1016/j.pmatsci.2019.01.003.
41. Guo, F.Q.; Enouf, S.J.; Poon, S.J.; Shiflet, G.J. Formation of Ductile Al-Based Metallic Glasses without Rare-Earth Elements. *Philos. Mag. Lett.* **2001**, *81*, 203–211, doi:10.1080/09500830010017042.
42. Jambur, V.; Tangpatjaroen, C.; Xi, J.; Tarnsangpradit, J.; Gao, M.; Sheng, H.; Perepezko, J.H.; Szlufarska, I. Effects of Minor Alloying on the Mechanical Properties of Al Based Metallic Glasses. *J. Alloys Compd.* **2021**, *854*, 157266, doi:10.1016/j.jallcom.2020.157266.
43. Xu, D.; Duan, G.; Johnson, W.L.; Garland, C. Formation and Properties of New Ni-Based Amorphous Alloys with Critical Casting Thickness up to 5 Mm. *Acta Mater.* **2004**, *52*, 3493–3497, doi:10.1016/j.actamat.2004.04.001.
44. Ma, X.; Zhen, N.; Guo, J.; Li, Q.; Chang, C.; Sun, Y. Preparation of Ni-Based Bulk Metallic Glasses with High Corrosion Resistance. *J. Non-Cryst. Solids* **2016**, *443*, 91–96, doi:10.1016/j.jnoncrysol.2016.04.020.
45. Ma, Z.; Li, Q.; Xie, L.; Chang, C.; Ma, X.; Zhang, G. Effects of Heavy Rare Earth Elements on Properties of Fe₄₁Co₇Cr₁₅Mo₁₄C₁₅B₆RE₂ (RE = Y, Lu, Tm, Tb) Bulk Metallic Glasses. *J. Non-Cryst. Solids* **2024**, *641*, 123136, doi:10.1016/j.jnoncrysol.2024.123136.
46. Ma, S.; Lu, J.; Wang, Y.; Li, Y.; Wang, X.; Zeng, Q.; Zhang, W.; Yao, M. Role of Rare Earth Elements Addition in Enhancing Glass-Forming Ability and Magnetic Softness of a Co₇₅B₂₅ Metallic Glass: Theoretical Prediction and Experimental Verification. *J. Mater. Res. Technol.* **2023**, *26*, 6193–6204, doi:10.1016/j.jmrt.2023.08.296.
47. Deng, L.; Zhou, B.; Yang, H.; Jiang, X.; Jiang, B.; Zhang, X. Roles of Minor Rare-Earth Elements Addition in Formation and Properties of Cu–Zr–Al Bulk Metallic Glasses. *J. Alloys Compd.* **2015**, *632*, 429–434, doi:10.1016/j.jallcom.2015.01.036.
48. Álvarez, P.; Gorria, P.; Sánchez Marcos, J.; Fernández Barquín, L.; Blanco, J.A. The Role of Boron on the Magneto-Caloric Effect of FeZrB Metallic Glasses. *Intermetallics* **2010**, *18*, 2464–2467, doi:10.1016/j.intermet.2010.07.018.
49. Wang, J.; Wang, L.; Guan, S.; Zhu, S.; Li, R.; Zhang, T. Effects of Boron Content on the Glass-Forming Ability and Mechanical Properties of Co–B–Ta Glassy Alloys. *J. Alloys Compd.* **2014**, *617*, 7–11, doi:10.1016/j.jallcom.2014.07.187.
50. Kim, J.T.; Hong, S.H.; Bian, X.; Gokuldoss, P.K.; Song, K.; Eckert, J.; Park, J.M.; Kim, K.B. Effect of Boron Addition on Thermal and Mechanical Properties of Co–Cr–Mo–C–(B) Glass-Forming Alloys. *Intermetallics* **2018**, *99*, 1–7, doi:10.1016/j.intermet.2018.05.006.

51. Choi-Yim, H.; Busch, R.; Johnson, W.L. The Effect of Silicon on the Glass Forming Ability of the Cu₄₇Ti₃₄Zr₁₁Ni₈ Bulk Metallic Glass Forming Alloy during Processing of Composites. *J. Appl. Phys.* **1998**, *83*, 7993–7997, doi:10.1063/1.367981.
52. Rife, G.; Chan, P.C.C.; Aust, K.T.; Waseda, Y. Corrosion of Iron-, Nickel- and Cobalt-Base Metallic Glasses Containing Boron and Silicon Metalloids. *Mater. Sci. Eng.* **1981**, *48*, 73–79, doi:10.1016/0025-5416(81)90067-7.
53. Schnabel, V.; Evertz, S.; Rueß, H.; Music, D.; Schneider, J.M. Stiffness and Toughness Prediction of Co–Fe–Ta–B Metallic Glasses, Alloyed with Y, Zr, Nb, Mo, Hf, W, C, N and O by Ab Initio Molecular Dynamics. *J. Phys. Condens. Matter* **2015**, *27*, 105502, doi:10.1088/0953-8984/27/10/105502.
54. Zhang, J.; Ma, S.; Wang, H.; Kubota, T.; Li, Y.; Kato, H.; Umetsu, R.Y.; Yao, M.; Zhang, W. Effects and Mechanisms of Nb and Fe Additions on Glass-Forming Ability and Magnetic Properties of a Co_{71.5}Gd_{3.5}B₂₅ Metallic Glass. *J. Alloys Compd.* **2023**, *968*, 171875, doi:10.1016/j.jallcom.2023.171875.
55. Zhang, S.; Wei, C.; Shi, Z.; Zhang, H.; Ma, M. Effect of Fe Addition on the Glass-Forming Ability, Stability, and Mechanical Properties of Zr₅₀Cu₃₄-xFe_xAl₈Ag₈ Metallic Glasses. *J. Alloys Compd.* **2022**, *929*, 167334, doi:10.1016/j.jallcom.2022.167334.
56. Tan, J.; Pan, F.S.; Zhang, Y.; Wang, Z.; Stoica, M.; Sun, B.A.; Kühn, U.; Eckert, J. Effect of Fe Addition on Glass Forming Ability and Mechanical Properties in Zr–Co–Al–(Fe) Bulk Metallic Glasses. *Mater. Sci. Eng. A* **2012**, *539*, 124–127, doi:10.1016/j.msea.2012.01.068.
57. Li, Y.H.; Zhang, W.; Dong, C.; Qiang, J.B.; Fukuhara, M.; Makino, A.; Inoue, A. Effects of Ni Addition on the Glass-Forming Ability, Mechanical Properties and Corrosion Resistance of Zr–Cu–Al Bulk Metallic Glasses. *Mater. Sci. Eng. A* **2011**, *528*, 8551–8556, doi:10.1016/j.msea.2011.07.077.
58. Ma, X.; Li, Q.; Xie, L.; Chang, C.; Li, H. Effect of Ni Addition on the Properties of CoMoPB Bulk Metallic Glasses. *J. Non-Cryst. Solids* **2022**, *587*, 121573, doi:10.1016/j.jnoncrsol.2022.121573.
59. Li, D.; Zhu, Z.; Zhang, H.; Wang, A.; Hu, Z. The Influence of Zr Substitution for Nb on the Corrosion Behaviors of the Ni–Nb–Zr Bulk Metallic Glasses. *Sci. China Phys. Mech. Astron.* **2012**, *55*, 2362–2366, doi:10.1007/s11433-012-4918-z.
60. Park, S.H.; Lim, K.R.; Na, M.Y.; Kim, K.C.; Kim, W.T.; Kim, D.H. Effect of Minor Addition of Zr on the Oxidation Behavior of Ti–Cu Metallic Glasses. *Met. Mater. Int.* **2016**, *22*, 229–235, doi:10.1007/s12540-016-5587-7.
61. Lin, X.H.; Johnson, W.L. Formation of Ti–Zr–Cu–Ni Bulk Metallic Glasses. *J. Appl. Phys.* **1995**, *78*, 6514–6519, doi:10.1063/1.360537.
62. Cole, K.M.; Kirk, D.W.; Singh, C.V.; Thorpe, S.J. Role of Niobium and Oxygen Concentration on Glass Forming Ability and Crystallization Behavior of Zr–Ni–Al–Cu–Nb Bulk Metallic Glasses with Low Copper Concentration. *J. Non-Cryst. Solids* **2016**, *445–446*, 88–94, doi:10.1016/j.jnoncrsol.2016.05.015.
63. Bao, F.; Li, Y.; Zhu, Z.; Liang, X.; Zhang, Y.; Zhang, W. Enhancement of Glass-Forming Ability and Thermal Stability of a Soft Magnetic Co₇₅B₂₅ Metallic Glass by Micro-Alloying Y and Nb. *J. Iron Steel Res. Int.* **2021**, *28*, 597–603, doi:10.1007/s42243-020-00489-8.
64. Kucuk, I.; Aykol, M.; Uzun, O.; Yildirim, M.; Kabaer, M.; Duman, N.; Yilmaz, F.; Erturk, K.; Akdeniz, M.V.; Mekhrabov, A.O. Effect of (Mo, W) Substitution for Nb on Glass Forming Ability and Magnetic Properties of Fe–Co-Based Bulk Amorphous Alloys Fabricated by Centrifugal Casting. *J. Alloys Compd.* **2011**, *509*, 2334–2337, doi:10.1016/j.jallcom.2010.11.011.
65. Wang, Y.; Jiang, S.L.; Zheng, Y.G.; Ke, W.; Sun, W.H.; Wang, J.Q. Effect of Molybdenum, Manganese and Tungsten Contents on the Corrosion Behavior and Hardness of Iron-Based Metallic Glasses. *Mater. Corros.* **2014**, *65*, 733–741, doi:10.1002/maco.201206740.
66. Jia, Y.; Zeng, S.; Shan, S.; Zhang, L.; Fan, C.; Zhang, B.; Zhan, Z.; Liu, R.; Wang, W. Effect of Copper Addition on the Glass Forming Ability of a Fe–Co Based Alloy. *J. Alloys Compd.* **2007**, *440*, 113–116, doi:10.1016/j.jallcom.2006.09.018.
67. Jilani, S.; Khalid, F.A. Role of Copper Addition on Properties of Bulk Metallic Glass Materials. *Mater. Sci. Eng. A* **2016**, *663*, 17–20, doi:10.1016/j.msea.2016.03.109.
68. Liang, D.; Wei, X.; Chang, C.; Li, J.; Wang, X.; Shen, J. Effect of W Addition on the Glass Forming Ability and Mechanical Properties of Fe-Based Metallic Glass. *J. Alloys Compd.* **2018**, *731*, 1146–1150, doi:10.1016/j.jallcom.2017.10.104.
69. Shi, H.; Zhao, W.; Wei, X.; Ding, Y.; Shen, X.; Liu, W. Effect of Ti Addition on Mechanical Properties and Corrosion Resistance of Ni-Free Zr-Based Bulk Metallic Glasses for Potential Biomedical Applications. *J. Alloys Compd.* **2020**, *815*, 152636, doi:10.1016/j.jallcom.2019.152636.
70. Tan, C.G.; Jiang, W.J.; Zhang, Z.C.; Wu, X.Q.; Lin, J.G. The Effect of Ti-Addition on the Corrosion Behavior of the Partially Crystallized Ni-Based Bulk Metallic Glasses. *Mater. Chem. Phys.* **2008**, *108*, 29–32, doi:10.1016/j.matchemphys.2007.08.036.
71. Zhou, W.; Kong, L.T.; Li, J.F.; Zhou, Y.H. Effects of Cr Addition on Glass-Forming Ability and Mechanical Properties of Cu–Zr–Al Bulk Metallic Glass. *J. Mater. Sci.* **2012**, *47*, 4996–5001, doi:10.1007/s10853-012-6375-5.

72. Wang, S.L.; Li, H.X.; Zhang, X.F.; Yi, S. Effects of Cr Contents in Fe-Based Bulk Metallic Glasses on the Glass Forming Ability and the Corrosion Resistance. *Mater. Chem. Phys.* **2009**, *113*, 878–883, doi:10.1016/j.matchemphys.2008.08.057.
73. Liu, L.; Chan, K.C.; Sun, M.; Chen, Q. The Effect of the Addition of Ta on the Structure, Crystallization and Mechanical Properties of Zr–Cu–Ni–Al–Ta Bulk Metallic Glasses. *Mater. Sci. Eng. A* **2007**, *445–446*, 697–706, doi:10.1016/j.msea.2006.10.004.
74. Wang, W.H.; Bian, P.W.; Z.; Zhang, Y.; Pan, M.X.; Zhao, D.Q. Role of Addition in Formation and Properties of Zr-Based Bulk Metallic Glasses. *Intermetallics* **2002**, *10*, 1249–1257, doi:10.1016/S0966-9795(02)00140-1.
75. Tsai, P.H.; Li, T.H.; Hsu, K.T.; Ke, J.H.; Jang, J.S.C.; Chu, J.P. Coating Thickness Effect of Metallic Glass Thin Film on the Fatigue-Properties Improvement of 7075 Aluminum Alloy. *Thin Solid Films* **2019**, *677*, 68–72, doi:10.1016/j.tsf.2019.03.021.
76. Kobayashi, A.; Yano, S.; Kimura, H.; Inoue, A. Mechanical Property of Fe-Base Metallic Glass Coating Formed by Gas Tunnel Type Plasma Spraying. *Surf. Coat. Technol.* **2008**, *202*, 2513–2518, doi:10.1016/j.surfcoat.2007.09.011.
77. Li, N.; Ma, J.; Li, N.; Ma, J. Thermoplastic Forming of Metallic Glasses. In *Metallic Glasses - Properties and Processing*; IntechOpen, 2018 ISBN 978-1-78923-721-4.
78. Josserond, C. Metallic Glasses : Forming, Structure and Properties Available online: <https://simap.grenoble-inp.fr/en/research/metallic-glasses-forming-structure-and-properties> (accessed on 14 March 2024).
79. Van Toan, N.; Tuoi, T.T.K.; Tsai, Y.-C.; Lin, Y.-C.; Ono, T. Micro-Fabricated Pressure Sensor Using 50 Nm-Thick of Pd-Based Metallic Glass Freestanding Membrane. *Sci. Rep.* **2020**, *10*, 10108, doi:10.1038/s41598-020-67150-y.
80. Metallic Glasses: Down to the Wire. *NPG Asia Mater.* **2011**, 1–1, doi:10.1038/asiamat.2011.23.
81. Kumar, G.; Desai, A.; Schroers, J. Bulk Metallic Glass: The Smaller the Better. *Adv. Mater.* **2011**, *23*, 461–476, doi:10.1002/adma.201002148.
82. Bordeenithikasem, P.; Shen, Y.; Tsai, H.-L.; Hofmann, D.C. Enhanced Mechanical Properties of Additively Manufactured Bulk Metallic Glasses Produced through Laser Foil Printing from Continuous Sheetmetal Feedstock. *Addit. Manuf.* **2018**, *19*, 95–103, doi:10.1016/j.addma.2017.11.010.
83. Schroers, J.; Hodges, T.M.; Kumar, G.; Raman, H.; Barnes, A.J.; Pham, Q.; Waniuk, T.A. Thermoplastic Blow Molding of Metals. *Mater. Today* **2011**, *14*, 14–19, doi:10.1016/S1369-7021(11)70018-9.
84. Zhang, C.; Ouyang, D.; Pauly, S.; Liu, L. 3D Printing of Bulk Metallic Glasses. *Mater. Sci. Eng. R Rep.* **2021**, *145*, 100625, doi:10.1016/j.mser.2021.100625.
85. Li, J.B.; Lin, H.C.; Jang, J.S.C.; Kuo, C.N.; Huang, J.C. Novel Open-Cell Bulk Metallic Glass Foams with Promising Characteristics. *Mater. Lett.* **2013**, *105*, 140–143, doi:10.1016/j.matlet.2013.04.071.
86. Inoue, A.; Takeuchi, A. Recent Development and Application Products of Bulk Glassy Alloys. *Acta Mater.* **2011**, *59*, 2243–2267, doi:10.1016/j.actamat.2010.11.027.
87. Group, S.M. Low-Pressure Casting of Bulk Metallic Glasses for Gears and Other Applications Available online: <https://www.techbriefs.com/component/content/article/22405-npo-49318> (accessed on 11 April 2024).
88. Patel, S.K.; Swain, B.K.; Behera, A.; Mohapatra, S.S.; Patel, S.K.; Swain, B.K.; Behera, A.; Mohapatra, S.S. Metallic Glasses: A Revolution in Material Science. In *Metallic Glasses*; IntechOpen, 2020 ISBN 978-1-78985-488-6.
89. Aqida, S.N.; Shah, L.H.; Naher, S.; Brabazon, D. 5.04 - Rapid Solidification Processing and Bulk Metallic Glass Casting. In *Comprehensive Materials Processing*; Hashmi, S., Batalha, G.F., Van Tyne, C.J., Yilbas, B., Eds.; Elsevier: Oxford, 2014; pp. 69–88 ISBN 978-0-08-096533-8.
90. Gao, W.J.; Zhang, W.W.; Zhang, T.; Yang, C.; Huang, X.S.; Liu, Z.Y.; Wang, Z.; Li, W.H.; Li, W.R.; Li, L.; et al. Large Tensile Plasticity in Zr-Based Metallic Glass/Stainless Steel Interpenetrating-Phase Composites Prepared by High Pressure Die Casting. *Compos. Part B Eng.* **2021**, *224*, 109226, doi:10.1016/j.compositesb.2021.109226.
91. Niu, X.P.; Hu, B.H.; Pinwill, I.; Li, H. Vacuum Assisted High Pressure Die Casting of Aluminium Alloys. *J. Mater. Process. Technol.* **2000**, *105*, 119–127, doi:10.1016/S0924-0136(00)00545-8.
92. Materials | Free Full-Text | Near-Net Forming Complex Shaped Zr-Based Bulk Metallic Glasses by High Pressure Die Casting Available online: <https://www.mdpi.com/1996-1944/11/11/2338> (accessed on 1 January 2024).
93. Liu, L.H.; Gao, W.J.; Huang, X.S.; Zhang, T.; Liu, Z.Y.; Yang, C.; Zhang, W.W.; Li, W.R.; Li, L.; Li, P.J. Shear-Accelerated Crystallization of Glass-Forming Metallic Liquids in High-Pressure Die Casting. *J. Mater. Sci. Technol.* **2022**, *117*, 146–157, doi:10.1016/j.jmst.2021.11.047.
94. Ramasamy, P.; Szabo, A.; Borzel, S.; Eckert, J.; Stoica, M.; Bárdos, A. High Pressure Die Casting of Fe-Based Metallic Glass. *Sci. Rep.* **2016**, *6*, 35258, doi:10.1038/srep35258.
95. Liu, L.; Zhang, T.; Liu, Z.; Wang, C.; He, L.; Li, P.; Li, W.; Li, L. Abnormal Increase of Glass Forming Ability under Rising Mold Temperature in High Pressure Die Casting. *Mater. Lett.* **2019**, *247*, 215–218, doi:10.1016/j.matlet.2019.03.127.

96. Liu, L.H.; Ma, J.; Yu, C.Y.; Huang, X.S.; He, L.J.; Zhang, L.C.; Li, P.J.; Liu, Z.Y. Determination of Forming Ability of High Pressure Die Casting for Zr-Based Metallic Glass. *J. Mater. Process. Technol.* **2017**, *244*, 87–96, doi:10.1016/j.jmatprotec.2017.01.015.
97. Zhao, Y.; Kou, S.; Suo, H.; Wang, R.; Ding, Y. Overheating Effects on Thermal Stability and Mechanical Properties of Cu₃₆Zr₄₈Ag₈Al₈ Bulk Metallic Glass. *Mater. Des.* **2010**, *31*, 1029–1032, doi:10.1016/j.matdes.2009.07.028.
98. Kim, Y.J.; Busch, R.; Johnson, W.L.; Rulison, A.J.; Rhim, W.K. Experimental Determination of a Time-Temperature-Transformation Diagram of the Undercooled Zr_{41.2}Ti_{13.8}Cu_{12.5}Ni_{10.0}Be_{22.5} Alloy Using the Containerless Electrostatic Levitation Processing Technique. *Appl. Phys. Lett.* **1996**, *68*, 1057–1059, doi:10.1063/1.116247.
99. Zhang, G.; Wang, Q.; Yuan, C.; Yang, W.; Zhou, J.; Xue, L.; Hu, F.; Sun, B.; Shen, B. Effects of Cu Additions on Mechanical and Soft-Magnetic Properties of CoFeBSiNb Bulk Metallic Glasses. *J. Alloys Compd.* **2018**, *737*, 815–820, doi:10.1016/j.jallcom.2017.12.176.
100. Functional Applications of Metallic Glasses in Electrocatalysis - Hu - 2019 - ChemCatChem - Wiley Online Library Available online: <https://chemistry-europe.onlinelibrary.wiley.com/doi/10.1002/cctc.201900293> (accessed on 2 January 2024).
101. Yu, P.; Zhang, N.Z.; Cui, Y.T.; Wen, L.; Zeng, Z.Y.; Xia, L. Achieving an Enhanced Magneto-Caloric Effect by Melt Spinning a Gd₅₅Co₂₅Al₂₀ Bulk Metallic Glass into Amorphous Ribbons. *J. Alloys Compd.* **2016**, *655*, 353–356, doi:10.1016/j.jallcom.2015.09.205.
102. Hilzinger, H. Applications of Metallic Glasses in the Electronics Industry. *IEEE Trans. Magn.* **1985**, *21*, 2020–2025, doi:10.1109/TMAG.1985.1064009.
103. Development of Ferromagnetic Metallic Glasses into Low Loss Power Transformer Cores - ProQuest Available online: <https://www.proquest.com/openview/bba2489fadb0cba750453f057b687c43/1?pq-origsite=gscholar&cbl=18750&diss=y> (accessed on 2 January 2024).
104. Ramanan, V.R.V. Metallic Glasses in Distribution Transformer Applications: An Update. *J. Mater. Eng.* **1991**, *13*, 119–127, doi:10.1007/BF02995816.
105. Nanocrystalline and Nanocomposite Permanent Magnets by Melt Spinning Technique Available online: https://cpb.iphy.ac.cn/article/2018/1962/cpb_27_11_117502.html (accessed on 19 November 2024).
106. Wu, Y.; Zhang, Z.; Chen, W.; Li, Z. A Multiple Twin-Roller Casting Technique for Producing Metallic Glass and Metallic Glass Composite Strips. *Materials* **2019**, *12*, 3842, doi:10.3390/ma12233842.
107. Review on Plasma Atomizer Technology for Metal Powder | MATEC Web of Conferences Available online: https://www.matec-conferences.org/articles/mateconf/abs/2019/18/mateconf_iiw18_05004/mateconf_iiw18_05004.html (accessed on 6 March 2024).
108. Beckers, D.; Ellendt, N.; Fritsching, U.; Uhlenwinkel, V. Impact of Process Flow Conditions on Particle Morphology in Metal Powder Production via Gas Atomization. *Adv. Powder Technol.* **2020**, *31*, 300–311, doi:10.1016/j.apt.2019.10.022.
109. Achelis, L.; Uhlenwinkel, V. Characterisation of Metal Powders Generated by a Pressure-Gas-Atomiser. *Mater. Sci. Eng. A* **2008**, *477*, 15–20, doi:10.1016/j.msea.2007.07.095.
110. Özbilen, S. Satellite Formation Mechanism in Gas Atomised Powders. *Powder Metall.* **1999**, *42*, 70–78, doi:10.1179/pom.1999.42.1.70.
111. Asgarian, A.; Tang, Z.; Bussmann, M.; Chattopadhyay, K. Water Atomisation of Metal Powders: Effect of Water Spray Configuration. *Powder Metall.* **2020**, *63*, 288–299, doi:10.1080/00325899.2020.1802558.
112. Laha, T.; Balani, K.; Agarwal, A.; Patil, S.; Seal, S. Synthesis of Nanostructured Spherical Aluminum Oxide Powders by Plasma Engineering. *Metall. Mater. Trans. A* **2005**, *36*, 301–309, doi:10.1007/s11661-005-0303-0.
113. Jahns, K.; Bappert, R.; Böhlke, P.; Krupp, U. Additive Manufacturing of CuCr1Zr by Development of a Gas Atomization and Laser Powder Bed Fusion Routine. *Int. J. Adv. Manuf. Technol.* **2020**, *107*, 2151–2161, doi:10.1007/s00170-020-04941-7.
114. Soong, S.Z.; Lai, W.L.; Kay Lup, A.N. Atomization of Metal and Alloy Powders: Processes, Parameters, and Properties. *AIChE J.* **2023**, *69*, e18217, doi:10.1002/aic.18217.
115. Wallner, S. Powder Production Technologies. *BHM Berg- Hüttenmänn. Monatshefte* **2019**, *164*, 108–111, doi:10.1007/s00501-019-0832-2.
116. (1) (PDF) Selective Laser Melting of 316L Austenitic Stainless Steel: Detailed Process Understanding Using Multiphysics Simulation and Experimentation Available online: https://www.researchgate.net/publication/352480236_Selective_Laser_Melting_of_316L_Austenitic_Stainless_Steel_Detailed_Process_Understanding_Using_Multiphysics_Simulation_and_Experimentation (accessed on 2 January 2024).
117. Wang, L.; Wang, H.; Liu, Y.; Fu, Z.; Peng, T.; Shen, J.; Zhou, S.; Yan, M.; Wang, G.; Dai, Y. Selective Laser Melting Helps Fabricate Record-Large Bulk Metallic Glass: Experiments, Simulation and Demonstrative Part. *J. Alloys Compd.* **2019**, *808*, 151731, doi:10.1016/j.jallcom.2019.151731.

118. Ouyang, D.; Zhang, P.; Zhang, C.; Liu, L. Understanding of Crystallization Behaviors in Laser 3D Printing of Bulk Metallic Glasses. *Appl. Mater. Today* **2021**, *23*, 100988, doi:10.1016/j.apmt.2021.100988.
119. Yang, C.; Zhang, C.; Xing, W.; Liu, L. 3D Printing of Zr-Based Bulk Metallic Glasses with Complex Geometries and Enhanced Catalytic Properties. *Intermetallics* **2018**, *94*, 22–28, doi:10.1016/j.intermet.2017.12.018.
120. Wu, W.; Li, X.; Liu, Q.; Hsi Fuh, J.Y.; Zheng, A.; Zhou, Y.; Ren, L.; Li, G. Additive Manufacturing of Bulk Metallic Glass: Principles, Materials and Prospects. *Mater. Today Adv.* **2022**, *16*, 100319, doi:10.1016/j.mtadv.2022.100319.
121. Lashgari, H.R.; Ferry, M.; Li, S. Additive Manufacturing of Bulk Metallic Glasses: Fundamental Principle, Current/Future Developments and Applications. *J. Mater. Sci. Technol.* **2022**, *119*, 131–149, doi:10.1016/j.jmst.2021.09.068.
122. Zhang, C.; Li, X.; Liu, S.-Q.; Liu, H.; Yu, L.-J.; Liu, L. 3D Printing of Zr-Based Bulk Metallic Glasses and Components for Potential Biomedical Applications. *J. Alloys Compd.* **2019**, *790*, 963–973, doi:10.1016/j.jallcom.2019.03.275.
123. Zhao, R.; Chen, C.; Wang, W.; Cao, T.; Shuai, S.; Xu, S.; Hu, T.; Liao, H.; Wang, J.; Ren, Z. On the Role of Volumetric Energy Density in the Microstructure and Mechanical Properties of Laser Powder Bed Fusion Ti-6Al-4V Alloy. *Addit. Manuf.* **2022**, *51*, 102605, doi:10.1016/j.addma.2022.102605.
124. Donik, Č.; Kraner, J.; Paulin, I.; Godec, M. Influence of the Energy Density for Selective Laser Melting on the Microstructure and Mechanical Properties of Stainless Steel. *Metals* **2020**, *10*, 919, doi:10.3390/met10070919.
125. Nong, X.D.; Zhou, X.L.; Ren, Y.X. Fabrication and Characterization of Fe-Based Metallic Glasses by Selective Laser Melting. *Opt. Laser Technol.* **2019**, *109*, 20–26, doi:10.1016/j.optlastec.2018.07.059.
126. Aboulkhair, N.T.; Everitt, N.M.; Ashcroft, I.; Tuck, C. Reducing Porosity in AlSi10Mg Parts Processed by Selective Laser Melting. *Addit. Manuf.* **2014**, *1–4*, 77–86, doi:10.1016/j.addma.2014.08.001.
127. Li, N.; Zhang, J.; Xing, W.; Ouyang, D.; Liu, L. 3D Printing of Fe-Based Bulk Metallic Glass Composites with Combined High Strength and Fracture Toughness. *Mater. Des.* **2018**, *143*, 285–296, doi:10.1016/j.matdes.2018.01.061.
128. Haboudou, A.; Peyre, P.; Vannes, A.B.; Peix, G. Reduction of Porosity Content Generated during Nd:YAG Laser Welding of A356 and AA5083 Aluminium Alloys. *Mater. Sci. Eng. A* **2003**, *363*, 40–52, doi:10.1016/S0921-5093(03)00637-3.
129. Thermocapillary Mechanism of Melt Displacement during Keyhole Formation by the Laser Beam - IOPscience Available online: https://iopscience.iop.org/article/10.1088/0022-3727/42/17/175501/meta?casa_token=IEERo6p99Y8AAAAA:wWZx7temPXssYjCmARWV8qa5pYERK1rDmHaBTBp9FQlKJuAuvrA7MUxJS_k3BWfR_G-wKXcXdqqx (accessed on 16 March 2023).
130. Ma, C.; Zhao, J.; Cao, C.; Lin, T.-C.; Li, X. Fundamental Study on Laser Interactions With Nanoparticles-Reinforced Metals—Part II: Effect of Nanoparticles on Surface Tension, Viscosity, and Laser Melting. *J. Manuf. Sci. Eng.* **2016**, *138*, doi:10.1115/1.4033446.
131. Giorgiutti-Dauphiné, F.; Pauchard, L. Drying Drops. *Eur. Phys. J. E* **2018**, *41*, 32, doi:10.1140/epje/i2018-11639-2.
132. Cabanettes, F.; Joubert, A.; Chardon, G.; Dumas, V.; Rech, J.; Grosjean, C.; Dimkovski, Z. Topography of as Built Surfaces Generated in Metal Additive Manufacturing: A Multi Scale Analysis from Form to Roughness. *Precis. Eng.* **2018**, *52*, 249–265, doi:10.1016/j.precisioneng.2018.01.002.
133. Jiang, Q.; Zhang, P.; Tan, J.; Yu, Z.; Tian, Y.; Ma, S.; Wu, D. Influence of the Microstructure on Mechanical Properties of SLM Additive Manufacturing Fe-Based Bulk Metallic Glasses. *J. Alloys Compd.* **2022**, *894*, 162525, doi:10.1016/j.jallcom.2021.162525.
134. Zou, Y.M.; Wu, Y.S.; Li, K.F.; Tan, C.L.; Qiu, Z.G.; Zeng, D.C. Selective Laser Melting of Crack-Free Fe-Based Bulk Metallic Glass via Chessboard Scanning Strategy. *Mater. Lett.* **2020**, *272*, 127824, doi:10.1016/j.matlet.2020.127824.
135. Gu, D.; He, B. Finite Element Simulation and Experimental Investigation of Residual Stresses in Selective Laser Melted Ti–Ni Shape Memory Alloy. *Comput. Mater. Sci.* **2016**, *117*, 221–232, doi:10.1016/j.commatsci.2016.01.044.
136. Gaur, A.; Pandel, U.; Sharma, S. A Study of Investigating the Effects of Variables and Assessing the Efficiency of Air Plasma Spray as a Coating Technique. *Mater. Today Proc.* **2023**, doi:10.1016/j.matpr.2023.11.096.
137. Bijalwan, P.; Kumar, A.; Nayak, S.K.; Banerjee, A.; Dutta, M.; Laha, T. Microstructure and Corrosion Behavior of Fe-Based Amorphous Composite Coatings Developed by Atmospheric Plasma Spraying. *J. Alloys Compd.* **2019**, *796*, 47–54, doi:10.1016/j.jallcom.2019.05.046.
138. Moss, M.; Smith, D.L.; Lefever, R.A. METASTABLE PHASES AND SUPERCONDUCTORS PRODUCED BY PLASMA-JET SPRAYING. *Appl. Phys. Lett.* **1964**, *5*, 120–121, doi:10.1063/1.1723612.
139. Huang, B.; Zhang, C.; Zhang, G.; Liao, H. Wear and Corrosion Resistant Performance of Thermal-Sprayed Fe-Based Amorphous Coatings: A Review. *Surf. Coat. Technol.* **2019**, *377*, 124896, doi:10.1016/j.surfcoat.2019.124896.

140. Hui, R.; Wang, Z.; Kesler, O.; Rose, L.; Jankovic, J.; Yick, S.; Maric, R.; Ghosh, D. Thermal Plasma Spraying for SOFCs: Applications, Potential Advantages, and Challenges. *J. Power Sources* **2007**, *170*, 308–323, doi:10.1016/j.jpowsour.2007.03.075.
141. Tang, L.; He, P.; Kang, J.; Wang, L.; Ding, S.; Chen, S.; Zhu, X.; Xie, F.; Zhou, L.; Ma, G.; et al. Significantly Enhanced Mechanical and Tribological Properties of Co-Based Alloy Coatings by Annealing Treatment. *Tribol. Int.* **2020**, *146*, 106265, doi:10.1016/j.triboint.2020.106265.
142. Lee, J.; Lee, S.; Han, H.N.; Kim, W.; Hwang, N.-M. Yttrium Oxyfluoride Coatings Deposited by Suspension Plasma Spraying Using Coaxial Feeding. *Coatings* **2020**, *10*, 481, doi:10.3390/coatings10050481.
143. An, Y.; Hou, G.; Chen, J.; Zhao, X.; Liu, G.; Zhou, H.; Chen, J. Microstructure and Tribological Properties of Iron-Based Metallic Glass Coatings Prepared by Atmospheric Plasma Spraying. *Vacuum* **2014**, *107*, 132–140, doi:10.1016/j.vacuum.2014.04.021.
144. Jiang, C.; Xing, Y.; Zhang, F.; Hao, J. Microstructure and Corrosion Resistance of Fe/Mo Composite Amorphous Coatings Prepared by Air Plasma Spraying. *Int. J. Miner. Metall. Mater.* **2012**, *19*, 657–662, doi:10.1007/s12613-012-0609-z.
145. Liu, G.; An, Y.; Guo, Z.; Chen, J.; Hou, G.; Chen, J. Structure and Corrosion Behavior of Iron-Based Metallic Glass Coatings Prepared by LPPS. *Appl. Surf. Sci.* **2012**, *258*, 5380–5386, doi:10.1016/j.apsusc.2012.02.015.
146. Sodeoka, S.; Suzuki, M.; Ueno, K. Effects of High-Pressure Plasma Spraying for Yttria-Stabilized Zirconia Coating. *J. Therm. Spray Technol.* **1996**, *5*, 277–282, doi:10.1007/BF02645878.
147. Pawlowski, L. Suspension and Solution Thermal Spray Coatings. *Surf. Coat. Technol.* **2009**, *203*, 2807–2829, doi:10.1016/j.surfcoat.2009.03.005.
148. Fauchais, P.; Joulia, A.; Goutier, S.; Chazelas, C.; Vardelle, M.; Vardelle, A.; Rossignol, S. Suspension and Solution Plasma Spraying. *J. Phys. Appl. Phys.* **2013**, *46*, doi:10.1088/0022-3727/46/22/224015.
149. Fan, W.; Bai, Y. Review of Suspension and Solution Precursor Plasma Sprayed Thermal Barrier Coatings. *Ceram. Int.* **2016**, *42*, 14299–14312, doi:10.1016/j.ceramint.2016.06.063.
150. Nouri, A.; Sola, A. Powder Morphology in Thermal Spraying. *J. Adv. Manuf. Process.* **2019**, *1*, e10020, doi:10.1002/amp.2.10020.
151. Killinger, A. 4 - Status and Future Trends in Suspension Spray Techniques. In *Future Development of Thermal Spray Coatings*; Espallargas, N., Ed.; Woodhead Publishing, 2015; pp. 81–122 ISBN 978-0-85709-769-9.
152. Yin, Z.; Tao, S.; Zhou, X.; Ding, C. Particle In-Flight Behavior and Its Influence on the Microstructure and Mechanical Properties of Plasma-Sprayed Al₂O₃ Coatings. *J. Eur. Ceram. Soc.* **2008**, *28*, 1143–1148, doi:10.1016/j.jeurceramsoc.2007.09.050.
153. Zhang, H.; Xie, Y.; Huang, L.; Huang, S.; Zheng, X.; Chen, G. Effect of Feedstock Particle Sizes on Wear Resistance of Plasma Sprayed Fe-Based Amorphous Coatings. *Surf. Coat. Technol.* **2014**, *258*, 495–502, doi:10.1016/j.surfcoat.2014.08.050.
154. Zhang, C.; Guo, R.Q.; Yang, Y.; Wu, Y.; Liu, L. Influence of the Size of Spraying Powders on the Microstructure and Corrosion Resistance of Fe-Based Amorphous Coating. *Electrochimica Acta* **2011**, *56*, 6380–6388, doi:10.1016/j.electacta.2011.05.020.
155. Niu, Y.; Zheng, X.; Liu, X.; Ji, H.; Ding, C. Influence of Powder Size on Characteristics of Air Plasma Sprayed Silicon Coatings. *Ceram. Int.* **2012**, *38*, 5897–5905, doi:10.1016/j.ceramint.2012.03.080.
156. Souza, C.A.C.; Ribeiro, D.V.; Kiminami, C.S. Corrosion Resistance of Fe-Cr-Based Amorphous Alloys: An Overview. *J. Non-Cryst. Solids* **2016**, *442*, 56–66, doi:10.1016/j.jnoncrysol.2016.04.009.
157. Suresh, K.; Yugeswaran, S.; Rao, K.P.; Kobayashi, A.; Shum, P.W. Sliding Wear Behavior of Gas Tunnel Type Plasma Sprayed Ni-Based Metallic Glass Composite Coatings. *Vacuum* **2013**, *88*, 114–117, doi:10.1016/j.vacuum.2012.02.010.
158. Yugeswaran, S.; Kobayashi, A. Metallic Glass Coatings Fabricated by Gas Tunnel Type Plasma Spraying. *Vacuum* **2014**, *110*, 177–182, doi:10.1016/j.vacuum.2014.04.016.
159. Bijalwan, P.; Singh, C.; Kumar, A.; Sarkar, K.; Rani, N.; Laha, T.; Banerjee, A.; Mondal, K. Corrosion Behaviour of Plasma Sprayed Fe Based Metallic Glass (Fe₇₃Cr₂Si₁₁B₁₁C₃ (At%)) Coatings in 3.5% NaCl Solution. *J. Non-Cryst. Solids* **2021**, *567*, 120913, doi:10.1016/j.jnoncrysol.2021.120913.
160. Kim, J.; Kang, K.; Yoon, S.; Lee, C. Enhancement of Metallic Glass Properties of Cu-Based BMG Coating by Shroud Plasma Spraying. *Surf. Coat. Technol.* **2011**, *205*, 3020–3026, doi:10.1016/j.surfcoat.2010.11.012.
161. Du, P.; Wu, Z.; Li, K.; Xiang, T.; Xie, G. Porous Ti-Based Bulk Metallic Glass Orthopedic Biomaterial with High Strength and Low Young's Modulus Produced by One Step SPS. *J. Mater. Res. Technol.* **2021**, *13*, 251–259, doi:10.1016/j.jmrt.2021.04.084.
162. Kim, K.-W.; Ham, G.-S.; Cho, G.-S.; Kim, C.P.; Park, S.-C.; Lee, K.-A. Microstructures and Corrosion Properties of Novel Fe_{46.8}-Mo_{30.6}-Cr_{16.6}-C_{4.3}-B_{1.7} Metallic Glass Coatings Manufactured by Vacuum Plasma Spray Process. *Intermetallics* **2021**, *130*, 107061, doi:10.1016/j.intermet.2020.107061.

163. Li, G.; Gan, Y.; Liu, C.; Shi, Y.; Zhao, Y.; Kou, S. Corrosion and Wear Resistance of Fe-Based Amorphous Coatings. *Coatings* **2020**, *10*, 73, doi:10.3390/coatings10010073.
164. Factors That Influence Splat Formation Available online: <https://www.sciencelearn.org.nz/images/252-factors-that-influence-splat-formation> (accessed on 12 March 2024).
165. A Structural Model for Metallic Glasses | Nature Materials Available online: <https://www.nature.com/articles/nmat1219> (accessed on 5 January 2024).
166. Miracle, D.B. The Efficient Cluster Packing Model – An Atomic Structural Model for Metallic Glasses. *Acta Mater.* **2006**, *54*, 4317–4336, doi:10.1016/j.actamat.2006.06.002.
167. Atomic Packing and Short-to-Medium-Range Order in Metallic Glasses | Nature Available online: <https://www.nature.com/articles/nature04421> (accessed on 5 January 2024).
168. Ashby, M.F.; Greer, A.L. Metallic Glasses as Structural Materials. *Scr. Mater.* **2006**, *54*, 321–326, doi:10.1016/j.scriptamat.2005.09.051.
169. Nazhat, S.N.; Rodríguez, J.V.C. 13 - Dynamic Mechanical Properties of Bone Cements. In *Orthopaedic Bone Cements*; Deb, S., Ed.; Woodhead Publishing Series in Biomaterials; Woodhead Publishing, 2008; pp. 296–310 ISBN 978-1-84569-376-3.
170. Zhang, H.; Subhash, G.; Jing, X.; Kecskes, L.; Dowding, R. Evaluation of Hardness–Yield Strength Relationships for Bulk Metallic Glasses. *Philos. Mag. Lett.* **2006**, *86*, 333–345, doi:10.1080/09500830600788935.
171. Wang, J.; Li, R.; Hua, N.; Zhang, T. Co-Based Ternary Bulk Metallic Glasses with Ultrahigh Strength and Plasticity. *J. Mater. Res.* **2011**, *26*, 2072–2079, doi:10.1557/jmr.2011.187.
172. Zhang, H.; Qian, Y.; Zhang, L.; Jiang, M.; Huang, H.; Yan, J. Significant Improvement in Surface Hardness of Zr-Based Metallic Glass by Nanosecond Pulsed Laser Irradiation in Graphite Powder Water Suspension. *Surf. Coat. Technol.* **2023**, *454*, 129195, doi:10.1016/j.surfcoat.2022.129195.
173. Sarker, S.; Tang-Kong, R.; Schoepner, R.; Ward, L.; Hasan, N.A.; Van Campen, D.G.; Takeuchi, I.; Hatrick-Simpers, J.; Zakutayev, A.; Packard, C.E.; et al. Discovering Exceptionally Hard and Wear-Resistant Metallic Glasses by Combining Machine-Learning with High Throughput Experimentation. *Appl. Phys. Rev.* **2022**, *9*, 011403, doi:10.1063/5.0068207.
174. Wang, W.H. The Elastic Properties, Elastic Models and Elastic Perspectives of Metallic Glasses. *Prog. Mater. Sci.* **2012**, *57*, 487–656, doi:10.1016/j.pmatsci.2011.07.001.
175. Inoue, A.; Shen, B.L.; Koshiba, H.; Kato, H.; Yavari, A.R. Ultra-High Strength above 5000 MPa and Soft Magnetic Properties of Co–Fe–Ta–B Bulk Glassy Alloys. *Acta Mater.* **2004**, *52*, 1631–1637, doi:10.1016/j.actamat.2003.12.008.
176. Lai, L.; He, R.; Ding, K.; Liu, T.; Liu, R.; Chen, Y.; Guo, S. Ternary Co–Mo–B Bulk Metallic Glasses with Ultrahigh Strength and Good Ductility. *J. Non-Cryst. Solids* **2019**, *524*, 119657, doi:10.1016/j.jnoncrysol.2019.119657.
177. Xin-Quan, W.; Jia-Zi, B.; Ran, L. Development of Ultrahigh Strength Bulk Metallic Glasses. *ACTA Phys. Sin.* **2017**, *66*.
178. Zhu, C.L.; Wang, Q.; Wang, Y.M.; Qiang, J.B.; Dong, C. Co–B–Si–Ta Bulk Metallic Glasses Designed Using Cluster Line and Alloying. *J. Alloys Compd.* **2010**, *504*, S34–S37, doi:10.1016/j.jallcom.2010.04.065.
179. Prakash, B. Abrasive Wear Behaviour of Fe, Co and Ni Based Metallic Glasses. *Wear* **2005**, *258*, 217–224, doi:10.1016/j.wear.2004.09.010.
180. Si, J.J.; Wang, T.; Wu, Y.D.; Cai, Y.H.; Chen, X.H.; Wang, W.Y.; Liu, Z.K.; Hui, X.D. Cr-Based Bulk Metallic Glasses with Ultrahigh Hardness. *Appl. Phys. Lett.* **2015**, *106*, doi:10.1063/1.4923210.
181. Chen, H.S.; Krause, J.T.; Coleman, E. Elastic Constants, Hardness and Their Implications to Flow Properties of Metallic Glasses. *J. Non-Cryst. Solids* **1975**, *18*, 157–171, doi:10.1016/0022-3093(75)90018-6.
182. Zhang, Y.; Zhao, D.Q.; Wei, B.C.; Wen, P.; Pan, M.X.; Wang, W.H. Formation and Properties of Zr₄₈Nb₈Fe₈Cu₁₂Be₂₄ Bulk Metallic Glass. *J. Mater. Res.* **2001**, *16*, 1675–1679, doi:10.1557/JMR.2001.0232.
183. Gu, X.; Shiflet, G.J.; Guo, F.Q.; Poon, S.J. Mg–Ca–Zn Bulk Metallic Glasses with High Strength and Significant Ductility. *J. Mater. Res.* **2005**, *20*, 1935–1938, doi:10.1557/JMR.2005.0245.
184. Prakash, B.; Hiratsuka, K. Sliding Wear Behaviour of Some Fe-, Co- and Ni-Based Metallic Glasses during Rubbing against Bearing Steel. *Tribol. Lett.* **2000**, *8*, 153–160, doi:10.1023/a:1019191303146.
185. Laws, K.J.; Shamlaye, K.F.; Gun, B.; Ferry, M. Synthesis of Copper-Based Bulk Metallic Glasses in the Ternary Cu–Mg–Ca System. *J. Alloys Compd.* **2009**, *486*, L27–L29, doi:10.1016/j.jallcom.2009.06.205.
186. Lai, L.; Ding, K.; Liu, T.; Chen, Y.; Guo, S. Ternary Co–W–B Bulk Metallic Glasses with Ultrahigh Strength. *J. Non-Cryst. Solids* **2020**, *544*, 120194, doi:10.1016/j.jnoncrysol.2020.120194.
187. Oliver, W.C.; Pharr, G.M. An Improved Technique for Determining Hardness and Elastic Modulus Using Load and Displacement Sensing Indentation Experiments. *J. Mater. Res.* **1992**, *7*, 1564–1583, doi:10.1557/JMR.1992.1564.
188. Instrumented indentation testing (IIT) :: Anton Paar Wiki Available online: <https://wiki.anton-paar.com/pl-pl/badanie-metoda-indentacji-instrumentalnej-iit/> (accessed on 8 January 2021).

189. Sneddon, I.N. The Relation between Load and Penetration in the Axisymmetric Boussinesq Problem for a Punch of Arbitrary Profile. *Int. J. Eng. Sci.* **1965**, *3*, 47–57, doi:10.1016/0020-7225(65)90019-4.
190. Madge, S.V.; Louzguine-Luzgin, D.V.; Lewandowski, J.J.; Greer, A.L. Toughness, Extrinsic Effects and Poisson's Ratio of Bulk Metallic Glasses. *Acta Mater.* **2012**, *60*, 4800–4809, doi:10.1016/j.actamat.2012.05.025.
191. Wei, Y.; Lei, X.; Huo, L.-S.; Wang, W.-H.; Greer, A.L. Towards More Uniform Deformation in Metallic Glasses: The Role of Poisson's Ratio. *Mater. Sci. Eng. A* **2013**, *560*, 510–517, doi:10.1016/j.msea.2012.09.096.
192. Jiang, M.; Dai, L. Intrinsic Correlation between Fragility and Bulk Modulus in Metallic Glasses. *Phys. Rev. B* **2007**, *76*, 054204, doi:10.1103/PhysRevB.76.054204.
193. Cheng, Y.Q.; Cao, A.J.; Ma, E. Correlation between the Elastic Modulus and the Intrinsic Plastic Behavior of Metallic Glasses: The Roles of Atomic Configuration and Alloy Composition. *Acta Mater.* **2009**, *57*, 3253–3267, doi:10.1016/j.actamat.2009.03.027.
194. Baricco, M.; Baser, T.A.; Das, J.; Eckert, J. Correlation between Poisson Ratio and Mohr–Coulomb Coefficient in Metallic Glasses. *J. Alloys Compd.* **2009**, *483*, 125–131, doi:10.1016/j.jallcom.2008.07.213.
195. Keryvin, V.; Hoang, V.H.; Shen, J. Hardness, Toughness, Brittleness and Cracking Systems in an Iron-Based Bulk Metallic Glass by Indentation. *Intermetallics* **2009**, *17*, 211–217, doi:10.1016/j.intermet.2008.08.017.
196. Shi, M.; Liu, Z.; Zhang, T. Effects of Metalloid B Addition on the Glass Formation, Magnetic and Mechanical Properties of FePCB Bulk Metallic Glasses. *J. Mater. Sci. Technol.* **2015**, *31*, 493–497, doi:10.1016/j.jmst.2014.10.009.
197. Zhang, T.; Yang, Q.; Ji, Y.; Li, R.; Pang, S.; Wang, J.; Xu, T. Centimeter-Scale-Diameter Co-Based Bulk Metallic Glasses with Fracture Strength Exceeding 5000 MPa. *Chin. Sci. Bull.* **2011**, *56*, 3972–3977, doi:10.1007/s11434-011-4765-8.
198. Lai, L.; He, R.; Ding, K.; Liu, T.; Liu, R.; Chen, Y.; Guo, S. Ternary Co-Mo-B Bulk Metallic Glasses with Ultrahigh Strength and Good Ductility. *J. Non-Cryst. Solids* **2019**, *524*, 119657, doi:10.1016/j.jnoncrysol.2019.119657.
199. Cardarelli, F. *Materials Handbook: A Concise Desktop Reference*; 2nd ed.; Springer-Verlag: London, 2008; ISBN 978-1-84628-669-8.
200. Singh, D.; Mandal, R.K.; Tiwari, R.S.; Srivastava, O.N.; Singh, D.; Mandal, R.K.; Tiwari, R.S.; Srivastava, O.N. Mechanical Behavior of Zr-Based Metallic Glasses and Their Nanocomposites. In *Metallic Glasses - Formation and Properties*; IntechOpen, 2016 ISBN 978-953-51-2512-9.
201. Shrivastava, A. 3 - Plastic Properties and Testing. In *Introduction to Plastics Engineering*; Shrivastava, A., Ed.; Plastics Design Library; William Andrew Publishing, 2018; pp. 49–110 ISBN 978-0-323-39500-7.
202. Greer, A.L.; Rutherford, K.L.; Hutchings, I.M. Wear Resistance of Amorphous Alloys and Related Materials. *Int. Mater. Rev.* **2002**, *47*, 87–112, doi:10.1179/095066001225001067.
203. Liao, Z.; Hua, N.; Chen, W.; Huang, Y.; Zhang, T. Correlations between the Wear Resistance and Properties of Bulk Metallic Glasses. *Intermetallics* **2018**, *93*, 290–298, doi:10.1016/j.intermet.2017.10.008.
204. Kumar, A.; Li, D.Y. Can the H/E Ratio Be Generalized as an Index for the Wear Resistance of Materials? *Mater. Chem. Phys.* **2022**, *275*, 125245, doi:10.1016/j.matchemphys.2021.125245.
205. Amri, A.; Jiang, Z.-T.; Zhao, X.; Xie, Z.; Yin, C.-Y.; Ali, N.; Mondinos, N.; Rahman, M.M.; Habibi, D. Tailoring the Physicochemical and Mechanical Properties of Optical Copper–Cobalt Oxide Thin Films through Annealing Treatment. *Surf. Coat. Technol.* **2014**, *239*, 212–221, doi:10.1016/j.surfcoat.2013.11.044.
206. Zhai, W.; Bai, L.; Zhou, R.; Fan, X.; Kang, G.; Liu, Y.; Zhou, K. Recent Progress on Wear-Resistant Materials: Designs, Properties, and Applications. *Adv. Sci.* **2021**, *8*, 2003739, doi:10.1002/advs.202003739.
207. Tang, Y.; Pan, H.; Li, D.Y. Contribution of Cold-Work to the Wear Resistance of Materials and Its Limitation – A Study Combining Molecular Dynamics Modeling and Experimental Investigation. *Wear* **2021**, *476*, 203642, doi:10.1016/j.wear.2021.203642.
208. Wang, W.H. Dynamic Relaxations and Relaxation-Property Relationships in Metallic Glasses. *Prog. Mater. Sci.* **2019**, *106*, 100561, doi:10.1016/j.pmatsci.2019.03.006.
209. Chen, M. A Brief Overview of Bulk Metallic Glasses. *NPG Asia Mater.* **2011**, *3*, 82–90, doi:10.1038/asiamat.2011.30.
210. Chen, M. Mechanical Behavior of Metallic Glasses: Microscopic Understanding of Strength and Ductility. *Annu. Rev. Mater. Res.* **2008**, *38*, 445–469, doi:10.1146/annurev.matsci.38.060407.130226.
211. Wang, W.H. Bulk Metallic Glasses with Functional Physical Properties. *Adv. Mater.* **2009**, *21*, 4524–4544, doi:10.1002/adma.200901053.
212. Inoue, A. Stabilization of Metallic Supercooled Liquid and Bulk Amorphous Alloys. *Acta Mater.* **2000**, *48*, 279–306, doi:10.1016/S1359-6454(99)00300-6.
213. Wang, W.H.; Dong, C.; Shek, C.H. Bulk Metallic Glasses. *Mater. Sci. Eng. R Rep.* **2004**, *44*, 45–89, doi:10.1016/j.mser.2004.03.001.
214. Wang, W.H. Roles of Minor Additions in Formation and Properties of Bulk Metallic Glasses. *Prog. Mater. Sci.* **2007**, *52*, 540–596, doi:10.1016/j.pmatsci.2006.07.003.

215. Schuh, C.A.; Hufnagel, T.C.; Ramamurty, U. Mechanical Behavior of Amorphous Alloys. *Acta Mater.* **2007**, *55*, 4067–4109.
216. Johnson, W.L. Bulk Glass-Forming Metallic Alloys: Science and Technology. *MRS Bull.* **1999**, *24*, 42–56.
217. Kabadev, A.; Hossain, S.; Larsson, P. Molecular Dynamics Simulations as a Tool to Understand Drug Solubilization in Pharmaceutical Systems. In *Comprehensive Computational Chemistry (First Edition)*; Yáñez, M., Boyd, R.J., Eds.; Elsevier: Oxford, 2024; pp. 865–885 ISBN 978-0-12-823256-9.
218. Cohen, M.H.; Turnbull, D. Molecular Transport in Liquids and Glasses. *J. Chem. Phys.* **1959**, *31*, 1164–1169.
219. Free-Volume Model of the Amorphous Phase: Glass Transition | The Journal of Chemical Physics | AIP Publishing Available online: <https://pubs.aip.org/aip/jcp/article-abstract/34/1/120/207179/Free-Volume-Model-of-the-Amorphous-Phase-Glass> (accessed on 21 March 2024).
220. On the Free-Volume Model of the Liquid-Glass Transition | The Journal of Chemical Physics | AIP Publishing Available online: <https://pubs.aip.org/aip/jcp/article-abstract/52/6/3038/772535/On-the-Free-Volume-Model-of-the-Liquid-Glass> (accessed on 21 March 2024).
221. Gornostyrev, Y.N.; Katsnelson, M.I.; Trefilov, A.V. Close Packing of Atoms, Geometric Frustrations and the Formation of Heterogeneous States in Crystals. *J. Phys. Condens. Matter* **1997**, *9*, 7837–7844, doi:10.1088/0953-8984/9/37/014.
222. Spaepen, F. A Microscopic Mechanism for Steady State Inhomogeneous Flow in Metallic Glasses. *Acta Metall.* **1977**, *25*, 407–415, doi:10.1016/0001-6160(77)90232-2.
223. Plastic Deformation in Metallic Glasses - ScienceDirect Available online: <https://www.sciencedirect.com/science/article/abs/pii/0001616079900555> (accessed on 21 March 2024).
224. Chen, M.; Inoue, A.; Zhang, W.; Sakurai, T. Extraordinary Plasticity of Ductile Bulk Metallic Glasses. *Phys. Rev. Lett.* **2006**, *96*, 245502, doi:10.1103/PhysRevLett.96.245502.
225. Schroers, J.; Johnson, W.L. Ductile Bulk Metallic Glass. *Phys. Rev. Lett.* **2004**, *93*, 255506, doi:10.1103/PhysRevLett.93.255506.
226. Das, J.; Tang, M.B.; Kim, K.B.; Theissmann, R.; Baier, F.; Wang, W.H.; Eckert, J. “Work-Hardenable” Ductile Bulk Metallic Glass. *Phys. Rev. Lett.* **2005**, *94*, 205501, doi:10.1103/PhysRevLett.94.205501.
227. Kim, K.B.; Das, J.; Venkataraman, S.; Yi, S.; Eckert, J. Work Hardening Ability of Ductile Ti₄₅Cu₄₀Ni_{7.5}Zr₅Sn_{2.5} and Cu_{47.5}Zr_{47.5}Al₅ Bulk Metallic Glasses. *Appl. Phys. Lett.* **2006**, *89*, doi:10.1063/1.2337534.
228. Chen, H.S. Glassy Metals. *Rep. Prog. Phys.* **1980**, *43*, 353, doi:10.1088/0034-4885/43/4/001.
229. Lewandowski *, J.J.; Wang, W.H.; Greer, A.L. Intrinsic Plasticity or Brittleness of Metallic Glasses. *Philos. Mag. Lett.* **2005**, *85*, 77–87, doi:10.1080/09500830500080474.
230. Critical Poisson’s Ratio for Plasticity in Fe–Mo–C–B–Ln Bulk Amorphous Steel | Applied Physics Letters | AIP Publishing Available online: <https://pubs.aip.org/aip/apl/article-abstract/88/21/211905/331090/Critical-Poisson-s-ratio-for-plasticity-in-Fe-Mo-C?redirectedFrom=fulltext> (accessed on 4 April 2024).
231. Li, H.; Subhash, G.; Gao, X.-L.; Kecskes, L.J.; Dowding, R.J. Negative Strain Rate Sensitivity and Compositional Dependence of Fracture Strength in Zr/Hf Based Bulk Metallic Glasses. *Scr. Mater.* **2003**, *49*, 1087–1092, doi:10.1016/j.scriptamat.2003.08.012.
232. Zhang, H.; Subhash, G.; Kecskes, L.J.; Dowding, R.J. Mechanical Behavior of Bulk (ZrHf)TiCuNiAl Amorphous Alloys. *Scr. Mater.* **2003**, *49*, 447–452, doi:10.1016/S1359-6462(03)00295-1.
233. Ultrahigh Strength Al-Based Amorphous Alloys Containing Sc | Journal of Materials Research | Cambridge Core Available online: <https://www.cambridge.org/core/journals/journal-of-materials-research/article/abs/ultrahigh-strength-albased-amorphous-alloys-containing-sc/37F863C7719E957441FD9847218F8711> (accessed on 4 January 2024).
234. BURTON *Amorphous Metallic Alloys: Amorphous Metallic Alloys*; Elsevier, 2013; ISBN 978-1-4831-9243-7.
235. Formation and Mechanical Properties of Cu–Hf–Ti Bulk Glassy Alloys [Article Retracted] | Journal of Materials Research | Cambridge Core Available online: <https://www.cambridge.org/core/journals/journal-of-materials-research/article/formation-and-mechanical-properties-of-cuhfti-bulk-glassy-alloys-article-retracted/78293B8D5F576465BCEFD4936B7C0A9> (accessed on 4 January 2024).
236. Inoue, A.; Shen, B.L.; Chang, C.T. Super-High Strength of over 4000 MPa for Fe-Based Bulk Glassy Alloys in [(Fe_{1-x}Cox)_{0.75}B_{0.25}Si_{0.05}]₉₆Nb₄ System. *Acta Mater.* **2004**, *52*, 4093–4099, doi:10.1016/j.actamat.2004.05.022.
237. Conner, R.D.; Dandliker, R.B.; Johnson, W.L. Mechanical Properties of Tungsten and Steel Fiber Reinforced Zr_{41.25}Ti_{13.75}Cu_{12.5}Ni₁₀Be_{22.5} Metallic Glass Matrix Composites. *Acta Mater.* **1998**, *46*, 6089–6102, doi:10.1016/S1359-6454(98)00275-4.
238. Jin, K.; Löffler, J.F. Bulk Metallic Glass Formation in Zr–Cu–Fe–Al Alloys. *Appl. Phys. Lett.* **2005**, *86*, 241909, doi:10.1063/1.1948513.
239. Donovan, P.E.; Stobbs, W.M. The Structure of Shear Bands in Metallic Glasses. *Acta Metall.* **1981**, *29*, 1419–1436, doi:10.1016/0001-6160(81)90177-2.

240. Plastic Flow and Fracture of Pd40Ni40P20 Metallic Glass under an Indentor | Journal of Materials Science Available online: <https://link.springer.com/article/10.1007/BF01107437> (accessed on 4 January 2024).
241. Keryvin, V.; Eswar Prasad, K.; Gueguen, Y.; Sanglebœuf, J.-C.; Ramamurty, U. Temperature Dependence of Mechanical Properties and Pressure Sensitivity in Metallic Glasses below Glass Transition. *Philos. Mag.* **2008**, *88*, 1773–1790, doi:10.1080/14786430802286971.
242. Lee, J.K.; Bae, D.H.; Kim, W.T.; Kim, D.H. Effect of Liquid Temperature on Thermal Stability and Crystallization Behavior of Ni-Based Amorphous Alloys. *Mater. Sci. Eng. A* **2004**, *375–377*, 332–335, doi:10.1016/j.msea.2003.10.103.
243. Zhu, Z.W.; Zheng, S.J.; Zhang, H.F.; Ding, B.Z.; Hu, Z.Q.; Liaw, P.K.; Wang, Y.D.; Ren, Y. Plasticity of Bulk Metallic Glasses Improved by Controlling the Solidification Condition. *J. Mater. Res.* **2008**, *23*, 941–948, doi:10.1557/jmr.2008.0127.
244. Mondal, K.; Ohkubo, T.; Toyama, T.; Nagai, Y.; Hasegawa, M.; Hono, K. The Effect of Nanocrystallization and Free Volume on the Room Temperature Plasticity of Zr-Based Bulk Metallic Glasses. *Acta Mater.* **2008**, *56*, 5329–5339, doi:10.1016/j.actamat.2008.07.012.
245. Mondal, K.; Ohkubo, T.; Mukai, T.; Hono, K. Glass Forming Ability and Mechanical Properties of Quinary Zr-Based Bulk Metallic Glasses. *Mater. Trans.* **2007**, *48*, 1322–1326, doi:10.2320/matertrans.MF200621.
246. Kumar, G.; Ohkubo, T.; Hono, K. Effect of Melt Temperature on the Mechanical Properties of Bulk Metallic Glasses. *J. Mater. Res.* **2009**, *24*, 2353–2360, doi:10.1557/jmr.2009.0272.
247. Pang, S.J.; Zhang, T.; Asami, K.; Inoue, A. Synthesis of Fe–Cr–Mo–C–B–P Bulk Metallic Glasses with High Corrosion Resistance. *Acta Mater.* **2002**, *50*, 489–497, doi:10.1016/S1359-6454(01)00366-4.
248. Redaei, H.; Rezaei, P.; Seifoddini, A.; Hasani, S. Effect of Cooling Rate on Glass Forming Ability of Novel Fe-Based Bulk Metallic Glass. *Acta Phys. Pol. A* **2020**, *138*, 265–267, doi:10.12693/APhysPolA.138.265.
249. Li, F.; Zhang, H.; Liu, X.; Yu, C.; Lu, Z. Effects of Cooling Rate on the Atomic Structure of Cu64Zr36 Binary Metallic Glass. *Comput. Mater. Sci.* **2018**, *141*, 59–67, doi:10.1016/j.commatsci.2017.09.026.
250. Yue, X.X.; Liu, C.T.; Pan, S.Y.; Inoue, A.; Liaw, P.K.; Fan, C. Effect of Cooling Rate on Structures and Mechanical Behavior of Cu50Zr50 Metallic Glass: A Molecular-Dynamics Study. *Phys. B Condens. Matter* **2018**, *547*, 48–54, doi:10.1016/j.physb.2018.07.030.
251. Makino, A.; Kubota, T.; Makabe, M.; Chang, C.T.; Inoue, A. FeSiBP Metallic Glasses with High Glass-Forming Ability and Excellent Magnetic Properties. *Mater. Sci. Eng. B* **2008**, *148*, 166–170, doi:10.1016/j.mseb.2007.09.010.
252. Qi, T.; Li, Y.; Takeuchi, A.; Xie, G.; Miao, H.; Zhang, W. Soft Magnetic Fe25Co25Ni25(B, Si)25 High Entropy Bulk Metallic Glasses. *Intermetallics* **2015**, *66*, 8–12, doi:10.1016/j.intermet.2015.06.015.
253. Bhattacharya, S.; Lass, E.A.; Poon, S.J.; Shiflet, G.J. High Thermal Stability of Soft Magnetic (Fe,Co)–Mo–B–C–P–Si Metallic Glasses. *J. Alloys Compd.* **2009**, *488*, 79–83, doi:10.1016/j.jallcom.2009.08.114.
254. Jiang, L.; Bao, M.; Dong, Y.; Yuan, Y.; Zhou, X.; Meng, X. Processing, Production and Anticorrosion Behavior of Metallic Glasses: A Critical Review. *J. Non-Cryst. Solids* **2023**, *612*, 122355, doi:10.1016/j.jnoncrysol.2023.122355.
255. Corrosion Behavior of CoCrCuFeMnNi High-Entropy Alloys Prepared by Hot Pressing Sintered in 3.5% NaCl Solution - ScienceDirect Available online: <https://www.sciencedirect.com/science/article/pii/S221137971932090X> (accessed on 17 March 2024).
256. Jin, Z.S.; Yang, Y.J.; Zhang, Z.P.; Ma, X.Z.; Lv, J.W.; Wang, F.L.; Ma, M.Z.; Zhang, X.Y.; Liu, R.P. Effect of Hf Substitution Cu on Glass-Forming Ability, Mechanical Properties and Corrosion Resistance of Ni-Free Zr–Ti–Cu–Al Bulk Metallic Glasses. *J. Alloys Compd.* **2019**, *806*, 668–675, doi:10.1016/j.jallcom.2019.07.240.
257. Figueira, G.; Dulnee, S.; Koga, G.Y.; Cataldi, T.P.; Kiminami, C.S.; Kaufman, M.J.; Gargarella, P. Influence of Thermomechanical Post-Treatment on the Corrosion Behavior of Ni57Nb33Zr5Co5 Bulk Metallic Glass. *Mater. Lett.* **2021**, *288*, 129350, doi:10.1016/j.matlet.2021.129350.
258. Wu, Z.; Du, P.; Xiang, T.; Li, K.; Xie, G. Ti-Based Bulk Metallic Glass Implantable Biomaterial with Adjustable Porosity Produced by a Novel Pressure Regulation Method in Spark Plasma Sintering. *Intermetallics* **2021**, *131*, 107105, doi:10.1016/j.intermet.2021.107105.
259. Materials | Free Full-Text | Glass-Forming Ability and Corrosion Resistance of Al88Y8–xFe4+x (x = 0, 1, 2 at.%) Alloys Available online: <https://www.mdpi.com/1996-1944/14/7/1581> (accessed on 16 March 2024).
260. Vasić, M.M.; Žák, T.; Pizúrová, N.; Roupcová, P.; Minić, D.M.; Minić, D.M. Thermally Induced Microstructural Transformations and Anti-Corrosion Properties of Co70Fe5Si10B15 Amorphous Alloy. *J. Non-Cryst. Solids* **2018**, *500*, 326–335, doi:10.1016/j.jnoncrysol.2018.08.017.
261. Jiang, D.; Cui, H.; Song, X.; Zhao, X.; Chen, H.; Ma, G.; Cui, Z. Corrosion Behavior of CoCrNiMoBC Coatings Obtained by Laser Cladding: Synergistic Effects of Composition and Microstructure. *J. Alloys Compd.* **2022**, *911*, 164984, doi:10.1016/j.jallcom.2022.164984.

262. Woo, J.-H.; Park, S.-Y.; Koo, D.; Song, M.H.; Park, H.; Kim, J.-Y. Highly Elastic and Corrosion-Resistive Metallic Glass Thin Films for Flexible Encapsulation. *ACS Appl. Mater. Interfaces* **2022**, *14*, 5578–5585, doi:10.1021/acsami.1c20551.
263. Lee, S.-Y. Deformation Mechanisms of Bulk Metallic Glass Matrix Composites Available online: <https://www.semanticscholar.org/paper/Deformation-mechanisms-of-bulk-metallic-glass-Lee/1205d96d9cab15806a53222f0ade61075dd076c4> (accessed on 17 March 2024).
264. Sharma, P.; Inoue, A. Chapter Twenty Seven - Metallic Glass. In *Handbook of Silicon Based MEMS Materials and Technologies*; Lindroos, V., Tilli, M., Lehto, A., Motooka, T., Eds.; Micro and Nano Technologies; William Andrew Publishing: Boston, 2010; pp. 447–472 ISBN 978-0-8155-1594-4.
265. Salimon, A.I.; Ashby, M.F.; Bréchet, Y.; Greer, A.L. Bulk Metallic Glasses: What Are They Good For? *Mater. Sci. Eng. A* **2004**, *375–377*, 385–388, doi:10.1016/j.msea.2003.10.167.
266. Kakiuchi, H.; Inoue, A.; Onuki, M.; Takano, Y.; Yamaguchi, T. Application of Zr-Based Bulk Glassy Alloys to Golf Clubs. *Mater. Trans.* **2001**, *42*, 678–681, doi:10.2320/matertrans.42.678.
267. Huang, J.C.; Chu, J.P.; Jang, J.S.C. Recent Progress in Metallic Glasses in Taiwan. *Intermetallics* **2009**, *17*, 973–987, doi:10.1016/j.intermet.2009.05.004.
268. Li, H.F.; Zheng, Y.F. Recent Advances in Bulk Metallic Glasses for Biomedical Applications. *Acta Biomater.* **2016**, *36*, 1–20, doi:10.1016/j.actbio.2016.03.047.
269. Disa, J.J.; Vossoughi, J.; Goldberg, N.H. A Comparison of Obsidian and Surgical Steel Scalpel Wound Healing in Rats. *Plast. Reconstr. Surg.* **1993**, *92*, 884.
270. Deng, Y.P.; Guan, Y.F.; Fowlkes, J.D.; Wen, S.Q.; Liu, F.X.; Pharr, G.M.; Liaw, P.K.; Liu, C.T.; Rack, P.D. A Combinatorial Thin Film Sputtering Approach for Synthesizing and Characterizing Ternary ZrCuAl Metallic Glasses. *Intermetallics* **2007**, *15*, 1208–1216, doi:10.1016/j.intermet.2007.02.011.
271. Khan, M.M.; Nemati, A.; Rahman, Z.U.; Shah, U.H.; Asgar, H.; Haider, W. Recent Advancements in Bulk Metallic Glasses and Their Applications: A Review. *Crit. Rev. Solid State Mater. Sci.* **2018**, *43*, 233–268, doi:10.1080/10408436.2017.1358149.
272. Lei, C.; Lei, J.; Yang, Z.; Zhou, Y. Improved Micro Fluxgate Sensor with Double-Layer Fe-Based Amorphous Core. *Microsyst. Technol.* **2013**, *19*, 167–172, doi:10.1007/s00542-012-1523-z.
273. Fukushima, T.; Hata, S.; Shimokohbe, A. A MEMS Conical Spring Actuator Array. *J. Microelectromechanical Syst.* **2005**, *14*, 243–253, doi:10.1109/JMEMS.2004.839345.
274. Inoue, A.; Shen, B.; Nishiyama, N. Development and Applications of Late Transition Metal Bulk Metallic Glasses. In *Bulk Metallic Glasses*; Miller, M., Liaw, P., Eds.; Springer US: Boston, MA, 2008; pp. 1–25 ISBN 978-0-387-48921-6.
275. Ray, R.; Tanner, L.E. Metallic Glasses with High Strengths and High Crystallization Temperatures. *J. Mater. Sci.* **1980**, *15*, 1599–1600, doi:10.1007/BF00752148.
276. Yazici, Z.; Hitit, A.; Yalcin, Y.; Ozgul, M. Effects of Minor Cu and Si Additions on Glass Forming Ability and Mechanical Properties of Co-Fe-Ta-B Bulk Metallic Glass. *Met. Mater. Int.* **2016**, *22*, 50–57, doi:10.1007/s12540-016-5220-9.
277. Inoue, A.; Shen, B.L.; Chang, C.T. Fe- and Co-Based Bulk Glassy Alloys with Ultrahigh Strength of over 4000MPa. *Intermetallics* **2006**, *14*, 936–944, doi:10.1016/j.intermet.2006.01.038.
278. Kim, J.T.; Hong, S.H.; Kim, Y.S.; Park, H.J.; Maity, T.; Chawake, N.M.; Prashanth, K.G.; Park, J.M.; Song, K.K.; Wang, W.M.; et al. Co-Cr-Mo-C-B Metallic Glasses with Wide Supercooled Liquid Region Obtained by Systematic Adjustment of the Metalloid Ratio. *J. Non-Cryst. Solids* **2019**, *505*, 310–319, doi:10.1016/j.jnoncrysol.2018.11.006.
279. Dun, C.; Liu, H.; Shen, B. Enhancement of Plasticity in Co-Nb-B Ternary Bulk Metallic Glasses with Ultrahigh Strength. *J. Non-Cryst. Solids* **2012**, *358*, 3060–3064, doi:10.1016/j.jnoncrysol.2012.08.007.
280. Wang, J.; Huang, L.; Zhu, S.; Li, Q.; Guan, S.; Zhang, T. Glass-Forming Ability, Fragility Parameter, and Mechanical Properties of Co-Ir-Ta-B Amorphous Alloys. *J. Alloys Compd.* **2013**, *576*, 375–379, doi:10.1016/j.jallcom.2013.05.218.
281. Liu, C.; Li, Q.; Huo, J.; Yang, W.; Chang, L.; Chang, C.; Sun, Y. Near Room-Temperature Magnetocaloric Effect of Co-Based Bulk Metallic Glass. *J. Magn. Magn. Mater.* **2018**, *446*, 162–165, doi:10.1016/j.jmmm.2017.09.026.
282. Wang, Q.; Zhou, J.; Zeng, Q.; Zhang, G.; Yin, K.; Liang, T.; Yang, W.; Stoica, M.; Sun, L.; Shen, B. Ductile Co-Based Bulk Metallic Glass with Superhigh Strength and Excellent Soft Magnetic Properties Induced by Modulation of Structural Heterogeneity. *Materialia* **2020**, *9*, 100561, doi:10.1016/j.mtla.2019.100561.
283. Dong, Y.; Man, Q.; Sun, H.; Shen, B.; Pang, S.; Zhang, T.; Makino, A.; Inoue, A. Glass-Forming Ability and Soft Magnetic Properties of (Co_{0.6}Fe_{0.3}Ni_{0.1})₆₇B₂₂+xSi₆-xNb₅ Bulk Glassy Alloys. *J. Alloys Compd.* **2011**, *509*, S206–S209, doi:10.1016/j.jallcom.2011.01.045.

284. Periodic Table of the Elements Available online: <https://www.sigmaaldrich.com/PL/en/technical-documents/technical-article/chemistry-and-synthesis/organic-reaction-toolbox/periodic-table-of-elements-names> (accessed on 3 February 2025).
285. Ren, J.; Li, Y.; Liang, X.; Kato, H.; Zhang, W. Role of Fe Substitution for Co on Thermal Stability and Glass-Forming Ability of Soft Magnetic Co-Based Co-Fe-B-P-C Metallic Glasses. *Intermetallics* **2022**, *147*, 107598, doi:10.1016/j.intermet.2022.107598.
286. Zhao, Y.; Li, X.; Liu, X.; Bi, J.; Wu, Y.; Xiao, R.; Li, R.; Zhang, T. Balancing Benefits of Strength, Plasticity and Glass-Forming Ability in Co-Based Metallic Glasses. *J. Mater. Sci. Technol.* **2021**, *86*, 110–116, doi:10.1016/j.jmst.2021.01.042.
287. Luo, N.; Huber, F.; Ciftci, N.; Wahl, L.; Bezold, A.; Neumeier, S.; Uhlenwinkel, V.; Travitzky, N.; Schmidt, M.; Zenk, C.H.; et al. Laser Powder Bed Fusion of FeCoBSiNb-Cu Bulk Metallic Glass Composites: Processing, Microstructure and Mechanical Properties. *Mater. Sci. Eng. A* **2022**, *849*, 143405, doi:10.1016/j.msea.2022.143405.
288. Yuan, C.C.; Lv, Z.W.; Pang, C.M.; Zhu, W.W.; Wang, X.-L.; Shen, B.L. Pronounced Nanoindentation Creep Deformation in Cu-Doped CoFe-Based Metallic Glasses. *J. Alloys Compd.* **2019**, *806*, 246–253, doi:10.1016/j.jallcom.2019.07.226.
289. Jiang, S.; Wang, H.; Estevez, D.; Huang, Y.; Zhang, L.; Shen, H.; Ning, Z.; Qin, F.; Sun, J. Surface Microstructural Design to Improve Mechanical and Giant Magneto-Impedance Properties of Melt-Extracted CoFe-Based Amorphous Wires. *Mater. Des.* **2021**, *204*, 109642, doi:10.1016/j.matdes.2021.109642.
290. Pardo, A.; Merino, M.C.; Otero, E.; López, M.D.; M'hich, A. Influence of Cr Additions on Corrosion Resistance of Fe- and Co-Based Metallic Glasses and Nanocrystals in H₂SO₄. *J. Non-Cryst. Solids* **2006**, *352*, 3179–3190, doi:10.1016/j.jnoncrysol.2006.05.021.
291. Ma, X.; Wang, T.; Li, M.; Li, P.; Xie, L.; Zhang, G.; Chang, C.; Li, Q. Preparation and Properties of New Non-Magnetic Co-Based Bulk Metallic Glasses. *Results Phys.* **2024**, *58*, 107532, doi:10.1016/j.rinp.2024.107532.
292. Zhou, Y.; Wang, T. High Stability and High Corrosion Resistance of a Class of Co–Cr–Mo–Nb–B High-Entropy Metallic Glasses. *J. Mater. Res. Technol.* **2024**, *30*, 256–266, doi:10.1016/j.jmrt.2024.03.035.
293. Liang, X.; Li, Y.; Bao, F.; Zhu, Z.; Zhang, H.; Zhang, W. Roles of Y and Fe Contents on Glass-Forming Ability, Thermal Stability, and Magnetic Properties of Co-Based Co–Fe–Y–B Bulk Metallic Glasses. *Intermetallics* **2021**, *132*, 107135, doi:10.1016/j.intermet.2021.107135.
294. Lu, J.; Li, Y.; Ma, S.; Li, W.; Bao, F.; Zhu, Z.; Zeng, Q.; Zhang, H.; Yao, M.; Zhang, W. Novel Soft Magnetic Co-Based Ternary Co–Er–B Bulk Metallic Glasses. *Acta Metall. Sin. Engl. Lett.* **2024**, doi:10.1007/s40195-024-01722-z.
295. Dastani, M.M.; AL-Ali, M.H.; Moradi, M. Influence of Current Annealing on the Magneto-Impedance Response of Co-Based Ribbons Arising from Surface Structural Improvement. *J. Non-Cryst. Solids* **2019**, *516*, 9–13, doi:10.1016/j.jnoncrysol.2019.01.018.
296. Zhao, C.; Pan, L.; Li, X.; Ma, L.; Liu, Q.; Wang, J. Optimization of Magnetoimpedance Effect in Co-Based Ribbon by Laser Patterning for Sensor Arrays Application. *J. Phys. -Appl. Phys.* **2018**, *51*, 045005, doi:10.1088/1361-6463/aaa1af.
297. Makino, A.; Kubota, T.; Chang, C.; Makabe, M.; Inoue, A. FeSiBP Bulk Metallic Glasses with Unusual Combination of High Magnetization and High Glass-Forming Ability. *Mater. Trans.* **2007**, *48*, 3024–3027, doi:10.2320/matertrans.MRP2007198.
298. Dai, J.; Wang, Y.G.; Yang, L.; Xia, G.T.; Zeng, Q.S.; Lou, H.B. Structural Aspects of Magnetic Softening in Fe-Based Metallic Glass during Annealing. *Scr. Mater.* **2017**, *127*, 88–91, doi:10.1016/j.scriptamat.2016.09.006.
299. Liu, X.; Bi, J.; Meng, Z.; Li, R.; Li, Y.; Zhang, T. Tribological Behaviors of High-Hardness Co-Based Amorphous Coatings Fabricated by Laser Cladding. *Tribol. Int.* **2021**, *162*, 107142, doi:10.1016/j.triboint.2021.107142.
300. Wang, J.; Kaban, I.; Levyskyi, V.; Li, R.; Han, J.; Stoica, M.; Gumeniuk, R.; Nielsch, K. Ultra-High Strength Co–Ta–B Bulk Metallic Glasses: Glass Formation, Thermal Stability and Crystallization. *J. Alloys Compd.* **2021**, *860*, 158398, doi:10.1016/j.jallcom.2020.158398.
301. Dun, C.; Liu, H.; Hou, L.; Xue, L.; Dou, L.; Yang, W.; Zhao, Y.; Shen, B. Ductile Co–Nb–B Bulk Metallic Glass with Ultrahigh Strength. *J. Non-Cryst. Solids* **2014**, *386*, 121–123, doi:10.1016/j.jnoncrysol.2013.12.004.
302. Shen, B.; Inoue, A. Enhancement of the Fracture Strength and Glass-Forming Ability of CoFeTaB Bulk Glassy Alloy. *J. Phys. Condens. Matter* **2005**, *17*, 5647–5653, doi:10.1088/0953-8984/17/37/003.
303. Man, Q.; Sun, H.; Dong, Y.; Shen, B.; Kimura, H.; Makino, A.; Inoue, A. Enhancement of Glass-Forming Ability of CoFeBSiNb Bulk Glassy Alloys with Excellent Soft-Magnetic Properties and Superhigh Strength. *Intermetallics* **2010**, *18*, 1876–1879, doi:10.1016/j.intermet.2010.02.047.
304. Zheng, H.; Yao, W.; Sun, H.; Tong, G. Highly Enhanced Microwave Absorption Properties of CoFeBSiNb Metallic Glasses through Corrosion. *J. Magn. Magn. Mater.* **2018**, *468*, 109–114, doi:10.1016/j.jmmm.2018.07.083.
305. Huang, D.; Li, Y.; Yang, Y.; Zhu, Z.; Zhang, W. Soft Magnetic Co-Based Co–Fe–B–Si–P Bulk Metallic Glasses with High Saturation Magnetic Flux Density of over 1.2 T. *J. Alloys Compd.* **2020**, *843*, 154862, doi:10.1016/j.jallcom.2020.154862.

306. Aihemaiti, N.; Li, Q.; Li, M.; Wang, T.; Chang, C.; Ma, X. Preparation and Properties of CoFeMoPB Bulk Metallic Glasses. *Intermetallics* **2020**, *123*, 106834, doi:10.1016/j.intermet.2020.106834.
307. Zhang, L.; Wang, C.; Han, L.; Dong, C. Influence of Laser Power on Microstructure and Properties of Laser Clad Co-Based Amorphous Composite Coatings. *Surf. Interfaces* **2017**, *6*, 18–23, doi:10.1016/j.surf.2016.11.006.
308. Jiang, Q.Y. Improvement of Microstructure, Hardness, and Mechanical Properties of Cobalt-Based Amorphous Coating Via Laser Cladding. *Strength Mater.* **2019**, *51*, 450–461, doi:10.1007/s11223-019-00091-8.
309. Zhao, J.; Gao, Q.; Wang, H.; Shu, F.; Zhao, H.; He, W.; Yu, Z. Microstructure and Mechanical Properties of Co-Based Alloy Coatings Fabricated by Laser Cladding and Plasma Arc Spray Welding. *J. Alloys Compd.* **2019**, *785*, 846–854, doi:10.1016/j.jallcom.2019.01.056.
310. Liu, X.; Bi, J.; Meng, Z.; Ke, Y.; Li, R.; Zhang, T. Development of Co-Based Amorphous Composite Coatings Synthesized by Laser Cladding for Neutron Shielding. *Materials* **2021**, *14*, 279, doi:10.3390/ma14020279.
311. Zhang, G.; Zhang, H.; Yue, S.; Cheng, R.; Wang, A.; He, A.; Dong, Y.; Ni, H.; Liu, C.-T. Preparation of Non-Magnetic and Ductile Co-Based Bulk Metallic Glasses with High GFA and Hardness. *Intermetallics* **2019**, *107*, 47–52, doi:10.1016/j.intermet.2019.01.012.
312. Murray, C.; Sun, S.; Gaschler, W.; Doyle, H.; Betley, T.; Kagan, C. Colloidal Synthesis of Nanocrystals and Nanocrystal Superlattices. *IBM J. Res. Dev.* **2001**, *45*, 47–56, doi:10.1147/rd.451.0047.
313. Yang, H.T.; Su, Y.K.; Shen, C.M.; Yang, T.Z.; Gao, H.J. Synthesis and Magnetic Properties of ϵ -Cobalt Nanoparticles. *Surf. Interface Anal.* **2004**, *36*, 155–160, doi:10.1002/sia.1675.
314. Ackland, K.; Masood, A.; Kulkarni, S.; Stamenov, P. Ultra-Soft Magnetic Co-Fe-B-Si-Nb Amorphous Alloys for High Frequency Power Applications. *AIP Adv.* **2018**, *8*, 056129, doi:10.1063/1.5007707.
315. Pinzón-Escobar, E.; Montiel, H.; García, A.; Alvarez, G. Magnetic and Electrical Properties of Vitrovac/Au/Vitrovac Multilayered Obtained by Means of Magnetron Sputtering. *J. Phys. Conf. Ser.* **2021**, *1723*, 012025, doi:10.1088/1742-6596/1723/1/012025.
316. Kekalo, I.; Stolyarov, V.; Taranichev, V. *The Effect of Annealing on the Laws of Magnetization and Magnetization Reversal in Amorphous Alloys*; Amorphous Metal Alloys, Metallurgy; Moscow, 1983;
317. Nosenko, A.V.; Kyrylchuk, V.V.; Semen'ko, M.P.; Nowicki, M.; Marusenkova, A.; Mika, T.M.; Semyrga, O.M.; Zelinska, G.M.; Nosenko, V.K. Soft Magnetic Cobalt Based Amorphous Alloys with Low Saturation Induction. *J. Magn. Magn. Mater.* **2020**, *515*, 167328, doi:10.1016/j.jmmm.2020.167328.
318. Syypien, A. Microstructural and Mechanical Characterization of Interfacial Phenomena Occurring in Brazing Ti-6Al-4V Alloy Using TiZrCuPd Amorphous Ribbons. *J. Mater. Eng. Perform.* **2023**, doi:10.1007/s11665-023-08181-0.
319. Li, D.; Zhang, L.; Li, G.; Lu, Z.; Zhou, S. Reducing the Core Loss of Amorphous Cores for Distribution Transformers. *Prog. Nat. Sci. Mater. Int.* **2012**, *22*, 244–249, doi:10.1016/j.pnsc.2012.04.005.
320. Hosko, J.; Janotova, I.; Svec, P.; Janickovic, D.; Vlasak, G.; Illekova, E.; Matko, I.; Svec, P. Preparation of Thin Ribbon and Bulk Glassy Alloys in CoFeBSiNb(Ga) Using Planar Flow Casting and Suction Casting Methods. *J. Non-Cryst. Solids* **2012**, *358*, 1545–1549, doi:10.1016/j.jnoncrystol.2012.04.016.
321. Dong, Y.; Wang, A.; Man, Q.; Shen, B. (Co_{1-x}Fe_x)₆₈B_{21.9}Si_{5.1}Nb₅ Bulk Glassy Alloys with High Glass-Forming Ability, Excellent Soft-Magnetic Properties and Superhigh Fracture Strength. *Intermetallics* **2012**, *23*, 63–67, doi:10.1016/j.intermet.2011.12.020.
322. Sun, H.; Man, Q.; Dong, Y.; Shen, B.; Kimura, H.; Makino, A.; Inoue, A. Effect of Nb Addition on the Glass-Forming Ability, Mechanical and Soft-Magnetic Properties in (Co_{0.942}Fe_{0.058})_{72-x}Nb_xB_{22.4}Si_{5.6} Bulk Glassy Alloys. *J. Alloys Compd.* **2010**, *504*, S31–S33, doi:10.1016/j.jallcom.2010.03.044.
323. Shen, B.; Chang, C.; Kubota, T.; Inoue, A. Superhigh Strength and Excellent Soft-Magnetic Properties of [(Co_{1-x}Fe_x)_{0.75}B_{0.25}Si_{0.05}]₉₆Nb₄ Bulk Glassy Alloys. *J. Appl. Phys.* **2006**, *100*, 013515, doi:10.1063/1.2211207.
324. Hou, L.; Wang, Q.; Yang, W.; Shen, B. Enhanced Plasticity of FeCoBSiNb Bulk Glassy Alloys by Controlling the Structure Heterogeneity with Cu Addition. *J. Non-Cryst. Solids* **2019**, *505*, 181–187, doi:10.1016/j.jnoncrystol.2018.11.015.
325. Stoica, M.; Scudino, S.; Bednarčík, J.; Kaban, I.; Eckert, J. FeCoSiBNbCu Bulk Metallic Glass with Large Compressive Deformability Studied by Time-Resolved Synchrotron X-Ray Diffraction. *J. Appl. Phys.* **2014**, *115*, 053520, doi:10.1063/1.4864671.
326. Shen, B.; Men, H.; Inoue, A. Mechanical Properties of FeCoBSiNbCu Bulk Glassy Alloy Composite.; OnePetro, July 1 2007.
327. Wang, J.; Li, R.; Hua, N.; Zhang, T. Co-Based Ternary Bulk Metallic Glasses with Ultrahigh Strength and Plasticity. *J. Mater. Res.* **2011**, *26*, 2072–2079, doi:10.1557/jmr.2011.187.
328. Inoue, A.; Shen, B.; Koshiba, H.; Kato, H.; Yavari, A.R. Cobalt-Based Bulk Glassy Alloy with Ultrahigh Strength and Soft Magnetic Properties. *Nat. Mater.* **2003**, *2*, 661–663, doi:10.1038/nmat982.

329. Pilarczyk, W.; Jung, T.; Babilas, R. The Influence of Technological Parameters of the Casting Process on the Structure and Selected Properties of Iron-Based Metallic Glasses. *Acta Phys. Pol. A* **2016**, *130*, 923–926, doi:10.12693/APhysPolA.130.923.
330. Kuś, A.; Pilarczyk, W.; Małachowska, A.; Ambroziak, A.; Gębara, P. Investigation of Mechanical and Magnetic Properties of Co-Based Amorphous Powders Obtained by Atomization. *Mater. Basel Switz.* **2021**, *14*, 7357, doi:10.3390/ma14237357.
331. Gärtner, F.; Stoltenhoff, T.; Schmidt, T.; Kreye, H. The Cold Spray Process and Its Potential for Industrial Applications. *J. Therm. Spray Technol.* **2006**, *15*, 223–232, doi:10.1361/105996306X108110.
332. Celotto, S.; Pattison, J.; Ho, J.S.; Johnson, A.N.; O'Neill, W. 5 - The Economics of the Cold Spray Process. In *The Cold Spray Materials Deposition Process*; Champagne, V.K., Ed.; Woodhead Publishing Series in Metals and Surface Engineering; Woodhead Publishing, 2007; pp. 72–101 ISBN 978-1-84569-181-3.
333. Whiting, J.; Fox, J. Characterization of Feedstock in the Powder Bed Fusion Process: Sources of Variation in Particle Size Distribution and the Factors That Influence Them. **2016**.
334. Nam, Y.G.; Koo, B.; Chang, M.S.; Yang, S.; Yu, J.; Park, Y.H.; Jeong, J.W. Selective Laser Melting Vitrification of Amorphous Soft Magnetic Alloys with Help of Double-Scanning-Induced Compositional Homogeneity. *Mater. Lett.* **2020**, *261*, 127068, doi:10.1016/j.matlet.2019.127068.
335. Gao, S.; Yan, X.; Chang, C.; Aubry, E.; He, P.; Liu, M.; Liao, H.; Fenineche, N. Microstructure and Magnetic Properties of FeSiBCrC Soft Magnetic Alloy Manufactured by Selective Laser Melting. *Mater. Lett.* **2021**, *290*, 129469, doi:10.1016/j.matlet.2021.129469.
336. Kuś, A.; Rajtúková, V.; Pilarczyk, W.; Hudák, R.; Mehner, T.; Maj, Ł.; Lampke, T.; Małachowska, A. First Attempt to Print Co-Based Alloys with High Glass Forming Ability by Selective Laser Melting. *J. Alloys Compd.* **2024**, *995*, 174680, doi:10.1016/j.jallcom.2024.174680.
337. Sysmex FPIA-3000 Allows Rapid Particle Size and Shape Characterization and Its Importance to the Toner Industry Available online: <https://www.azom.com/article.aspx?ArticleID=3932> (accessed on 28 June 2024).
338. Oliver, W.C.; Pharr, G.M. An Improved Technique for Determining Hardness and Elastic Modulus Using Load and Displacement Sensing Indentation Experiments. *J. Mater. Res.* **1992**, *7*, 1564–1583, doi:10.1557/JMR.1992.1564.
339. Gademawla, E.; Koura, M.; Maksoud, T.; Elewa, I.; Soliman, H. Roughness Parameters. *J. Mater. Process. Technol.* **2002**, *123*, 133–145, doi:10.1016/S0924-0136(02)00060-2.
340. Gábor, F.; Sándor, H.; Czifra, Á. Microgeometry Tests of 'Contradictory' Surfaces with Various Evaluation Techniques. *Acta Polytech. Hung.* **2007**, *4*.
341. Whitehead, S. a.; Shearer, A. c.; Watts, D. c.; Wilson, N. h. f. Comparison of Methods for Measuring Surface Roughness of Ceramic. *J. Oral Rehabil.* **1995**, *22*, 421–427, doi:10.1111/j.1365-2842.1995.tb00795.x.
342. Dzierwa, A.; Pawlus, P. Wear of a Rough Disc in Dry Sliding Contact with a Smooth Ball: Experiment and Modeling. *Arch. Civ. Mech. Eng.* **2021**, *21*, 85, doi:10.1007/s43452-021-00240-4.
343. Dai, T.; Wang, N. Study on Magnetic Properties and Degradability of Gas Atomization Fe-Based (Fe-Si-B-P) Amorphous Powder. *J. Supercond. Nov. Magn.* **2019**, *32*, 3699–3702, doi:10.1007/s10948-019-05164-y.
344. Alvarez, K.L.; Manuel Martin, J.; Ipatov, M.; Dominguez, L.; Gonzalez, J. Magnetic Properties of Annealed Amorphous Fe_{72.5}Si_{12.5}B₁₅ Alloy Obtained by Gas Atomization Technique. *IEEE Trans. Magn.* **2018**, *54*, 2002405, doi:10.1109/TMAG.2018.2839258.
345. Ciftci, N.; Ellendt, N.; von Bargen, R.; Henein, H.; Maedler, L.; Uhlenwinkel, V. Atomization and Characterization of a Glass Forming Alloy {(Fe_{0.6}Co_{0.4})(0.75)B_{0.2}Si_{0.05}}(96)Nb-4. *J. Non-Cryst. Solids* **2014**, *394*, 36–42, doi:10.1016/j.jnoncrysol.2014.03.023.
346. Miura, A.; Dong, W.; Fukue, M.; Yodoshi, N.; Takagi, K.; Kawasaki, A. Preparation of Fe-Based Monodisperse Spherical Particles with Fully Glassy Phase. *J. Alloys Compd.* **2011**, *509*, 5581–5586, doi:10.1016/j.jallcom.2011.02.044.
347. Shen, B.; Chang, C.; Kubota, T.; Inoue, A. Superhigh Strength and Excellent Soft-Magnetic Properties of [(Co_{1-x}Fe_x)_{0.75}B_{0.2}Si_{0.05}]₉₆Nb₄ Bulk Glassy Alloys. *J. Appl. Phys.* **2006**, *100*, 013515, doi:10.1063/1.2211207.
348. Pengjun, F.; Yi, X.; Xinggang, L.; Ya, C. Influence of Atomizing Gas and Cooling Rate on Solidification Characterization of Nickel-Based Superalloy Powders. *Rare Met. Mater. Eng.* **2018**, *47*, 423–430, doi:10.1016/S1875-5372(18)30082-1.
349. Liang, X.; Erenc-Sedziak, T.; Kowalczyk, M.; Kulik, T.; Xu, B. Evaluation on the Reliability of Criteria for Glass-Forming Ability of Fe(Co)-Based Bulk Metallic Glasses. *J. Mater. Process. Technol.* **2008**, *204*, 465–468, doi:10.1016/j.jmatprotec.2007.12.048.
350. Srivastava, R.M.; Eckert, J.; Löser, W.; Dhindaw, B.K.; Schultz, L. Cooling Rate Evaluation for Bulk Amorphous Alloys from Eutectic Microstructures in Casting Processes. *Mater. Trans.* **2002**, *43*, 1670–1675, doi:10.2320/matertrans.43.1670.

351. Liu, N.; Ma, T.; Liao, C.; Liu, G.; Mota, R.M.O.; Liu, J.; Sohn, S.; Kube, S.; Zhao, S.; Singer, J.P.; et al. Combinatorial Measurement of Critical Cooling Rates in Aluminum-Base Metallic Glass Forming Alloys. *Sci. Rep.* **2021**, *11*, 3903, doi:10.1038/s41598-021-83384-w.
352. Li, X.P.; Kang, C.W.; Huang, H.; Sercombe, T.B. The Role of a Low-Energy-Density Re-Scan in Fabricating Crack-Free Al₈₅Ni₅Y₆Co₂Fe₂ Bulk Metallic Glass Composites via Selective Laser Melting. *Mater. Des.* **2014**, *63*, 407–411, doi:10.1016/j.matdes.2014.06.022.
353. Weingarten, C.; Buchbinder, D.; Pirch, N.; Meiners, W.; Wissenbach, K.; Poprawe, R. Formation and Reduction of Hydrogen Porosity during Selective Laser Melting of AlSi10Mg. *J. Mater. Process. Technol.* **2015**, *221*, 112–120, doi:10.1016/j.jmatprotec.2015.02.013.
354. Microstructural Porosity in Additive Manufacturing: The Formation and Detection of Pores in Metal Parts Fabricated by Powder Bed Fusion., doi:10.1002/amp2.10021.
355. Król, M.; Tański, T. Surface Quality Research for Selective Laser Melting of Ti-6Al-4V Alloy. *Arch. Metall. Mater.* **2016**, doi:10.1515/amm-2016-0213.
356. Boutaous, M.; Liu, X.; Siginer, D.A.; Xin, S. Balling Phenomenon in Metallic Laser Based 3D Printing Process. *Int. J. Therm. Sci.* **2021**, *167*, 107011, doi:10.1016/j.ijthermalsci.2021.107011.
357. Kuś, A.; Rajtúková, V.; Pilarczyk, W.; Hudák, R.; Mehner, T.; Maj, Ł.; Lampke, T.; Małachowska, A. First Co- Based Bulk Metallic Glass Printed by Selective Laser Melting. Accepted to print in the Metallurgical and Materials Transactions A
358. Liu, Y.; Yang, Y.; Wang, D. A Study on the Residual Stress during Selective Laser Melting (SLM) of Metallic Powder. *Int. J. Adv. Manuf. Technol.* **2016**, *87*, 647–656, doi:10.1007/s00170-016-8466-y.
359. Xing, W.; Ouyang, D.; Li, N.; Liu, L. Insight into Micro-Cracking in 3D-Printed Fe-Based BMGs by Selective Laser Melting. *Intermetallics* **2018**, *103*, 101–106, doi:10.1016/j.intermet.2018.10.011.
360. Liu, H.; Jiang, Y.; Yang, D.; Jiang, Q.; Yang, W. Pores and Cracks in the Metallic Glasses Prepared by Laser Powder Bed Fusion. *J. Mater. Res. Technol.* **2023**, *26*, 3070–3089, doi:10.1016/j.jmrt.2023.08.061.
361. Jiang, C.; Liu, W.; Wang, G.; Chen, Y.; Xing, Y.; Zhang, C.; Dargusch, M. The Corrosion Behaviours of Plasma-Sprayed Fe-Based Amorphous Coatings. *Surf. Eng.* **2018**, *34*, 634–639, doi:10.1080/02670844.2017.1319647.
362. An, Y.; Hou, G.; Chen, J.; Zhao, X.; Liu, G.; Zhou, H.; Chen, J. Microstructure and Tribological Properties of Iron-Based Metallic Glass Coatings Prepared by Atmospheric Plasma Spraying. *Vacuum* **2014**, *107*, 132–140, doi:10.1016/j.vacuum.2014.04.021.
363. Palásti-Kovács, B.; Sipos, S.; Czifra, Á. INTERPRETATION OF “R_z = 4×Ra” AND OTHER ROUGHNESS PARAMETERS IN THE EVALUATION OF MACHINED SURFACES.
364. Vardelle, M.; Vardelle, A.; Fauchais, P. Spray Parameters and Particle Behavior Relationships during Plasma Spraying. *J. Therm. Spray Technol.* **1993**, *2*, 79–91, doi:10.1007/BF02647426.
365. Zhou, Y.; Ma, G.; Wang, H.; Li, G.-L.; Chen, S.; Wang, H.; Ming-Liu Fabrication and Characterization of Supersonic Plasma Sprayed Fe-Based Amorphous Metallic Coatings. *Mater. Des.* **2016**, *110*, 332–339, doi:10.1016/j.matdes.2016.08.003.
366. Zhang, C.; Chu, Z.; Wei, F.; Qin, W.; Yang, Y.; Dong, Y.; Huang, D.; Wang, L. Optimizing Process and the Properties of the Sprayed Fe-Based Metallic Glassy Coating by Plasma Spraying. *Surf. Coat. Technol.* **2017**, *319*, 1–5, doi:10.1016/j.surfcoat.2017.03.063.
367. Hua, N.; Chen, W.; Wang, W.; Lu, H.; Ye, X.; Li, G.; Lin, C.; Huang, X. Tribological Behavior of a Ni-Free Zr-Based Bulk Metallic Glass with Potential for Biomedical Applications. *Mater. Sci. Eng. C* **2016**, *66*, 268–277, doi:10.1016/j.msec.2016.04.078.
368. Wang, Y.; Shi, L.; Duan, D.; Li, S.; Xu, J. Tribological Properties of Zr₆₁Ti₂Cu₂₅Al₁₂ Bulk Metallic Glass under Simulated Physiological Conditions. *Mater. Sci. Eng. C* **2014**, *37*, 292–304, doi:10.1016/j.msec.2014.01.016.
369. Rahaman, M.L.; Zhang, L.; Liu, M.; Liu, W. Surface Roughness Effect on the Friction and Wear of Bulk Metallic Glasses. *Wear* **2015**, 332–333, 1231–1237, doi:10.1016/j.wear.2014.11.030.
370. Iebba, M.; Astarita, A.; Mistretta, D.; Colonna, I.; Liberini, M.; Scherillo, F.; Pirozzi, C.; Borrelli, R.; Franchitti, S.; Squillace, A. Influence of Powder Characteristics on Formation of Porosity in Additive Manufacturing of Ti-6Al-4V Components. *J. Mater. Eng. Perform.* **2017**, *26*, 4138–4147, doi:10.1007/s11665-017-2796-2.
371. Sola, A.; Nouri, A. Microstructural Porosity in Additive Manufacturing: The Formation and Detection of Pores in Metal Parts Fabricated by Powder Bed Fusion. *J. Adv. Manuf. Process.* **2019**, *1*, e10021, doi:10.1002/amp2.10021.
372. Aboulkhair, N.T.; Everitt, N.M.; Ashcroft, I.; Tuck, C. Reducing Porosity in AlSi10Mg Parts Processed by Selective Laser Melting. *Addit. Manuf.* **2014**, *1–4*, 77–86, doi:10.1016/j.addma.2014.08.001.
373. Li, L.; SUN, H.; FANG, Y.; ZHENG, J. Co-Based Soft Magnetic Bulk Glassy Alloys Optimized for Glass-Forming Ability and Plasticity. *Bull. Mater. Sci.* **2016**, *39*, 691–695, doi:10.1007/s12034-016-1207-x.

374. Rau, A.; Chakrabarty, K.; Gullion, W.; Baker, P.A.; Bikmukhametov, I.; Martens, R.L.; Thompson, G.B.; Catledge, S.A. A Diffusion Approach for Plasma Synthesis of Superhard Tantalum Borides. *J. Mater. Res.* **2020**, *35*, 481–490, doi:10.1557/jmr.2019.357.
375. Deng, L.; Wang, S.; Wang, P.; Kühn, U.; Pauly, S. Selective Laser Melting of a Ti-Based Bulk Metallic Glass. *Mater. Lett.* **2018**, *212*, 346–349, doi:10.1016/j.matlet.2017.10.130.
376. Leitnaker, J.M.; Bowman, M.G.; Gilles, P.W. High-Temperature Phase Studies in the Tantalum-Boron System between Ta and TaB. *J. Electrochem. Soc.* **1961**, *108*, 568, doi:10.1149/1.2428137.
377. Ketkaew, J.; Liu, Z.; Chen, W.; Schroers, J. Critical Crystallization for Embrittlement in Metallic Glasses. *Phys. Rev. Lett.* **2015**, *115*, 265502, doi:10.1103/PhysRevLett.115.265502.
378. Bernard, C.; Keryvin, V. Crystalline Defects in Bulk Metallic Glasses: Consequences on Fracture Toughness Determination and Ductility. *J. Phys. Condens. Matter* **2020**, *32*, 483001, doi:10.1088/1361-648X/abaa7f.
379. Monfared, A.; Liu, W.; Zhang, L. Metallic Glass Hardening after Thermoplastic Forming. *Mater. Sci. Eng. A* **2018**, *725*, 181–186, doi:10.1016/j.msea.2018.04.021.
380. Li, D.; Zhang, X.; Li, J.; Zhao, L.; Wang, F.; Chen, X. Insight into the Elastic Anisotropy and Thermodynamics Properties of Tantalum Borides. *Vacuum* **2019**, *169*, 108883, doi:10.1016/j.vacuum.2019.108883.
381. Šroba, V.; Fiantok, T.; Truchlý, M.; Roch, T.; Zahoran, M.; Grančič, B.; Švec, P., Jr.; Nagy, Š.; Izai, V.; Kúš, P.; et al. Structure Evolution and Mechanical Properties of Hard Tantalum Diboride Films. *J. Vac. Sci. Technol. A* **2020**, *38*, 033408, doi:10.1116/6.0000155.
382. Espinosa, J.R.; Vega, C.; Valeriani, C.; Frenkel, D.; Sanz, E. Heterogeneous versus Homogeneous Crystal Nucleation of Hard Spheres. *Soft Matter* **2019**, *15*, 9625–9631, doi:10.1039/c9sm01142k.
383. Wang, G.; Liaw, P.K.; Senkov, O.N.; Miracle, D.B. The Duality of Fracture Behavior in a Ca-Based Bulk-Metallic Glass. *Metall. Mater. Trans. A* **2011**, *42*, 1499–1503, doi:10.1007/s11661-010-0533-7.
384. Fornell, J.; González, S.; Rossinyol, E.; Suriñach, S.; Baró, M.D.; Louzguine-Luzgin, D.V.; Perepezko, J.H.; Sort, J.; Inoue, A. Enhanced Mechanical Properties Due to Structural Changes Induced by Devitrification in Fe–Co–B–Si–Nb Bulk Metallic Glass. *Acta Mater.* **2010**, *58*, 6256–6266, doi:10.1016/j.actamat.2010.07.047.
385. Courtney, T.H. *Mechanical Behavior of Materials: Second Edition*; Waveland Press, 2005; ISBN 978-1-4786-0838-7.
386. Pang, L.L.; Inoue, A.; Zanaeva, E.N.; Wang, F.; Bazlov, A.I.; Han, Y.; Kong, F.L.; Zhu, S.L.; Shull, R.B. Nanocrystallization, Good Soft Magnetic Properties and Ultrahigh Mechanical Strength for Fe₈₂-85B₁₃-16Si₁Cu₁ Amorphous Alloys. *J. Alloys Compd.* **2019**, *785*, 25–37, doi:10.1016/j.jallcom.2019.01.150.
387. Tkatch, V.I.; Limanovskii, A.I.; Denisenko, S.N.; Rassolov, S.G. The Effect of the Melt-Spinning Processing Parameters on the Rate of Cooling. *Mater. Sci. Eng. A* **2002**, *323*, 91–96, doi:10.1016/S0921-5093(01)01346-6.
388. Wang, Q.; Zhu, C.L.; Li, Y.H.; Cheng, X.; Chen, W.R.; Wu, J.; Qiang, J.B.; Wang, Y.M.; Dong, C. Co- and Fe-Based Multicomponent Bulk Metallic Glasses Designed by Cluster Line and Minor Alloying. *J. Mater. Res.* **2008**, *23*, 1543–1550, doi:10.1557/JMR.2008.0210.
389. Beketov, I.V.; Pérez, R.; Bagazeev, A.V.; Vazquez, M.; Medvedev, A.I.; Safronov, A.; Kurlyandskaya, G.V. Magnetic Nanoparticles of (Co_{0.94}Fe_{0.06})₇₂Si₁₂B₁₅ and Fe₇₈Si₉B₁₃ Obtained by Electric Explosion of Amorphous Wires. *Key Eng. Mater.* **2015**, *644*, 203–206, doi:10.4028/www.scientific.net/KEM.644.203.
390. Laurila, T.; Vuorinen, V.; Mattila, T.; Turunen, M.; Paulasto-Kröckel, M.; Kivilahti, J. Introduction to Mechanics of Materials. In: 2012; pp. 25–43 ISBN 978-1-4471-2469-6.
391. Dai, F.-Z.; Zhou, Y.; Sun, W. Segregation of Solute Atoms (Y, Nb, Ta, Mo and W) in ZrB₂ Grain Boundaries and Their Effects on Grain Boundary Strengths: A First-Principles Investigation. *Acta Mater.* **2017**, *127*, 312–318, doi:10.1016/j.actamat.2017.01.048.
392. Gao, S.; Song, Z.; He, B.; Zhou, L.; Hou, J. Effect of Ta Addition on Solidification Microstructure and Element Segregation of IN617B Nickel-Base Superalloy. *Trans. Nonferrous Met. Soc. China* **2022**, *32*, 559–568, doi:10.1016/S1003-6326(22)65815-1.
393. Ma, C. Fundamental Study on Laser Interaction with Metal Matrix Nanocomposites. Ph.D., Ann Arbor, United States.
394. Ouyang, D.; Xing, W.; Li, N.; Li, Y.; Liu, L. Structural Evolutions in 3D-Printed Fe-Based Metallic Glass Fabricated by Selective Laser Melting. *Addit. Manuf.* **2018**, *23*, 246–252, doi:10.1016/j.addma.2018.08.020.
395. Lu, Y.; Huang, Y.; Wu, J.; Lu, X.; Qin, Z.; Daisenberger, D.; Chiu, Y.-L. Graded Structure of Laser Direct Manufacturing Bulk Metallic Glass. *Intermetallics* **2018**, *103*, 67–71, doi:10.1016/j.intermet.2018.10.005.

IX. LIST OF TABLES

Tab. 1. Summary of the quantitative criteria proposed to evaluate the GFA [7]	15
Tab. 2. Examples of reported influence of the addition of chemical elements to metallic glasses	18
Tab. 3. Typical gases used for plasma generation for plasma spraying coating depositions [140]	28
Tab. 4. Properties of metallic glasses related to potential applications [168]	31
Tab. 5. Index of symbols for nanoindentation measurements	33
Tab. 6. Comparison of Poisson ratio for metallic glasses	35
Tab. 7. Review of the mechanical properties of bulk metallic glasses [170]	40
Tab. 8. Current and possible applications of BMGs [265]	44
Tab. 9. Review of the literature (state-of-the-art)	51
Tab. 10. Review of the literature of Co-based alloys with high glass-forming ability	57
Tab. 11. Chemical composition of the alloy CoBFeSiNb	57
Tab. 12. Chemical composition of the alloy CoBFeTaSiCu	58
Tab. 13. a) parameters of the casting of ribbons by melt spinning, b) the example of ribbons developed by similar parameters by the same casting set [329]	59
Tab. 14. Components used to manufacture Co-based alloys	59
Tab. 15. Review of parameters of Fe-based alloys printing with high glass-forming ability [117,133,334,335]	61
Tab. 16. Matrix of preliminary parameters for SLM printing [336]	62
Tab. 17. The second stage parameters for SLM printing a) $\text{Co}_{47.6}\text{B}_{21.9}\text{Fe}_{20.4}\text{Si}_{5.1}\text{Nb}_5$, b) $\text{Co}_{42}\text{B}_{26.5}\text{Fe}_{20}\text{Ta}_{5.5}\text{Si}_5\text{Cu}_1$ [336]	63
Tab. 18. Results of the nanoindentation test of $\text{Co}_{47.6}\text{B}_{21.9}\text{Fe}_{20.4}\text{Si}_{5.1}\text{Nb}_5$	72
Tab. 19. Results of the nanoindentation test of $\text{Co}_{47.6}\text{B}_{21.9}\text{Fe}_{20.4}\text{Si}_{5.1}\text{Nb}_5$	74
Tab. 20. Microstructure of the second printing stage of $\text{Co}_{47.6}\text{B}_{21.9}\text{Fe}_{20.4}\text{Si}_{5.1}\text{Nb}_5$. Digital microscopy	76
Tab. 21. Types of voids in the SLM samples	77
Tab. 22. The second stage of the printing of $\text{Co}_{47.6}\text{B}_{21.9}\text{Fe}_{20.4}\text{Si}_{5.1}\text{Nb}_5$ samples a) density of samples and c) calculated energy density (ED). Values are marked with color showing from the highest to lowest values b)	77
Tab. 23. Results of the nanoindentation test of $\text{Co}_{47.6}\text{B}_{21.9}\text{Fe}_{20.4}\text{Si}_{5.1}\text{Nb}_5$	80
Tab. 24. Surface of atmospheric plasma sprayed samples of $\text{Co}_{47.6}\text{B}_{21.9}\text{Fe}_{20.4}\text{Si}_{5.1}\text{Nb}_5\%$ at	82
Tab. 25. Porosity analysis based on the SEM images of plasma sprayed coatings of $\text{Co}_{47.6}\text{B}_{21.9}\text{Fe}_{20.4}\text{Si}_{5.1}\text{Nb}_5\%$ at	83
Tab. 26. Nanoindentation results of CoBFeSiNb coating developed via atmospheric plasma spraying	85
Tab. 27. Surface of atmospheric plasma sprayed samples after wear test of $\text{Co}_{47.6}\text{B}_{21.9}\text{Fe}_{20.4}\text{Si}_{5.1}\text{Nb}_5\%$ at	85
Tab. 28. Results of the nanoindentation test of $\text{Co}_{42}\text{B}_{26.5}\text{Fe}_{20}\text{Ta}_{5.5}\text{Si}_5\text{Cu}_1$	90
Tab. 29. Results of the nanoindentation test of $\text{Co}_{42}\text{B}_{26.5}\text{Fe}_{20}\text{Ta}_{5.5}\text{Si}_5\text{Cu}_1$	93
Tab. 30. Results of the nanoindentation test of $\text{Co}_{42}\text{B}_{26.5}\text{Fe}_{20}\text{Ta}_{5.5}\text{Si}_5\text{Cu}_1$	94
Tab. 31. Microstructure of the second printing stage of $\text{Co}_{42}\text{B}_{26.5}\text{Fe}_{20}\text{Ta}_{5.5}\text{Si}_5\text{Cu}_1$. Digital microscopy	97
Tab. 32. The second stage of the printing of $\text{Co}_{42}\text{B}_{26.5}\text{Fe}_{20}\text{Ta}_{5.5}\text{Si}_5\text{Cu}_1$ samples a) density of samples and c) calculated energy density (ED) [336]. Values are marked with color scale b)	98

Tab. 33. Results of the nanoindentation test of $\text{Co}_{42}\text{B}_{26.5}\text{Fe}_{20}\text{Ta}_{5.5}\text{Si}_5\text{Cu}_1$	100
Tab. 34. Surface of atmospheric plasma sprayed samples $\text{Co}_{42}\text{B}_{26.5}\text{Fe}_{20}\text{Ta}_{5.5}\text{Si}_5\text{Cu}_1$	103
Tab. 35. Porosity analyzed based on the SEM images of plasma sprayed coatings $\text{Co}_{42}\text{B}_{26.5}\text{Fe}_{20}\text{Ta}_{5.5}\text{Si}_5\text{Cu}_1$	104
Tab. 36. Nanoindentation results of $\text{Co}_{42}\text{B}_{26.5}\text{Fe}_{20}\text{Ta}_{5.5}\text{Si}_5\text{Cu}_1$ coating developed via atmospheric plasma spraying	105
Tab. 37. Surface of atmospheric plasma sprayed samples after wear test $\text{Co}_{42}\text{B}_{26.5}\text{Fe}_{20}\text{Ta}_{5.5}\text{Si}_5\text{Cu}_1$ % at.....	106
Tab. 38. Thermal analysis of alloys like $\text{Co}_{47.6}\text{B}_{21.9}\text{Fe}_{20.4}\text{Si}_{5.1}\text{Nb}_5$	107
Tab. 39. Types of voids in the SLM samples.....	111
Tab. 40. Summary of $\text{Co}_{47.6}\text{B}_{21.9}\text{Fe}_{20.4}\text{Si}_{5.1}\text{Nb}_5$ development technologies analysis	117
Tab. 41. Thermal analysis of $\text{Co}_{42}\text{B}_{26.5}\text{Fe}_{20}\text{Ta}_{5.5}\text{Si}_5\text{Cu}_1$	119
Tab. 42. Hardness comparison of CoBFeTaSiCu	122
Tab. 43. Summary of $\text{Co}_{42}\text{B}_{26.5}\text{Fe}_{20}\text{Ta}_{5.5}\text{Si}_5\text{Cu}_1$ development technologies analysis	129
Tab. 44. Indentation hardness and structure of samples developed by casting, SLM and APS from alloy $\text{Co}_{47.6}\text{B}_{21.9}\text{Fe}_{20.4}\text{Si}_{5.1}\text{Nb}_5$ (I.CoNb) and $\text{Co}_{42}\text{B}_{26.5}\text{Fe}_{20}\text{Ta}_{5.5}\text{Si}_5\text{Cu}_1$ (II.CoTa).....	130

X. LIST OF FIGURES

Fig. 1. Samples of different structures in the solid state	13
Fig. 2. a) Time-temperature-transformation diagram with marked R_c [15], b) phase transition of amorphous metal upon cooling using in situ TEM [16], RT- room temperature	14
Fig. 3. Graphic representation of the glass transition with differential thermal analysis (DTA) [18]	15
Fig. 4. Term used for alloys with amorphous structure. In the center the X-ray diffraction representation of amorphous metal and examples of applications from work [33]	16
Fig. 5. Percentage of MG classified by base material. The inset table in the upper right corner highlights the number of times an chemical element is counted in all MG compositions reported as of December 2021 [34].....	17
Fig. 6. Possible shapes of metallic glasses successfully developed.....	21
Fig. 7. Classification of metallic glasses manufacturing technologies [88]	22
Fig. 8. Schematic illustration of BMG development by a) suction die casting system [99] b) high pressure die casting with cooling system [35]	23
Fig. 9. a) schematic illustration of the single-roll melt-spinning method [105] b) example of MG ribbon alloys: I- metallic glass Vit.1, II- metallic glass $ZrCuAlNi$, III- metallic glass composite $ZrCuNiBe + \beta-Ti$ crystals [106]	24
Fig. 10. Atomization methods scheme [113–115]	25
Fig. 11. Schematic illustration of the selective laser melting process [116].....	26
Fig. 12. Selective laser melting $Zr_{55}Cu_{30}Ni_{15}Al_{10}$ metallic glasses samples with different type of geometry a) cubic, b) hollow, c) lattice [119]	26
Fig. 13. Schematic illustration of plasma spraying gun a) with radial powder supply and [141] b) with axial powder supply [142].....	27
Fig. 14. Example of Fe-based MG coating obtained by atmospheric plasma spraying [163]..	29
Fig. 15. Detailed factors of plasma spraying process that influence on the splats formation [164]	30
Fig. 16. The relationship between hardness and wear resistance for metallic glasses. The red stars and description “Current investigation” indicate measurements from source [173]	32
Fig. 17. The scheme of differences in indentation depths according to the Oliver and Pharr research. h_m (or h_{max})- maximum indentation depth, h_c - contact depth of the indenter, h_s - difference between h_m and h_c [188].....	34
Fig. 18. Plot F (load) versus h (indentation depth) of indentation test with formula for S (stiffens) of the sample [188]	34
Fig. 19. Schematic representation of the yield (metals, composites and polymers) at room temperature or flexural strength (ceramics) as a function of Young’s modulus. Red presents the metallic glasses and orange presents the crystalline metals. [168,200]	36
Fig. 20. Correlation between specific wear resistance (W_s) and index including bulk modulus (B), Poisson’s ratio (ν) [203]	38
Fig. 21. a- typical <i>polyhedral clusters of the solute atoms found in MGs- $Ni_{81}B_{19}$, $Ni_{80}P_{20}$ and $Zr_{84}Pt_{16}$. Z8, Z9 etc. represents the coordination number of solute atom (number of atoms a central atom carries as its closest neighbors [217]) [167]; b, c, d- presents the typical cluster connection found in $Ni_{81}B_{19}$, $Ni_{80}P_{20}$ and $Zr_{84}Pt_{16}$, respectively. Voronix index (e.g. $<0,2,8,0>$) indicate the type of cluster (delineate with red dash circles) and FS, VS, ES represent the type of atoms sharing between the clusters and stand for face-sharing, vortex- sharing and edge-</i>	

<i>sharing, respectively. The bonds between atoms in the center clusters are not shown for clarity</i> [167]	39
Fig. 22. Correlation of the fracture energy E with the elastic modulus ratio G/B for selected as-cast metallic glasses [210,229]	40
Fig. 23. Summary of factors influencing on anticorrosion properties of metallic glasses [254]	42
Fig. 24. Volumetric changes of alloy during cooling with different cooling rates [263]	43
Fig. 25. Use of MG in surgical knives[267,268]	45
Fig. 26. Fluxgate sensor with Fe-based MG core a) schematic view b) development sensor [272]; c) Conical spring actuator developed with $Pd_{76}Cu_7Si_{17}$ metallic glass [273]	46
Fig. 27. Smallest geared-motor made of Zr-based MG a) schematic view of gear, b) MG gear c) assembled geared-motor- the smallest $d = 0.9$ mm, and the conventional $d = 1.5$ mm [86] .	47
Fig. 28. Most popular chemical elements present in Co-based metallic glasses marked with red frame [284].....	48
Fig. 29. Review of Co-based alloys with high glass-forming ability showing the relationship between D_c (critical diameter), compressive strength, and plastic strain [286]	49
Fig. 30. Potentiodynamic polarization curves of the $Co_{71-x}Ni_xMo_9P_{14}B_6$ ($x = 15, 20, 30$ at.%) obtained at room temperature in 3.5 wt.% NaCl solution (top) and 1 M HCl solution (bottom) [58]	50
Fig. 31. Anodic potentiodynamic polarization curves for $Co_{73.5-x}Si_{13.5}B_9Nb_3Cu_1Cr_x$ ($x=0, 8$) at different concentrations of H_2SO_4 [290]	51
Fig. 32. Fully amorphous Co-based metallic glasses with different shapes. a) Cast rods with diameters of 3.5 mm, 4 mm and 4.5 mm $CoFeNiBSiNb$ [283], b) gas atomized $CoTaB$ powder used to develop c) Co-based MG coatings [278]	52
Fig. 33. Correlation between hardness and density for metallic glasses [174–186]	53
Fig. 34. Research plan for Ph.D. thesis for obtaining samples for further test.....	54
Fig. 35. Analysis performed on all forms of samples obtained from $Co_{47.6}B_{21.9}Fe_{20.4}Si_{5.1}Nb_5$ and $Co_{42}B_{26.5}Fe_{20}Ta_{5.5}Si_5Cu_1$ in this thesis	55
Fig. 36. Graph showing the properties comparison (marked as an arrows) done in the <i>Discussion</i> chapter in this thesis	56
Fig. 37. Criteria for the alloys that will be investigated in the thesis.....	56
Fig. 38. Vacuum induction furnace VIM-LAB 50-60 used for alloying and casting for later atomization	60
Fig. 39. a) Schematic illustration of the atomization process [330] b) highest alloy temperatures in the atomization process to obtain a homogeneous liquid state.....	60
Fig. 40. Vortex mixer for powder fraction segregation Fritsch Analysette 3 Pro with sets of sieves and the fraction purpose in this work	61
Fig. 41. a) mLab Concept Laser printer, b) schematic illustration of scanning strategy [336]	62
Fig. 42. Atmospheric plasma spraying a) image of feedstock feeding into the plasma jet and b) image of coating development by spraying samples mounted on a rotational holder	64
Fig. 43. SEM powder images of $Co_{47.6}B_{21.9}Fe_{20.4}Si_{5.1}Nb_5$	69
Fig. 44. Particle size analysis of $Co_{47.6}B_{21.9}Fe_{20.4}Si_{5.1}Nb_5$ [330]	70
Fig. 45. Example of a) EDS analysis of chemical composition homogeneity and b) SEM image of the analyzed metallography section of $Co_{47.6}B_{21.9}Fe_{20.4}Si_{5.1}Nb_5$. White dotted line shows the analyzed particle	70
Fig. 46. X-ray diffractogram of $CoBFeSiNb$ alloy in form of powder	71
Fig. 47. Differential thermal analysis of $Co_{47.6}B_{21.9}Fe_{20.4}Si_{5.1}Nb_5$ powder	71
Fig. 48. Cast plate of $Co_{47.6}B_{21.9}Fe_{20.4}Si_{5.1}Nb_5$	72

Fig. 49. SEM of cast plate images with topographic (a, c) and material contrast (b, d). Image of the fracture (a, b) and cross-section (c, d)	73
Fig. 50. X-ray diffractogram of $\text{Co}_{47.6}\text{B}_{21.9}\text{Fe}_{20.4}\text{Si}_{5.1}\text{Nb}_5$ plate	73
Fig. 51. Differential scanning calorimetry of cast plate of $\text{Co}_{47.6}\text{B}_{21.9}\text{Fe}_{20.4}\text{Si}_{5.1}\text{Nb}_5$	73
Fig. 52. Example of indents done by nanohardness testing	74
Fig. 53. Results of the first-stage printing of $\text{Co}_{47.6}\text{B}_{21.9}\text{Fe}_{20.4}\text{Si}_{5.1}\text{Nb}_5$, x- sample destroyed in the process	75
Fig. 54. SEM images of six selected samples from the second stage of $\text{Co}_{47.6}\text{B}_{21.9}\text{Fe}_{20.4}\text{Si}_{5.1}\text{Nb}_5$ printing, in the description the laser power, scanning speed and energy destiny used for manufacturing samples	78
Fig. 55. X-ray diffractograms of BMG of $\text{Co}_{47.6}\text{B}_{21.9}\text{Fe}_{20.4}\text{Si}_{5.1}\text{Nb}_5$	79
Fig. 56. Nanoindentation analysis of $\text{Co}_{47.6}\text{B}_{21.9}\text{Fe}_{20.4}\text{Si}_{5.1}\text{Nb}_5$ a) hardness, b) elastic module.	79
Fig. 57. Different scanning calorimetry of SLM sample of $\text{Co}_{47.6}\text{B}_{21.9}\text{Fe}_{20.4}\text{Si}_{5.1}\text{Nb}_5$	80
Fig. 58. Analysis of the $\text{Co}_{47.6}\text{B}_{21.9}\text{Fe}_{20.4}\text{Si}_{5.1}\text{Nb}_5$ P65_v500 BMG sample developed by SLM a)-f) energy dispersive spectroscopy (EDS) map conduct with scanning transmission electron microscopy (STEM), g) TEM, selected area electrons diffraction (SAED) pattern	81
Fig. 59. Macroscopic image of the CoBFeSiNb coating developed by atmospheric plasma spraying, disk in diameter of 30 mm	81
Fig. 60. APS coatings of $\text{Co}_{47.6}\text{B}_{21.9}\text{Fe}_{20.4}\text{Si}_{5.1}\text{Nb}_5$ developed with different spraying distances	82
Fig. 61. Comparison of cross-section of the atmospheric plasma sprayed coatings of $\text{Co}_{47.6}\text{B}_{21.9}\text{Fe}_{20.4}\text{Si}_{5.1}\text{Nb}_5$ with spraying distance a) 90 mm and b) 110 mm	83
Fig. 62. X-ray diffractogram of plasma sprayed $\text{Co}_{47.6}\text{B}_{21.9}\text{Fe}_{20.4}\text{Si}_{5.1}\text{Nb}_5$	84
Fig. 63. Differential scanning calorimetry of plasma sprayed $\text{Co}_{47.6}\text{B}_{21.9}\text{Fe}_{20.4}\text{Si}_{5.1}\text{Nb}_5$	84
Fig. 64. Specific wear resistance of atmospheric plasma sprayed CoBFeSiNb alloy with high glass forming ability	86
Fig. 65. SEM powder images of $\text{Co}_{42}\text{B}_{26.5}\text{Fe}_{20}\text{Ta}_{5.5}\text{Si}_5\text{Cu}_1$	87
Fig. 66. Particle size analysis of $\text{Co}_{42}\text{B}_{26.5}\text{Fe}_{20}\text{Ta}_{5.5}\text{Si}_5\text{Cu}_1$ [330]	88
Fig. 67. Example of a) EDS analysis of the homogeneity of the chemical composition and b) SEM image of the metallography section analyzed of $\text{Co}_{42}\text{B}_{26.5}\text{Fe}_{20}\text{Ta}_{5.5}\text{Si}_5\text{Cu}_1$. White-dotted line shows the analyzed particle	88
Fig. 68. X-ray diffractogram of $\text{Co}_{42}\text{B}_{26.5}\text{Fe}_{20}\text{Ta}_{5.5}\text{Si}_5\text{Cu}_1$ powder	89
Fig. 69. Differential thermal analysis of $\text{Co}_{42}\text{B}_{26.5}\text{Fe}_{20}\text{Ta}_{5.5}\text{Si}_5\text{Cu}_1$	89
Fig. 70. Cast plate of $\text{Co}_{42}\text{B}_{26.5}\text{Fe}_{20}\text{Ta}_{5.5}\text{Si}_5\text{Cu}_1$ image	90
Fig. 71. SEM images of cast plate with EDS analysis of line marked with white dotted line	91
Fig. 72. X-ray diffractogram of $\text{Co}_{42}\text{B}_{26.5}\text{Fe}_{20}\text{Ta}_{5.5}\text{Si}_5\text{Cu}_1$ plate	92
Fig. 73. Differential thermal analysis of cast plate	92
Fig. 74. $\text{Co}_{42}\text{B}_{26.5}\text{Fe}_{20}\text{Ta}_{5.5}\text{Si}_5\text{Cu}_1$ ribbon, surface view from the wheel (a) and from the top (b)	93
Fig. 75. SEM images of $\text{Co}_{42}\text{B}_{26.5}\text{Fe}_{20}\text{Ta}_{5.5}\text{Si}_5\text{Cu}_1$ ribbon with BSE a) and SE b) contrast	93
Fig. 76. X-ray diffractogram of $\text{Co}_{42}\text{B}_{26.5}\text{Fe}_{20}\text{Ta}_{5.5}\text{Si}_5\text{Cu}_1$ ribbon	94
Fig. 77. Macro image of $\text{Co}_{42}\text{B}_{26.5}\text{Fe}_{20}\text{Ta}_{5.5}\text{Si}_5\text{Cu}_1$ samples (5 x 5 x 7 mm) from the first stage of an experiment. Laser power used for printing a) 55 W, b) 75 W, and c) 95 W [336]	95
Fig. 78. Results of the first-stage printing of $\text{Co}_{42}\text{B}_{26.5}\text{Fe}_{20}\text{Ta}_{5.5}\text{Si}_5\text{Cu}_1$ [336]	95
Fig. 79. SEM images of three chosen samples from the second stage of the printing of CoBFeTaSiCu (a-c) and example X-ray diffraction	99
Fig. 80. X-ray diffractograms of $\text{Co}_{42}\text{B}_{26.5}\text{Fe}_{20}\text{Ta}_{5.5}\text{Si}_5\text{Cu}_1$ SLM samples	99
Fig. 81. SEM sample P75_v800 a) BSE contrast, x100, b) BSE contrast, x500, c) SE contrast, x1000	100

Fig. 82. Differential scanning calorimetry of $\text{Co}_{42}\text{B}_{26.5}\text{Fe}_{20}\text{Ta}_{5.5}\text{Si}_5\text{Cu}_1$	101
Fig. 83. Transmission electron microscopy (TEM) diffraction images of a) reference b) amorphous regions c) composite region	101
Fig. 84. Analysis of $\text{Co}_{42}\text{B}_{26.5}\text{Fe}_{20}\text{Ta}_{5.5}\text{Si}_5\text{Cu}_1$ P75_v800 BMG sample developed by SLM a)-f) energy dispersive spectroscopy (EDS) map conduct with scanning transmission electron microscopy (STEM), g) reference image	102
Fig. 85. Macroscopic image of the CoBFeTaSiCu coating developed by atmospheric plasma spraying with polished surface.....	102
Fig. 86. Plasma spraying coatings of $\text{Co}_{42}\text{B}_{26.5}\text{Fe}_{20}\text{Ta}_{5.5}\text{Si}_5\text{Cu}_1$ developed with different spraying distance	104
Fig. 87. X-ray diffractograms of plasma sprayed $\text{Co}_{42}\text{B}_{26.5}\text{Fe}_{20}\text{Ta}_{5.5}\text{Si}_5\text{Cu}_1$	105
Fig. 88. Differential scanning calorimetry of plasma sprayed $\text{Co}_{42}\text{B}_{26.5}\text{Fe}_{20}\text{Ta}_{5.5}\text{Si}_5\text{Cu}_1$	105
Fig. 89. Specific wear resistance of atmospheric plasma sprayed CoBFeTaSiCu alloy with high glass forming ability	106
Fig. 90. Correlation between density of samples and energy density in the CoBFeSiNb samples printed with SLM	112
Fig. 91. Visualization of the conducted comparison of $\text{Co}_{47.6}\text{B}_{21.9}\text{Fe}_{20.4}\text{Si}_{5.1}\text{Nb}_5$	116
Fig. 92. Visualization of the conducted comparison of $\text{Co}_{42}\text{B}_{26.5}\text{Fe}_{20}\text{Ta}_{5.5}\text{Si}_5\text{Cu}_1$	128
Fig. 93. Visualization of the conducted comparison between $\text{Co}_{47.6}\text{B}_{21.9}\text{Fe}_{20.4}\text{Si}_{5.1}\text{Nb}_5$ and $\text{Co}_{42}\text{B}_{26.5}\text{Fe}_{20}\text{Ta}_{5.5}\text{Si}_5\text{Cu}_1$	130